

Syracuse University

SURFACE

Dissertations - ALL

SURFACE

August 2017

QUBIT COUPLED MECHANICAL RESONATOR IN AN ELECTROMECHANICAL SYSTEM

Yu Hao

Syracuse University

Follow this and additional works at: <https://surface.syr.edu/etd>



Part of the [Physical Sciences and Mathematics Commons](#)

Recommended Citation

Hao, Yu, "QUBIT COUPLED MECHANICAL RESONATOR IN AN ELECTROMECHANICAL SYSTEM" (2017).

Dissertations - ALL. 790.

<https://surface.syr.edu/etd/790>

This Dissertation is brought to you for free and open access by the SURFACE at SURFACE. It has been accepted for inclusion in Dissertations - ALL by an authorized administrator of SURFACE. For more information, please contact surface@syr.edu.

Abstract

This thesis describes the development of a hybrid quantum electromechanical system. In this system the mechanical resonator is capacitively coupled to a superconducting transmon which is embedded in a superconducting coplanar waveguide (CPW) cavity. The difficulty of achieving high quality of superconducting qubit in a high-quality voltage-biased cavity is overcome by integrating a superconducting reflective T-filter to the cavity. Further spectroscopic and pulsed measurements of the hybrid system demonstrate interactions between the ultra-high frequency mechanical resonator and transmon qubit. The noise of mechanical resonator close to ground state is measured by looking at the spectroscopy of the transmon. At last, fabrication and tests of membrane resonators are discussed.

**QUBIT COUPLED MECHANICAL
RESONATOR IN AN
ELECTROMECHANICAL SYSTEM**

by

Yu Hao

B.S., Nanjing University, 2010

DISSERTATION

Submitted in partial fulfillment of the requirements for the
degree of Doctor of Philosophy in Physics

Syracuse University

August 2017

Copyright ©2017 Yu Hao

All rights reserved

Acknowledgements

Firstly, I would like to express my deepest gratitude to my advisor, Professor Matthew LaHaye, not only for the financial support, but more importantly for his patience and encouragement throughout my Ph.D. study. His motivation and passion to science taught me what is deep inside a scientist. He also strongly influenced me on critical thinking and intuitions in physics.

My sincere gratitude also goes to Professor Britton Plourde. As a more experienced physicist in the experimental physics, he offered plenty of help from sharing lab instruments to fabrication recipes, and he is always willing to offer constructive suggestions and sharing knowledges and insights.

I would like to thank the rest of my thesis committee Professor Arindam Chakraborty, Professor Liviu Movileanu, Professor Jennifer Schwarz and Professor Joseph Paulsen. Their questions and comments are also insightful and enlightening.

My sincere thanks also go to the former Post-doc Dr. Francisco Rouxinol. He instructed me from scratch and inspired me in many aspects of research, such as fabrication, measurements and analysis. It is always eyes-opening talking to him, and it is precious memory to collaborate with him.

I thank my colleagues Dr. Matt Ware for teaching me knowledges of pulsed measurements; Dr. Chunhua Song for help on designing filters and Helmholtz coil, Dr. Matt Hutching for discussion about transmon and experiments. And I will thank Dr Ibrahim Nsanzineza, Dr daniela bogorin, and Caleb Howington for the help of research and lab work. I thank our theoretical collaborators Dr. Frederico Brito, Dr. Amir Caldeira. Dr. Elinor Irish for the help on theory and insightful suggestions for experiments.

Thanks to my friends of life Kai Luo, Yuan Zhong, Xu Zhou, Jiao He for the trust and appreciation we built between each other. Thanks to my dear friends at Syracuse

Duanduan Wan, Wei Jiang, Jie Yang, Di Sun, Zhenghua Zhou, Yu Chen, Dapeng Jing, Tao Zhang, Haozhi Wang, Yu Zhang for making me feel at home, for sharing happiness and bitterness, and for witnessing growth of each other at No.1 snowy city in the US. Thanks to cats Dandan and Wangwang for accompany when I wrote this thesis.

Most importantly I would like to thank my parents, who support me with unconditional support and endless love. Although Chinese culture pays extra attention to family reunion, they always encourage me to pursue my dreams oversea. Their personalities of braveness and persistence have become part of me.

To my parents

Contents

1	Introduction	xix
1.1	History and introduction	xix
1.2	Organization of thesis	1
2	Theory	3
2.1	cQED	3
2.1.1	Microwave cavity	3
2.1.2	Quantization of Electrical Harmonic Oscillator	6
2.1.3	Josephson junction	8
2.1.4	Cooper Pair Box	10
2.1.5	SQUID or Split junction	12
2.1.6	Transmon with adjustable Josephson energy	14
2.2	Mechanical resonator	17
2.3	Hybrid system of Mechanical resonator, Qubit and Cavity	18
2.4	dispersive coupling limit and rotating wave approximation	22
2.4.1	Rotating wave approximation	22
2.4.2	cavity dispersive shift	23
2.4.3	dispersive shift for transmon energy	24
2.5	Mechanical resonator as a dissipative bath	25

3	Design consideration	28
3.1	Broadband Filter and biased CPW cavity	28
3.1.1	Leakage and isolation of bias circuitry	29
3.1.2	Ground planes to protect from cross-talk	31
3.1.3	Lumped element reflective filter	31
3.1.4	T-filter biased CPW cavity	35
3.1.5	Radiation loss of qubit though the filter	35
3.2	Single resonance lumped LC	37
3.3	Transmon design	38
3.3.1	Relaxation and spontaneous emission	39
3.3.2	Dephasing time	40
3.4	Mechanical resonator	42
3.4.1	Beam	42
3.4.2	Membrane	43
3.4.3	Clamping loss	46
3.4.4	Differential mode of coupling	47
4	Fridge and measurement setup	49
4.1	Cryogenics cables and Filtering	49
4.1.1	RF input	51
4.1.2	RF output	53
4.1.3	dc Input line	54
4.1.4	Flux bias line	55
4.2	Magnetic shielding	55
4.3	Demodulation	57
4.3.1	heterodyne detection and heterodyne board	58

4.3.2	Digital homodyne and IQ extraction	60
4.3.3	Result	62
4.4	Measurement signal setup	63
4.4.1	Instrument setup	63
4.4.2	Time-domain Pulses	66
5	Fabrication	70
5.1	photolithography	72
5.1.1	Negative pattern and etching	74
5.1.2	Positive pattern and lift-off	76
5.1.3	CPW fabrication recipe	77
5.1.4	Nb etching recipe using PT720	77
5.2	E-beam lithography	78
5.2.1	Double angle evaporation and Josephson junctions	78
5.2.2	Josephson junction e-beam recipe	80
5.2.3	double angle evaporation recipe	81
5.3	Mechanical resonator deposition and releasing	82
5.3.1	MR e-beam recipe	84
5.3.2	MR hole etch recipe	86
5.4	Membrane	89
5.4.1	Membrane recipe	91
6	Filtered CPW cavity	94
6.1	Reflective T-filter	95
6.2	Filter biased CPW cavity	95
6.2.1	Frequency dependence of transmission	97

6.2.2	Power dependence	98
6.2.3	Gate dependence	100
6.2.4	Coupling strength dependence	102
6.2.5	First harmonic of the cavity	104
7	Transmon characteristic	107
7.1	Single tone spectroscopy	108
7.1.1	Flux dependence	109
7.1.2	Stability of flux period	111
7.1.3	Resonance limit of cavity and transmon higher states	112
7.2	Two tone spectroscopy	114
7.2.1	Qubit spectroscopy	114
7.2.2	Cavity photon number splitting	117
7.3	Time domain measurement	124
7.3.1	Rabi oscillation	124
7.3.2	Longitude Relaxation measurement	127
7.3.3	Ramsey interference and dephasing measurement	128
8	Hybrid system of Cavity-Transmon-MR	130
8.1	Continuous single tone	131
8.1.1	Single tone cavity spectroscopy at 0V	131
8.1.2	One tone cavity spectroscopy with gate voltage	136
8.1.3	Voltage dependence	137
8.2	Pulsed Cavity spectrum	138
8.2.1	Pulsed one tone	138
8.2.2	Voltage dependence	141

8.3	Continuous Qubit spectrum	143
8.4	Pulsed Qubit spectrum	144
8.4.1	Decoherence times	148
8.5	Temperature of system	150
8.5.1	effective temperature without voltage	150
8.5.2	Heating at high voltage	152
8.6	Conclusion	156
9	Membrane Resonator	157
9.1	Motional capacitance of MR	157
9.2	MR coupled to LC resonator	160
9.3	Measurement Results	162
9.3.1	Voltage dependence of doubly clamped Membrane	163
9.3.2	Voltage dependence of Free-free membrane	164
9.3.3	Power dependence of doubly Clamped membrane	166
9.3.4	Temperature dependence of doubly Clamped membrane	168
9.4	Conclusion	168
10	Future work	169
10.1	Dispersive shift of higher energy states	170
10.2	Using two photon g-f transition as a probe	171
10.3	Comparison of splitting in g-e and g-f transition	172
11	Conclusion	176

12 Appendix	178
12.1 High angle SEM tricks	178
12.2 Tools	180
12.2.1 Super cable Cutter	180
12.2.2 Twisted pair	180
12.3 Best MR coupling mode	182
12.4 Transmon Capacitance matrix	185
12.5 Interesting images	187
Bibliography	190

List of Figures

1.1	Gravitational wave dectector	xx
1.2	SEM of Silicon beam in Ref.[1]	xxi
1.3	SEM images of quantum electromechanical systems	1
2.1	schematic drawing of CPW cavity	4
2.2	cavity response, amplitude and phase	5
2.3	Sketch drawing of an electrical harmonic oscillator	6
2.4	Sketch drawing of a Josephson junction	8
2.5	Schematic drawing of a voltage biased Josephson junction	10
2.6	Schematic drawing of SQUID	12
2.7	Transmon with split junctions	14
2.8	Energy levels of transmon	15
2.9	Energy difference of adjacent transmon states	16
2.10	Simulation of element in overlap matrix n	16
2.11	Mechanical resonator and mode shape	17
2.12	Schematic drawing of the hybrid electromechanical system	19
2.13	Cavity dispersive shift	23
2.14	Simulation of number splitting	25
3.1	Optical image of old sample of hybrid system	29

3.2	Comparison of cavity leakage	30
3.3	Simulation of cross-talk problem	32
3.4	Design of reflective T-filter	33
3.5	Transmission property of reflective T-filter	34
3.6	Simulation of self-resonance of T-filter	35
3.7	Numerical simulation of Filter biased CPW cavity's harmonics	36
3.8	Purcell limit of Filter biased CPW cavity	36
3.9	CAD drawing of a lumped element LC transmission cavity.	37
3.10	Simulated transmission property of a lumped element LC cavity	38
3.11	Derivatives of transmon energy vs flux	41
3.12	Simulation of the mechanical resonator mode shapes	43
3.13	Simulation of Doubly clamped membrane resonator	44
3.14	Simulation of Free-free membrane resonator	45
3.15	Simulated force of free-free membrane legs vs leg position	46
3.16	Differential mode of free-free membrane	48
4.1	Fridge lines set up	50
4.2	Transmission measurement of RF input line.	52
4.3	Transmission measurement of dc line	54
4.4	Transmission measurement of Superconducting twisted pair	56
4.5	Photo of Cyroperm magnetic shielding.	56
4.6	Photo of home-made heterodyne board	58
4.7	Schematic drawing of heterodyne detection circuit	59
4.8	Transmissional test of home-made Heterodyne board.	62
4.9	Schematic drawing of instrument setup of pulse synchronization and analysis circuit.	64

4.10	Schematic drawing of Pulses doing quasi-continuous measurement of qubit spectroscopy	67
4.11	Schematic drawing of Pulses doing Rabi oscillation.	68
4.12	Schematic drawing of Pulses doing relaxation measurement.	68
4.13	Schematic drawing of Pulses doing Ramsey oscillation.	69
5.1	Optical picture and SEM images of hybrid system sample	71
5.2	Sketch map of photolithography using etching and lift-off process	73
5.3	SEM images of Nb etching	75
5.4	flagging from lift-off process.	76
5.5	Diagram of double angle evaporation process	79
5.6	SEM images of Josephson junction	80
5.7	Diagram of Mechanical resonator deposition and releasing	83
5.8	SEM images of different mechanical resonators.	85
5.9	SEM images of membrane	87
5.10	Diagram of membrane resonator deposition and releasing	88
5.11	SEM images of resist residues	90
6.1	Images of T-filter	95
6.2	Transmission measurement of T-filter	96
6.3	Schematic drawing of T-filter biased CPW cavity.	96
6.4	Transmission measurement of Filter biased CPW cavity	97
6.5	Transmission measurement of Filter biased CPW cavity, zoom-in	98
6.6	Power dependence of cavity	99
6.7	Gate dependence of cavity	101
6.8	Traces of cavity transmission at 0V and 20V	103
6.9	Loaded quality factor of cavity vs coupling capacitance	104

6.10	Simulation of cavity 1st harmonic	105
6.11	Transmission of cavity 1st harmonic	105
6.12	Transmission through gate port	106
7.1	Schematic drawing of hybrid system	107
7.2	Cavity response at two different flux bias	109
7.3	2-d map of cavity dispersive shift	110
7.4	Flux periods summary	112
7.5	Qubit induced splitting in cavity response	113
7.6	2-d map of qubit-cavity spectrum	115
7.7	Power dependence of qubit spectroscopy	116
7.8	Photon number splitting of g-e, g-f transition	118
7.9	Driven power dependence of number splitting	120
7.10	Photon number dependence of number splitting	121
7.11	Excitation power dependence of qubit spectrum	122
7.12	Rabi oscillation	124
7.13	2-d map of Rabi oscillation	125
7.14	Power dependence of Rabi oscillation	126
7.15	Relaxation measurement of a transmon qubit	127
7.16	Frequency and power dependence of Ramsey pulses	128
7.17	Ramsey oscillation of a transmon qubit	129
8.1	Schematic drawing of cavity-transmon-MR hybrid system.	131
8.2	One tone spectrum of cavity-transmon-MR system.	133
8.3	Cavity spectrum of hybrid system at -9.5V	134
8.4	Comparison of split-up positions with transmon-MR resonances	135

8.5	Measurements and simulation of single-tone spectroscopy of the cavity mode near gap	137
8.6	Numerical simulations of the expected populations of the transmon states	139
8.7	Pulsed measurement of single-tone cavity spectroscopy near the gap . . .	140
8.8	Pulsed measurements of single-tone cavity spectroscopy at different bias voltage	141
8.9	Comparison of cavity spectrum when qubit is excited by heated MR or coherent microwave.	142
8.10	Two-tone spectroscopy of transmon near the gap	145
8.11	Pulsed two tone spectroscopy of transmon near the gap	146
8.12	Extracted width of transmon resonance vs flux	148
8.13	Transmon relaxation time	149
8.14	Transmon dephasing time	149
8.15	Photon number splitting at 0V and -7V	151
8.16	Transmon temperature estimate	152
8.17	Simulation of chip heating	154
8.18	Simulation of temperature at qubit or MR area	154
8.19	Schematic drawing of thermal coupling of transmon and mechanical resonator.	155
9.1	Electro-mechanical model of MR	158
9.2	Sketch drawing of LC mis-match circuit	160
9.3	Reflection measurement of tunable LC resonator	161
9.4	Response of a doubly clamped membrane	162
9.5	Voltage dependence of doubly clamped membranes	163
9.6	Voltage dependence of a free-free membrane.	165
9.7	Power dependence of membrane resonance	166

9.8	Temperature dependence of membrane resonance	167
10.1	Qubit sensitivity of different transitions	171
10.2	Simulation of transmon spectrum against microwave power.	173
10.3	Simulated phonon number splitting of qubit, n=5	174
10.4	Simulated phonon number splitting of qubit, n=3	175
12.1	Charging effect of SEM	179
12.2	Schematic drawing of making superconducting twisted pair.	181
12.3	Schematic drawing of making superconducting twisted pair.	181
12.4	Transmon capacitance matrix	186
12.5	Data of “I got wifi”	188
12.6	Data of “fire”	188
12.7	Rainbow of photo resist	189
12.8	Data of “Ninja Turtle”	189

Chapter 1

Introduction

1.1 History and introduction

The origin of the quantum electromechanical system dates back to the early development of gravitational wave(GW) detection using mass-resonance transducer, and a noise temperature of 1.1 mK was achieved.[2, 3]. Thereafter superconducting technology played a more important role in GW detecting with low temperature superconducting bars and superconducting quantum interference devices (SQUID)[4] or superconducting microwave resonators[5].

A second path traces back to the development of new superconducting devices - like the superconducting single-electron transistor[4] - and new mechanical fabrication and detection techniques in the 1990s. These developments lead in the following decade to the emergence of nanoelectromechanical systems with integrated superconducting circuitry, which enabled detection of nanomechanical motion with sensitivity approaching the quantum limit[7]. This showed the way to a new frontier and great potential for

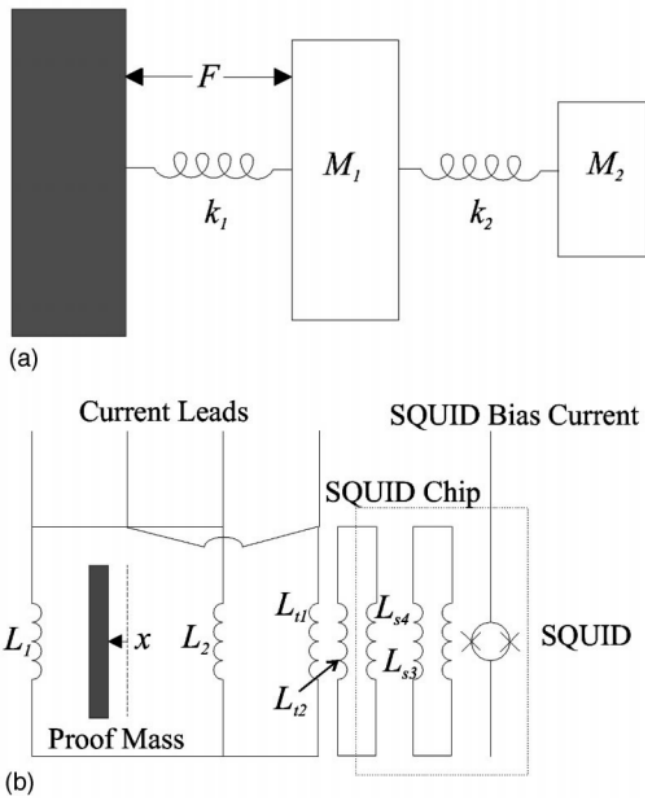


Figure 1.1: Figure from Ref.[6]. (a) Mechanical model of antenna with transducer mass. (b) Circuit diagram of the transducer.

using these systems to explore macroscopic quantum effects[8].

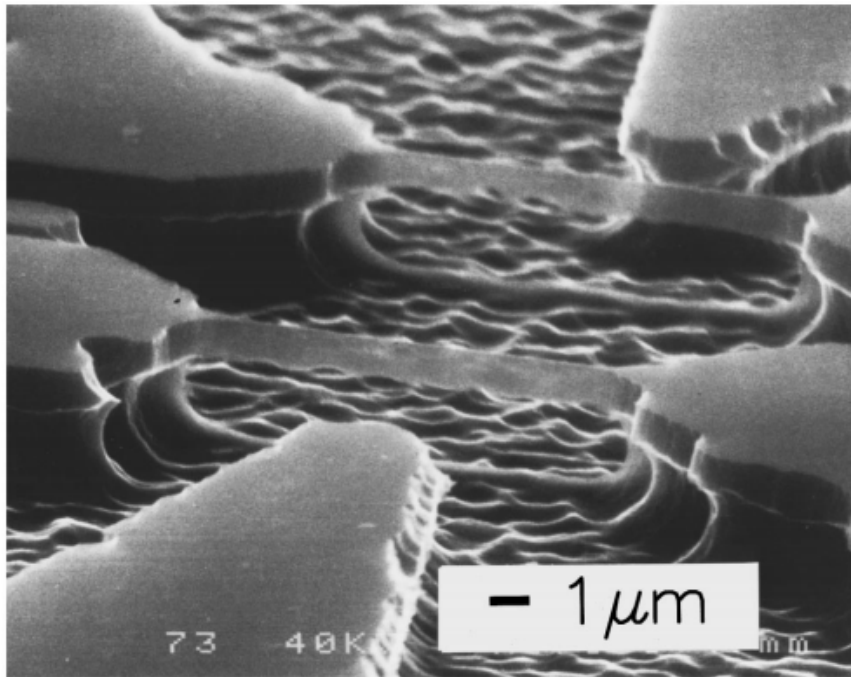


Figure 1.2: SEM micrograph of an undercut Si beam from [1].

Over the last decade more developments in superconducting circuit technology - including superconducting quantum bit (Qubits) and circuit QED - began to enable the study of basic quantum effects in mechanical structures on a micro to nanoscale.

The first demonstration of the interaction of flexural mode of nano-mechanical resonator and a superconducting phase qubit was conducted in in 2009[9]. In this experiment a charge qubit or cooper pair box (CPB) is far detuned with nano-mechanical resonator. Interaction built by electrical fluctuation between qubit and mechanical resonator dipersively shifts the resonance of nano-mechanical resonator depend on the state of the qubit. In 2010 a big improvement was done in demonstrating the first use of superconducting charge qubit to measure the quantum property of mechanical piezo-disk[10]. Further single quantum excitation in phonon was shown, taking the first step to complete quantum control of a mechanical system. This work was a milestone in quantum physics com-

munity. More recently in 2013, dispersive interactions between a transmon qubit and a mechanical drumhead was observed.[11] This result shows the evidence of Stark shifts in qubit's energy, which is proportional to the number of quanta in mechanical resonator.

The goal of this research in this thesis is to develop a new quantum electromechanical system using the qubit and superconducting circuit technology developed in the last decade to develop a platform for performing more advanced quantum measurements of mechanical systems.

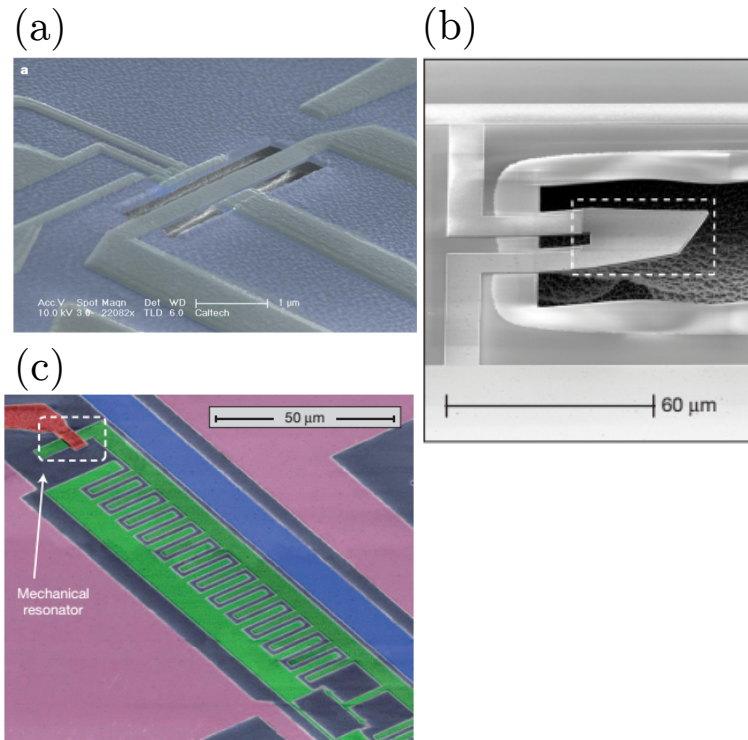


Figure 1.3: SEM images of quantum electromechanical systems. (a)Ref.[9],(b)[10],(c)[11]

1.2 Organization of thesis

The thesis is organized as following: Chapter 2 gives a basic description of cQED and theory exploring the hybrid system of qubit coupled mechanical system. Chapter 3 connects

the basic theory to experimental realization of each separate element of the hybrid system, voltage biased cavity, transmon qubit and mechanical resonator. In Chapter 4 fridge wiring and signal processing is discussed in details. Next chapter 5 shows the design and fabrication of the cavity, qubit and mechanical resonator. This section contains technical considerations and recipes of each step. Chapter 6 to chapter 8 present successive experimental results of voltage biased cavity, transmon, the coupled transmon+qubit system. Chapter 6 demonstrates the realization of T-filter biased superconducting CPW cavity, which serves as a tool to probe the state of qubit whose characteristics are presented in Chapter 7. Chapter 8 is the main results of hybrid electro-mechanical system which consists of a transmon qubit coupled nano-mechanical resonator embedded in T-filter biased CPW cavity. In chapter 9 represents separated results of membrane developed very recently, which can be incorporate into qubit coupled system in the future.

Chapter 2

Theory

Electro-mechanical systems usually involve separate elements with various different degree of freedom. For example in superconducting qubit, Cooper pairs staying in a Bose-Einstein condensed state can be described by a free variable: the phase of wave-function. While in a mechanical resonator, collective movement of atoms in a bulk of metal forms the motional degree of freedom. In this chapter I will theoretically analyze the hybrid system by studying the basics of each element and get into the description of the coupled system in different regime of coupling and dissipation strength.

2.1 cQED

2.1.1 Microwave cavity

Microwave cavities are used in cQED as a very basic tool to generate and control photons at discrete frequencies with high quality factor. There are different types of super-

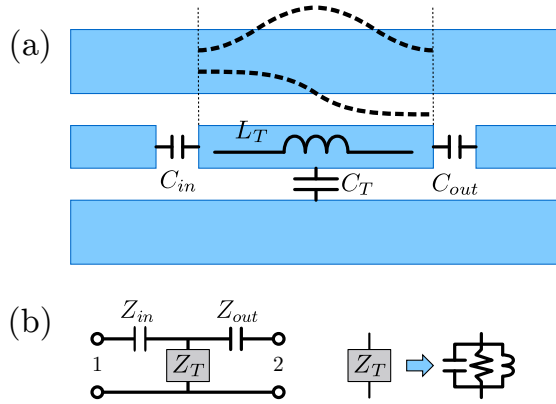


Figure 2.1: (a) Schematic drawing of a CPW cavity which is formed by breaking the center line of a transmission line. The blue color indicates ground planes and center line made by a thin layer of metal. The two break points function as input/output capacitors C_{in}/C_{out} coupling to the external circuitry, as well as define the position of anti-nodes of eigen modes (dashed lines). The equivalent inductance and capacitance of the cavity is denoted as L_T and C_T . (b) equivalent impedance network of CPW cavity.

conducting microwave cavities: 2-dimensional (2-d) or 3-dimensional (3-d), reflective or transmissional, transmission line type or lumped element type. Here we first show the classical analysis of a half-wave co-planar wave-guide (CPW) cavity using equivalent but general lumped element circuit model, which can be applied to all types of microwave cavity.

A CPW cavity is a segment of 2d transmission line, which is only capacitively coupled to ground plane and input/output transmission lines, see Fig 2.1(a). The length of center line determines the frequencies of modes inside the cavity by constraining the break points as anti-nodes of eigen modes. The fundamental mode has electrical field node in the center and anti-nodes at two ends. In our experiments, the length of cavities is about 10 mm, resulting a fundamental mode ~ 5 GHz. The frequency response of each cavity mode can be probed by applying microwaves to the input port and measuring the transmitted signal at the output port. Such transmission measurements provide a way to probe the CPW mode's interaction with other systems, such as a nanoresonator or

superconducting qubit.

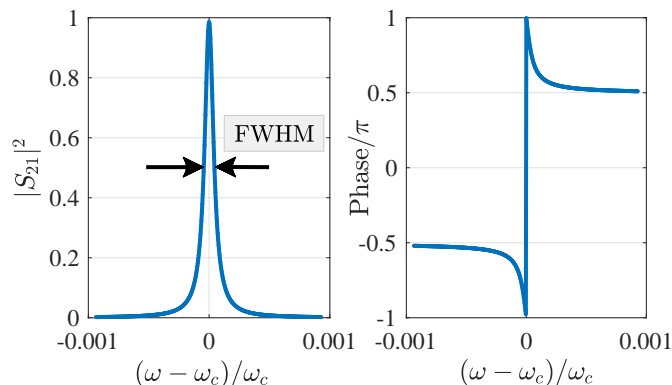


Figure 2.2: Simulated transmitted signal of a CPW-type cavity mode. (a) the square of the amplitude $|S_{21}|$ is proportional to the power passing through the cavity. The curve has a Lorentz shape with a quality factor $\approx 10^4$. The FWHM $\delta\omega$ is indicated by arrows. (b) the phase of S_{21} in the unit of π .

CPW cavity To model the transmission characteristics of the CPW-type cavity, a simplified circuit model is employed, as shown in Fig 2.1(b). In this model C_T and L_T are the capacitance and inductance of the cavity, and the resistor is added to account for internal loss such as substrate dissipation. Following the standard method of network analysis [12], the total impedance of the cavity tank is

$$Z_T = \frac{1}{i\omega C_T + \frac{1}{i\omega L_T} + \frac{1}{R}} \quad (2.1)$$

With the input(output) impedance $Z_{in(out)} = Z_0 + \frac{1}{i\omega C_{in(out)}}$, we can build the impedance matrix

$$\mathbf{Z} = \begin{bmatrix} Z_{in} + Z_T & Z_T \\ Z_T & Z_{out} + Z_T \end{bmatrix}$$

The scatter matrix is $\mathbf{S} = (\mathbf{Z} - Z_0\mathbf{I})/(\mathbf{Z} + Z_0\mathbf{I})$, where $Z_0 = 50\Omega$ and \mathbf{I} is the unit matrix.

The transmitted amplitude is given by

$$S_{21} = \frac{2Z_0Z_T}{(Z_{out} + Z_{in} + 2Z_0)Z_T + Z_{in}Z_{out} + Z_0(Z_{in} + Z_{out}) + Z_0^2} \quad (2.2)$$

The transmission function takes a form of

$$S_{21} = \frac{1}{1 + i2Q(\omega - \omega_c)/\omega_c} \quad (2.3)$$

where $\omega_c = \frac{1}{L_T(C_T + C_{in} + C_{out})}$, as shown in Fig 2.2. The quality factor

$$Q = \left(\frac{1}{Q_i} + \frac{1}{Q_c} \right)^{-1}$$

where $Q_i = C_T\omega_c R$ is the internal quality factor and $Q_c = \frac{C_T}{\omega_c Z_0(C_{in}^2 + C_{out}^2)}$ called coupling quality factor describe how fast the photon are tunneled to external circuit from the cavity. The “full width at half maximum” (FWHM)= ω_c/Q is the width of the curve measured between points are half of the maximum on vertical axis.

2.1.2 Quantization of Electrical Harmonic Oscillator

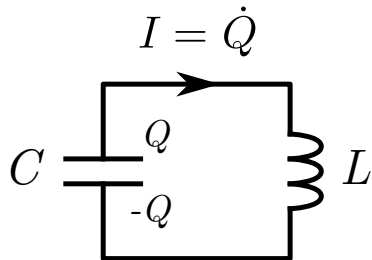


Figure 2.3: Sketch drawing of an electrical harmonic oscillator. It consists of a capacitor C and inductor L . The current following in the circuit is denoted as I , and the charge on the capacitor is Q .

In cQED it is typical to model cavities as a quantum harmonic oscillator. To develop theory in a concrete way, I'll start with quantization of a electrical harmonic oscillator consisting of a capacitor and an inductor in parallel, see Fig 2.3. One can choose charge Q as the free variable of the system and write the Lagrangian \mathcal{L} as

$$\mathcal{L} = \frac{1}{2}L\dot{Q}^2 - \frac{1}{2}\frac{Q^2}{C} \quad (2.4)$$

Following the standard method in classical mechanics we can find the canonical momentum of free variable Q :

$$\Phi = \frac{\partial \mathcal{L}}{\partial \dot{Q}} = L\dot{Q}$$

and from Lagrangian \mathcal{L} we can find out its Hamiltonian H

$$\begin{aligned} H &= \Phi \cdot \dot{Q} - \mathcal{L} \\ &= \frac{1}{2}\frac{\hat{\Phi}^2}{L} + \frac{1}{2}\frac{\hat{Q}^2}{C} \end{aligned} \quad (2.5)$$

Where $\hat{\Phi}$ is the canonical momentum operator of \hat{Q} and is the magnetic flux inside inductor L . The energy of the system is exchanging between the inductor and the capacitor at a angular frequency $\omega = \frac{1}{LC}$. We can further define “ladder operator” developed by Paul Dirac to simplify the Hamiltonian:

$$\begin{aligned} \hat{a} &= \frac{1}{\sqrt{2\hbar\omega}}\left(\frac{\hat{Q}}{\sqrt{C}} + i\frac{\hat{\Phi}}{\sqrt{L}}\right) \\ \hat{a}^\dagger &= \frac{1}{\sqrt{2\hbar\omega}}\left(\frac{\hat{Q}}{\sqrt{C}} - i\frac{\hat{\Phi}}{\sqrt{L}}\right) \\ H &= \left(\hat{a}^\dagger\hat{a} + \frac{1}{2}\right)\hbar\omega \end{aligned} \quad (2.6)$$

This is exact the same form as standard quantum harmonic oscillator with equally spaced

energy eigen-states.

2.1.3 Josephson junction

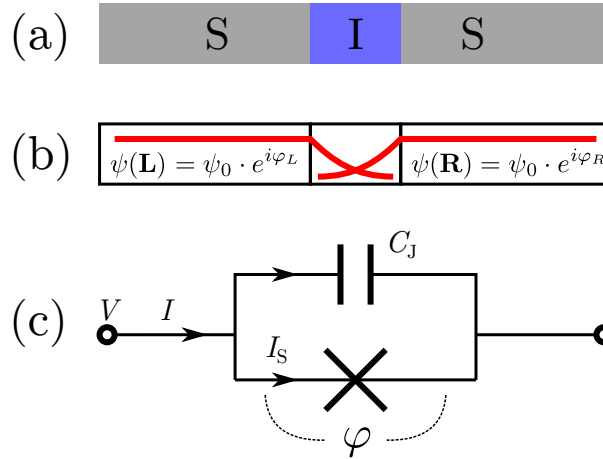


Figure 2.4: Sketch drawing of a Josephson junction. (a) Josephson junction structure consisting two superconducting metal (denoted as “S”) sandwiching a thin layer insulator (“I”). (b) Pseudo-wavefunction of Cooper pairs in different regime. The red line indicates decay of wavefunction from superconductor to insulator. (c) Equivalent electrical circuit of a Josephson junction. The “cross” represents an ideal Josephson junction and the capacitor represents its junction capacitance C_J

Josephson junction is a crucial element in transmon qubit system. It consists of two superconducting metal connecting by a non-superconducting inter-layer. In our experiment, we use insulator to form a S-I-S structure, where the superconductor is aluminum and the insulator is aluminum oxide, as shown in Fig 2.4(a).

GL theory The behavior of the Josephson junction can be described by a macroscopic method called “Ginzburg-Landau theory”. The state of Cooper pairs is described by a complex pseu-wavefunction $\psi(\mathbf{r})$, whose amplitude is related with local density of cooper pairs $|\psi(\mathbf{r})|^2 = n(\mathbf{r})$.

The basic postulate of GL is that ψ varies slowly in space, which is valid in our system. The size of junction is usually 100nm to microns in area and ~ 10 nm in thickness, which is much smaller than the wavelength (millimeters) of microwave signal (gigahertz).

As shown in Fig 2.4(b), the pseudo-wavefunction in the superconductors has constant charge density and different phases: φ_L and φ_R , the change is $\varphi = \varphi_R - \varphi_L$. Inside of insulator the wavefunctions extend and decay spatially as the red line shows. By combining the wavefunction and GL current expression (not shown here), we can obtain the relation between the superconducting current I_s and phase different φ

$$I_s = I_c \sin \varphi \quad (2.7)$$

where $I_c = \pi\Delta(0K)/2eR_n$ is the critical current of this junction and R_n is the resistance in normal state and $\Delta(T)$ is the gap energy at temperature T . The voltage across the junction is related with the phase difference $V = \dot{\Phi} = \frac{\phi_0}{2\pi}\dot{\varphi}$. The potential energy of the junction can be calculated by integrating the electrical work

$$U(\varphi) = \int I_s \cdot V dt = \int I_s \frac{\phi_0}{2\pi} d\varphi = \text{const.} - E_J \cos \varphi \quad (2.8)$$

where $E_J \equiv \frac{\hbar I_c}{2e}$ is called the Josephson energy of the junction.

Note this is the case with no presence of magnetic field. A SQUID system with magnetic field applied will be discussed later.

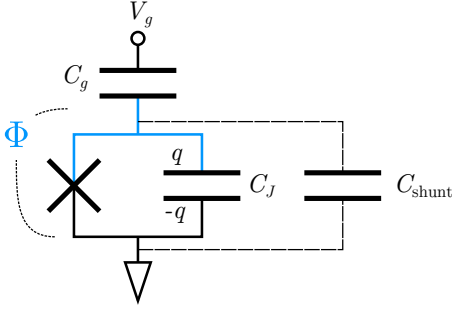


Figure 2.5: Schematic drawing of a voltage biased Josephson junction. The blue metal, usually called “island” is an isolated metal connected through a Josephson junction to ground and capacitively (C_g) coupled to voltage bias V . The wave-function phase of island is Φ . The capacitance of junction is denoted as C_J . In many cases, the junction is also shunted with a classical capacitor C_{shunt}

2.1.4 Cooper Pair Box

A voltage shunted Josephson junction is one of simplest quantum system, usually called Cooper pair box (CPB). In the limit that the junction capacitance is small, Coulomb Blockade effects dominant over the Josephson effect, and thus in this limit charge is a “good” quantum number of the system.

CPB Hamiltonian To describe the system, first we can write the Lagrangian of the system, without the loss of generality, the magnetic phase of ground superconductor is 0, the magnetic phase of island is Φ ,

$$\mathcal{L} = \frac{1}{2}C_g(V_g - \dot{\Phi})^2 + \frac{1}{2}C_J\dot{\Phi}^2 + E_J \cos(2\pi\frac{\Phi}{\Phi_0})$$

where V_g is the bias gate voltage and follow the standard method in classical mechanics finding the canonical momentum, which is equivalent to charge, $P_\Phi = \frac{\partial \mathcal{L}}{\partial \dot{\Phi}} = -C_g V_g + C_\Sigma \dot{\Phi}$, where $C_\Sigma = C_g + C_J$ is the total capacitance of the island. In many cases the island shunted with a classic capacitor C_{shunt} , this capacitance can be absorbed in to total

capacitance $C_\Sigma = C_g + C_J + C_{\text{shunt}}$.

The Hamiltonian of the system is obtained

$$\begin{aligned} H_{CPB} &= P_\Phi \cdot \dot{\Phi} - \mathcal{L} \\ &= \frac{1}{2C_\Sigma} (P_\Phi + C_g V_g)^2 - E_J \cos \varphi \end{aligned}$$

where $\varphi = 2\pi \frac{\Phi}{\Phi_0}$. This can be further simplified by letting $P_\Phi = -2ne$, n is the number of excessive Cooper pairs on the island and $n_g = C_g V_g / 2e$.

$$H_{CPB} = 4E_C (n - n_g)^2 - E_J \cos \varphi \quad (2.9)$$

where $E_C = \frac{e^2}{2C_\Sigma}$ is the energy needed to transfer one electron onto the island.

Commutation relation The commutation relation of charge number operator $\hat{n} = i \frac{\partial}{\partial \varphi}$ and $\hat{\varphi}$ inherited from Φ and P_Φ is

$$[\hat{n}, \hat{\varphi}] = i, \quad \Delta n \cdot \Delta \varphi \geq 1 \quad (2.10)$$

In the CPB limit where the total capacitance of island is small, $E_C \gg E_J$. The energy eigen-states are very close to charge number state, the energy of the system is dominated by how many pairs of electrons are tunneled on the island, and n describing the number Cooper pairs on the island is a good quantum number.

2.1.5 SQUID or Split junction

Gauge invariant phase In the presence of magnetic field, the phase difference φ does not have unique value. To overcome this difficulty, the phase is replaced by “gauge invariant phase”

$$\tilde{\varphi} \equiv \varphi - (2\pi/\Phi_0) \int \mathbf{A} \cdot d\mathbf{s}$$

where \mathbf{A} is the potential vector of magnetic field, and the integration loop goes from one side of junction to the other side. In terms of $\tilde{\varphi}$, the superconducting current is generalized as

$$I_s = I_c \sin \tilde{\varphi}$$

As long as no magnetic field is applied, $\mathbf{A} = 0$, $\tilde{\varphi}$ and φ are equivalent and exchangeable.

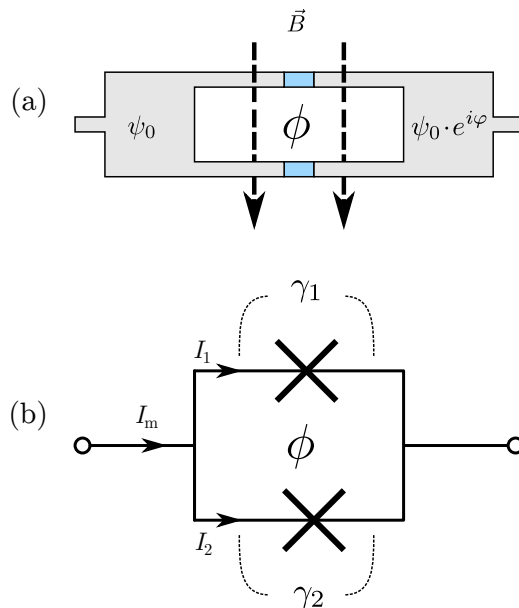


Figure 2.6: (a) Schematic drawing and (b) equivalent circuit of a split junction consisting of two identical junctions.

Split junction A SQUID has two Josephson junctions in parallel forming a loop. Magnetic field \vec{B} is applied inside the loop. We can also assume the wavefunction phase of left superconductor is 0 and that of the right is φ . In the presence of the magnetic field, we calculate the gauge invariant phase $\tilde{\varphi}_1$ and $\tilde{\varphi}_2$ across the top and bottom junction respectively.

$$\begin{aligned}\tilde{\varphi}_1 &= \varphi - \frac{2\pi}{\Phi_0} \int_1 \mathbf{A} \cdot d\mathbf{s} \\ \tilde{\varphi}_2 &= \varphi - \frac{2\pi}{\Phi_0} \int_2 \mathbf{A} \cdot d\mathbf{s}\end{aligned}$$

The total flux integrated across a hole has to be the multiples of flux quanta $\oint_{\text{hole}} \mathbf{A} \cdot d\mathbf{s} = N \cdot \Phi_0$, thus

$$\tilde{\varphi}_1 - \tilde{\varphi}_2 = \frac{2\pi\phi}{\Phi_0} \pmod{2\pi}$$

where $\phi = B \times \text{Area}$ is the total magnetic flux applied in the loop. In the case the two junctions are identical, the total potential energy of the system is

$$\begin{aligned}U(\varphi) &= -E_{J1} \cos \tilde{\varphi}_1 - E_{J2} \cos \tilde{\varphi}_2 \\ &= -E_{J,\text{eff}} \left| \cos\left(\frac{\pi\phi}{\Phi_0}\right) \right| \cos \varphi\end{aligned}\tag{2.11}$$

The result indicates that by applying external magnetic field, the effective Josephson energy is adjustable.

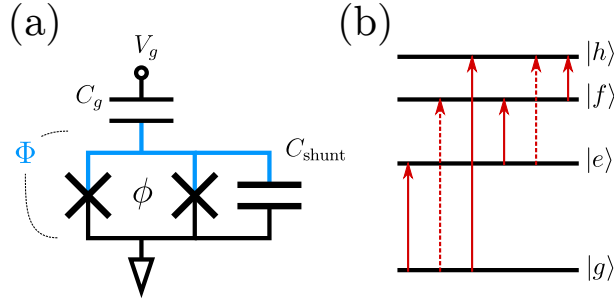


Figure 2.7: (a) Schematic drawing of a transmon with split junctions. (b) Schematic drawing of first four energy eigen-states. The red solid (dashed) lines represents transition allowed (forbidden) in golden rules or single photo excitation.

2.1.6 Transmon with adjustable Josephson energy

A transmon qubit is a CPB shunted with a large capacitor $C_{\text{shunt}} \gg C_J, C_g$ in Figure 2.7, the Hamiltonian of the system has a similar form of a CPB system[13, 14]

$$\hat{H} = 4E_C(\hat{n} - n_g)^2 - E_{J,\text{eff}}(\phi) \cos \hat{\phi} \quad (2.12)$$

$$= 4E_C(n - n_g)^2 |n\rangle\langle n| - \frac{1}{2}E_{J,\text{eff}}(\phi)(|n\rangle\langle n+1| + |n+1\rangle\langle n|) \quad (2.13)$$

where

$$E_{J,\text{eff}} = (E_{J1} + E_{J2}) \cos\left(\frac{\pi\Phi}{\Phi_0}\right) \sqrt{1 + d^2 \tan^2\left(\frac{\pi\Phi}{\Phi_0}\right)} \quad (2.14)$$

and $d = \frac{E_{J1} - E_{J2}}{E_{J1} + E_{J2}}$ is the asymmetry of the junctions. $|n\rangle$ is the charge number eigenstate of operator $\hat{n} |n\rangle = n |n\rangle$, representing n excessive cooper pairs reside on the island.

The energy eigen-states are denoted as $|g\rangle, |e\rangle, |f\rangle, |h\rangle$ and etc. as shown in Figure 2.8.

Unlike the harmonic oscillator, these states are not equally spaced. If we consider only the lowest two states, the system can be treated as two-level system, or a qubit. In the limit of $E_J \gg E_C$, the system behaves more “linearly”; the energy difference between levels approximates as $E_{j1} \approx (j-1)\sqrt{8E_J E_C} - \frac{j(j-1)}{2}E_C$ and energy difference of adjacent states goes to E_C as shown in Figure 2.9.

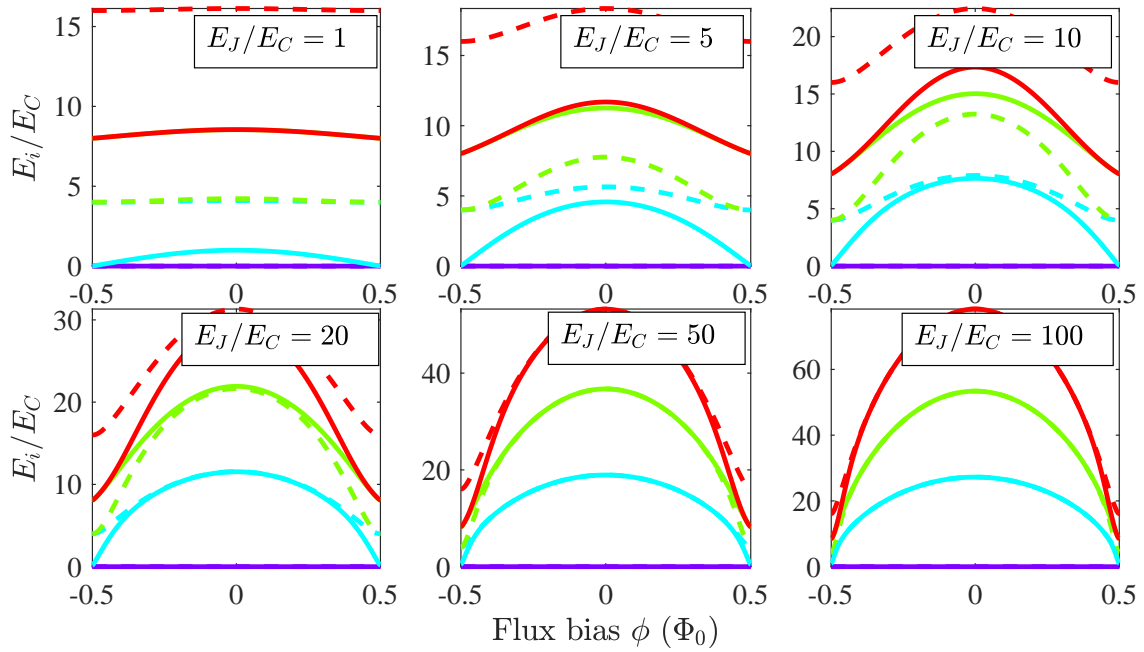


Figure 2.8: Analytic solution of CPB/transmon system's eigen-energies. In each plot, the four lowest energy eigen-states are plotted, same states are plotted in same color: purple- $|g\rangle$, blue- $|e\rangle$, green- $|g\rangle$, red- $|h\rangle$. The solid (dashed) line is the solution at $n_g = 0$ ($n_g = 0.5$).

The transmon/CPB system is normally capacitively coupled to other system or external detection circuits, resulting in an interaction strength that is proportional to \hat{n} , thus it is useful to check the overlap elements of operator $\langle i | \hat{n} | j \rangle$. See shown in Figure 2.10.

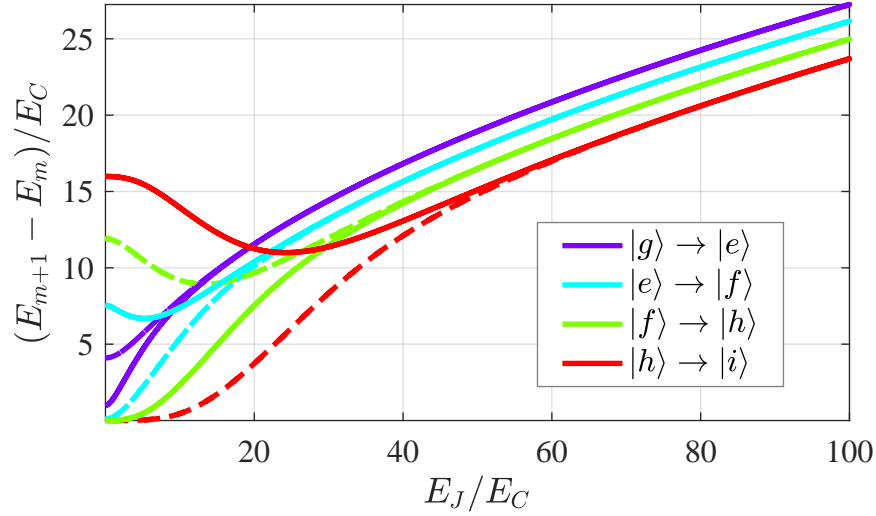


Figure 2.9: Energy difference of adjacent energy eigen-states as a function of E_J/E_C . The solid (dashed) line is the solution at $n_g = 0$ ($n_g = 0.5$).

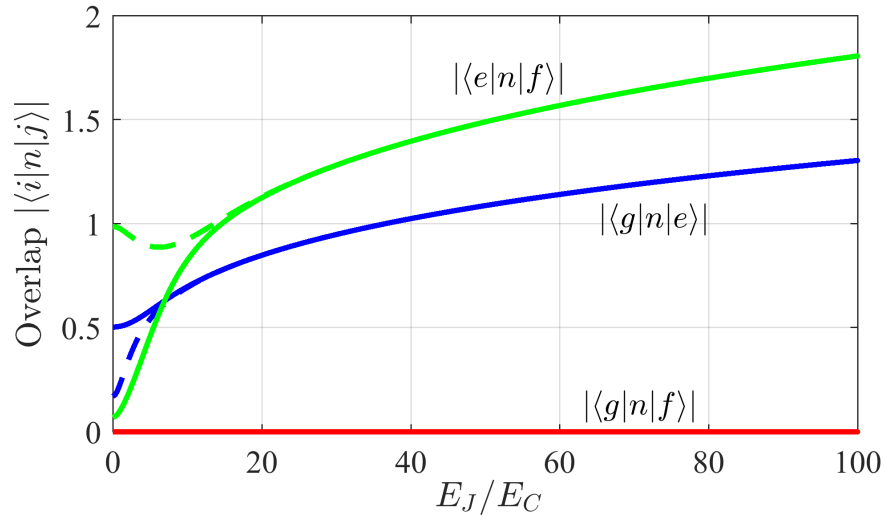


Figure 2.10: Analytic calculation of overlap elements of operator \hat{n} . The solid (dashed) line is the solution at $n_g = 0$ ($n_g = 0.5$).

2.2 Mechanical resonator

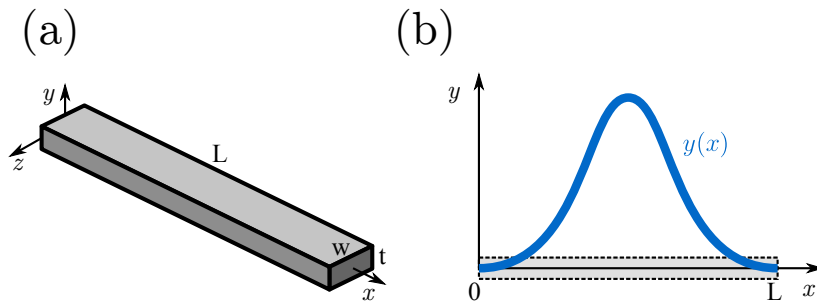


Figure 2.11: (a) sketch drawing of a long thin beam with two ends clamped. (b) Shape of fundamental mode of equivalent 1d string.

The mechanical resonator in our system is a beam or membrane whose degrees of freedom represent the vibrational motion of the different modes of the mechanical structure. Such resonators have been studied and utilized in many different contexts [10, 11, 13, 15, 16], and are well known to be accurately modelled by continuum elasticity theory. Here I will focus on the case of thin beam with clamped-clamped boundary conditions. The movement can be detected using qubit, opto-mechanical cavity, or magneto-motive detection or impedance match circuits. In this section, I will focus on the classical description of a doubly clamped beam as shown in Figure 2.11. The quantization of mechanical resonator is similar to that of electrical field, and for detailed process, please refer to Dr. Elinor Irish's thesis [17].

Assume the two sides of the long beam are clamped, and only movement on y and z directions are allowed. If we only care about the flexural movement on y -direction (coupling of the other directions are negligible), we can simply reduce it to a 1-d beam with two ends at $x = 0$ and $x = L$ fixed. Because the whole side walls of the beam are clamped, the two ends of the 1d string are flat. In the linear regime, the displacement of beam at position x

and time t , $Y(x, t)$ obeys the Euler-Bernoulli beam theory

$$\rho(x)S(x)\frac{\partial^2 Y}{\partial t^2} = -\frac{\partial^2}{\partial x^2} \left[E(x)I(x)\frac{\partial^2 Y}{\partial x^2} \right] \quad (2.15)$$

where ρ is the density of mass, E is Young's elastic module and $I(x) = \int y^2 dydz$ is the second moment of area. We further assume the cross section $S(x)$, and material properties are uniform. The general solution for this differential equation is

$$Y(x, t) = y(x)e^{i\omega t} \quad (2.16)$$

$$= (A_1 \sin(kx) + A_2 \cos(kx) + A_3 \sinh(kx) + A_4 \cosh(kx)) e^{i\omega t} \quad (2.17)$$

Assuming the clamped-clamped boundary conditions:

$$\begin{cases} y(0) = y(L) = 0 \\ y'(0) = y'(L) = 0 \end{cases} \quad (2.18)$$

we can get

$$\begin{cases} \cos(k_n L) \cdot \cosh(k_n L) = 1 \\ r_n = \frac{A_1}{A_2} = -\frac{A_4}{A_3} = \frac{\sin(k_n L) + \sinh(k_n)}{\cos(k_n L) - \cosh(k_n)} \\ \omega_n = \sqrt{\frac{EI k_n^4}{\rho S}} = \sqrt{\frac{Et^2 k_n^4}{12\rho}} \end{cases}$$

2.3 Hybrid system of Mechanical resonator, Qubit and Cavity

In the foregoing sections I have discussed the basics of all individual components. Now I will consider the whole hybrid system in which they are all coupled. First, the mechanical

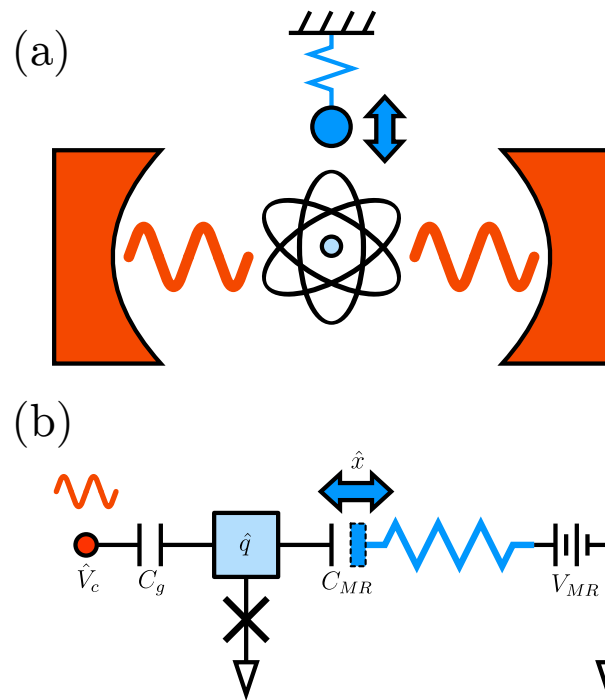


Figure 2.12: (a) schematic drawing of an atom coupled to a cavity and mechanical resonator. (b) Simplified circuit of a qubit capacitively coupled to a cavity \hat{V}_c and mechanical resonator \hat{x} .

resonator is capacitively (C_{MR}) coupled to transmon island, and when the mechanical resonator vibrates, the change of position results in change of capacitance. Along with biased voltage V_{MR} on the mechanical resonator, fluctuation in position degree of freedom generates charge fluctuation on qubit island and affects the state of qubit. To read out the state of the transmon qubit, the cavity is capacitively coupled through gate capacitance C_g . In this section, I will model the interaction between transmon with mechanical resonator and cavity.

Similarly to the case of CPB, the total applied charge on the transmon island is

$$Q = V_c \cdot C_g + V_{MR} \cdot C_{MR} \quad (2.19)$$

where V_c is the voltage fluctuation of the cavity coupled through gate C_g . V_{MR} and C_{MR} are the voltage bias on the mechanical resonator and its capacitance between the qubit island. We can separate the charge Q into two parts: the dc part can be canceled by Cooper pairs tunneling onto the island. The rf part is

$$\Delta Q = V_c \cdot C_g + V_{MR} \cdot \Delta C_{MR} \quad (2.20)$$

in which the first term is the standard interaction between cavity and qubit and the second term proportional to the change in C_{MR} is an effect of mechanical displacement. The Hamiltonian of transmon can be written as

$$H_q = 4E_C \left(\hat{n} - \frac{\hat{V}_c C_g}{2e} - \frac{V_{MR} \Delta \hat{C}}{2e} \right)^2 + E_j \cos \hat{\varphi} \quad (2.21)$$

$$\approx 4E_C \hat{n}^2 + E_j \cos \hat{\varphi} - \frac{4E_C C_g}{e} \hat{n} \cdot \hat{V}_c - \frac{4E_C V_{MR}}{e} \frac{\partial C_{MR}}{\partial x} \hat{n} \cdot \hat{x} \quad (2.22)$$

where x is the displacement of mechanical resonator, and $\frac{\partial C_{MR}}{\partial x} \simeq \frac{C_{MR}}{d}$ is the change in

transmon-MR capacitance respect to change in displacement. The first two terms are original Hamiltonian for transmon qubit and the last two are interactions with cavity and mechanical resonator. The terms including $\hat{V}_c \hat{x}$ describes the cross talk between cavity can mechanical resonator is normally very small and neglected (not shown). So the Hamiltonian of the whole system can be written by adding energies of cavity can mechanical resonator which we showed before

$$\begin{aligned}
H &= H_q + H_c + H_{MR} + H_{q,c} + H_{q,MR} \\
&= \hbar\omega_j |j\rangle\langle j| + \hbar\omega_c(\hat{c}^\dagger\hat{c} + 1/2) + \hbar\omega_{MR}(\hat{b}^\dagger\hat{b} + 1/2) \\
&\quad \hbar g(\hat{c}^\dagger + \hat{c}) \cdot \hat{n} + \hbar\lambda(\hat{b}^\dagger + \hat{b}) \cdot \hat{n}
\end{aligned} \tag{2.23}$$

where $|j\rangle$ is the energy eigen states of transmon [18], \hat{c} is the annihilation operator for cavity and \hat{b} is the annihilation operator for mechanical resonator.

$$g = \frac{2\beta e V_{zp}}{\hbar} \tag{2.24}$$

is the coupling strength of transmon-cavity interaction, and V_{zp} is the zero-point voltage fluctuation of cavity. It is also useful to define $gg_{ij} = g \langle i | n | j \rangle$, which is the matrix element representing the coupling term.

$$\lambda = -\frac{4E_C V_{MR}}{e \hbar} \frac{\partial C_{MR}}{\partial x} x_{zp} \quad \lambda_{ij} = \lambda \langle i | n | j \rangle \tag{2.25}$$

is the is the coupling strength of transmon-MR interaction, and x_{zp} is the zero-point displacement fluctuation of mechanical resonator.

2.4 dispersive coupling limit and rotating wave approximation

In our hybrid system, the cavity and qubit is dispersively coupled, $g \ll |\omega_c - \omega_q|$. Also we can tune the frequency of qubit such that $\lambda \ll |\omega_{MR} - \omega_q|$. It is useful to consider a general case where a qubit is dispersively coupled to a harmonic oscillator, and the analysis can be applied to explain behaviors such as dispersive shift, number splitting in both MR-qubit and cavity-qubit system.

2.4.1 Rotating wave approximation

Consider the general case when I qubit (denoted as q) and a harmonic oscillator (HO), the Hamiltonian of the system in Schrodinger picture

$$H = H_q + H_{HO} + H_{int} = \hbar\omega_q\sigma_z + \hbar\omega_{HO}a^\dagger a + \hbar g(a + a^\dagger)\sigma_x \quad (2.26)$$

where a, a^\dagger are ladder operator of a harmonic oscillator, which could represent a cavity or a mechanical resonator. This Hamiltonian can be rotated into interaction picture

$$\begin{aligned} \tilde{H}(t) = \frac{\hbar g}{2} & (a\sigma^- e^{-i(\omega_q + \omega_{HO})t} + a^\dagger\sigma^+ e^{i(\omega_q + \omega_{HO})t} \\ & + a\sigma^+ e^{-i(\omega_q - \omega_{HO})t} + a^\dagger\sigma^- e^{-i(\omega_q - \omega_{HO})t}) \end{aligned} \quad (2.27)$$

It has term containing slow rotating $\omega_q - \omega_{HO}$ and fast rotating $\omega_q + \omega_{HO}$ components. Since $|\omega_{HO} - \omega_q| \ll \omega_{HO} + \omega_q$ is assumed, the fast rotating terms will automatically averaged out and thus can be removed. This is called James Cummings rotating wave approximation. Then the interaction picture Hamiltonian is transformed back into Schrodinger

picture

$$H_{JC} = \hbar\omega_q\sigma_z + \hbar - \omega_{HO}a^\dagger a + \hbar g(a\sigma_+ + a^\dagger\sigma_-) \quad (2.28)$$

2.4.2 cavity dispersive shift

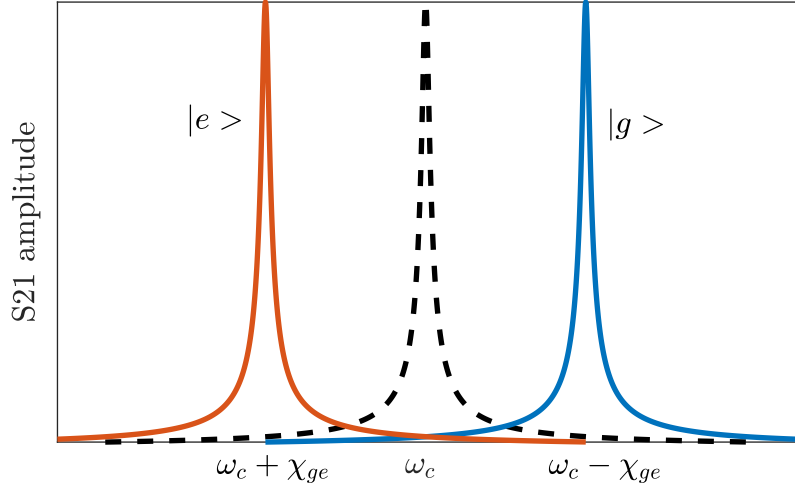


Figure 2.13: Simulated cavity response showing dispersive shift by interacting with qubit. The original cavity frequency is ω_c (dashed black line) and is shifted to $\omega_c - \chi_{ge}$ (blue solid line) or $\omega_c + \chi_{ge}$ (red solid line) depends on qubit state $|g\rangle$ or $|e\rangle$.

In our transmon-cavity system, or the hybrid MR-transmon-cavity system described by equation 2.23, if we make the transmon-MR coupling $\lambda = 0$ by setting the voltage to 0V, we can analyze the dispersive behavior of the cavity. By applying rotating wave approximation, we can get

$$H' = \hbar\omega |j\rangle\langle j| + \hbar |j\rangle\langle j| + \hbar a^\dagger a (\omega_c + (\chi_{j-1,j} - \chi_{j,j+1}) |j\rangle\langle j|) \quad (2.29)$$

where $\chi_{i,j} = \frac{\langle i | \hat{n} | j \rangle^2}{\omega_j - \omega_i - \omega_c}$ denotes dispersive shift due to transmon state transitions. To make the equation symmetric and uniform, I manually added non-existing term $\chi_{-1,0}$

and let it be zero (This equation is the same result as equation 3 in [18], and by adding non-existing term, the terms outside the Σ are absorbed). To clarify, the numbers 0,1,etc here are representing transmon state $|g\rangle$, $|e\rangle$, etc. We can see the effective energy for cavity is shifted, depending on the state of transmon

$$\omega'_c = \omega_c - \chi_{ge} |g\rangle\langle g| + (\chi_{ge} - \chi_{ef}) |e\rangle\langle e| + \dots \quad (2.30)$$

The energy of cavity now is transmon-state depended and can be used as a method to measure the state of qubit[13, 14].

2.4.3 dispersive shift for transmon energy

photon number splitting This sections aims to discuss the basics of harmonic oscillator induced shift in qubit energy. In our transmon-cavity experiment in chapter 7 and hybrid MR-transmon-cavity experiment, we clearly see multiple peaks of transmon energies. This so-called “photon number splitting” was first done by Schuster *et al*[19] in dispersive limit in circuit QED. And coherent number state of phonon was observed by O’Connell[10].

Here I will derive the induced number splitting and follow Clerk’s analytical method[20] to simulate the peaks. Similarly we can calculate the effective energy for transmon states

$$\omega'_j = \omega_j - \chi_{j-1,j} + (\chi_{j-1,j} - \chi_{j,j+1})a^\dagger a \quad (2.31)$$

There is a term that is proportional to $a^\dagger a$, which is the number operator of the harmonic oscillator. It suggests that, the original degenerate states are now shifted depending on the number state of harmonic oscillator. If we further assume a strong dispersive coupling

that the dispersive shift is bigger than all relevant dissipation, such as coherence time $2\pi/T_1$, $2\pi/T_2^*$ for qubit, κ_c for cavity, κ_{MR} for mechanical resonator

$$\chi_{j-1,j} - \chi_{j,j+1} \gtrsim [\Gamma_q, \kappa_a, \text{other dissipation}] \quad (2.32)$$

then the individual peaks are separate far enough to distinguish individual number state.

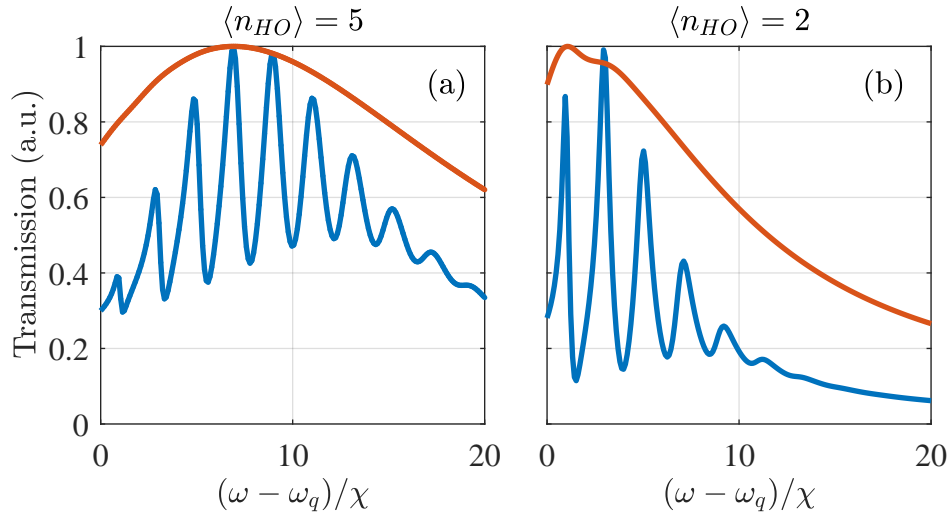


Figure 2.14: Simulated number splitting for qubit. Qubit energy $\omega_q = 4\text{GHz}$, and harmonic oscillator frequency $\omega_{HO} = 100\text{MHz}$, and the coupling strength $\lambda = 10\text{MHz}$. In (a), the average harmonic oscillator number $n_{HO} = 5$, and in (b) $n_{HO} = 2$. The blue curves are in strong dispersive limit where $\kappa_{HO} = 1\text{MHz}$ and $\Gamma_q = 1\text{MHz}$, while the red curves are in weaker regime where the dissipation are both 10MHz . It is clear that in strong dispersive limit, individual peaks are sharp enough to observe number state.

2.5 Mechanical resonator as a dissipative bath

Noise is an unavoidable topic in classic and quantum system. In this section, I will focus on only the quantum noise generated from the mechanical resonator. In quantum mechanics, even when a system is at absolute zero temperature, there will be quantum

fluctuation due to zero-point fluctuation [21, 22]. Here I also discuss a special case where the transmon energy and Mechanical resonator is close, $\lambda \sim |\omega_{ge} - \omega_{MR}|$ and the coupling strength is smaller than the dissipation rate of mechanical resonator $\lambda \lesssim \kappa_{MR}$. In this limit, the mechanical resonator is treated as a dissipative bath coupled to the transmon. Using perturbation theory and expanding to the lowest order, the noise from the resonator's position fluctuation is added to the background noise of the qubit.

We consider only the lowest two states of the transmon as a two level quantum system that is coupled to a mechanical resonator though

$$H_{int} = \frac{\lambda}{x_{zp}} \hat{x}(t) \hat{\sigma}_x \quad (2.33)$$

where $\lambda = \lambda_{ge}$ in equation 2.25. x_{zp} is the zero-point fluctuation of mechanical resonator, $\hat{x}(t) = \hat{b}^\dagger + \hat{b}$ in equation 2.23 is the position operator as a function of t.

We define $S_x(\pm\omega)$ as the displacement spectral density, which can be related to the imaginary part of its response function $\chi_x''(\omega)$, by well-known fluctuation-dissipation theorem as

$$S_x(\omega) = 2\hbar \langle n(\omega) + 1 \rangle \chi_x''(\omega) \quad S_x(-\omega) = 2\hbar \langle n(\omega) \rangle \chi_x''(\omega) \quad (2.34)$$

where

$$\chi_x''(\omega) = \frac{1}{m} \frac{\kappa_{MR}\omega}{(\omega_{MR}^2 - \omega^2)^2 + 4\omega^2(\kappa_{MR}/2)^2} \quad (2.35)$$

where $n(\omega)$ is the thermal occupation number as a function of resonator frequency. At

regime near resonator frequency $\omega \approx \pm\omega_{MR}$, we can show that

$$S_x(\omega) = x_{zp}^2 \frac{\kappa_{MR}\langle n+1 \rangle}{(\omega - \omega_{MR})^2 + (\kappa_{MR}/2)^2} \quad (2.36)$$

$$S_x(-\omega) = x_{zp}^2 \frac{\kappa_{MR}\langle n \rangle}{(\omega - \omega_{MR})^2 + (\kappa_{MR}/2)^2} \quad (2.37)$$

The MR-induced decay and excitation of qubit is

$$\Gamma_{\uparrow,MR}(\omega_{ge}) = \frac{\lambda^2}{x_{zp}^2 \hbar^2} S_x(-\omega_{ge}) \quad \Gamma_{\downarrow,MR}(\omega_{ge}) = \frac{\lambda^2}{x_{zp}^2 \hbar^2} S_x(\omega_{ge}) \quad (2.38)$$

Here the qubit energy ω_{ge} is treated as a variable that be tuned experimentally. We assume that other source of relaxation and dissipation for the qubit Γ_B is uncorrelated with the displacement degree of freedom of mechanical resonator. For narrow enough range that ω_{ge} varies, $\Delta\omega_{ge} \sim \Gamma_{MR} \ll \omega_{ge}$, Γ_B is independent with frequency. The total qubit linewidth is written as

$$\gamma(\omega_{ge}) = \Gamma_{\uparrow,MR} + \Gamma_{\downarrow,MR} + \Gamma_B = \frac{\lambda^2}{x_{zp}^2 \hbar^2} (S_x(-\omega_{ge}) + S_x(\omega_{ge})) + \Gamma_B \quad (2.39)$$

then, in the limit of $\langle n \rangle \ll 1$, the qubit linewidth has a simple Lorentz form:

$$\gamma(\omega_{ge}) = \frac{\lambda^2}{\hbar^2} \frac{\kappa_{MR}}{(\omega_{ge} - \omega_{MR})^2 + (\kappa_{MR}/2)^2} + \Gamma_B \quad (2.40)$$

Chapter 3

Design consideration

In this chapter, I will discuss important design considerations and realistic parameter ranges for implementing our experiments. The discussion will be divided into three parts: cavity, qubit and mechanical resonator. In each part I will talk about the advantages and disadvantages for different parameter regime and show related simulations.

3.1 Broadband Filter and biased CPW cavity

In this section, I will present the design of a reflective stop band filter. This function of this filter is to supply dc voltage bias into the low-loss superconducting co-planar waveguide (CPW) cavity, and thus control the coupling strength of mechanical resonator to transmon qubit. The characteristics of the filter is studied using numerical simulation and demonstrated insertion losses greater than 20 dB in the range of 3-10 GHz, which enables the suitability of filter in a number of applications including qubit-coupled mechanical system and circuit QED.

3.1.1 Leakage and isolation of bias circuitry

Leakage The integration of biasing circuitry in microwave cavity is one of the important technical issues in realization of qubit and cavity coupled mechanical system, cQED and quantum dynamics[11, 23, 24]. In these scenarios, these inserted biasing lines, such as potentials and currents, serve a variety of functions such as maintaining a device's operating state or establishing tunable electrostatic interactions between devices. However, if not carefully engineered, the introduction of the bias circuitry may degrade the quality of a cavity through increased external circuit loading and radiative losses.

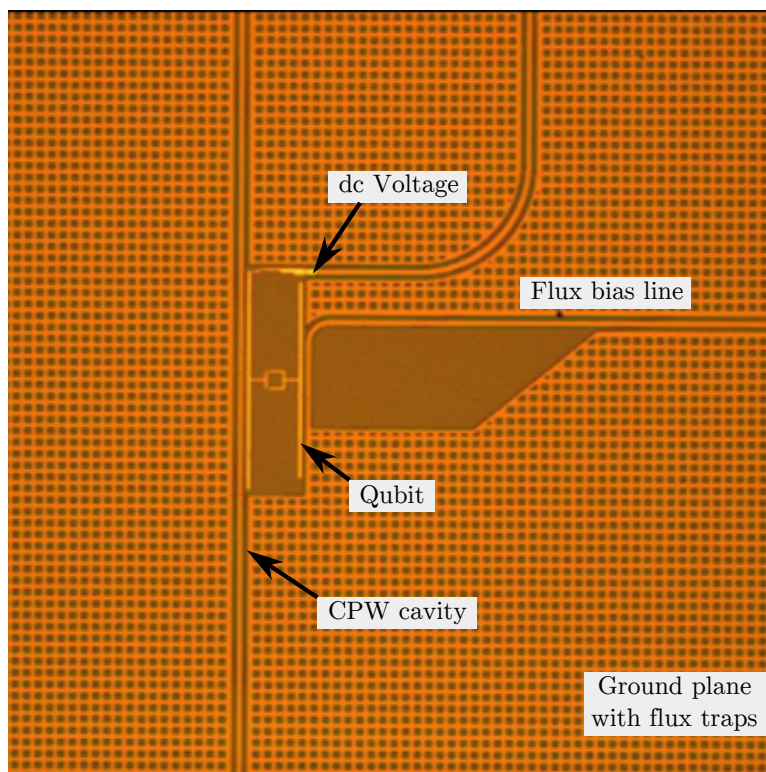


Figure 3.1: Optical image of a second version qubit coupled mechanical resonator embedded in CPW cavity. The dc voltage bias line is directly inserted into the pocket.

In regard to our system, the issue rises when a flux line and a voltage bias line are introduced to the pocket of qubit. The additional biasing lines are in close proximity to

CPW center line resulting in unwanted leakage: the coupling between biasing line and cavity center line causes a significant decrease in quality factor of cavity. To prove this, I measured the transmission of sample with directly inserted dc voltage line (design in Figure 3.1), and as a comparison I shorted the dc voltage line by wire bonding and then dip-tested the transmission property of the cavity at 4K, see Fig. 3.2. It is observed that the peak at fundamental mode gets broader and wider, also a second peak appears at higher frequency, indicating strong spurious coupling inside the cavity.

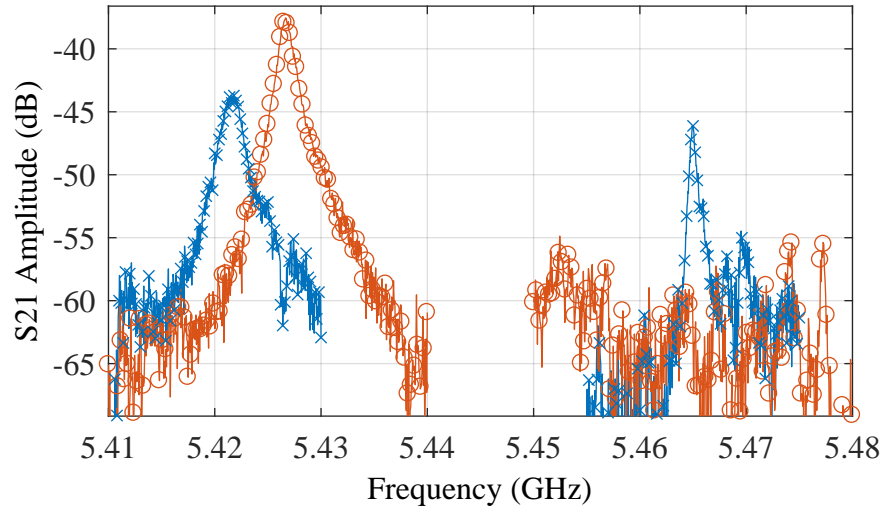


Figure 3.2: Comparison of CPW cavity resonance (5.425 GHz) with a voltage bias circuitry. The blue cross lines are from CPW with dc and flux biasing lines added directly. The red circled lines are from the same sample but biasing circuits removed by wire bond shorting. It is apparent that the main peak(around 5.43GHz) is degraded and shifted by biasing circuitry, and also second peak appears due to unwanted cross-talk. Note the maximum amplitude of red curve is far from 0dB because of high temperature.

The intuitive solution to this issue is: first, better isolation between CPW and inserted circuitry, normally this is limited by the distance and pattern of design; second, protection of signal from going outside the superconducting cavity by adding a reflective filter on bias line.

3.1.2 Ground planes to protect from cross-talk

In the ideal case when the cavity center line is inside on a total closure of metal, there could be no any cross-talk to external circuitry. This indicates bigger ground area and closer ground plane may help with decreasing cross-talk. To study this effect, I did simulation using Sonnet, See Figure 3.3. Number “1”(“3”) represents the coupling finger from cavity, “2”(“4”) represents the dc voltage gate. The floating metal in between is the island of qubit. The three metal are patterned in a way similar to our second version sample. As a comparison in (b), more ground planes are added to surround the electrodes to increase the capacitance of 3 and ground, 4 and ground, without changing the capacitance between 3 and island, 4 and island. Numerical simulation of transmission property shows great suppression in cross-talk between the two ports.

3.1.3 Lumped element reflective filter

Filter property The second method is by inserting a reflective filter on the bias circuitry. For a successful filter design, a few requirements have to be satisfied: first, the microwave signal, usually GHz range, leaking through the bias line is reflected back with little dissipation and phase change, so that the equivalent impedance of the bias line is sufficiently high; Second, dc and low frequency is allowed to pass with no attenuation; Third, the dimension needs to be appropriate so that it can be engineered on the same chip together with cavity, for our sample, smaller than 4mm.

There are several ways to design this reflective filter. It could be a narrow band-stop filter, which has a very high isolation at specific frequency but is disadvantageous when the cavity frequency might change from temperature change, dispersive shift from qubit, fabrication difference, coupling capacitor change, etc, the isolation varies a lot. Instead

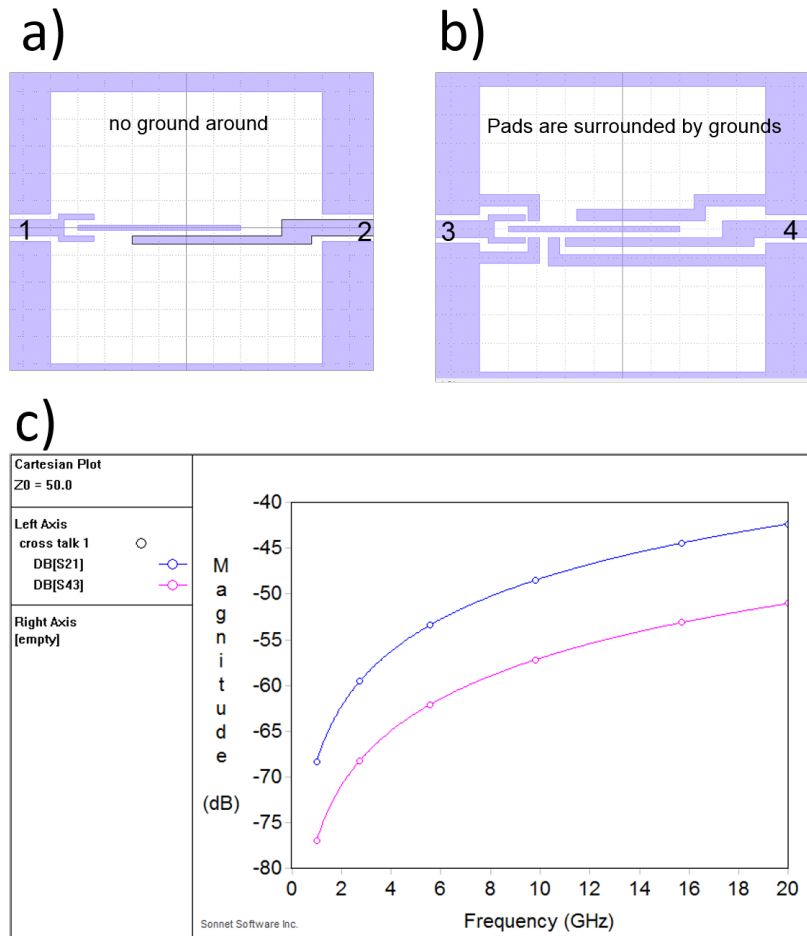


Figure 3.3: Comparison of cross-talk with more ground plane. (a) and (b) are snapshots of original CAD files. The metal pieces connected to the edges are grounded. There is a floating island in the center representing qubit island. “1,2,3,4” are the microwave ports ended with 50Ω . (c) Finite element simulation result using Sonnet. The blue (red) curve is the transmission from 1 to 2 (3 to 4) receptively. A 10dB smaller amplitude indicates the cross-talk being suppressed one order of magnitude.

I chose to design a broadband reflective filter with high enough isolation in stop band, and the lifetime of qubit is not limited by radiative loss through the filter.

The filter can be building either using lumped element or transmission lines as in these work ([25, 26]). I tried both ways and both work from simulation. The reason I chose lumped element is that it is more condensed in dimension. A smaller dimension gives more flexibility to integrate with other circuits, and the higher order modes are usually pushed up to higher frequency.

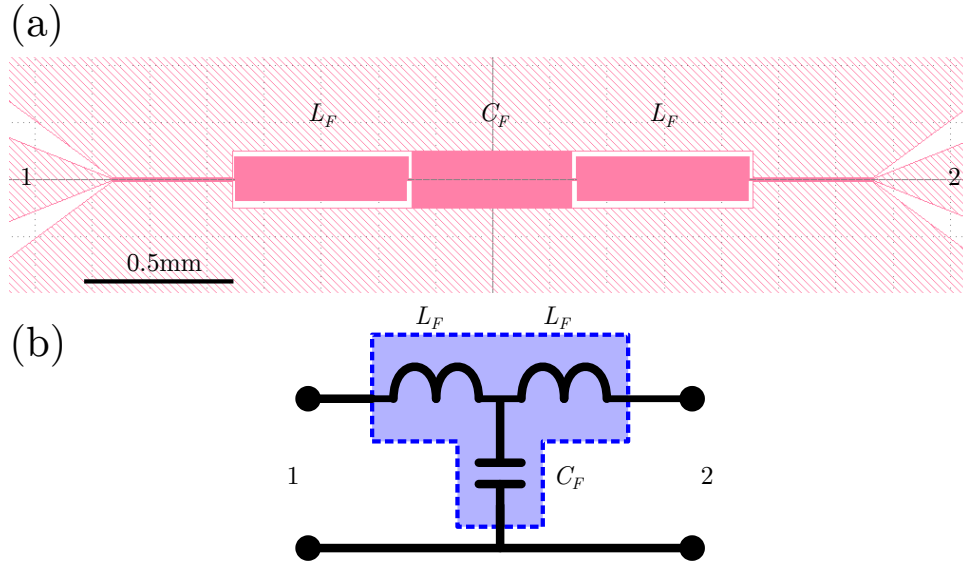


Figure 3.4: Design of reflective T-filter. (a) A snapshot of CAD file for reflective filter. The input and output ports are on at two ends. The filter consists of 3 parts: 2 meander inductor L_F sandwiching a inter-digit capacitor C_F . (b) Schematic drawing of reflective filter. The blue area indicates the filter capacitor and inductor. 1 and 2 are input/output ports to external 50Ω lines.

Figure 3.4(a) shows the CAD file of our reflective T-filter, which consists of two meander inductor sandwiching a inter-digit capacitor. Ideally arbitrary large values for L_F and C_F will give better isolation, however these parameters are limited by the realistic size of the meander and interdigit capacitor. A feasible choice is: the inductance of each inductor $L_F=5.5$ nH, and the filter capacitor $C_F=1500$ fF.

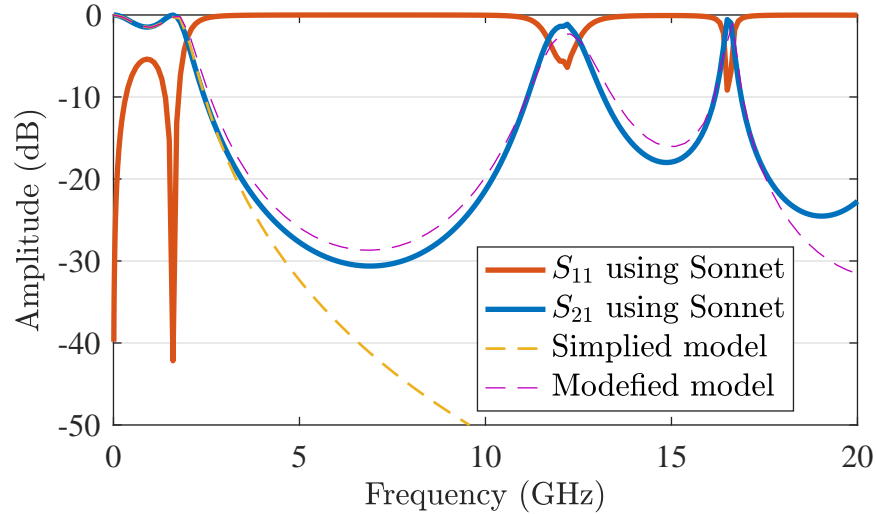


Figure 3.5: Transmission property of reflective T-filter. The red (blue) solid line is numerical simulation using Sonnet. The yellow dashed line is analytic result using lumped element model. Purple dashed line is analytic result using modified lumped element. The data of measurement see chapter 6

The microwave property were investigated using analytical analyze and numerical simulation using commercial software Sonnet¹. See Figure 3.5. At low frequency the meander and inductor behave as a lumped element, giving a stop band from its filter resonance $\omega_F = 1/\sqrt{L_F C_F} \approx 2\text{GHz}$, and the isolation at 5GHz is around 25dB. As the frequency increases, the wavelength get closer to the dimension of the inductor and capacitor, $\sim 1\text{mm}$, the lumped element approximation is no longer valid. At 13GHz the meander inductor's self-resonance dominates the behavior resulting a second minimum in isolation. The self-resonance is further proved by checking the current density inside the filter, see Figure 3.6.

¹www.sonnetsoftware.com

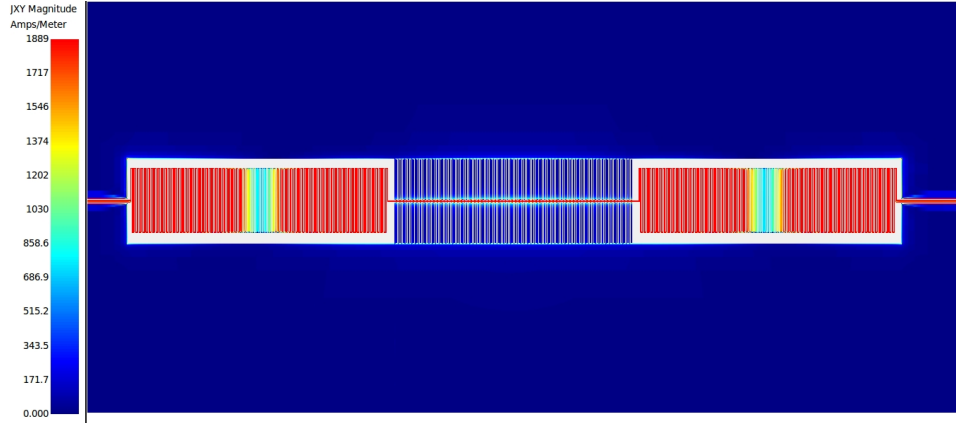


Figure 3.6: Current density map of T-filter at the first self-resonance at around 13GHz. The color scale indicates the density of current. The color in the capacitor fingers is uniform. Current minimum in inductor proves a self-resonance and is no longer valid being treated as a lumped element.

3.1.4 T-filter biased CPW cavity

To integrate the bias in to cavity, we connect a third line to the center of CPW cavity. It is a voltage node of the fundamental mode thus bringing minimal change to the cavity. But it is a anti-node for the second mode, so bigger damping is expected for the 10GHz mode. See Figure 3.7.

3.1.5 Radiation loss of qubit though the filter

For our goal of using qubit to probe the motion of mechanical resonator, it is critical to engineer a protected environment for qubit embedded in the cavity. To investigate the filter induced damping, we estimated the lifetime T_1 of qubit embedded near the anti-node of cavity fundamental mode, by calculating the admittance seen by the qubit as a function of frequency, following the method in Houck's work. The shunt capacitance of qubit is $C_{shunt}=100$ fF and is coupled to the cavity by $C_c=10$ fF. The cavity is assumed to have symmetric coupling capacitors $C_k=10$ fF.

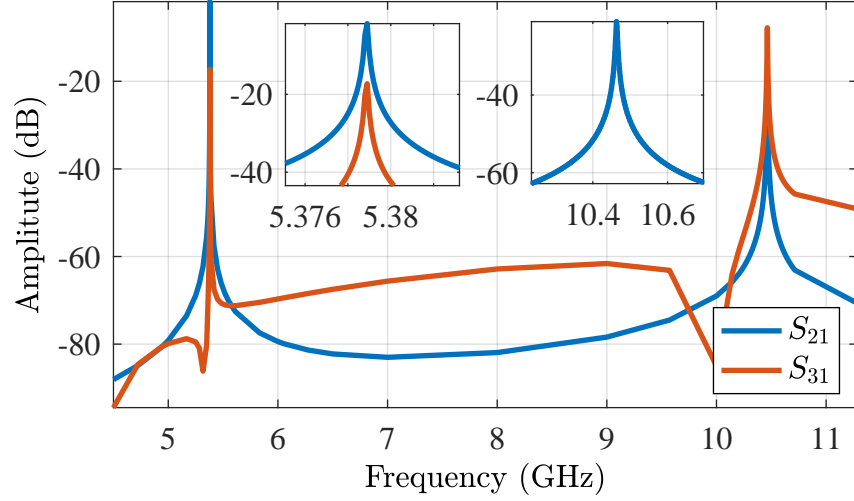


Figure 3.7: Numerical simulation of Filter biased CPW cavity. The first two modes are plotted. The inset is a zoom-in a S_{21} of the fundamental peak with quality factor $Q_{L,1}=53k$ and the second peak with quality factor $Q_{L,2}=2.7k$.

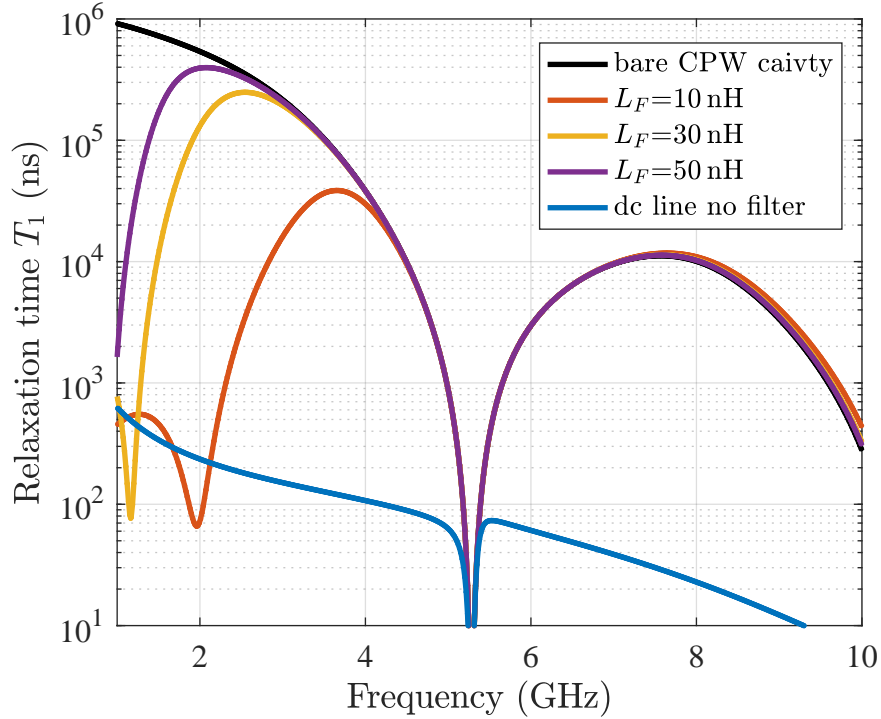


Figure 3.8: Estimated relaxation lifetime T_1 of transmon/charge type qubit embedded in filter-biased CPW cavity. The colored solid lines indicate scenarios with different L_F . For comparison, the black dashed line is for a CPW cavity without inserted dc voltage line and filter, and the blue line for with dc voltage line without filter.

Figure 3.8 shows the expected relaxation time of qubit respected to qubit’s frequency. For the chosen parameters $L_F=10$ nH and $C_F=1500$ fF, it increases dramatically the lifetime of qubit in the range >3 GHz, and around 5 GHz, the qubit lifetime is limited by Purcell effect of the cavity itself.

3.2 Single resonance lumped LC

Besides co-planer waveguide cavity, I also designed cavity using lumped element. Unlike CPW cavity, the dimension of lumped element cavity is usually much smaller than the wavelength and thus higher order resonance is pushed to high frequency, leaving only one single resonance at a relatively large range. Figure 3.9 shows the design of a lumped LC cavity design, which consists two inter-digit capacitors and one meander inductor in the center. The cavity is capacitively coupled to input/output ports denoted as “1” and “2”. The sample (red) is put in a pocket and is capacitively coupled to cavity finger and a bias line denoted as “3”.

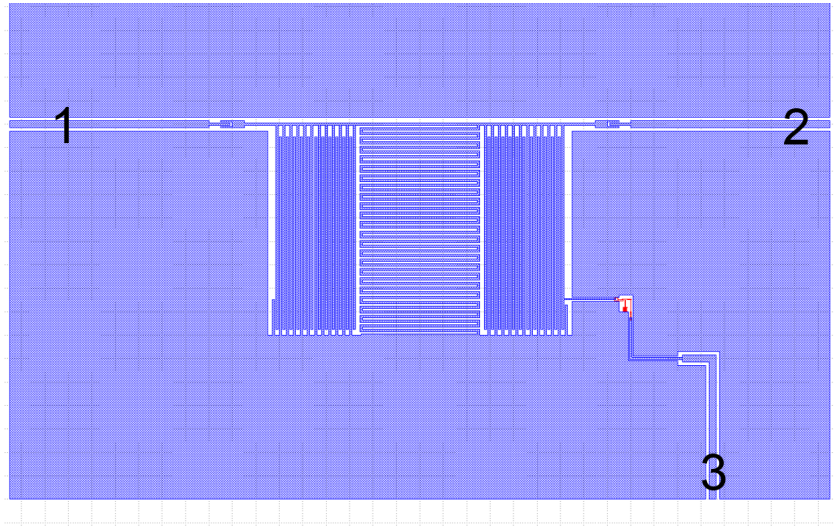


Figure 3.9: CAD drawing of a lumped element LC transmission cavity.

The response property of the cavity is studied numerically using Sonnet finite element simulation, see Figure 3.10.

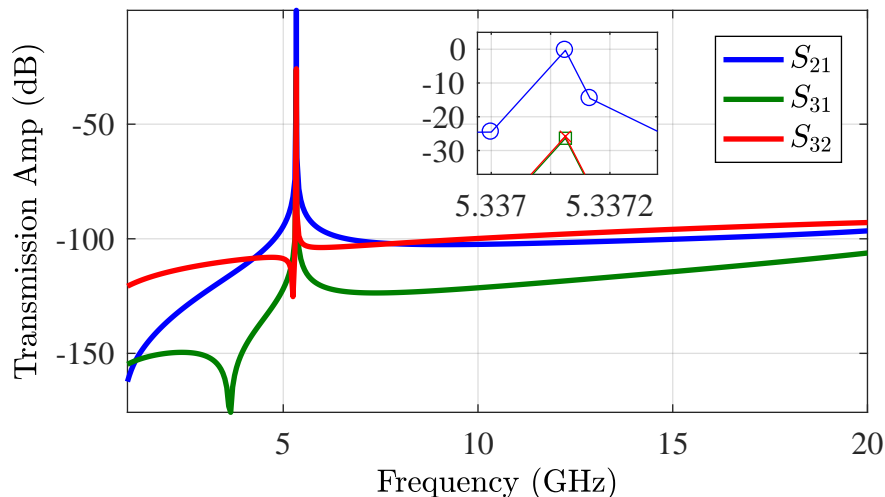


Figure 3.10: Numerical simulation of transmission property of a lumped element LC cavity, as shown in Figure 3.9. Only one peak is observed at 5GHz within range of 0-20GHz. The inset is a zoom-in at the peaks of curves. The leakage S_{31} is more than 20dB small than the S_{21} indicating good isolation between the cavity and gate.

3.3 Transmon design

The interaction between a CPB/transmon and a mechanical resonator is

$$H_{q,MR} = \hbar\lambda(b^\dagger + b)\hat{n} \quad (3.1)$$

and it can be separated into two parts

$$H_{q,MR} = \left(\frac{4E_C}{\hbar}\hat{n}\right) \cdot \left(\frac{V_{MR}}{e}\frac{\partial C_{MR}}{\partial x}x_{zp}\hat{x}\right) \quad (3.2)$$

where the first part acts on the transmon resulting in dispersive shift χ_{ij} as discussed in chapter 2, the second term acts on the mechanical resonator system resulting in total charge fluctuation.

One of our goal for this system is to probe the number state of mechanical resonator. To achieve this goal, we need to engineer the system in strong dispersive limit: the coupling strength of transmon-qubit interaction needs to be dominant compared to all dissipation in the system, the dephasing time T_2 , the dissipation rate of nano-mechanical resonator κ_{MR}

$$\lambda > \left[\frac{2\pi}{T_1}, \frac{2\pi}{T_2^*}, \kappa_{MR}, \text{etc.} \right] \quad (3.3)$$

3.3.1 Relaxation and spontaneous emission

Relaxation is a process when an excited qubit gets back to its ground state (at sufficiently low temperature). Relaxation time T_1 can be influenced by many factors such as properties of materials, fabrication defects, material agings and design of external circuitry. The intrinsic loss of qubit is usually dominated by the materials, and the external loss mechanism, or spontaneous emission is controlled by circuitry coupled to the qubit. In the section, I will discuss the estimation of T_1 based on spontaneous emission. For more detailed discussion, refer to Ref. [39].

In our system, qubit is embedded in a superconducting qubit and it is capacitively coupled to cavity, which is used to dispersively detect the state of qubit. Here I will assume the qubit is only coupled to the fundamental mode of cavity, because higher harmonic modes are even further detuned from qubit energy. This analysis can be generalized to all other

modes. It is shown the Purcell rate for a dispersive decay is

$$\gamma_q = \left(\frac{g}{\Delta}\right)^2 \kappa \quad (3.4)$$

where g is the coupling of qubit to external circuitry, $\Delta = |\omega_q - \omega_c|$ is the energy difference of cavity and qubit, and κ is loss rate of photons in external circuitry. One can further find the energy loss rate by calculating the electrical conductance $Y(\omega) = 1/Z(\omega)$ of external circuitry, the relaxation is

$$T_1 \leq \frac{C_q}{\text{Re}[Y(\omega)]} \quad (3.5)$$

This method is applied to analyze the radiation loss of qubit through filter biased cavity, see figure 3.8

3.3.2 Dephasing time

Dephasing is a mechanism of quantum system returning to classic behavior. In solid-state systems, microscopic modes and noise is a strong source of decoherence of qubit, such as charge background fluctuation, current or magnetic field variance from material or control circuits. And because the linewidth of qubit, or the dephasing time T_2^* highly depends on dephasing rate

$$1/T_2^* = \Gamma_\phi + 1/2T_1 \quad (3.6)$$

it is important to estimate the dephasing rate of qubit.

It is shown in Hutching's paper[27], dephasing rate

$$\Gamma_\phi = 2\pi \sqrt{A_\phi |\ln 2\pi f_{IF} t|} \frac{\partial f_{ge}}{\partial \phi} \quad (3.7)$$

where the flux noise power spectrum is $S_\phi(f) = A_\phi/|f|$ and f_{IF} is the infrared cut-off frequency, t is on the order of $1/\Gamma_\phi$, ϕ is the flux bias in the unit of Φ_0 . Here I first show the numerical calculations of qubit energies f_{ge} and its derivatives against flux bias ϕ , see figure 3.11.

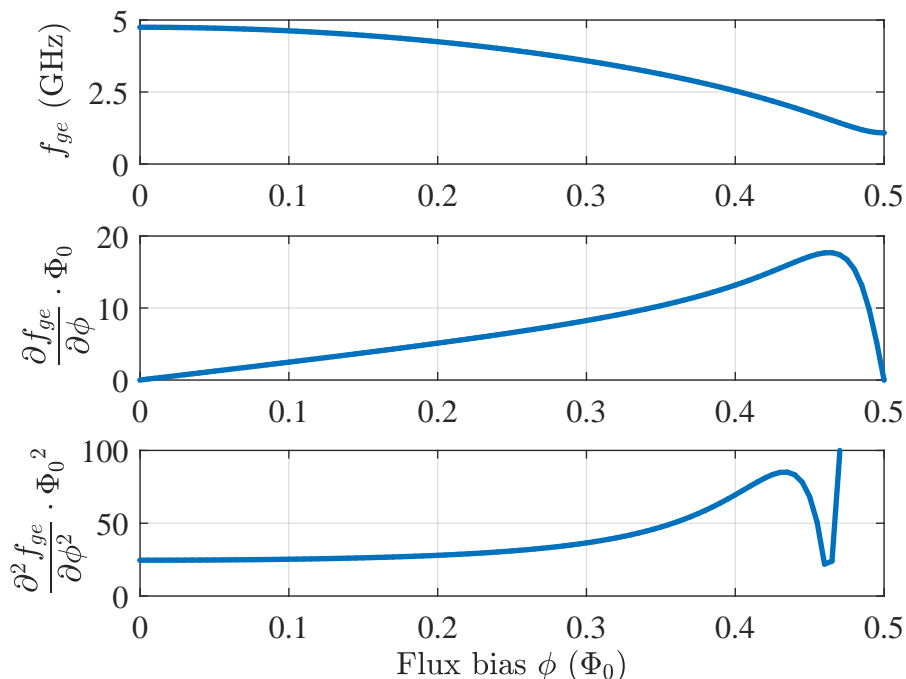


Figure 3.11: Numerically calculated qubit energy, and the derivatives of energy respected to ϕ . The transmon parameters are the same as in chapter 8

To gain a numerical estimation of dephasing time of our qubit, I will use the same value in Hutching's paper⁸. $A_\phi^{1/2} = 1.4\mu\Phi_0$, $t = 1\mu s$, $f_{IR} = 1\text{Hz}$. At $\phi = 0.32$, where the qubit is in resonance with mechanical resonator, $\frac{\partial f_{ge}}{\partial \phi} = 10$ and in chapter 8, and at $f_{ge} = 4\text{GHz}$, $\frac{\partial f_{ge}}{\partial \phi} = 6$. For relaxation time, I use $T_1 = 15\mu s$. One can find $T_2^*(f_{ge}=4\text{GHz}) = 4.6\mu s$, and $T_2^*(f_{ge}=3.5\text{GHz}) = 2.9\mu s$. This is very close to the value we found in hybrid cavity-transmon-MR experiment.

3.4 Mechanical resonator

There are different types of mechanical resonator, doubly clamped beam, suspended cantilever, metal membranes, piezo-sheets, oscillation modes in diamond and etc.. Among them, doubly clamped beam has the least difficulty to fabricate and to model.

3.4.1 Beam

Length dependence For a doubly clamped beam, the first question is what dimensions give the biggest zero-point fluctuations? For the following discussion, the MR frequency ω_{MR} is fixed. Also for the sake of fabrication, the thickness of the metal layer has very little flexibility, so we fix the width of the , one can show that

$$x_{zp} \cdot L^{3/2} = \text{constant} \quad (3.8)$$

where L is the length of the beam, x_{zp} is zero-point fluctuation in displacement degree of freedom. Along with MR-transmon coupling capacitance $C_{MR} = \epsilon_0 \frac{S}{d} \propto L$, I obtain:

$$H_{q,MR} = \left(\frac{4E_C}{\hbar} \hat{n} \right) \cdot \left(\frac{V_{MR}}{e} \frac{\partial C_{MR}}{\partial x} x_{zp} \hat{x} \right) \propto \frac{\partial C_{MR}}{\partial x} x_{zp} \propto L^{-\frac{1}{2}} \quad (3.9)$$

This suggests that to enhance the coupling strength, smaller length of beam is preferred. In the end it will be limited by the fabrication techniques, especially the thickness (10s of nanometers) of beam.

Simulation results Most metal or metalized beam resonators' fundamental mode are in radio frequency range $10^4 \sim 10^8$ Hz. To couple with qubit in resonance limit, we chose

to use the third modes of beam.

Figure 3.12 shows the COMSOL simulation results of our mechanical resonator. The dimensions of the beam is $700\text{nm} \times 45\text{nm} \times 100\text{nm}$. The surface is set to be a 3nm thick aluminum oxide layer, which has roughly 3 times bigger Young's Module compared to aluminum, and is critical especially for small dimensions. The numerical result is shown in Figure 3.12. The fundamental flexural mode is 708MHz and the third mode is 3.4GHz.

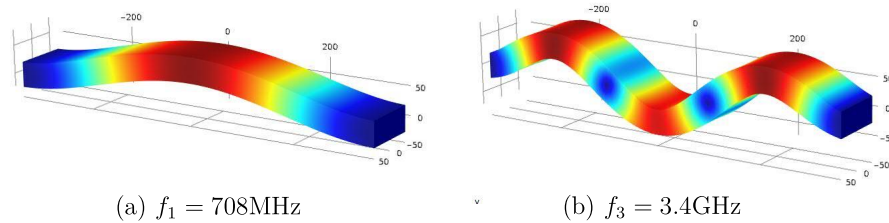


Figure 3.12: Finite element simulation using COMSOL. Color scale represents the displacement at different position. (a) Fundamental mode at 708MHz. (b) Third mode at 3.4GHz.

3.4.2 Membrane

Membrane style resonator is advantageous for its possibility of big area and thus big capacitance. But the frequency is relatively lower than beam resonator. It is designed to engineer dispersive coupling with qubit.

The most common membrane is edge clamped membrane. It is easier to model and simulate, and also easier to fabricate using standard nanotechnologies. The other type I am developing is called “free-free” membrane, because the two ends are free with anchors. The fabrication details are described in chapter 5 and here I am only showing the simulation results of the two types of membrane.

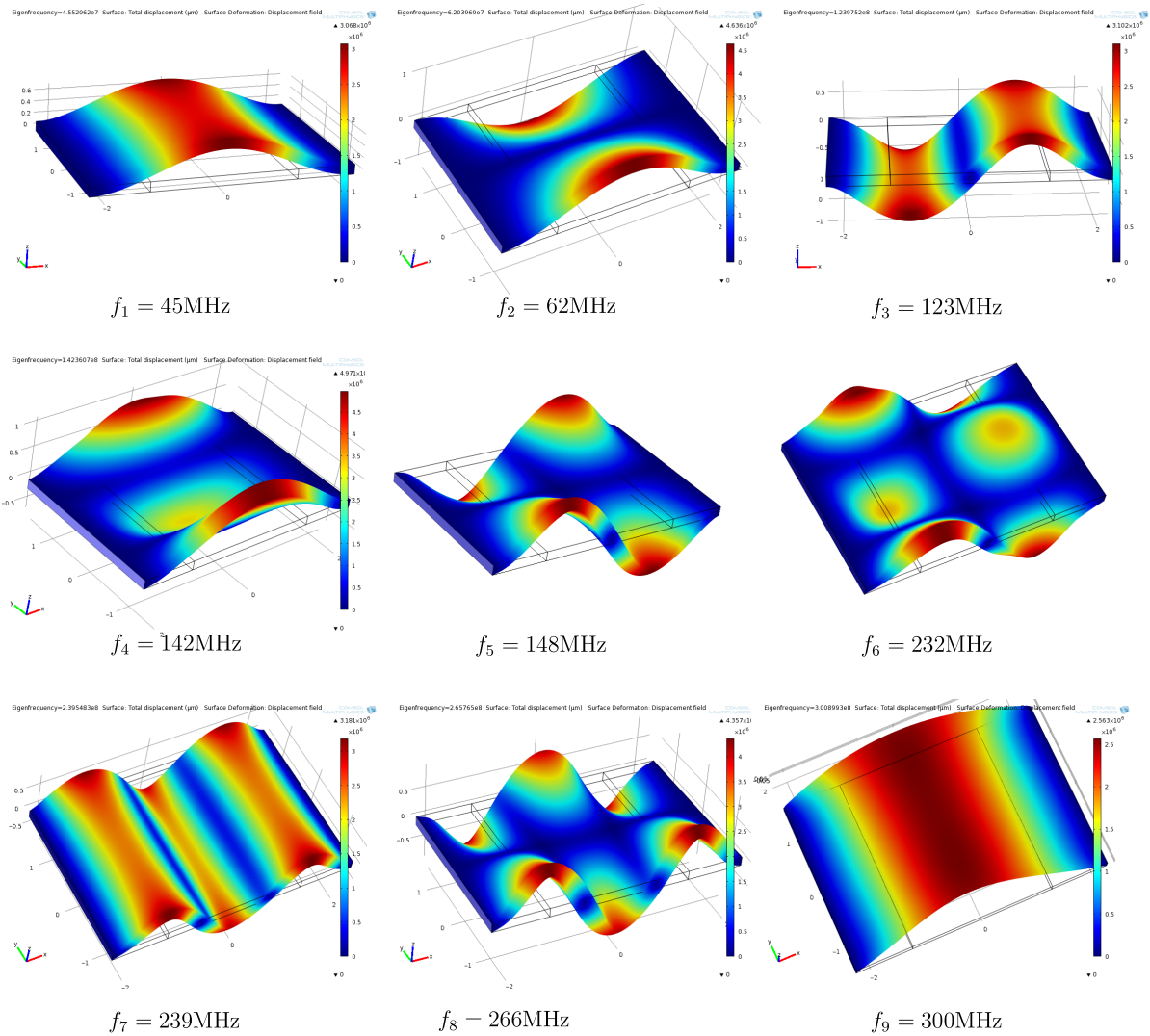


Figure 3.13: Finite element COMSOL simulation of doubly clamped membrane ($4.5\mu\text{m} \times 3\mu\text{m} \times 250\text{nm}$). The membrane are clamped on both longitude edges. The nine subplots are nine lowest flexural mode with frequency labeled below it. Color scale represents the displacement at different position.

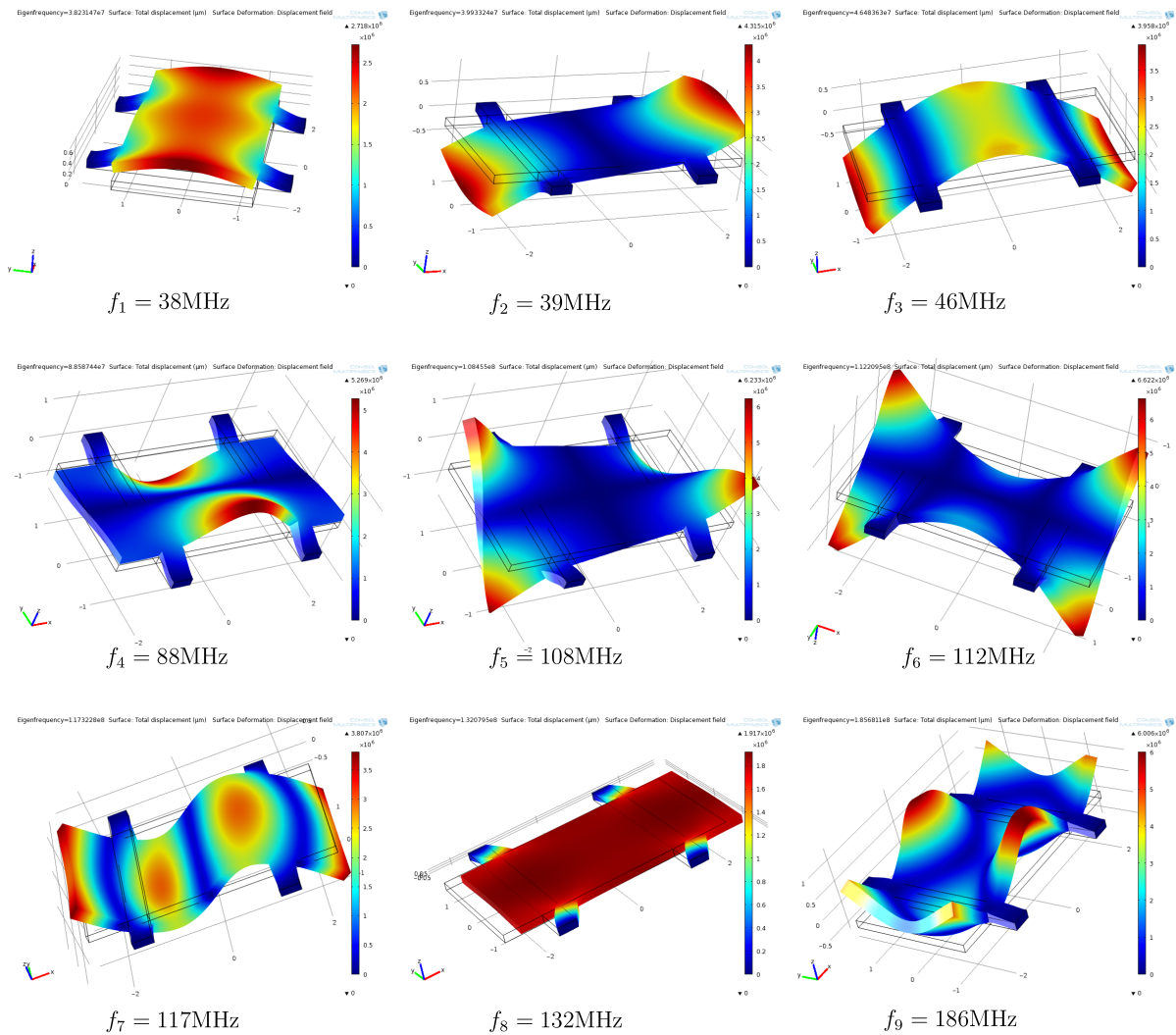


Figure 3.14: Finite element COMSOL simulation of free-free membrane ($5\mu\text{m} \times 2.5\mu\text{m} \times 250\text{nm}$). The membrane is clamped at the four ear-like anchors whose position is optimized to have minimal loss. The nine subplots are nine lowest flexural mode with frequency labeled below it. Color scale represents the displacement at different position. f_3 is the desired “free-free” mode.

3.4.3 Clamping loss

The displacement degree of freedom of a mechanical resonator is a collective movement of atoms. Different loss mechanism present limit the coherent dynamics of the system. For a nanometer-scale mechanical system, clamping loss is a major one: the elastic collective wave are scattered and lost through its supports. This mechanism is carefully studied by Wilson-rae. The mechanical resonator is coupled to a thermal bath of harmonic oscillators through the supports. The final clamping quality factor is shown in table.I in [28].

For our 3.4GHz mechanical resonator mode, comparing the calculated quality factor and measured factor, we believe clamping loss is one of the dominating mechanism.

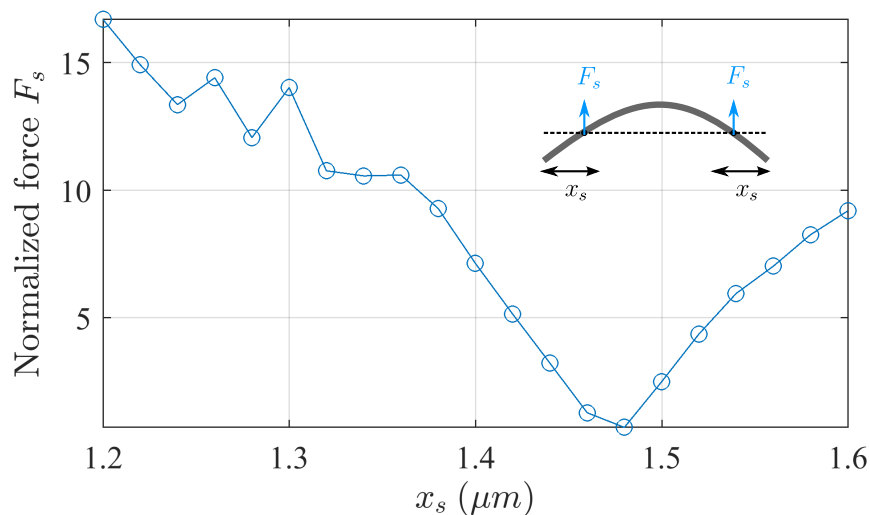


Figure 3.15: Numerical simulated force $|F_s|$ as a function of support position x_s . The bending mode shape is shown in the inset. At $x_s \approx 1.47\mu\text{m}$, the force reaches its minimum suggesting a minimal clamping loss.

One of the methods to reduce clamping loss is to move the supports to the nodes, where the displacement is zero and therefore no first order elastic force is applied. This optimal point can be found when the overall displacement of the mode is zero. When I design

the free-free membrane, the important step is simulate the forces on the supports. This is done by moving the position (x_s) of the symmetric supports shown in inlet of Figure 3.15. F_s is the vertical force applied on the anchor, whose amplitude is plotted in Figure 3.15. The force reaches a minimum at $x_s \approx 1.47\mu\text{m}$.

3.4.4 Differential mode of coupling

Simulated results in Figure 3.12 shows that unlike the doubly clamped membrane, there are more modes at lower frequency that might couple with gate pad, resulting in spurious peaks or broadening of the peak. Here I propose a different “differential mode” to couple with the transmon pads. The two pads from transmon are denoted as “+” and “-” in Figure 3.16, “-” pads sitting one the side are connected with a wire. By making the total area of “+” and “-” pads, it is possible to avoid coupling with all other mode, leaving only the free-free mode coupled with transmon. Table. 3.1 summarizes the coupling $\frac{\partial C_{MR}}{\partial x}\Big|_{\text{mode } i}$ relative to $\frac{\partial C_{MR}}{\partial x}\Big|_{\text{mode } 3}$, where i is the order number in Figure 3.14.

mode number i	f_i (MHz)	coupling ratio
1	38	9.28E-3
2	40	9.05E-4
3	46	1
4	89	5.70E-5
5	108	1.56E-5
6	112	2.87E-5
7	117	1.59E-5
8	132	3.53E-5
9	186	7.35E-2

Table 3.1: The relative coupling strength $\frac{\partial C_{MR}}{\partial x}\Big|_{\text{mode } i}$ as a function of order number of a free-free membrane. Besides the desired mode 3, coupling of all the other modes are high suppressed.

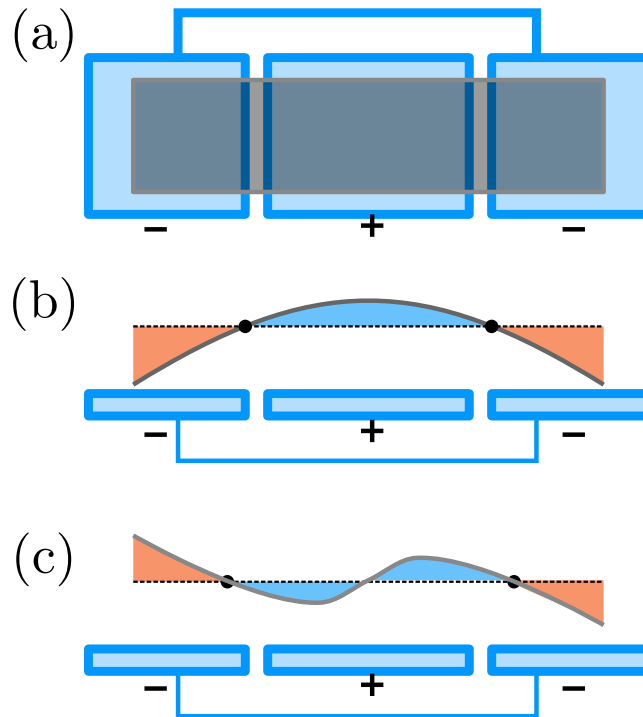


Figure 3.16: Differential coupling mode of free-free membrane to a and two pads (denoted as “+” and “-”) of a transmon. (a) (top view) Schematic drawing of bottom pads (blue) and top suspended free-free membrane. (b) (side view) The top membrane is in the 3rd “free-free” mode. The blue (red) area represents the capacitance change to “+” (“-”) pad. (c) same view as in (b) but for a spurious mode in which the upward and downward displacements cancel the total coupling.

Chapter 4

Fridge and measurement setup

In this chapter, the experimental setup is discussed. The dilution fridge and cryogenic environment provides a cold and quite environment for the sample by controlling the temperature and transmits the signal into and outside from the sample. The signal is analyzed by external hardware software. The characteristic of the sample is retrieved from the measurement signal.

4.1 Cryogenics cables and Filtering

The fridge has multiple temperature stages ranging from room temperature to 30mK as shown in Figure 4.1. In order to perform measurements down to single photon level in cavity, $\langle n_c \rangle \sim 1$, both thermal noise isolation and measurement efficiency are critical in the set up, where the former offers a “quite” environment for the sample and the latter guarantees acceptable speed of measurement. A careful trade-off has to be made between both. The rules and principles of cryogenic design can be found in Pobell’s book[29].

The concern of isolation of thermal noise includes 4 different pathways: the RF input line, the RF output line, the dc input line, and the magnetic flux (current) control input line.

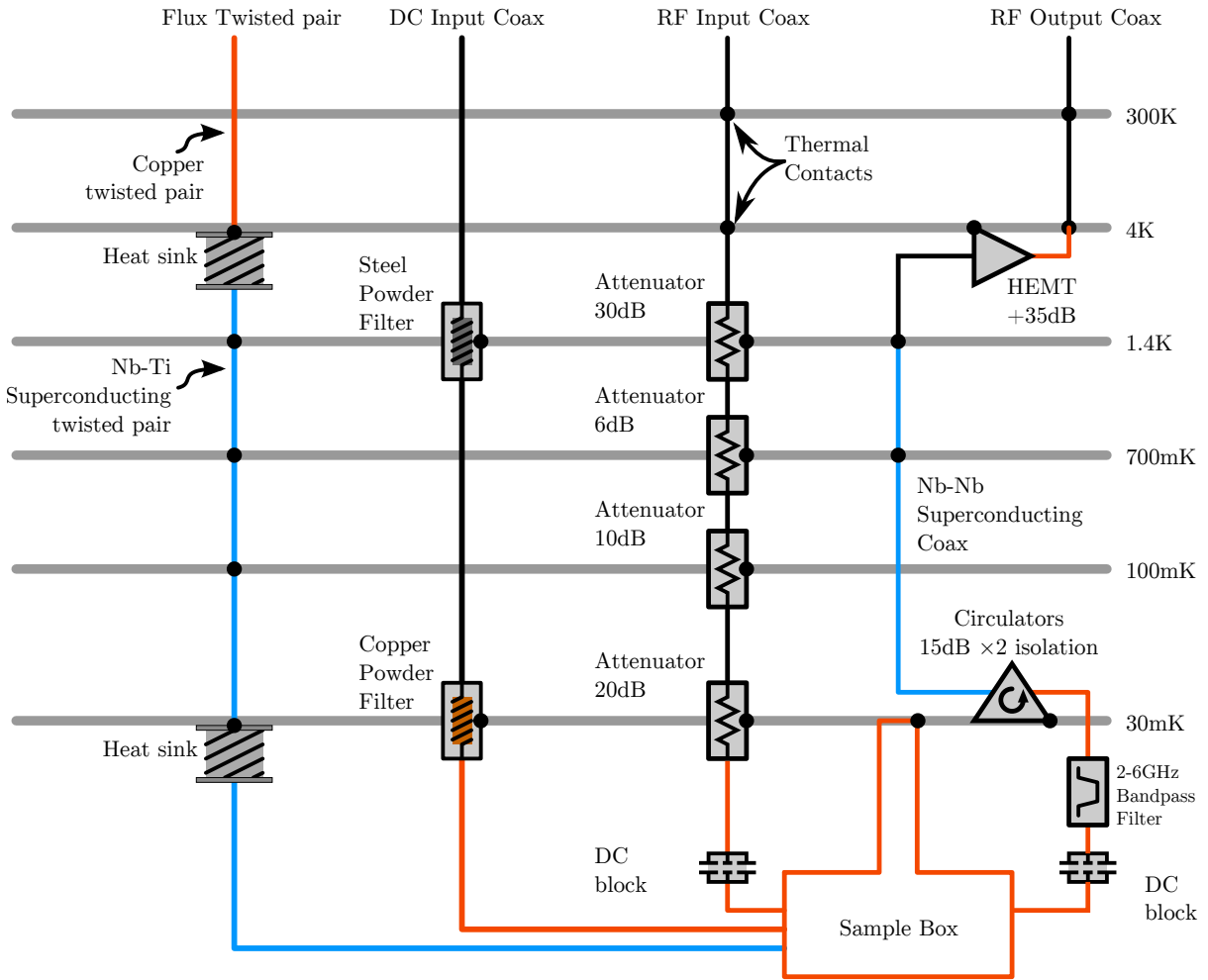


Figure 4.1: Schematic drawing of cable setup through different stages on fridge. Different stages are represented by thick light gray horizontal lines with its temperature (300K, 4K and etc.) on the right side. The sample locating at bottom of the figure, is clamped at the coldest stage of fridge. There are four lines connecting to it as shown on the top of figure. The color of cable indicates different material: black for stainless steel, orange for copper, and blue for superconducting metal. The big black points represents thermal anchor to stage.

Heat conduction consideration The material of the cable is also determined by heat transfer consideration between stages. If the connecting cable is within the same stage, copper is normally preferred. It is favored for its ease of bending and low loss of microwave signal. Copper is a good thermal conductor, 100s W/m·K[29]. Considering the thermal conductance, stainless steel cable is used to connect between stages. Stainless cable has much smaller thermal conductivity, tens W/m·K, it also brings extra microwave attenuation. In terms of heat conductivity, Superconducting material is much lower than normal metal, and is also advantageous for its low microwave loss ~ 0.1 dB/m. However compared to copper and stainless steel, it is more expensive in terms of price. Thus it is used On the output line.

4.1.1 RF input

Attenuation for thermal noise The RF input line serves for offering microwave driving power to the cavity as well as microwave control pulse for qubit. The noise outside the fridge at room temperature is added to the microwave signal injected. The frequency of microwave ranges from hundreds of MHz to more than 10GHz. For such a wide range of frequency, the simplest way is to filter out using broad band attenuators. The attenuation between stages is determined by thermal noise that radiates from higher temperature stage to sample. The noise spectrum of a resistive element is $S(\omega) = 4k_B T Z_0$ or $P(\omega) = k_B T \Delta f$, where $Z_0 = 50\Omega$ is standard impedance for RF lines, Δf is frequency bandwidth to integrate power. For example, the first attenuator is placed between the room temperature stage at the top of the fridge and 1K stage which is thermalized with 1K-pot, $S_{300K} = -173\text{dBm}/\sqrt{\text{Hz}}$ and $S_{1.4K} = -197\text{dBm}/\sqrt{\text{Hz}}$, the attenuation cutting all noise from the upper stage, should be bigger than $197 - 173 \approx 25\text{dB}$. To secure enough isolation, we insert a 30dB attenuator coaxial cables. Both the cables and attenuators

are tightly clamped in order to get fully thermalized to its stage.

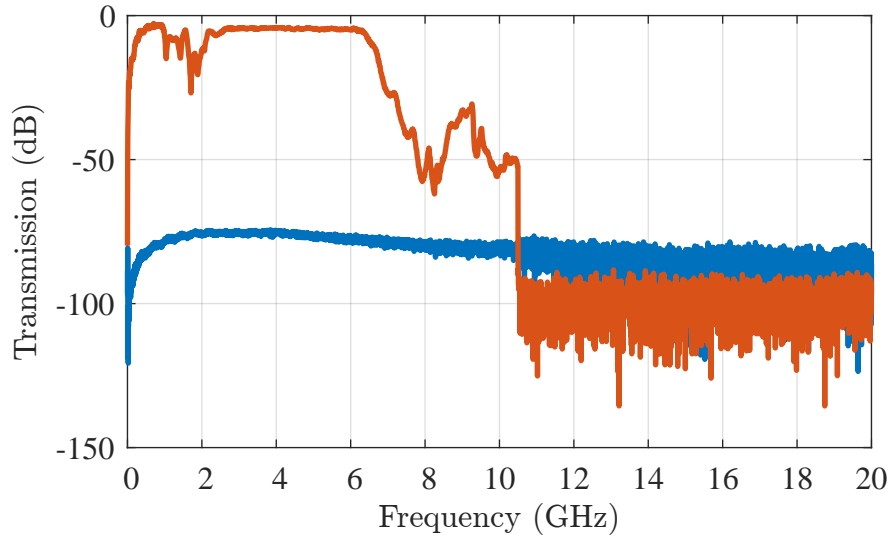


Figure 4.2: Transmission measurement of RF input line. The inset plot shows the whole range. Measured at room temperature.

Although bigger attenuation gives better isolation, it is not always feasible to increase total attenuation on the input line too much. For our filtered CPW cavity with $Q \sim 20000$, to have average one photon in the cavity, $\sim -143\text{dBm}$ is needed on the input port of cavity. Most of pulsed measurements to characterize qubit, around a hundred photons require -120dBm on the sample and -40dBm on top of fridge. However to perform bright-state measurement[30] or cavity side-band measurements[15, 31, 32], up to 10^9 phonon(this is huge power) or -50dBm is demanded. High attenuation on the input line sets the upper limit of power, and increases the complexity of outside circuits with more amplifiers. Furthermore a higher power may cause a high heat dissipation on the attenuators, eg, $-30\text{dBm}=1\mu\text{W}$ on mixing chamber, could easily heat up the fridge above the base temperature.

Note 75dB isolation in our setup, as shown in Figure 4.2, is more than needed,

$$S_{300\text{K}}/S_{30\text{mK}} = -173\text{dBm}/(-216\text{dBm}) = 40\text{dB}$$

The reason we put extra attenuation on the input line is that we once observed higher order excitation of qubit, and more aggressive attenuation helped us to rule out thermal noise problem from the fridge. The discussion of qubit temperature is discussed in Chapter 8.

4.1.2 RF output

The RF output is the microwave readout circuit for cavity. The design needs more delicate consideration: it requires isolation of noise from outside fridge and hotter stages, while signals from the sample can go out with no attenuation in an ideal case. This is possible by using circulators, which provide asymmetric transmission property. Each circulator has a very low loss on forward direction, and $\sim 15\text{dB}$ attenuation for reverse direction. Two circulators in series provide roughly 35dB isolation, which is sufficient to cut off noise from HEMT amplifier located at 4K stage.

Before reaching 4K stage, 2 segments of Nb superconducting cables are used, in order to introduce the least attenuation on the output line and isolate thermal conduct between mixing chamber and higher temperature stages.

Because the signal is too small (maybe smaller than -130dBm , much smaller than room temperature noise floor) compared to noise figure of room temperature amplifiers or read-out apparatus, it is amplified first by HEMT manufactured by Caltech¹ when reaching

¹<http://www.caltechmicrowave.org/amplifiers>

4K stage. HEMP, high-electron-mobility-transistor is a high power (35dB) amplifier with very low noise($\sim 3\text{K}$) over a wide bandwidth (1-20GHz). After 4K, the noise figure of the signal is dominated by HEMT noise and can be amplified even more outside the fridge at room temperature.

4.1.3 dc Input line

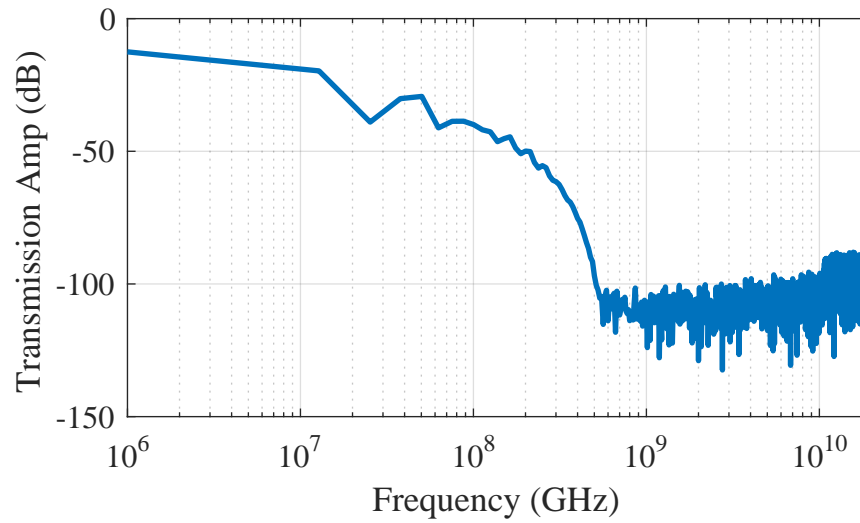


Figure 4.3: Transmission measurement of dc line 5 at room temperature.

The dc input lines provide voltage bias for MR-qubit coupling. It requires passing of dc or low frequency voltage signal and filtering all high frequency noise. Flexible stainless steel coaxial cable (Lakeshore Ultra miniature coaxial cable, type SS) is used from room temperature to mixing chamber for its low thermal conductivity and high attenuation (18 dB/m at 1 GHz). Four dc line are installed on fridge, on each of them two powder filters are inserted. Powder filter[33] has high attenuation and no self-resonance at high frequency ($>1\text{GHz}$). I made two different types of powder filters, stainless steel powder filter has a bigger attenuation than copper ones, but it is usually used only at 100mK or

above for the concern of not being fully thermalized [34, 35] and its potential anomalous heat capacity.

4.1.4 Flux bias line

The flux bias line controls the magnetic flux ϕ , changing total Josephson energy of qubit and thus changing the energy difference of qubit states. This line differs from the rest because it carries high, up to 10mA, current, compared to nano-amperes to micro-ampere in RF lines. Even 1Ω resistance on this line generates $(10\text{ mA})^2 \times 1\Omega = 10^{-4}\text{ W} = 100\mu\text{W}$ of heat load, which can heat up mixing chamber to 100 mK! The only way to avoid this heating is to use superconducting cable at cold stages. The superconducting wire, usually thin and resistive at normal state, needs to be very well thermalized at bobbins to keep below its transition temperature, otherwise heat generated at some point can heat up and turn the whole wire to normal state. For wire above 4K, we use twisted copper wire. The joint of copper and superconducting wire is thermalized at 4K stage.

The whole flux wire is twisted 200 turns/meter. Because adjacent loops in twisted pair cable have opposite direction thus it is much less affected by magnetic fluctuation[36]. Also the self-inductance of twisted pair is higher than straight wire, thus more reluctant to high frequency noise.

4.2 Magnetic shielding

The effective Josephson energy of the qubit $E_{J,\text{eff}} = E_{J,0} \cdot \left| \cos\left(\frac{\pi\phi}{\phi_0}\right) \right|$ is controlled by external magnetic field ϕ . In experiments, we use on-chip current line to provide the magnetic field. In order to have a few, say 3, flux periods in a $30\mu\text{m} \times 15\mu\text{m}$ square

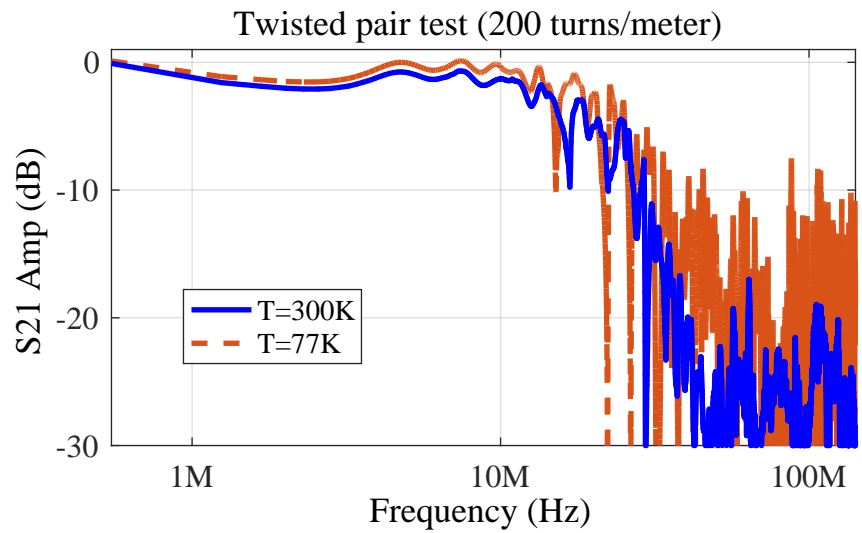


Figure 4.4: Transmission measurement of Superconducting twisted pair at room temperature and at 77K.

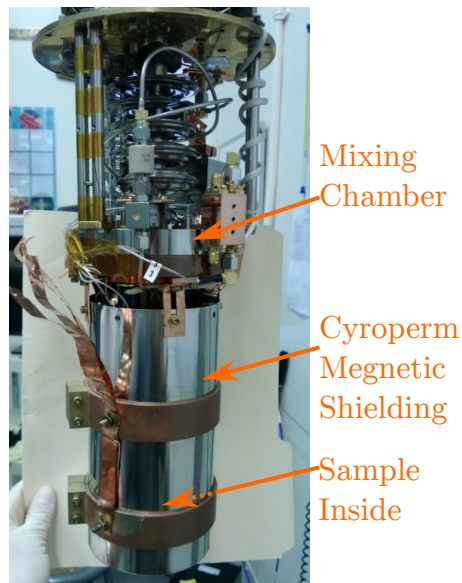


Figure 4.5: Photo of Cyroperm magnetic shielding.

loop from $100\ \mu\text{m}$ away, a magnetic field of 0.2 Gauss is needed. This is comparable with the Earth's magnetic field. And Other stuff such as a permanent magnet or a steel chair may cause a magnetic fluctuation roughly on the same order of magnitude. All these sources of flux noise can degrade the stability of system. In cancel the noise the sample is protected by commercial Cryoperm² magnetic shielding. This shield is cooled down to fridge base temperature using tight thermal contact as shown in Figure 4.5.

4.3 Demodulation

The frequency of cavity is $\sim 5\text{GHz}$. However we don't have a hardware to sampling and convert the signal at high enough speed (sampling rate must be higher than tens of giga-hertz). In order to extract the information, amplitude and phase, the GHz signal is usually mixed or down-converted to mega-hertz or dc range to digitize. Generally there are two methods, homodyne detection using IQ mixers or heterodyne detection by introducing another GHz signal detuned from the carrier frequency.

The homodyne detection is favored for two reasons, it requires a simpler circuit (less filtering, less sources and etc.) and thus is easier to work at a wider bandwidth. But the smaller dc offset (maybe frequency dependent) and drifts from IQ mixer limits the resolution for small signal. So we changed heterodyne detection from homodyne to get rid of dc offset problem. The giga-hertz signal is first mixed with a RF signal close to carrier frequency, and down-converted to IF frequency. The converted wave is furthermore digitally recorded by acquisition card, and the recorded signal is combined to extract both quadrature of original signal, which is called digital homodyne.

²<http://www.cryopermshielding.com/>

4.3.1 heterodyne detection and heterodyne board

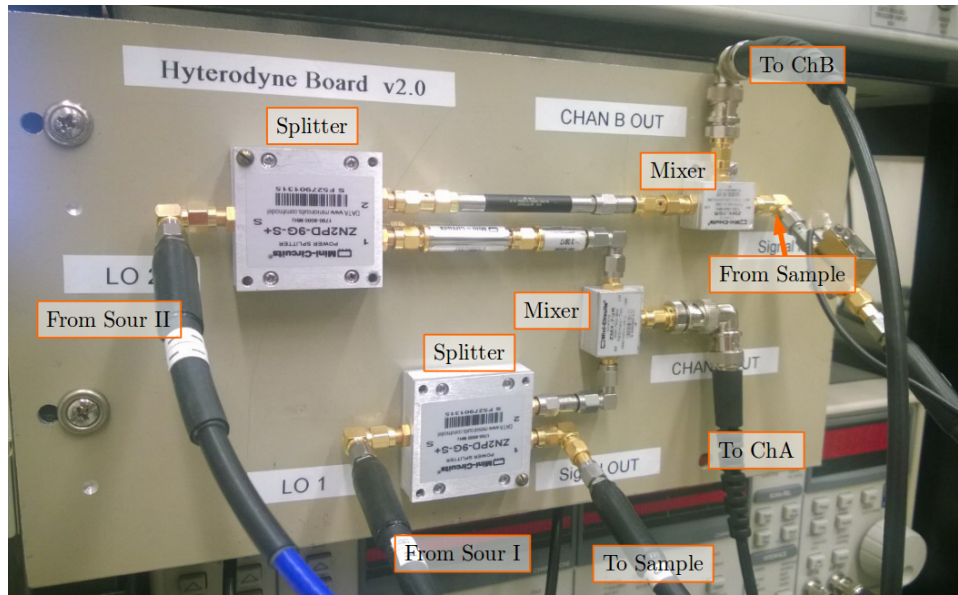


Figure 4.6: Photo of home-made heterodyne board.

IF frequency Because the information is encoded in IF signal, the heterodyne detection is much less affected by dc offset or $1/f$ noise by filtering around IF frequency. The choice of IF frequency is limited by some factors. The first one is sampling rate of acquisition card. The maximum speed of our Alazar card³ is 1GB/s for single channel, or 500MB/s for two channels. In order to get the complete wave of signal, the number of points per cycle needs to be much bigger than 4, which limits $f_{IF} \ll 100\text{MHz}$. But running at full speed of acquisition would result in more data to store in buffer and to transfer to memory, eventually slowing down data processing and increase total time of measurement without obtaining any new information. Secondly the lower bound of IF frequency is limited by the measurement time of one trace. Usually for continuous measurement, it is $\sim 100\mu\text{s}$, and for pulsed measurement, it is $4\mu\text{s}$. In single trace of data, the number of cycles needs to be much bigger than one, so $f_{IF} \gg 0.25\text{MHz}$. In earlier measurements,

³<http://www.alazartech.com>

we chose to use 4MHz. And then we changed to 10.7MHz because we found a narrow band-pass filter from Minicircuit⁴ centering at 10.7MHz (now shown in Figure 4.7), to filter out noise outside IF band.

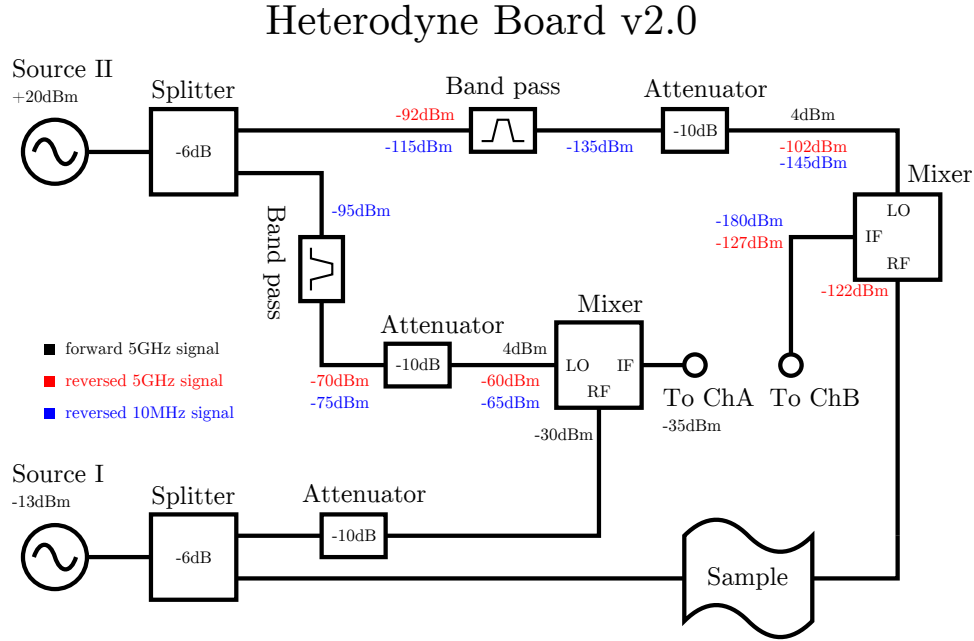


Figure 4.7: Schematic drawing of heterodyne detection circuit. The black squares represent electrical components in the whole circuit, including microwave sources and sample not on the board.

Signal processing The signal processing is first converted on home-made heterodyne board, see Figure 4.7. The 5GHz carrier frequency is generated from Source I, after passing by a splitter, it is sent to the sample located at the bottom right corner in Figure 4.7. The transmitted signal from the sample is first mixed with another RF signal with frequency slightly different $f_{IF} = f_{\text{Source I}} - f_{\text{Source II}} = 10.7\text{MHz}$ generated from Source II. The converted signal is then sent to Channel B to get digitally recorded. The other IF signal sent to Channel A is also mixed from Source I and II without passing the sample. It serves as a reference to canceling out the random initial phase difference $\phi_1(t) - \phi_2(t)$

⁴<http://www.cryopermshielding.com/>

between two sources. By comparing two down-converted signals using digital homodyne, both quadrature can be extracted.

cross-talk Introduction of a second RF frequency (the first one is splitted and sent to sample) causes cross-talk problem. There are two major cross-talks: first, the RF frequency from Source I can leak to the mixer through the other half of circuit (red in Figure 4.7), and similarly reference IF signal (blue in Figure 4.7) can go back-forward and arrive to Channel B. Adding up to original signal, these cross-talk may highly decrease the resolution of the system.

To avoid cross talk, I added attenuators and filters to improve isolation and clean the signals. Filters picks the correct frequency line, and kill noise outside the band. Attenuators between sources and mixers are used to damp reflected signals as well as coupled signals going backwards. In Figure 4.7, I calculated the power of 3 different signals: black texts indicating 5GHz forward signal; the coupled signal is in red text; and blue represents RF signals. The numbers are based on typical values from datasheet of components.

4.3.2 Digital homodyne and IQ extraction

The RF signals down-converted from home-made heterodyne board are filtered and amplified using series of SRS Preamplifiers, and then sent to Alazar acquisition board installed on the computer's mother board. The data is sampled at 100M samples/sec from both channels. To increase the speed of data processing, the raw data is processed using self-compiled dynamic link library file called by Labview. In the text following, I will show the strategy of quadrature extraction, also known as IQ extraction.

The reference signal sent to Channel A is

$$IF_r = \sin(2\pi f_{IF}t + \phi_1(t) - \phi_2(t))$$

where $\phi_1(t), \phi_2(t)$ are time dependent phases from source I and II. The amplitude of reference signal is constant within working range, so its amplitude is normalized to unity.

The Channel B IF signal is in similar form

$$IF_s = A(t) \sin(2\pi f_{IF}t + \phi_1(t) - \phi_2(t) + \Delta\phi(t))$$

where $A(t)$ is the amplitude and $\Delta\phi$ is phase delay coming from sample and connecting cables. The two IF signals are multiplied

$$\begin{aligned} I &= \langle IF_r \cdot IF_s \rangle \\ &= \langle \sin(2\pi f_{IF}t) \cdot A(t) \sin(2\pi f_{IF}t + \Delta\phi(t)) \rangle \\ &= A(t) \cos\left(\frac{\Delta\phi(t)}{2}\right) \end{aligned} \tag{4.1}$$

For Q , a $\frac{\pi}{2}$ phase-shifted reference IF is need. Since there is no such signal generated directly from hardware, it can be generated numerically inside software. Because both frequency and phase would shift over time on the time scale of second and even longer, a more practical way is by shifting the trace using interpolation. The shifted distance is calculated using fitted frequency, and this will be resulting in only phase and amplitude inaccuracy/noise, and amplitude noise can be re-calibrated by fitting its amplitude. Using

shifted reference, Q can be recovered as

$$\begin{aligned} Q &= \langle \sin(2\pi f_{IF}t) \cdot A(t) \cos(2\pi f_{IF}t + \Delta\phi(t)) \rangle \\ &= A(t) \sin(\Delta\phi(t))/2 \end{aligned} \quad (4.2)$$

as well as

$$\begin{aligned} A &= 4\sqrt{I^2 + Q^2} \\ \Delta\phi &= \arctan\left(\frac{I}{Q}\right) \end{aligned}$$

4.3.3 Result

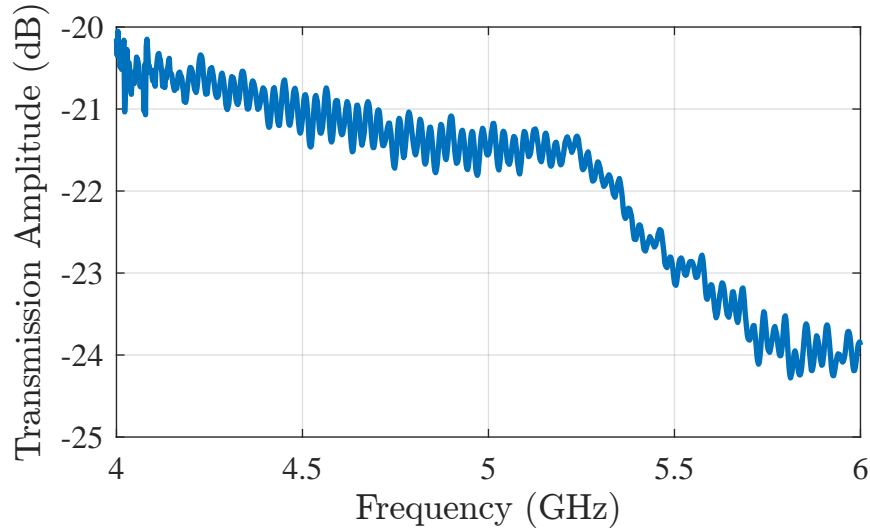


Figure 4.8: Transmissional test of home-made Heterodyne board. The curve shows a transmission measurement of a blue cable using Heterodyne board. Blue cable is a low loss transmission line. So the measurement is a test to characterize of the board and can also be used as a calibration for board. In the range of 4 to 6GHz, the amplitude is almost flat, with slightly change close to 6GHz. This slope is a result of all imperfection from all electrical components.

The test of Heterodyne board is done by measuring a blue cable from *minicircuit*, which

transmits microwave signal with almost constant low loss. The data acquisition is done by home-made Labview programs. See Figure 4.8 for details. The tested result for the blue cable shows small change (4dB over 2GHz), indicating the homemade Heterodyne board works as expected. And this curve also serves as the calibration for measurement done by this setup.

4.4 Measurement signal setup

In our measurement, there are two basic types of measurement, continuous measurement and pulsed measurement. Continuous measurement uses very long time (milliseconds), or always-on microwave to drive and measure the transmitted signal at the same time. It is advantageous for its simplicity in setup and control. Since the microwave is always on, one can only get average-over-time information of the sample. To fulfill state control and measurement, Pulses are used in time domain measurement of qubit. In this section, I will discuss the generation, synchronization and recording of pulses to drive and measure qubit at specific state.

4.4.1 Instrument setup

Pulses generation There are two types of pulses in the setup, pulsed square voltages and pulse microwave signals. The former is usually used to trigger or set components into specific state, and the latter is a short period of microwave signal at a constant frequency, to manipulate the state of qubit or cavity.

Pulsed squares in our setup is generated from Tektronix signal generator. Both channels are set in “Pulse” mode, generating pulsed square-shape signal. The amplitude is 5V to

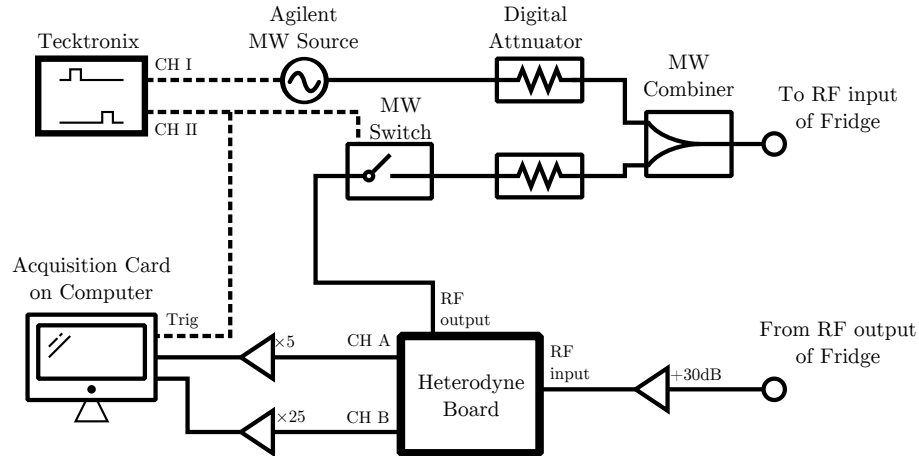


Figure 4.9: Schematic drawing of instrument setup of pulse synchronization and analysis circuit.

meet default settings of other components. Pulsed microwaves can be generated from different ways. Our Agilent microwave source can generate pulsed waves using built-in pulse module at specified frequency and amplitude. For sources without build-in function, pulsed microwave can be shaped with the help of 50Ω microwave switches, which can be controlled by pulsed square signals. The switch changes transmission of output port depending on the voltage state of control port. Pulsed squares simply turn on and off the switch to shape the envelop of the output microwave signal.

Synchronization Synchronization is crucial in time domain measurements. Controlling, detection and reading of the system requires time resolution down to nanoseconds. To keep the instruments in step, we use Tektronix as a timer. Two channels are matched by build-in clock. Channel I is used to start pulses to manipulate qubit: Agilent source runs in pulse mode, and the rising-up edge of square triggers source to output a pulsed microwave signal at specific frequency. Channel II is used to ramp up cavity to fulfill the “measurement” and trigger data acquisition. A microwave switch changes its output ports based on the Channel II voltage, thus turning “On” or “OFF” the transmitted

microwave to ring up or down the cavity. Channel II also triggers the acquisition card to digitize the input signal and save it in buffer.

data acquisition and processing Each time acquisition card is triggered, the input voltage is digitized and saved in its buffer in series. After a set of triggers, usually hundreds even thousands, all data are transferred to computer memory at once. Because the data is too large in size to save in hard disk, they are immediately processed in memory to extract amplitude and phase. This process is done by dynamic linked library compiled from C code.

Averaging and converting To increase the signal to noise, one usually repeat the measurement many times to reduce the noise and clean up the signal. The order of converting data and averaging needs delicate thinking. One option is to measure the same signal with same phase and average on acquisition card before IQ conversion, but this is not supported by our Alazar card. Or the repeated data can be averaged using software on computer. Either way requires accurate sharp trigger to line up the initial phase of each trace. When I tested this method, I saw drifts in phase between traces if the acquisition is trigger by reference signal in Channel A, thus straight averaging repeated traces would kill the signal. The third way is to extract I and Q for each trace, and then average I s and Q s to reduce noise. This method takes more CPU time to do more multiplication, but it is favored for being not sensitive to initial phase offset. While the time difference between two channels of Alazar in each triggered trace is 1ns, this is constant and much smaller than $1/10\text{MHz}=100\text{ns}$.

4.4.2 Time-domain Pulses

The time-domain measurement of qubit includes state manipulation and state detection. At the coldest stage of dilution fridge, $T=30\text{mK}$, for a qubit with 0-1 transition around 4GHz, $k_B T/\hbar\omega_q \ll 1$, it will relax to its ground state $|g\rangle$. The first pulse usually matches the qubit transition frequency and rotates the qubit along some axis. Similarly the cavity with a fundamental mode $\omega_c/2\pi \approx 5\text{GHz}$, stays on vacuum state $|n=0\rangle$. Due to dispersive interaction with qubit, the cavity frequency is no longer bare frequency, but changed by a dispersive shift $\delta\omega_c$ depending on the state of qubit. Because the measurement pulse's frequency is fixed, thus the state of qubit can be detected by whether this signal can excite the cavity[37, 38].

In the following I am showing the pulse sequences used to measure different properties of qubit.

Quasi Continuous

I start the measurement process by finding the qubit 0-1 transition frequency. This is can be done easily using continuous measurement setup. Or using the pulse measurement setup, we can do quasi-continuous measurement to pin down the qubit frequency.

Ideally the best way is to rotate qubit to its excited state $|e\rangle$ and then apply a measurement pulse to detect. However either the exact frequency or the optimistic strength of pulse is not decided yet. Instead, one can drive the qubit long enough and strong enough so it will end up on a mixed state. And the a measurement pulse is sent to distinguish between ground state and mixed state. The length of pulse is chosen at $40\mu\text{s}$, much longer than expected relaxation time of qubit. Followed is a $4\mu\text{s}$ pulse driving the cavity

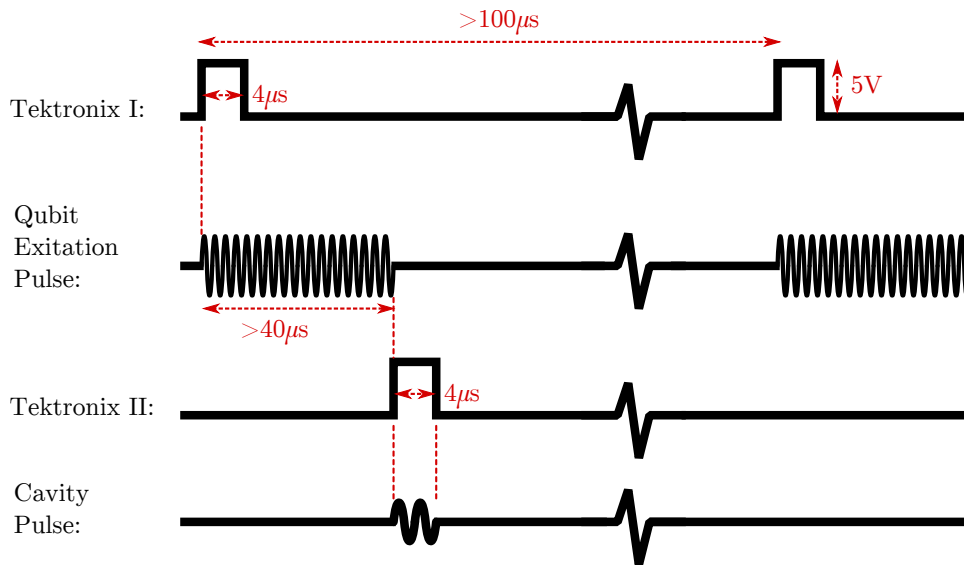


Figure 4.10: Schematic drawing of Pulses doing quasi-continuous measurement of qubit spectroscopy.

and $60\mu\text{s}$ with no pulses to relax the qubit back to ground state. See Figure 7.11

Rabi oscillation

Rabi oscillation, also known as Rabi cycle, is a process using coherent drive to “flip” the qubit between ground state $|g\rangle$ and excited state $|e\rangle$. One normally varies the length and frequency of the pulse to drive qubit, and perform a straight-away measurement to determine if the qubit is in $|g\rangle$ or $|e\rangle$.

Relaxation time

Relaxation time of a qubit describes how fast the qubit would return to its equilibrium (ground state in our measurement) from its excited state $|e\rangle$. This process obeys a simple exponential law in time $P_e = \exp(-t/T_1)$ [39]. First a π -pulse, whose length and frequency is decided from Rabi oscillation, is applied to flip the qubit to its excited state

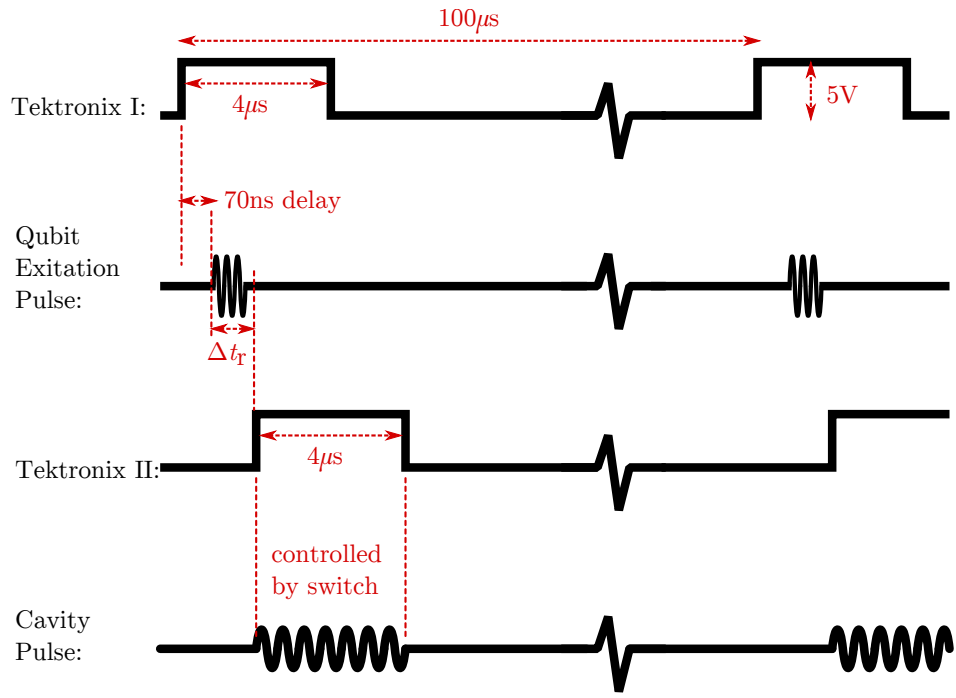


Figure 4.11: Schematic drawing of Pulses doing Rabi oscillation.

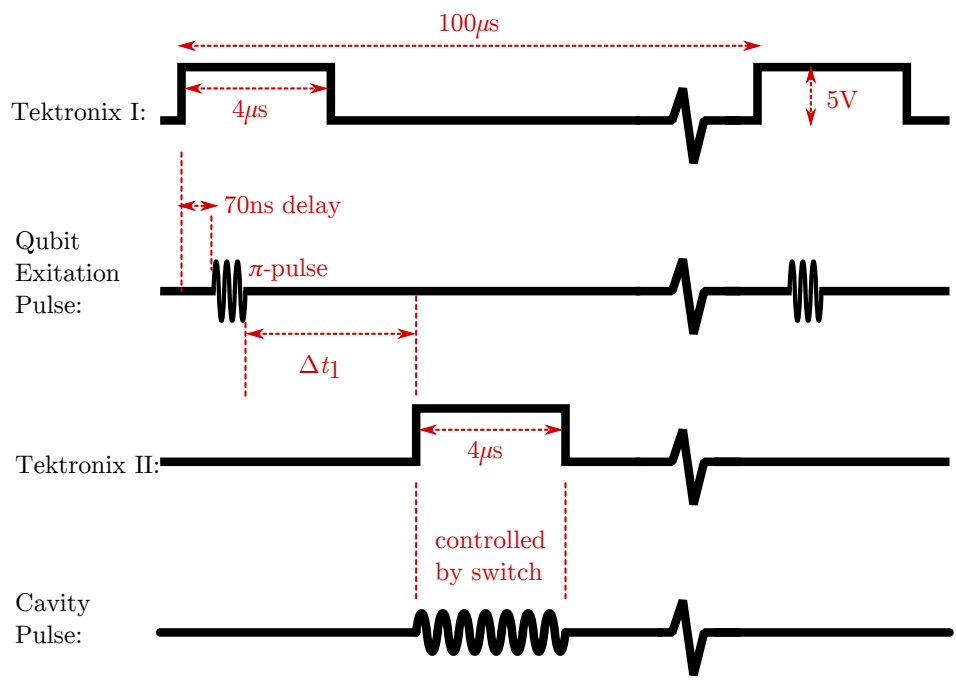


Figure 4.12: Schematic drawing of Pulses doing relaxation measurement.

$|e\rangle$. The system will then evolve only with dissipation due to internal or external noise. The measurement is then performed after a time delay Δt_1 . In the end the system is left to a full relaxation back to its initial state.

Ramsey oscillation

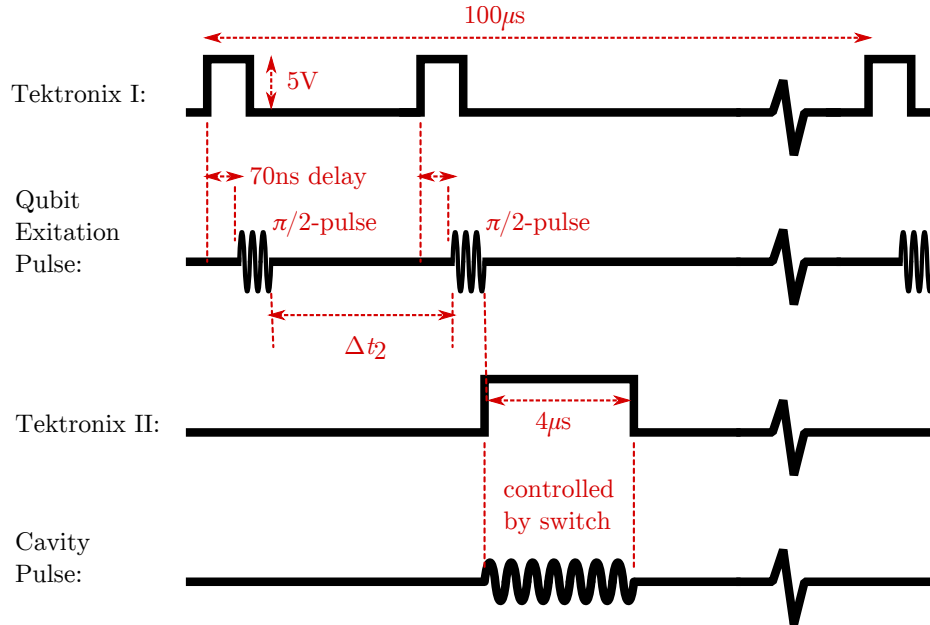


Figure 4.13: Schematic drawing of Pulses doing Ramsey oscillation.

Ramsey oscillation was first developed to measure atomic transition frequencies[40] and is widely used in superconducting qubits[41, 42]. As shown in Figure 4.13, three pulses are sent to the fridge. The first two pulses are at qubit frequency. Each rotates the qubit for quarter circle with a time space Δt_2 between them. Followed the second pulse immediately is a measurement pulse finding the possibility of qubit staying on ground state. Ramsey oscillation is sensitive to phase noise of qubit, so it is a good method to measure the dephasing time T_2^* .

Chapter 5

Fabrication

Micro-fabrication and nano-fabrication are a processes of manufacturing structures on micrometer scale or even nano-meter scale widely used in many areas of science and engineering. In our transmon-MR coupled system, the sample is composed of three different elements: a filter-biased CPW cavity, a 2d transmon qubit and a suspended mechanical resonator. Fab performed Cornell National Facility (CNF)¹ and the lab of Prof Britton Plourde at Syracuse University.

Elements in the system The filter-biased CPW cavity serves as environment seen by transmon qubit and mechanical resonator, it affects the the state of coupled system and detects the state. For a standard CPW cavity[5], also in our filter biased CPW cavity[43], the length of it determines it fundamental frequency. For $\omega_c/2\pi \approx 5\text{GHz}$, the length of center line is $\lambda/2 \approx 11\text{mm}$, seese Figure 5.2.

The transmon qubit is an artificial quantum system with unequal spaced energy eigen-

¹www.cnf.cornell.edu

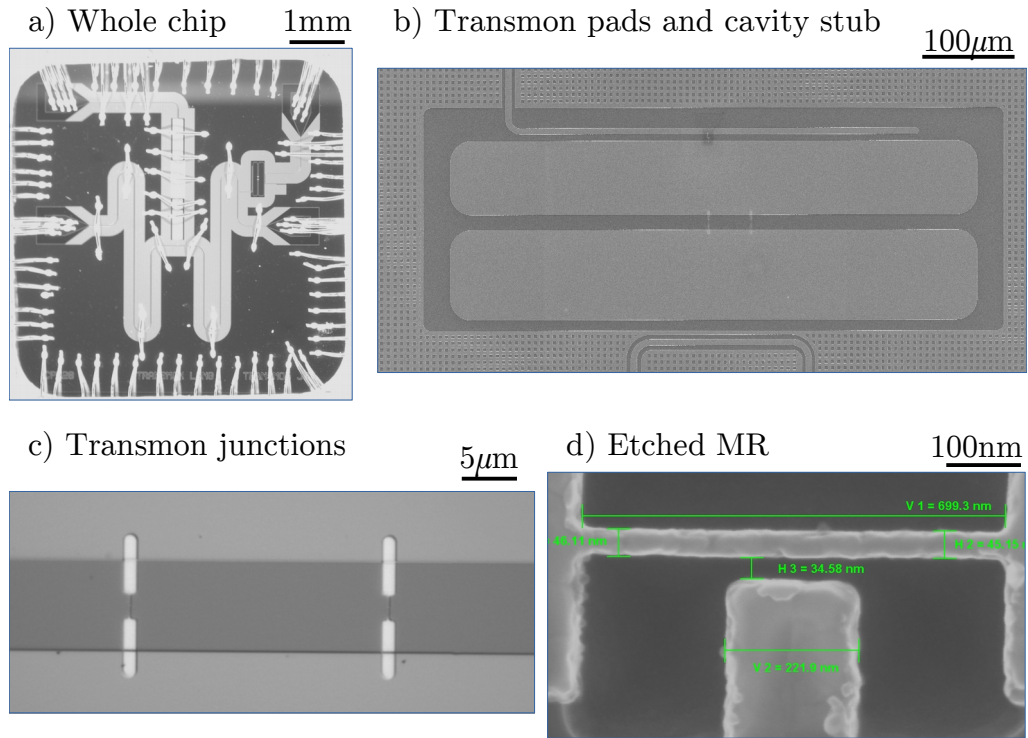


Figure 5.1: Optical picture and SEM images of sample at different scale. (a) A optical picture of the whole chip attached. Wire bonds connect the chip to printed circuit board (PCB) board. The black area is plain Nb and bright-looking area is patterned with flux traps on Nb. (b) SEM image of transmon area. The two big round-corner squares are island and shunt pad made of Nb. The stub on the top is connected to CPW center line. And the bottom line is flux bias control line. Between the 2 big pad are two Josephson junctions, and between cavity stub and island pad is the mechanical resonator made of Aluminum. (c) SEM image of Josephson junction area. The two gray color at top and bottom are transmon pad and dark area in the middle is Si substrate. Two white strips connecting the pads are Josephson junctions. (d) SEM image of suspended mechanical resonator. The 45nm wide beam clamped on both sides is the mechanical resonator, 35nm away from gate. Underneath is etched silicon hole.

states, among which the lowest two can be treated as two-level system[14]. Unlike an ideal harmonic oscillator system, this property of nonlinearity comes from its Josephson junctions, which has nonlinear inductance. A Josephson junction used in our sample is composed of two superconducting metals sandwiching a thin layer of insulation. The size of junction giving $E_J \sim 6\text{GHz}$ is designed to be $\sim 100\text{nm} \times 100\text{nm}$, which is roughly 100-1000 smaller in size compared to transmon pads and 10^5 smaller than CPW cavity, see Figure 5.6.

The third element is a suspended beam or membrane. Mechanical resonator varies a lot in size from millimeters to nanometers. In our experiment in order to achieve coupling with transmon qubit at different regime (resonance limit, dispersive limit) and coupling strength as big as possible, the width and gap between mechanical resonator and qubit is design to be tens of nanometers. It is very challenging to protect the structures while lift-off and releasing processes.

5.1 photolithography

Photolithography is a process using masks and lights to transfer pattern. Various photo-resist is used to protect or expose defined area on the substrate in other process(etching, deposition, etc.). There are mainly two different type of transferring pattern: negative pattern to etch, or positive pattern to deposit metal. In fabrication making our Nb cavities and transmon pads, etching process is more often used. And in recently developed membrane recipe, both methods are used sequentially to achieve multi-level structure.

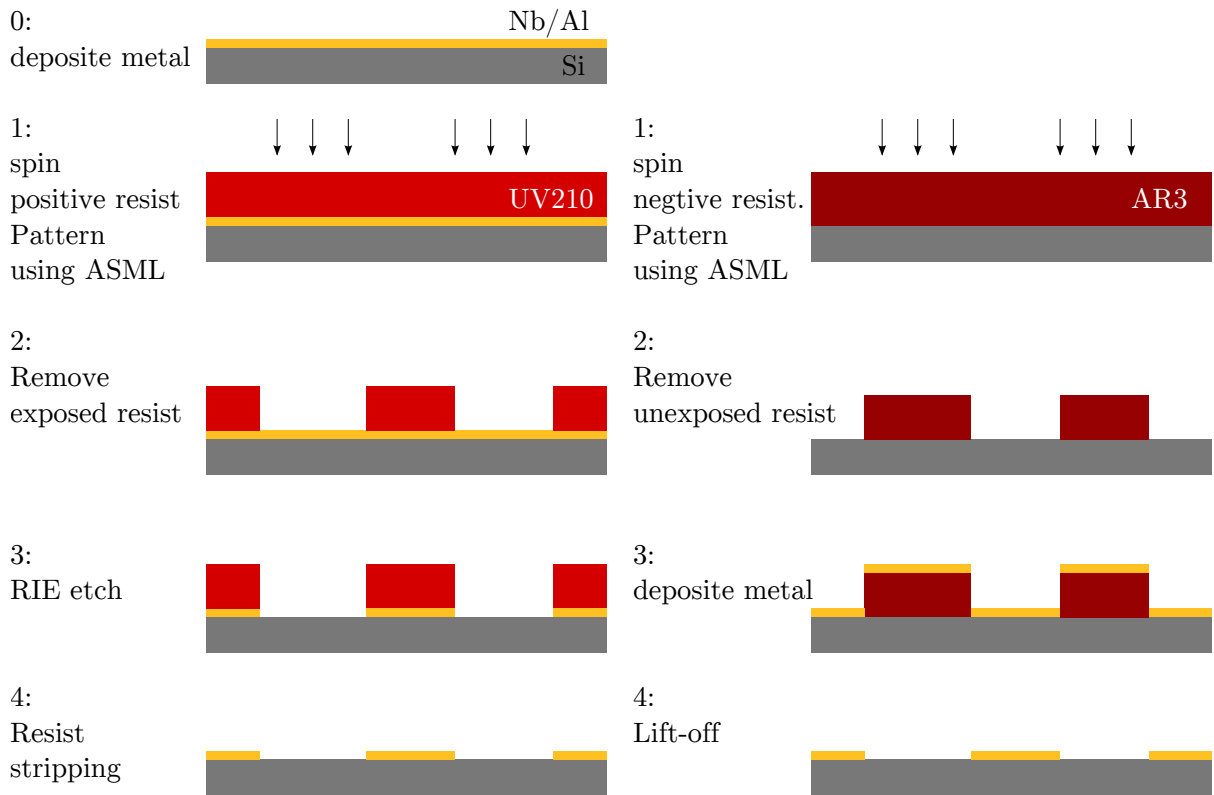


Figure 5.2: Sketch map of photolithography using etching and lift-off process. The left column shows the process using etching where the unwanted metal is etched out (negative pattern). The right column is using lift-off process where only desired metal can be deposited to the substrate (positive pattern) and kept after lift-off. The redish color indicates photo resist and yellow indicates metal.

5.1.1 Negative pattern and etching

Mask preparation Before working with wafer using steppers, a mask needs to be prepared using mask writer. A mask is a square glass covered with thin-layer chrome and photo-resist. The pattern of cavity and transmon pads are first designed and drawn using CAD software. Most of time I use *KLayout*² to draw and modify. Then the pattern is “written” onto the mask using *Heidelberg Mask Writer DWL2000* at CNF.

Transfer pattern using stepper The substrate is first prepared with one thin layer of metal (Al or Nb) fully covering the wafer surface. This can be done by sputtering or ebeam deposition (step 0 in Figure 5.2). Then the wafer is covered with positive resist, the exposed part of which will be removed by specific solvent. The pattern is transferred by blocking and letting light pass to shine at different position of wafer. The exposed resist is then removed in “develop” process.

I usually use *ASML 300C DUV Stepper* at CNF to print pattern onto wafer, because it has the best resolution, usability and speed among all steppers.

Reactive ion etching (RIE) Etching process uses chemical reaction to remove metal, silicon, polymer or other materials. Usually a reactive plasma is created using RF power source and bombardment of ions break the chemical bonds and remove materials. The directionality of the RIE etch is typically controlled by adjusting biasing voltage and gas pressure.

For Nb pattern in our sample, etching was done using *PT770/740 Etcher* at CNF.

²www.klayout.de

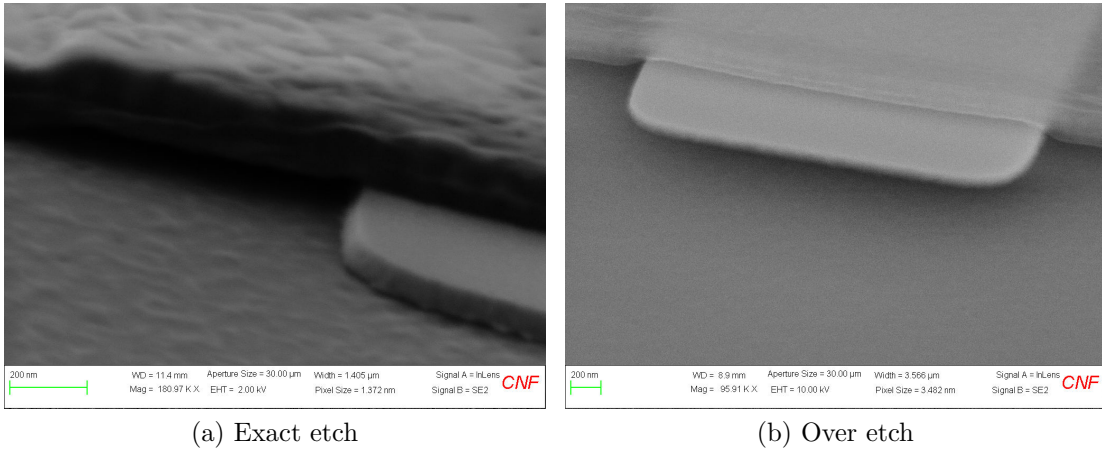


Figure 5.3: SEM images of two membrane samples showing an exact etch and an over etch. In both images, the bottom metal is made from Nb etching.

Etch rate and time are critical parameters. Typically the goal of this process is to accurately remove Nb without damaging silicon substrate or other protected Nb. Removing silicon substrate (over-etch) leaves deeper groove between metals and changes the effective dielectric constant of system. And as a result the total impedance of transmission line and mutual capacitance between each metal is off the designed value. Exact etching is very critical in membrane fabrication, because the gap distance control is delicate and very sensitive to manufacturing error in thickness. In some cases over etch can be intended: such as increasing the effective distance between metals and decreasing leaking current.

When the metal pattern is done correctly, the resist needs to be removed. This is done by dissolving resist in heated “hot bath” at CNF.

5.1.2 Positive pattern and lift-off

The lift-off process starts from an empty clean wafer. And negative resist is spun on the wafer. Similar stepper writing and develop steps are followed. Then the metal needs to be deposit on the wafer through sputtering or e beam deposition like step 0 in etching process. The last step is lift-off, where resist is removed using solvent along with metal deposited on resist. Only desired metal straight attached to substrate is kept.

One common problem of lift-off process is flagging. It happens when the resist is being stripped off, small pieces of thin metal on the wall of resist that is connected with bulk of metal on substrate fall down on the metal of substrate, see Figure 5.4. The flagging might touch with nearby metal if the gap is small.

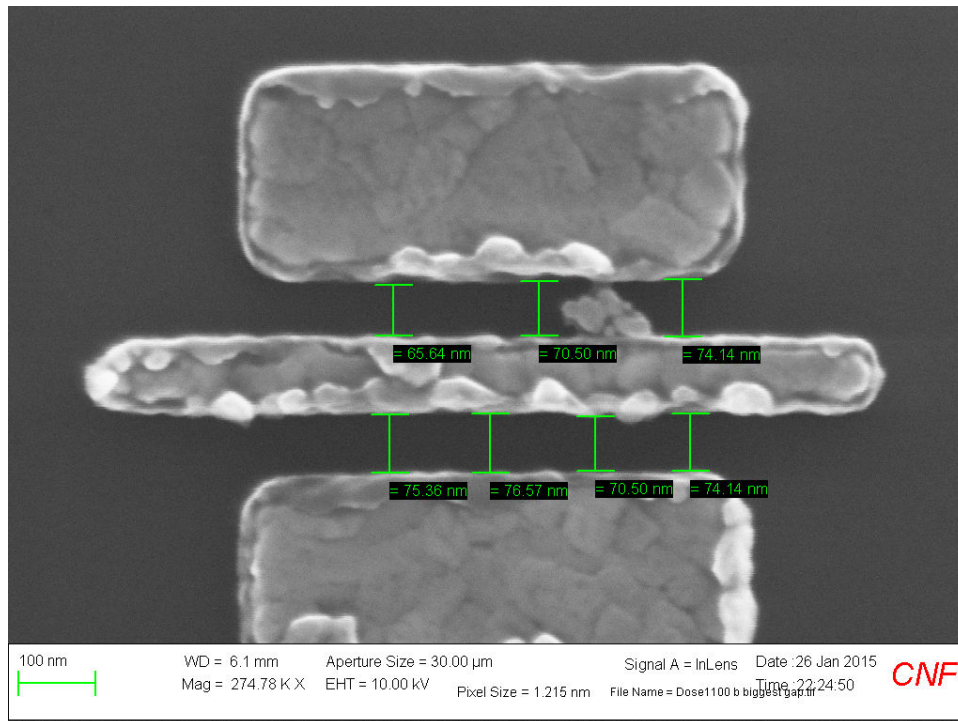


Figure 5.4: flagging from lift-off process.

5.1.3 CPW fabrication recipe

Here I will present the detailed photolithography recipe to fabricate filter biased CPW cavity and pads for transmon. This recipe also apply to similar patterns with dimensions in the range of μm to mm. It generates a uniform thickness single layer pattern made by niobium. The process is conducted at CNF.

1. Spin anti-reflective coating DSK manually or Gamma #1076
 - 3750rpm, 30sec, 1000rpm/s²
2. bake at 185 °C, 90sec
3. Spin photo resist UV210-Gs 0.6 manually or Gamma #1003
 - 2825rpm, 30sec, 1000rpm/s²
 - thickness=600nm
4. bake at 135 °C, 90sec
5. ASML writing pattern, dose=25
6. Post bake at 135 °C, 60sec
7. Develop UV210 manually or Gamma #2008
 - Hamatech Program #3: 726-mif-120sec-dp

5.1.4 Nb etching recipe using PT720

- Batch file: doeal1.prc
- main etch time: 4min 15sec
- gap: 20Ar + 20BCl₃ + 10Cl₂
- pressure: start=30mtorr; main=20mtorr

- power: DC 300V, ~85Watt
- mode: RIE

5.2 E-beam lithography

Electron-beam (e-beam) lithography is a technique of using focused electron beam to draw shapes on electron-sensitive materials. Accelerated electrons (primary electrons) by high voltage (up to tens of kilo-Volts) are absorbed by e-beam resist, and produce low speed electrons (secondary electron) through inelastic collision. Secondary electron are capable of breaking chemical bonds of e-beam resist and changing its solubility. The scattering effect of primary and secondary electrons limits the resolution of e-beam lithography, known as proximity effect. The newest generation of e-beam lithography system at CNF is *JEOL 9500* has point resolution up to 4nm!

In fabrication of Josephson junction and mechanical resonator, polymethyl methacrylate (PMMA) and copolymer (MMA) from *MicroChem* are developed using mixed 1:3 MIBK:IPA, to achieve the best resolution. The exposed e-beam resist needs to develop as soon as possible. According my and some of my colleagues' experience, the exposed area grows over time if not develop in time.

5.2.1 Double angle evaporation and Josephson junctions

Double angle evaporation also known as Niemeyer–Dolan technique is a technique to create multi-layer overlapping structure[44, 45]. It is used to create Josephson junctions for qubit, SQUID and other superconducting devices. The key structure of the resist is a suspended resist layer, see Figure 5.5. It is generated by two layer of resists, where the

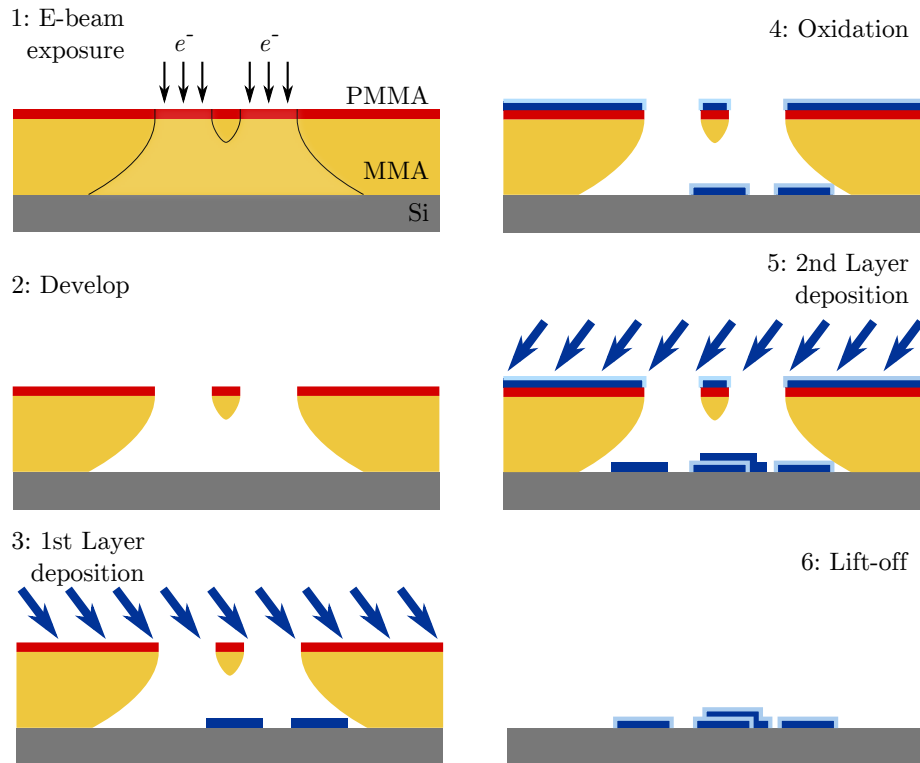


Figure 5.5: Diagram of double angle evaporation process. 1) Bi-layer e-beam resist is exposed to electron focused beam. The thick MMA layer is more sensitive than the top PMMA layer. The black line indicates the area affected by electron induced chemical reaction. 2) Resists after develop step. 3) 1st deposition at a tilted angle. 4) Oxidation step. 5) 2nd layer deposition at a different angle. 6) Lift-off step to remove unwanted metal and e-beam resist.

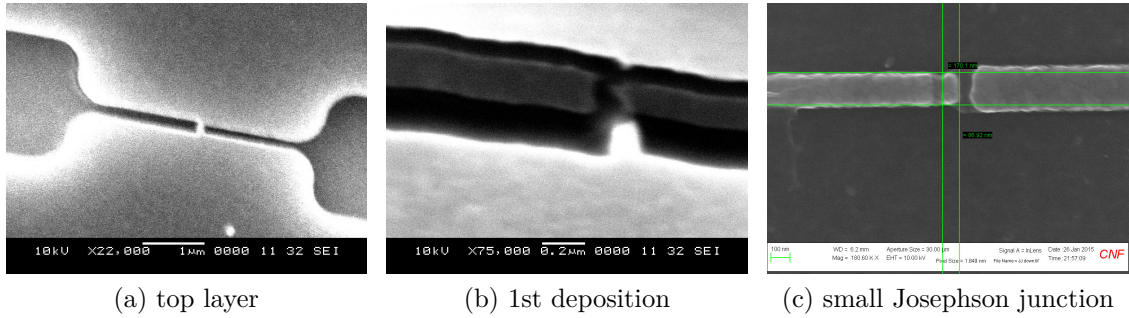


Figure 5.6: SEM images of evaporation and Josephson junction. (a) SEM image of bi-layer resist pattern after a straight deposition. (b) 1st layer Aluminum deposition. Note the suspended bridge is broken. (c) SEM image a Josephson junction with a small area ($87 \times 170 \text{nm}^2$) overlap.

thick bottom layer is more sensitive to electron than the top layer. We use 70nm PMMA as top layer and 600nm MMA as bottom layer. The dose of electron exposure is adjusted so that designed pattern is exactly printed on top layer. Because of scattering and high sensitivity the bottom layer is “over-dosed”, a undercut structure is formed in the develop step. In the two steps of Aluminum deposition (3) and (5) in Figure 5.5, the sample is tilted in two different angles, so the deposition are shifted to form overlaps. After the first deposition, low pressure oxygen gas, sometimes mixed with Argon, is introduced to generate insulation layer of the junctions. After the second layer of deposition, I add a post-oxidation step to grow aluminum oxide on the surface of Aluminum to protect the junction. In the end, the resists is removed in lift-off step.

5.2.2 Josephson junction e-beam recipe

Below presents the detailed e-beam lithography recipe to write patterns of Josephson junctions. The thickness of MMA and PMMA is optimized for small junction(tens of nanometers to sub-microns). The process is conducted at CNF. The deposition of metal is described in the next recipe.

1. 1st layer MMA
 - MMA(8.5)MMA Et(11%), 8.5 in ethyl
 - 2100rpm, 1000rpm/s², 60sec
 - thickness=600nm
 - bake 170 °C, 10min
2. 2nd layer PMMA
 - 2% 495MW PMMA in anasole
 - 2500rpm, 1000rpm/s², 60sec
 - thickness=70nm
 - bake 170 °C, 10min
3. E-beam dose=1000 μ C/cm² (this value changes over time)
4. develop
 - 80sec MIBK:IPA 1:3
 - 80sec IPA
 - Blow dry by nitrogen gas

5.2.3 double angle evaporation recipe

This recipe is to deposit double layer Aluminum Josephson junctions using written and developed resist pattern which is generated in the last recipe. One can also modify the recipe to deposit single layer Aluminum pattern. This process is conducted in Britton Plourde's Lab at Syracuse.

Note the deposition rate of Aluminum is not set directly by evaporation controller, it is affected by several conditions, such as the power of electron beam to heat the Aluminum

target, the size and temperature of Aluminum target and other uncontrollable parameters. Because some of conditions varies overtime, it is necessary change the e-beam power to keep the deposition in an acceptable range. The effect of deposition rate is carefully studied in Bordo's paper[46], and his results are consistent with my own observation.

1. load and pump chamber to $\sim 10^{-8}$ torr

2. ion milling 11sec

pressure: $2-3 \times 10^{-4}$ torr

3. 1st layer deposition

angle= -10°

1.5-2Å/s, 35nm

4. oxidation step

time ~ 20 min

pressure: 200 torr at Oxygen chamber

conditions above changes with junction size and resistance needed

5. 2nd layer deposition

- angle= 5°
- thickness: 70nm

6. post oxidation

5.3 Mechanical resonator deposition and releasing

One type of mechanical resonator in our system is a suspended beam. To achieve a high frequency (hundreds of MHz) and a high coupling strength, the width of beam is designed

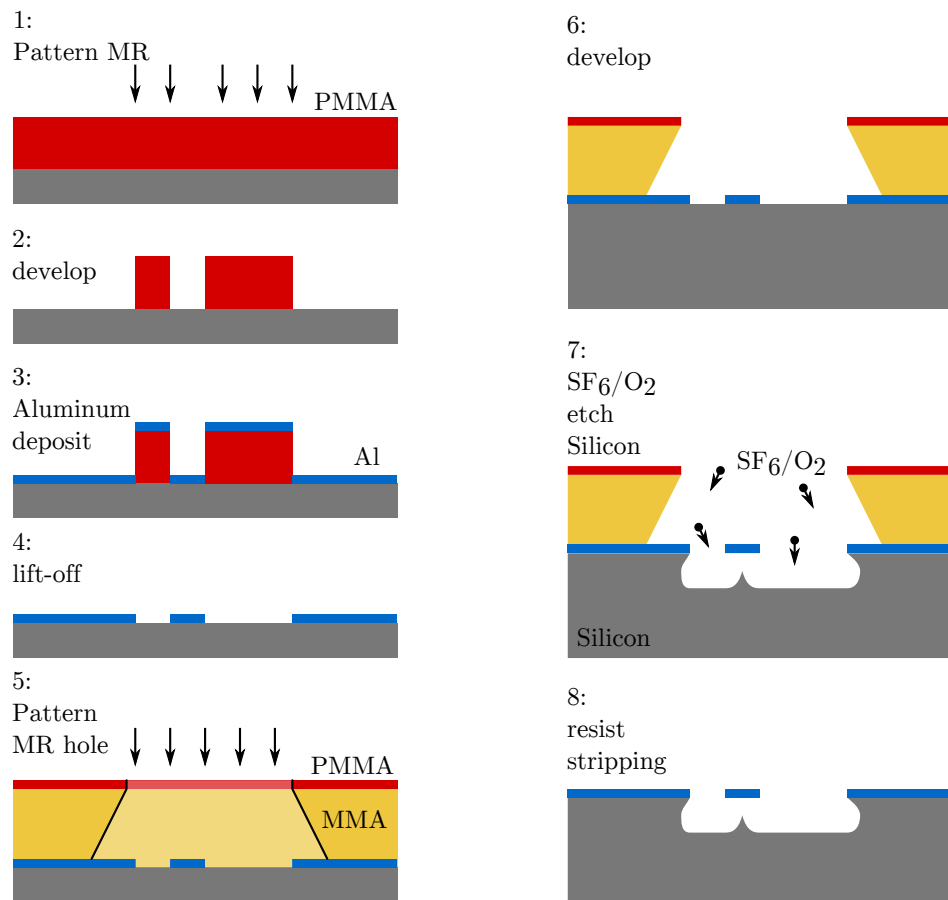


Figure 5.7: Diagram of Mechanical resonator deposition and releasing. (1) The MR is patterned on one single layer of PMMA using e-beam lithography. (2) develop. (3) Straight deposition of Aluminum mechanical resonator. (4) lift-off. (5) The hole is patterned on bi layer resist using e-beam. (6) Develop. (7) The unprotected silicon is etched using mixed Sulfur hexafluoride SF₆ and Oxygen O₂, to release suspended beam. (8) Resist stripping.

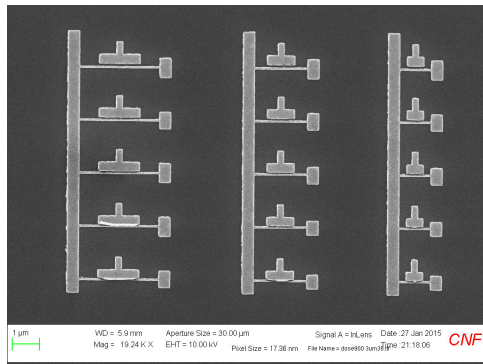
to be very small, ~ 50 nm. Because small gap distance gives bigger capacitance change $\frac{\partial C_{MR}}{\partial x}$, we want the gap to be as small as possible, see eq. 2.25. To achieve these goals, we chose to use single layer PMMA resist, which has the best resolution. Since electrons always scatter in resist, the thickness of resist shouldn't be too high to have straight walls. The height (to clarify this is the thickness of the layer) of beam is 100nm, thus the thickness of PMMA needs to be bigger and is chosen to be 200nm. The MR pattern is written using e-beam lithography, and developed in 1:3 MIBK:IPA. The Aluminum is then straight deposited to form the beam, and then the resist is stripped.

The releasing process starts with patterning the “hole” on a PMMA-MMA resist. Because in etch step, both resist and silicon substrate are etched and the resist serves as protect layer for substrate. Instead of using very thick (~ 600 nm) layer of PMMA, we choose to use a bi-layer PMMA-MMA resist, so we can apply the same dose in the e-beam recipe. After e-beam patterning and developing, the unprotected Si is then removed using SF_6/O_2 RIE etch. The pressure and power of etch process is adjusted to have more isotropic reaction, to remove silicon underneath the beam. Eventually the resist is stripped.

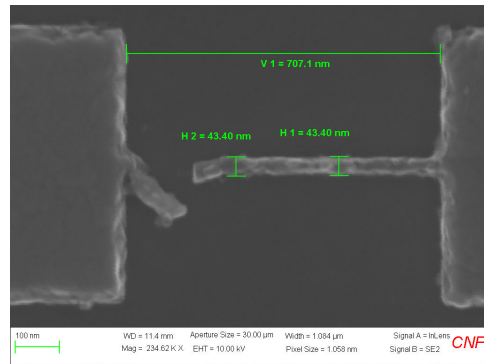
5.3.1 MR e-beam recipe

This recipe is to write single layer mechanical beam pattern using e-beam lithography at CNF. After the pattern is written and developed, one can deposit 100nm Aluminum using e-beam evaporator.

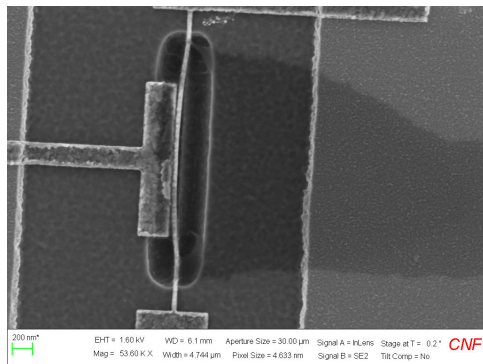
1. Single layer PMMA
 - 495 PMMA A4



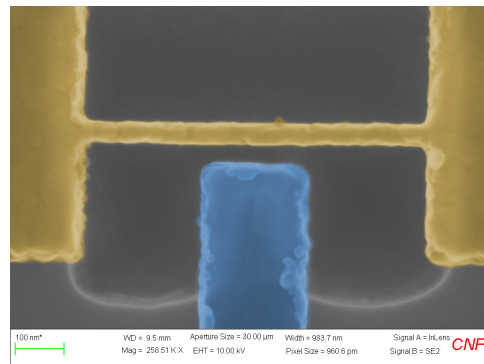
(a) test arrays of mechanical resonator



(b) broken beam



(c) snap-in beam



(d) False colored etched MR

Figure 5.8: SEM images of different mechanical resonators.

- 2000rpm, 1000rpm/s², 60sec
 - thickness=200nm
 - bake 170 °C, 10min
2. E-beam dose=1250 μ C/cm²
 3. develop in MIBK:IPA 1:3

5.3.2 MR hole etch recipe

After the mechanical resonator is deposited, the substrate underneath needs to be removed to release the mechanical resonator. This is done by first writing the hole using e-beam lithography and then etch the silicon under the mechanical resonator. The latter step is discussed in the next subsection.

1. bi-layer same as Josephson junction recipe
2. e-beam writing dose: 1000
3. Etch Silicon using Oxford 82
 - Recipe name: SF₆/O₂, SF₆=30sccm, O₂=10sccm
 - pressure: 200
 - time: 20sec
 - power: 100W
 - DC bias: 34V
4. Strip resist using DCM, rinsed by IPA and blow-dry.

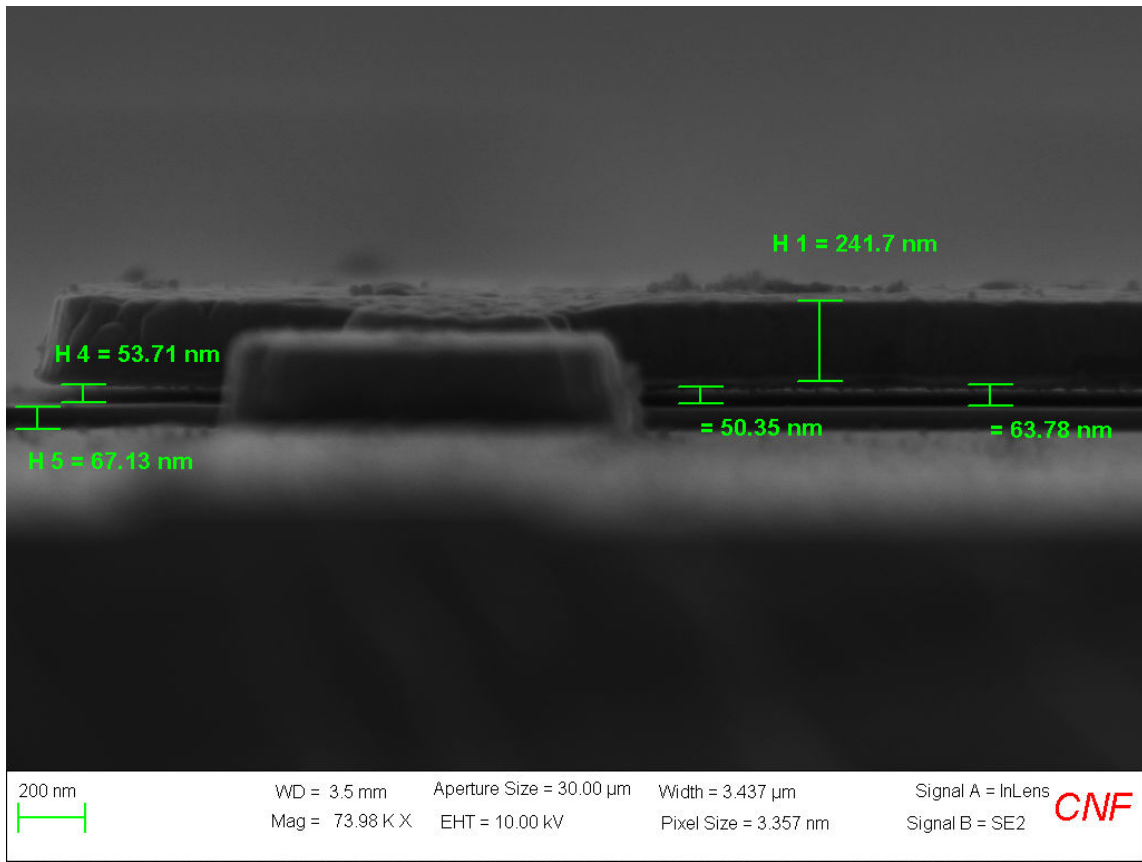
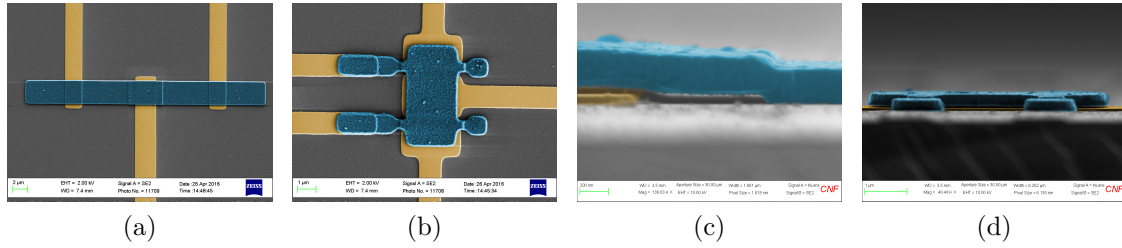


Figure 5.9: SEM images of membrane. (a)(b) top view of doubly-clamped/free-free membrane. (c)(d) side view of doubly-clamped/free-free membrane. (e) side view of free-free membrane with measurement bars

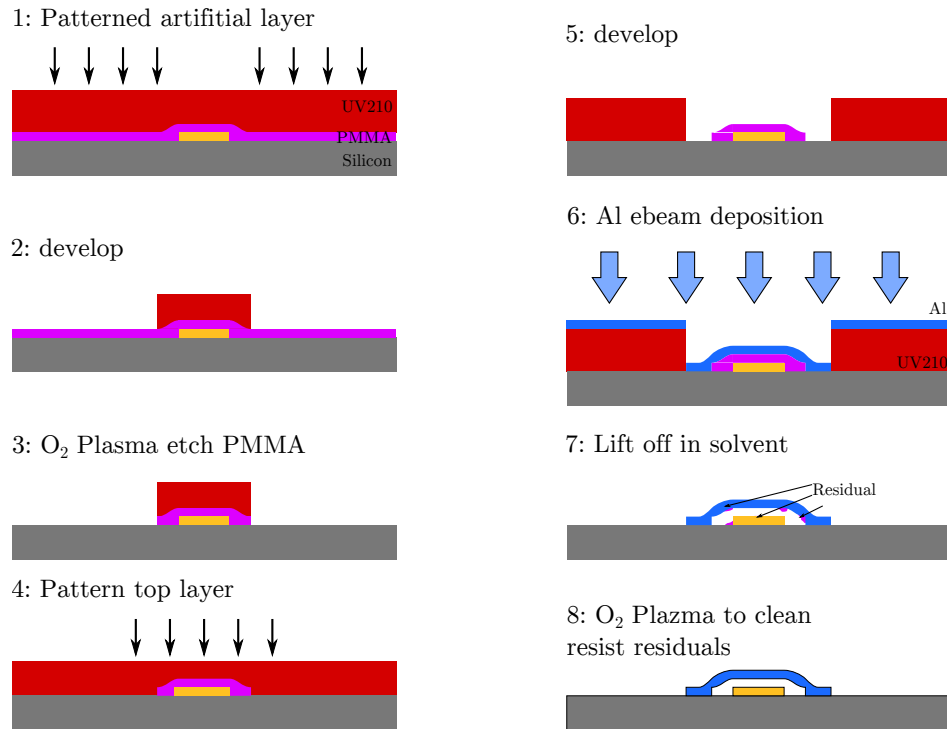


Figure 5.10: Diagram of membrane resonator deposition and releasing. (1) The MR is patterned on one single layer of PMMA using e-beam lithography. (2) develop. (3) Straight deposition of Aluminum mechanical resonator. (4) lift-off. (5) The hole is patterned on bi layer resist using e-beam. (6) Develop. (7) The unprotected silicon is etched using mixed Sulfur hexafluoride SF₆ and Oxygen O₂, to release suspended beam. (8) Resist stripping.

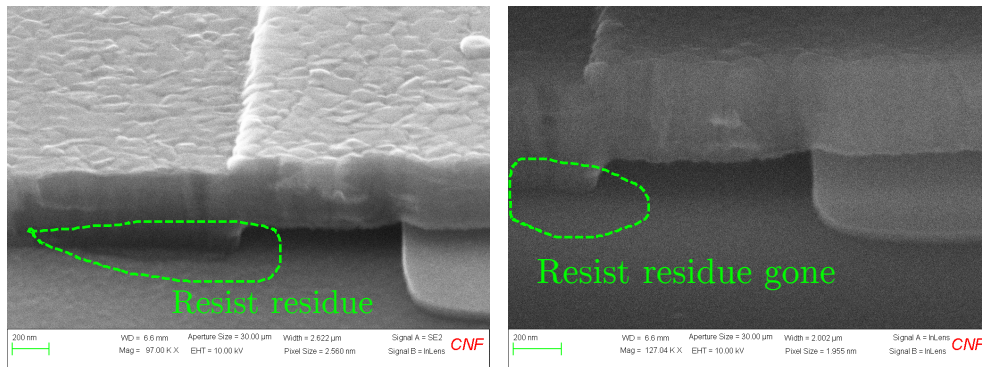
5.4 Membrane

Our membrane mechanical system is a multi-layer structure. It is advantageous for its bigger capacitance and coupling strength, but it adds complexity in fabrication.

The membrane fabrication uses PMMA as sacrificial layer to create gap between top and bottom layer. PMMA is favored for its resolution (up to a few nano-meters) and easy handling of its thickness, which will be the gap distance of membrane. Also PMMA is organic resist and can be easily removed using solvents commonly used in Josephson junction fabrication. Furthermore, removal of sacrificial layer doesn't require long time of etching, thus bringing less damage or contamination to system, especially along with fragile Josephson junctions.

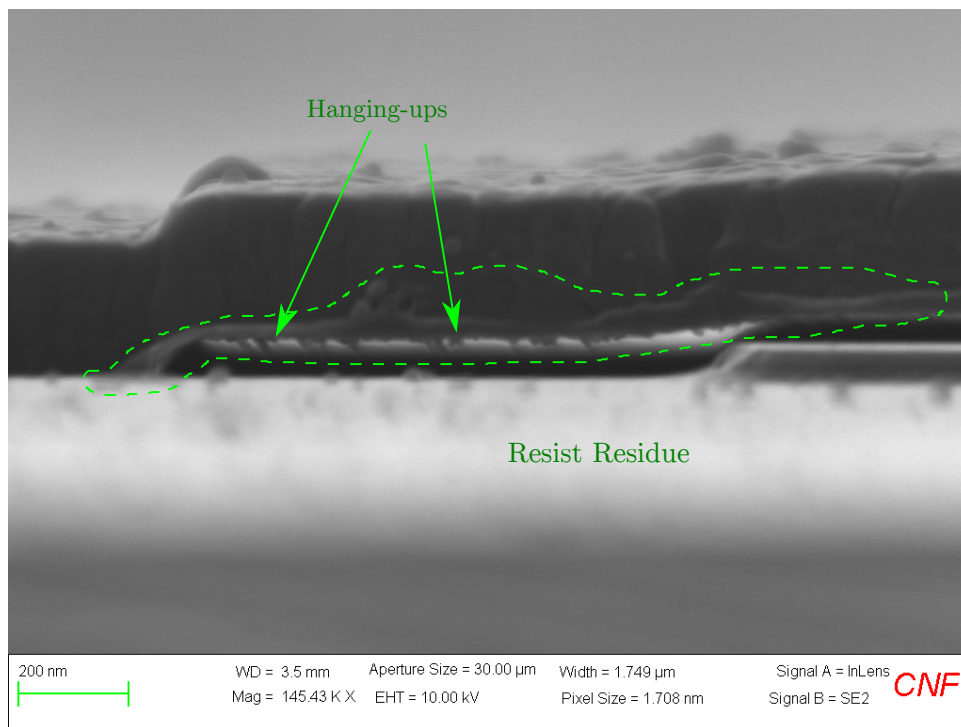
The bottom metallic layer is fabricated using standard photolithography method. The thickness of bottom layer is very crucial in defining the gap distance, over-etch of silicon should be avoided by careful calibration of etch and deposition time. Because both the Nb sputtering rate and RIE etch rate vary over time, I usually set the etch time at a minimal limit, and perform additional etches for small amount of time if needed.

The sacrificial layer of PMMA is then spun over the bottom layer and heated to decrease its solubility in the next develop step for photo resist. Then aligned pattern of gap is pattern using photolithography technique, written by ASML at CNF. The exposed PMMA is removed using anisotropic or directional oxygen plasma etching. Then the top layer is patterned using similar photolithography steps and then deposited using either Niobium sputtering or Aluminum e-beam deposition. The last step is to remove the sacrificial layer of PMMA: most of it can be easily dissolved in dichloromethane, Remover PG or acetone. The residues of resist is burned out in oxygen plasma asher.



(a) resist residues

(b) residues removed



(c)

Figure 5.11: Comparison of removing resist residues. (a) SEM image of membrane showing resist residues on the sidewall of membrane after standard lift-off using dichloromethane and isopropyl alcohol. (b) SEM image of membrane showing the resist residue is removed using additional oxygen plasma ashing. (c) side view of doubly clamped membrane. Residue on the side and hanging-ups in the gap are observed.

Residues of photo resist The residues of photo resist is normally on the scale of nanometers and thus invisible in optical microscope. However they strongly affect the property of mechanical movement of resonator as well as electro-magnetic dissipation[47, 48]. When I measure membrane resonator, I couldn't even see membrane signal before cleaning, See chapter 9. The amount of residues could differ from sample to sample. From some samples, it is possible to observe small hanging-ups inside the gap. Judging from the shape and color, I believe they are resist residues with strong chemical bonds to surface atoms. Further research needs to be done to understand this. See Fig 5.11 for comparison.

5.4.1 Membrane recipe

1. **Bottom layer** same as photolithography
 - Niobium thickness: 50nm
 - ASML writing bottom layer pattern, dose: MR=25, surrounding=28
 - etch time: 2min 30sec
2. **sacrificial layer PMMA**
 - 2% PMMA, 495PMMA A2
 - 1500rpm, 60sec, 1000rpm/s²
 - bake 170 °C, 10min
3. Photo resist UV210
 - 2825rpm, 30sec, 1000rpm/s²
 - bake 135 °C, 90sec
4. ASML writing sacrificial layer patttern, dose=22

5. post-bake
6. develop using Hamatech #3
7. Oxygen plasma etch sacrificial layer
 - recipe name: O2 stripping
 - time:20sec
 - Pressure: 60
 - Oxygen flow rate: 50sccm
 - power: 150
 - etch rate: 5nm/s
8. ASML flood expose with dose=150
9. post-bake and develop using Hamatech #3
10. **Top layer** spin UV210
11. ASML writing top layer pattern with dose=25
12. post-bake and develop
13. Aluminum e-beam deposition
 - deposition rate: 1.5-2Å/s
 - thickness: 250nm
14. lift-off
 - (a) Remover PG, heated at 70 °C, 2 hours
 - (b) DCM, heated at 45 °C, 1 hour
 - (c) rinsed in IPA and blow dry.
15. Oxygen Plasma ashing
 - Power: 900W
 - flow rate: 500sccm

- pressure: $\sim 1000\text{mTorr}$
- time: 6min

Chapter 6

Filtered CPW cavity

Superconducting 2-d cavity is an important tool in circuit QED, and it serves as a tool to study characteristics of superconducting electrons as well as coupled elements inside the cavity, such as spins [24], Nitrogen Vacancy superconducting qubits[37], mechanical systems[9–11, 20, 49–54] and other quantum systems. To build and control the embedded system, extra circuits need to be integrated into the cavity. However, if the introduced circuitry is not carefully designed, both the quality of the cavity and the embedded system may be highly degraded through external circuit loading or radiative loss[39].

In our qubit coupled mechanical resonator system, the coupling between the mechanical resonator and the transmon is proportional to the voltage applied to the mechanical resonator. In order to engineer a high quality cavity, we did separate experiments to investigate the microwave and other related properties of our T-filter biased superconducting cavity. In this chapter, first I will present the characteristic of a separate superconducting lumped element T-filter. And then I will show the results of filter biased cavity. Most of the results are published in Hao et al[43].

6.1 Reflective T-filter

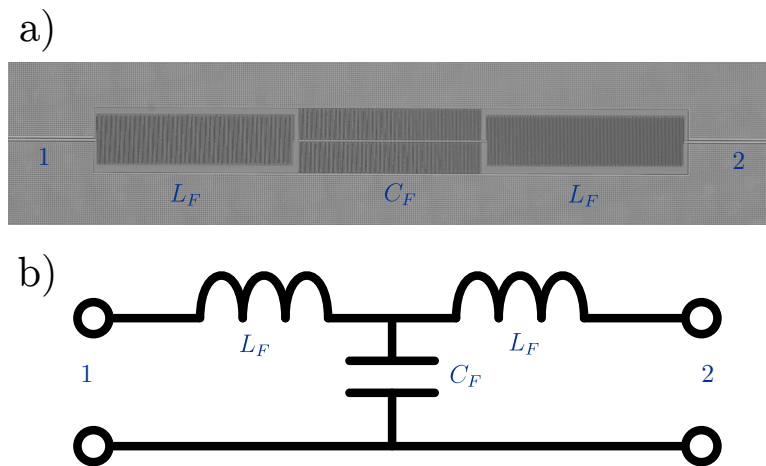


Figure 6.1: (a) Optical image of a T-filter. (b) Sketch drawing of the T-filter. The capacitance and inductance of the filter are denoted as C_F and L_F . The “1” and “2” are ports for transmission measurement.

We first perform transmission and reflection measurement of reflective T-filter described in chapter 2. The sample was cooled down to 4K on a dip probe and measured by Agilent N5230 Network Analyzer. No additional cryogenic attenuators and amplifiers were used. The calibrated data is shown in Figure 6.2. From the transmission measurement, S_{21} is observed to cut off around 2GHz, with a roll-off of 60dB/decade up to 4GHz, in agreement with both analytical estimation and Sonnet simulation. For frequency above 4GHz, the simple lumped element approximation no longer works, refer to Chapter 2 for detailed discussion.

6.2 Filter biased CPW cavity

To understand the characteristic of our T-Filter biased CPW cavity, we anchored the sample on our dilution fridge and cooled down to 30mK. Transmission measurements

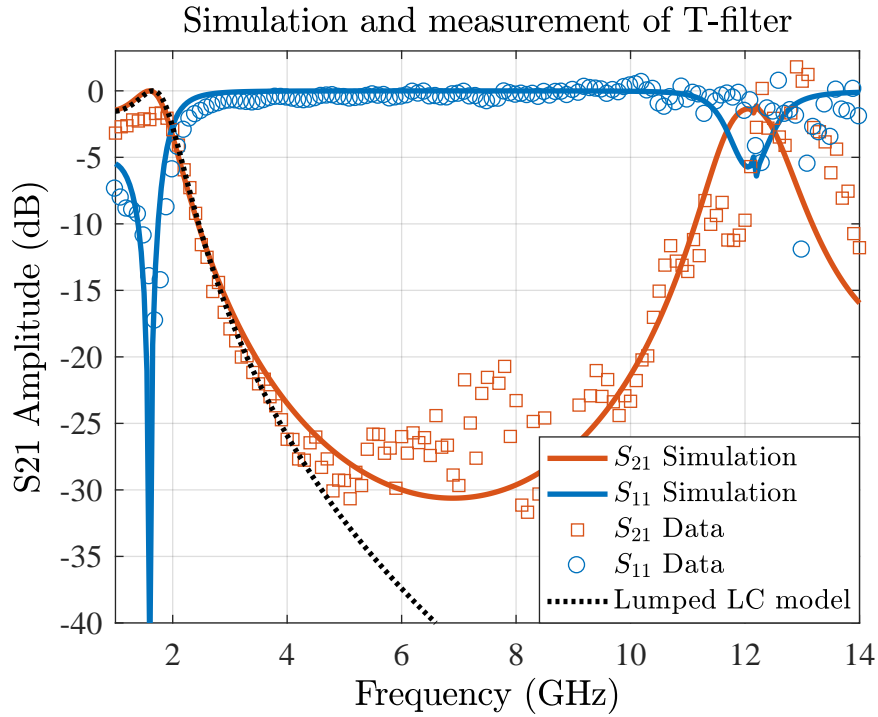


Figure 6.2: Measured and simulated transmission S_{21} and reflection S_{11} characteristics of a reflective T-filter (see inset) from 0.1 to 14GHz. The blue circles (red squares) represent the magnitude of S_{11} (S_{21}) measured at 4K. The black (red) solid line is the magnitude of simulated result from Sonnet. The black dotted lines shows the numerical result using lumped element network analyze.

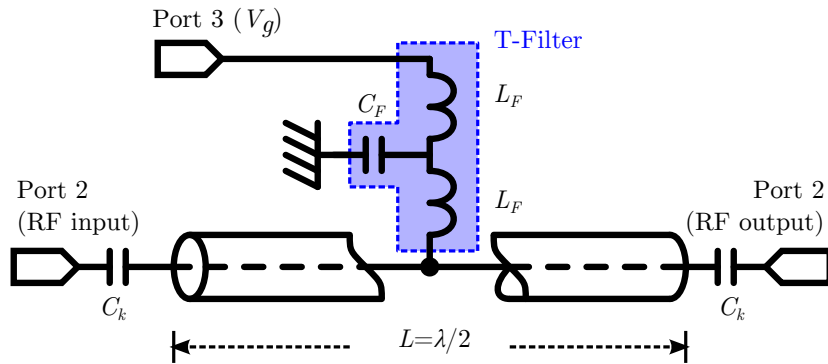


Figure 6.3: Schematic drawing of T-filter biased CPW cavity.

were performed at different conditions.

We cooled three samples with different length of coupling capacitor, 5, 15, 20 μm , corresponding to coupling capacitance $C_k \approx 1, 2, 2.5\text{fF}$. We denote the device I, II and III respectively.

6.2.1 Frequency dependence of transmission

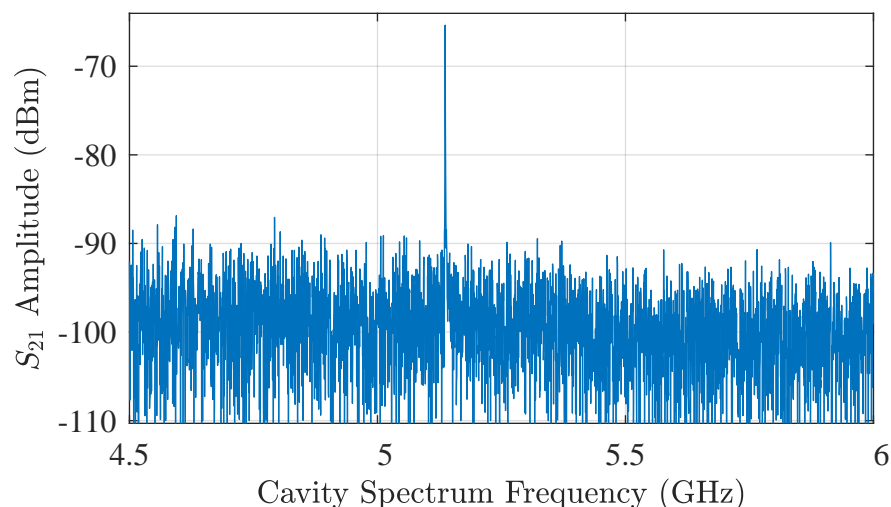


Figure 6.4: Transmission measurement of Filter biased CPW cavity, device I in a wide span. Input Power on the cavity is -100dBm. Only one peak shows up at 5.1GHz, which is the fundamental mode of the cavity. At all the other frequencies, the reading is dominated by HEMP thermal noise.

The frequency transmission of T-filter biased CPW cavity is measured using heterodyne board at continuous mode (refer to Chapter 4). A constant continuous high power (-100dBm at cavity input) microwave signal drives the cavity at a driven state, and the transmitted data is amplified and recorded. Figure 6.4 shows the transmission in a wide span. Only one sharp peak is observed at 5.1GHz, which is the fundamental mode of the cavity. A closer look up is shown in Figure 6.5. The quality factor and center frequency is

determined by fitting it to a Lorentzian shape function[5]. The extracted center frequency is 5.1366GHz in agreement with the design. The loaded quality factor $Q_l=244K$ with full transmission -8.21dB , which we believe is working at almost under-coupled region where $Q_i \lesssim Q_c$. This is the highest quality factor, also with smallest coupling capacitor, among all filter biased cavity we fabricated.

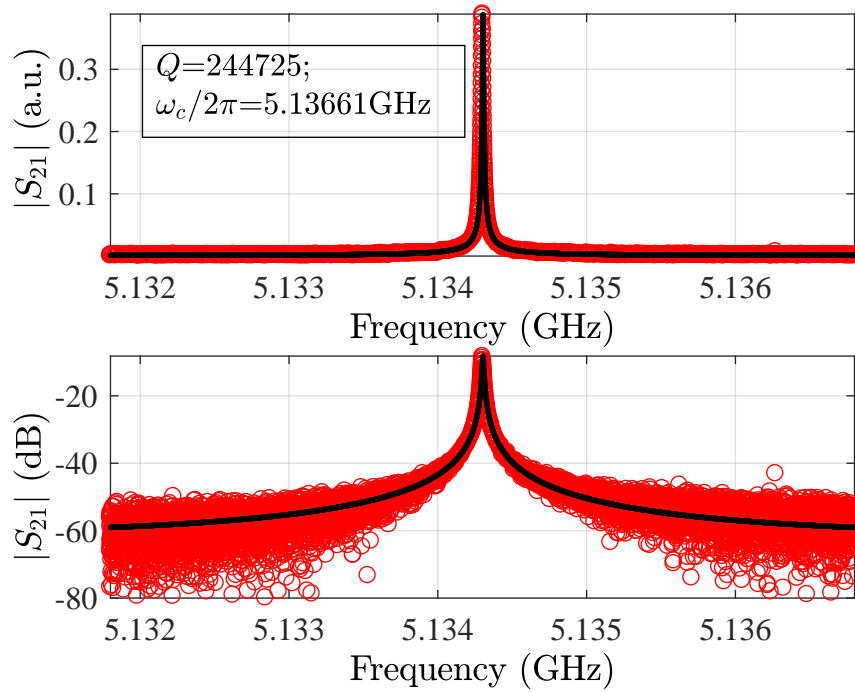


Figure 6.5: Transmission measurement of Filter biased CPW cavity, device I at fridge base temperature 30mK, measured by Heterodyne Board. The measured amplitude of S_{21} is shown as red circles in linear scale (top) and logarithm scale (bottom). The data is fitted to a Lorentzian shape which is represented by the black solid line. The extracted loaded quality factor $Q \approx 245k$ at large power -100dBm, corresponding to 2×10^5 photons in the cavity mode.

6.2.2 Power dependence

The excess noise of the 2-d thin film superconducting microwave resonators were carefully studied [5, 55]. It is believed a major source of the noise is from two-level systems (TLSs)

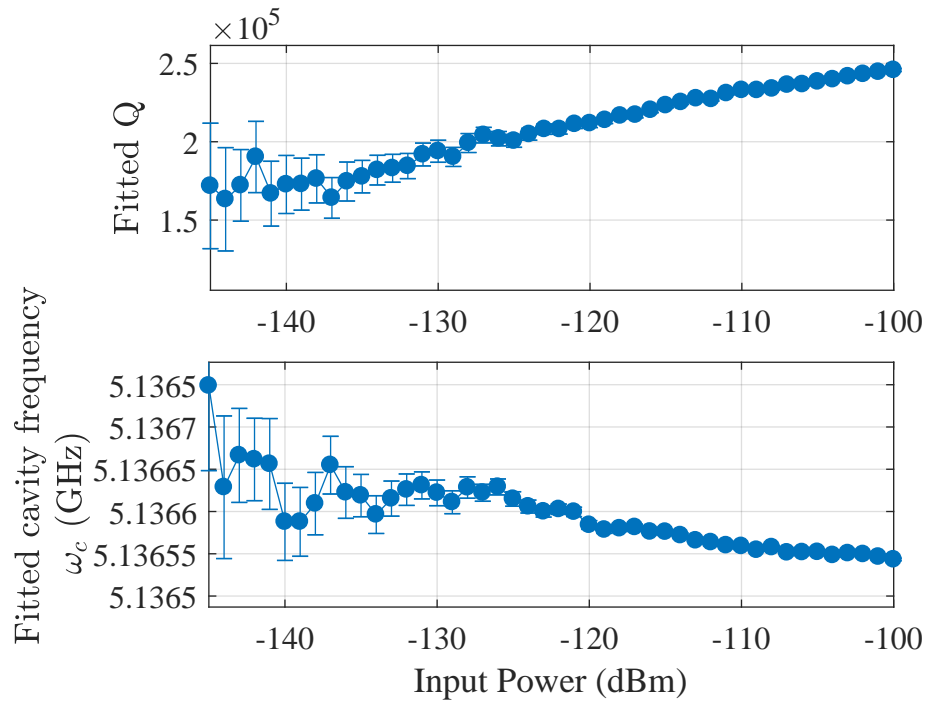


Figure 6.6: Extracted quality factors Q_L and center frequencies at different power of device I. The power is changed by controlling external digital attenuator. Integration time, number of averages and other experimental parameters were kept the same, so when the signal get small at low power, the error bar is bigger.

in dielectric materials[56, 57]. The TLS is assumed to be distributed and is observed to saturate at high power.

The total quality factor Q is determined by loss to external circuits and internal loss which is caused by TLS noise

$$\frac{1}{Q} = \frac{1}{Q_c} + \frac{1}{Q_i} \quad (6.1)$$

where Q_c is the coupling quality factor, and the Q_i is the internal quality factor.

The power dependence of our cavity is measured by varying the attenuation on the input line outside the fridge. A tunable digital attenuator is inserted after Heterodyne Board output. We measure transmission signal at different attenuation without changing integration time and other parameters, then extract the quality factor and center frequency by fitting to Lorentzian shape as shown in Figure 6.6. The quality factor drops as the power decreases as the typical CPW cavity.

6.2.3 Gate dependence

One goal of the inserted biased line is to apply voltage to the mechanical resonator, to control the coupling with transmon. In the standard model of transmon, cavity and mechanical resonator, it is assumed that the voltage brings no direct change in cavity response. It is essential to test dependence of gate voltage bias.

For our filter biased CPW cavity, we are able to apply high dc voltage at the center line of cavity. The gate voltage V_g controlling the coupling strength of mechanical resonator and qubit, see equation 2.25, is applied by external voltage source. In the model of qubit-MR system, it is assumed that the property of cavity (Q , power, frequency, and etc) is not directly dependent on gate Voltage. Thus it is necessary to study the dependence of gate

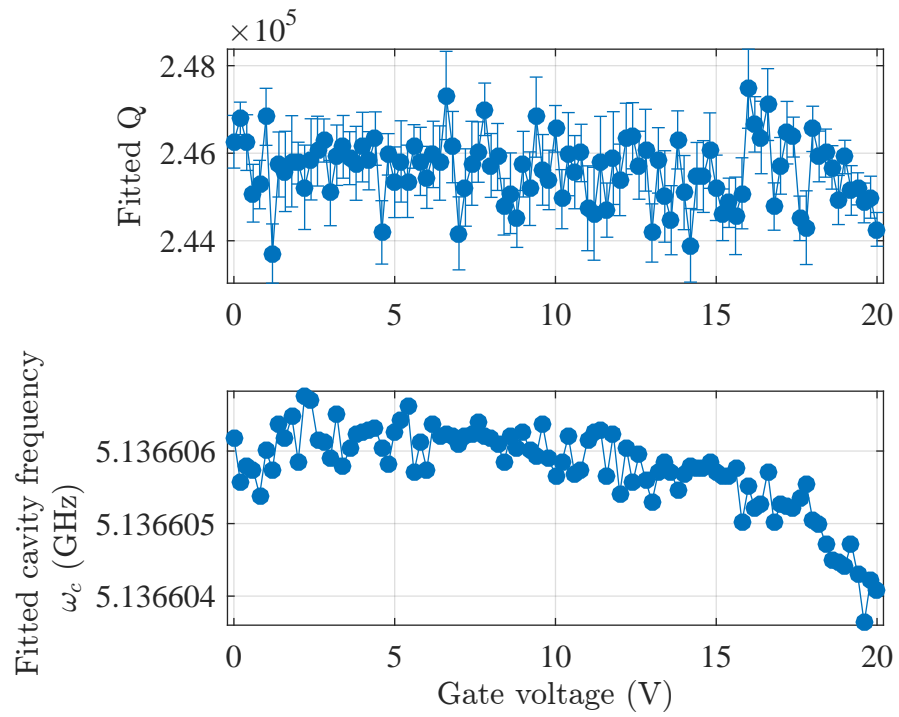


Figure 6.7: Extracted quality factors Q_L and center frequencies ω_c at different Gate voltage V_g .

voltage.

The gate dependence measurement is performed by varying the gate voltage V_g applied on Port 3 through one of the fridge DC lines with 2 powder filters. The voltage is varied from 0V to 20V. See Figure 6.7, each point is extracted from fitting a transmission measurement of cavity S_{21} at a high input power -100dBm. Up to 20V, there is no obvious change in quality factor $Q_L \sim 2.46 \times 10^5$. The fitted center frequency shows no change up to 10V and a drop $\sim 2\text{kHz}$ up to 20V, much smaller than the linewidth of resonance $\frac{\omega_c}{2\pi Q_L} = 21\text{kHz}$.

To test the limit of our system, we measured the transmission at 0V and 20V, at high power and single-photon limit low power. The results are shown in Figure 6.8. For a well-averaged curve, there is very little change in both center frequency ω_c and quality factor Q_L .

6.2.4 Coupling strength dependence

The typical CPW cavity Q_c increases proportionally to $1/C_k^2$ [5]. To test this dependence of coupling capacitance, we tested three samples with different coupling capacitors. As the standard method, we define $Q_L \equiv 1/Q_i + 1/Q_c$, where Q_c accounts for the losses to external circuitry through coupling capacitors, and Q_i stands for internal cavity losses. See Figure 6.9, we use $Q_i = 0.7 \times 10^6$ at high power (solid line) and $Q_i = 0.2 \times 10^6$ at low power (dashed line), where unsaturated two-level systems make a greater contribution to the internal dissipation. We can also estimate the contribution of filter loss to Q_i by measuring S_{31} through the filter Port 3

$$IL_F = S_{31}(\omega_c)/S_{21}(\omega_c) \quad (6.2)$$

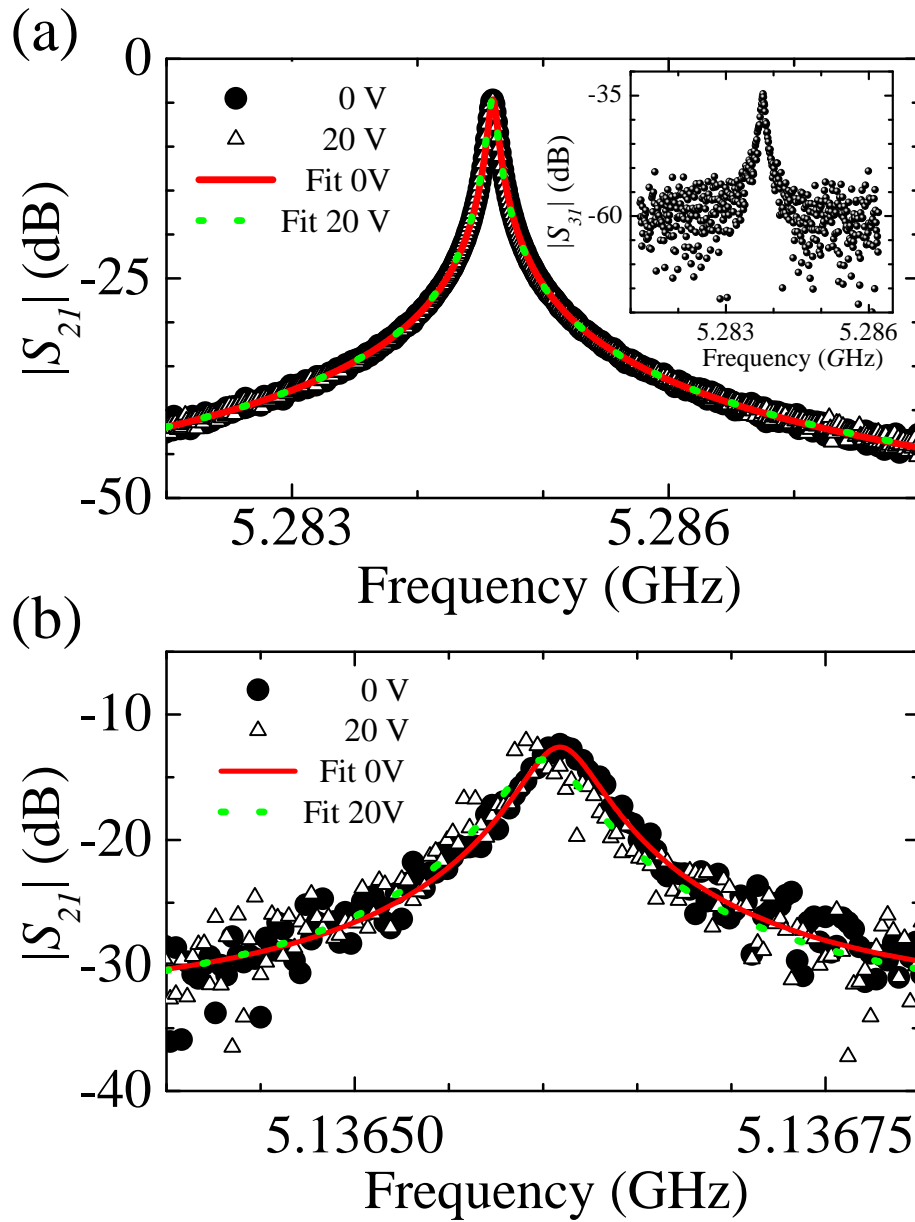


Figure 6.8: Traces of transmission measurements at 0V and 20V with high power (top) and low power (bottom) of device II.

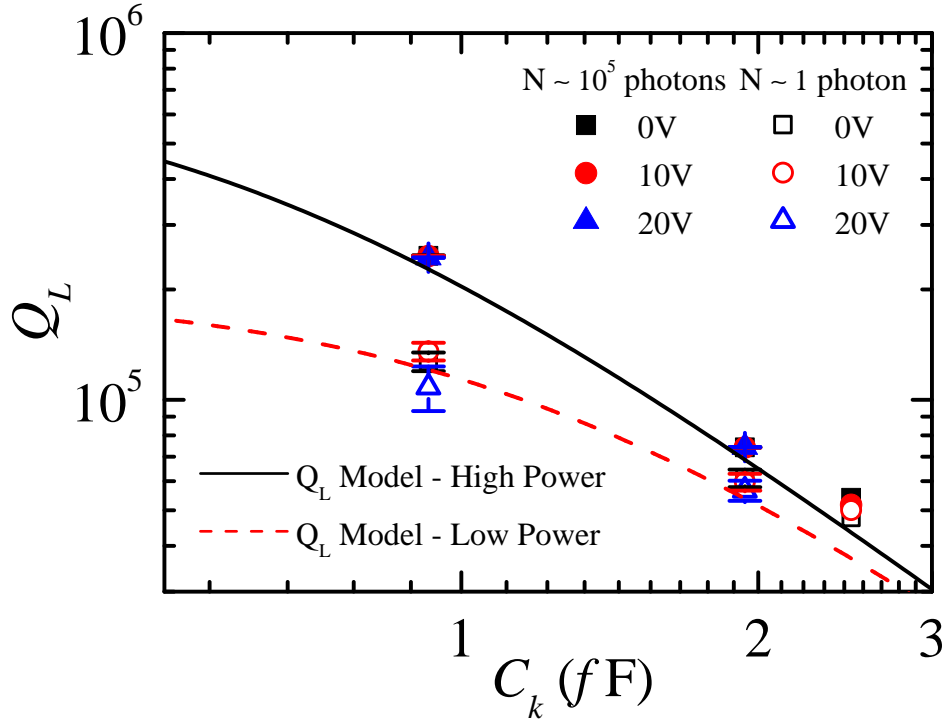


Figure 6.9: Loaded quality factor of cavity vs coupling capacitance

Read from inlet of Figure 6.9, $IL_F = -30dB$, indicating that 0.1% of the power escapes through the filter Port 3. This corresponds to a filter quality factor of $\sqrt{1000}Q_c = 3 \times 10^6$, and suggests that this bias circuit design can be integrated into cavities with Q_i as high as 10^6 , without degrading the total quality factor.

6.2.5 First harmonic of the cavity

To characterize the positioning from filter connecting to the voltage anti-node rather a node, we simulated and measured the transmission between cavity port and filter port at the first harmonic mode near 10GHz, see Figure 6.10. Transmission of S_{21} and S_{31} of the first harmonic is also performed using Agilent network analyzer, see Figure 6.11 and Figure 6.12. The loaded quality factor $Q_{L,1} \approx 2 - 3 \times 10^3$, which agrees well with

Sonnet simulation.

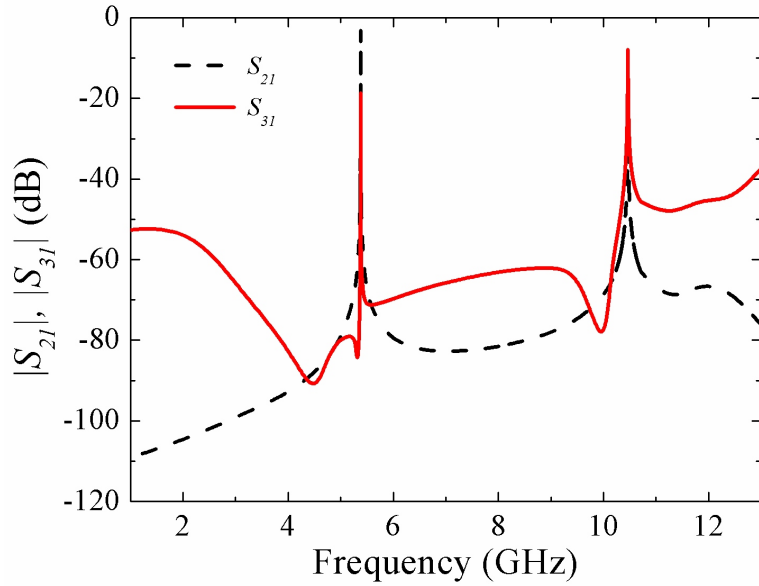


Figure 6.10: Sonnet simulation of transmission properties of Filter biased CPW cavity. The fundamental and 1st harmonics is shown.

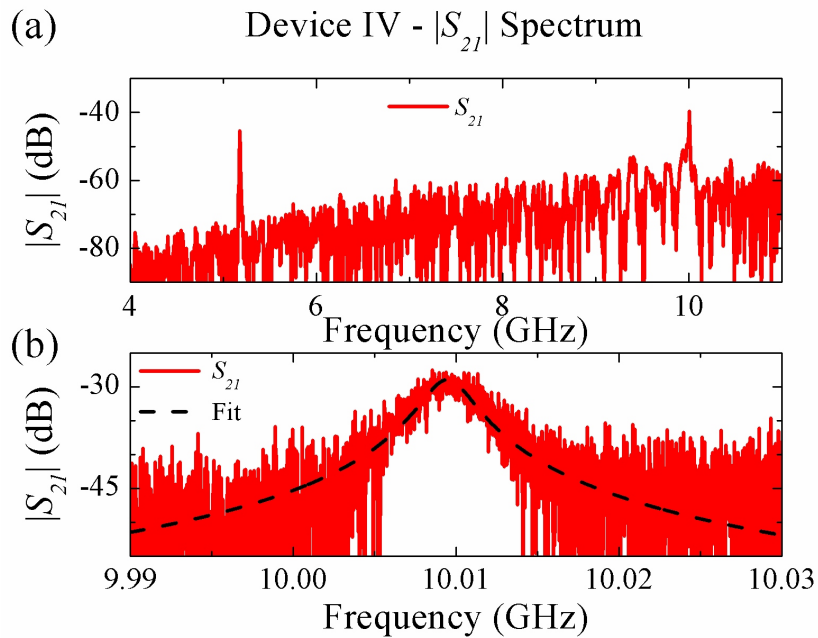


Figure 6.11: Transmission of S_{21} (a) in a wider span. (b) near the 1st harmonic.

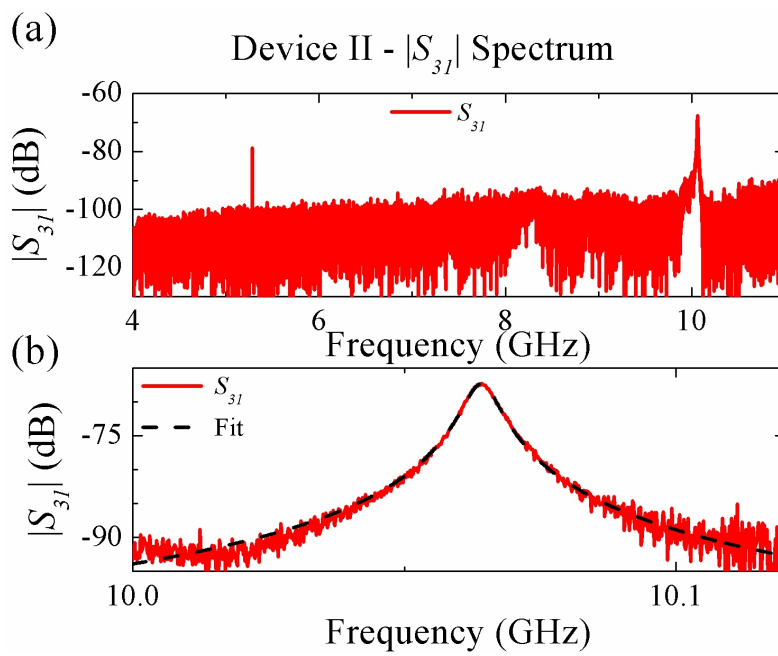


Figure 6.12: Transmission of S_{31} (a) in a wider span. (b) near the 1st harmonic.

Chapter 7

Transmon characteristic

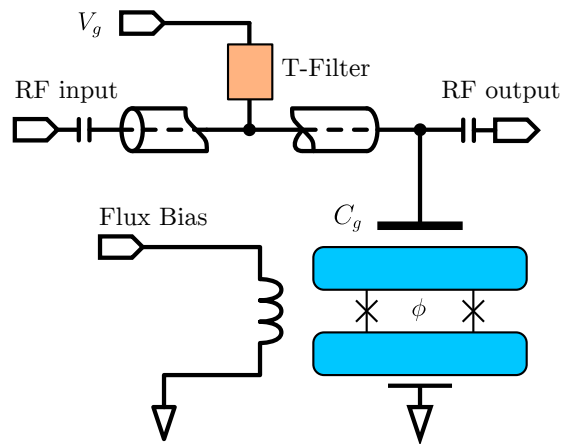


Figure 7.1: Schematic drawing of transmon capacitively coupled to T-filter biased CPW cavity.

This chapter will focus on exploring the characteristic of transmon I develop for our experiments. It is capacitively coupled to T-filter biased CPW cavity through coupling capacitor C_g . The bias flux ϕ of transmon is controlled by external flux line. The same design of transmon is then used to couple to a mechanical resonator in the next chapter. These results could serve as a good comparison for the transmon used in the qubit-coupled mechanical resonator experiment. Note despite the design is kept the

same, some parameters are improved in experiments due to better magnetic shielding and fabrication uncertainties. The transmon serves as a probe to charge or potential fluctuations induced by the mechanical resonator. The transmon and cavity system is identical to those in the hybrid cavity+transmon+mechanical resonator system. This experiment was done before we measured the hybrid system in order to extract the parameters in an independent experiment.

Parameter	Value
$\omega_c/2\pi$	4.937GHz
E_C/h	0.23GHz
E_{J0}/h	13.5GHz
T_1	12 μ s
T_2^*	0.43 μ s
β	0.17
$g/2\pi$	120MHz
$\lambda/(2\pi V_{NR})$	≈ 300 kHz/V
$\kappa_c/2\pi$	0.25MHz

Table 7.1: Summary of transmon and cavity parameters of sample in cavity-qubit experiment. The first set of values shows the CPW and transmon's characteristic energies, and T_1 and T_2^* for $\omega_{ge}/2\pi \simeq 4.3$ GHz. Note relaxation time T_1 and decoherence time T_2^* are lower than those in cavity-qubit-MR experiments with better magnetic shielding in Chapter 8

7.1 Single tone spectroscopy

We started our measurement by finding the resonance of cavity using continuous measurement setup. Based on the estimation of design parameters, the coupling strength is much smaller than detune $g \ll |\omega_{eg} - \omega_c|$, the coupled system should stay on a dressed state and qubit is very little excited. See Figure 7.2. The resonance of coupled system $\omega/2\pi \sim 4.9$ GHz is dispersive shifted cavity resonance when qubit is at ground state $|g\rangle$.

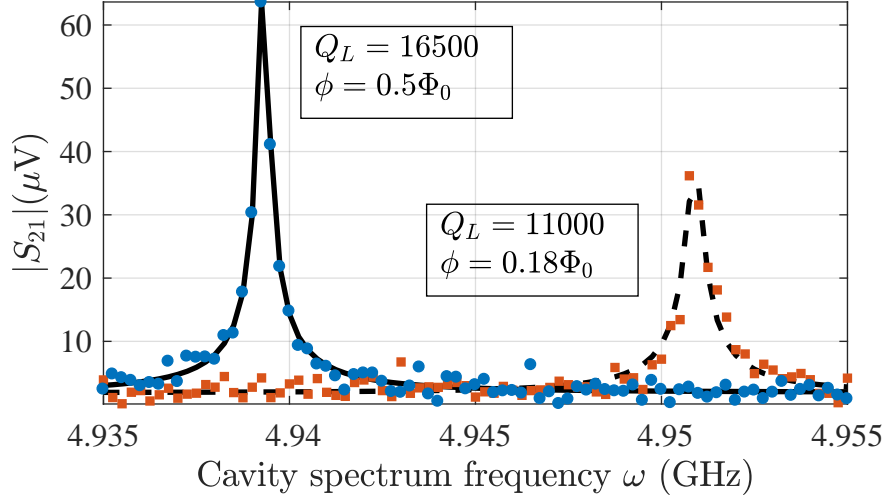


Figure 7.2: Cavity resonance at 2 different flux bias. Quality factor Q is extracted by fitting the resonance to Lorentz shape. The resonance shift between the 2 traces is due to dispersive coupling with qubit.

The loaded quality factor of cavity resonance $Q_L > 15k$ at base temperature.

7.1.1 Flux dependence

When the resonance of qubit ω_{ge} and cavity ω_c are far detuned from each other $|\omega_c - \omega_{ge}| \ll \omega_c + \omega_{ge}$, which is the case in this sample, it can be shown the resonance of the cavity is dispersively shifted due to interaction with qubit, see equation 2.30, depend on the state of qubit

$$\omega'_c = \omega_c \mp \chi_{ge} \quad (7.1)$$

In order to demonstrate this dispersive coupling, we vary the flux bias ϕ of transmon by changing the current of flux line, and sweep the frequency of cavity spectrum tone ω . See Figure 7.3. In this continuous single tone setup, refer to 4.3.1, the qubit and driven

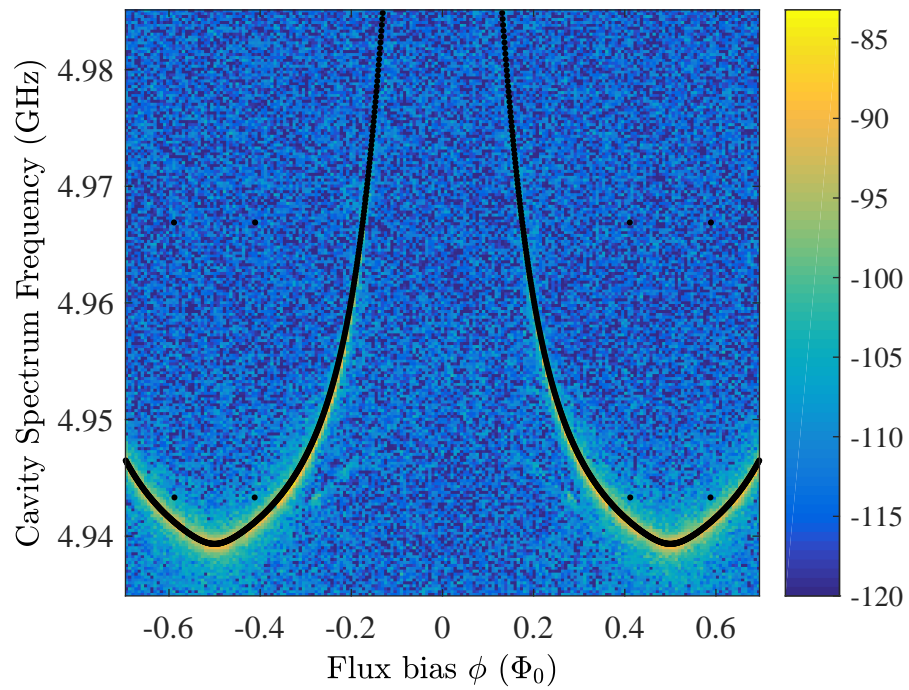


Figure 7.3: Dispersive shift of cavity resonance as a function of transmon flux bias ϕ . The color scale indicates the amplitude of transmitted signal. The black solid line is a simulation result using standard transmon cavity model.

cavity is on a dressed state. And because the transmon and cavity are far detuned, the qubit is very little excited, only one line of cavity spectroscopy is observed indicating qubit staying on $|g\rangle$.

flux The flux bias ϕ is controlled by external applied magnetic flux, more specifically the current in flux line supplied from applying DC voltage to a 500Ω resistor at room temperature. Because flux bias ϕ determines the effective total Josephson energy

$$E_{J,\text{eff}} = E_{J,0} \left| \cos\left(\frac{\pi\phi}{\Phi_0}\right) \right| \quad (7.2)$$

it should show a periodicity of flux quanta Φ_0 .

This single-tone cavity spectrum, see Figure 7.3, shows the pull from transmon depending on flux bias, and is explained by standard transmon-cavity model in dispersive regime [13, 14]. The simulation result agrees well with design and fitting parameters, see Table 7.1, for transmon qubits in cavity-transmon experiment and cavity-transmon-MR experiment. [cite Kock2007]

7.1.2 Stability of flux period

To build a quiet magnetic environment, the sample is first protected using Cryoperm shielding ¹ (see Figure 4.5) and superconducting metals to isolate macroscopic magnetic field outside from the earth and etc. On the chip, local magnetic fluctuation is further reduced by flux traps (holes on superconducting plain). Thus besides unavoidable fabrication error in dimension, the flux period or flux dependence should be constant within one cool-down and very small different between samples. To check this property, we

¹www.cryopermshielding.com

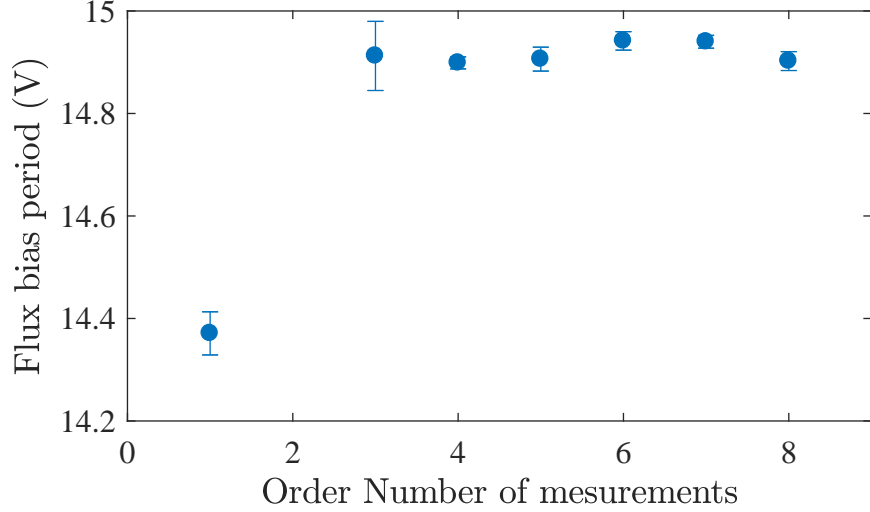


Figure 7.4: A summary of flux period extracted from flux dependence maps measured from several cool downs of two samples. The x-axis is the numbering of maps. No.1 is from a cavity-transmon measurement, and No.2 to 8 are from cavity-transmon-MR measurement. The transmon designs and fabrication steps are identical. The y-axis shows the fitted period as voltage of source, which supplies the current through a 500Ω resistor.

perform flux dependence measurements as in Figure 7.3 and extract the period using fitting program. We plotted the summary in Figure 7.4. We observe that for one sample, even after warming-ups and cooling-downs, the flux period changes very little.

7.1.3 Resonance limit of cavity and transmon higher states

Although the transmon g-e and cavity are in dispersive limit, the transmon's higher order excited states, are expected to have a cross or in resonance limit with cavity. To prove this, we zoom in the small gaps near bottom of cavity resonance, i.e. $\phi \sim 0.6\phi_0$, as shown in Figure 7.5. A detailed map shows there are 3 major visible gaps on cavity dispersive spectrum line. They are explained by a generalized model with a multi-level transmon the cavity. 6 lowest energy eigen-states ($|g\rangle$, $|e\rangle$, $|f\rangle$, $|h\rangle$, and etc.) are considered. I

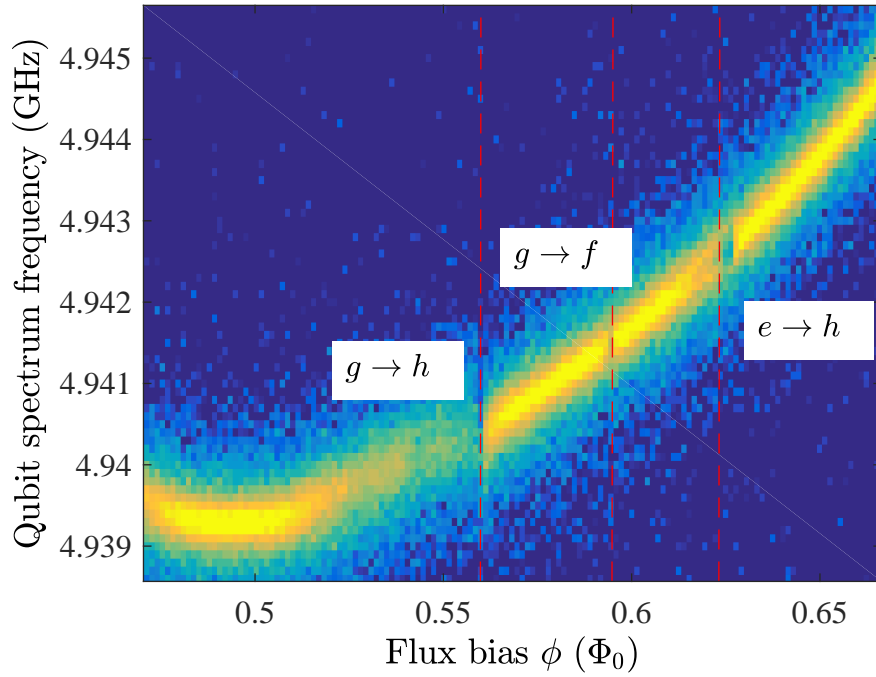


Figure 7.5: Qubit induced splitting in cavity response..Zoom-in of transmission of cavity as function of flux bias ϕ , showing qubit higher excited states crossing cavity resonance. The red dashed lines are simulated qubit transitions, where transmon is modeled as a 6-level system. Because the slope of dashed lines versus flux are very large in this frequency versus flux scale, they appear to be vertical.

plot 3 red lines to indicate transitions that match well with the gaps. The first gap is the avoided level crossing of g-h and cavity, similar to g-e with cavity. The second tiny gap matches transmon g-f transition, but it can not be explained by linear multi-level-transmon-cavity model since the coupling term $\langle g | \hat{n} | f \rangle$. One possible explanation turns to nonlinear higher order terms neglected in standard model. The third one is a double-track structure, and its frequency matches e-h transition in the model. The emergence of the gap is not predicted by the standard model because of low occupation number on the excited state, also refer to discussion of temperature of components in section 8.5.

7.2 Two tone spectroscopy

To directly observe the transition between transmon states, a second tone, qubit spectrum tone, is applied to the cavity with the cavity spectrum tone. The measurement is performed first in continuous mode where qubit and cavity are both constantly driven. The system evolves while the “measurement” is taken. Because measurement time ($\sim 1\text{ms}$) is much longer than relaxation ($\sim 10\mu\text{s}$) or dephasing time ($\lesssim 1\mu\text{s}$) of qubit, during the measurement the qubit can be treated as a mixed state.

7.2.1 Qubit spectroscopy

Two step measurement To find the spectroscopy of transmon qubit, a high power of qubit spectrum tone is applied to excite all possible transitions in the transmon-cavity system. To get the best contrast, a two step measurement is performed. First a single-tone cavity response map is taken to locate resonance $\omega'_c(\phi)$ numerically using Matlab. Then in the two tone measurement, for each flux bias ϕ , the cavity spectrum tone is fixed

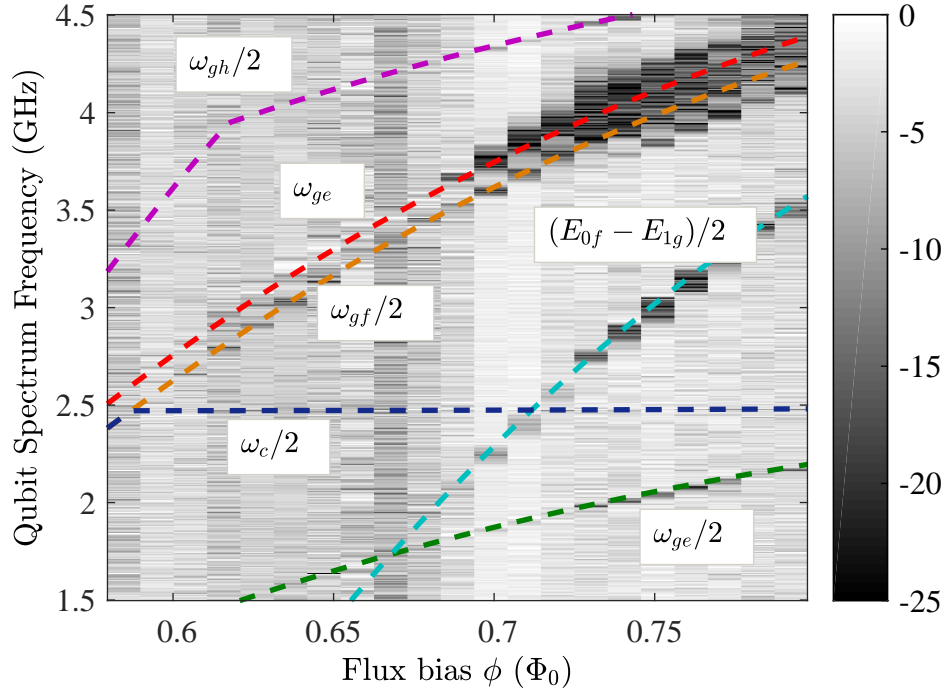


Figure 7.6: Two-tone spectroscopy of qubit-cavity system versus flux bias ϕ using high power excitation. For each flux bias, the frequency of cavity spectrum tone measuring the state of qubit is fixed at its resonance. Change in transmitted amplitude due to transitions of the coupled system appears as a dip (darker color). Colored dashed lines are numerical simulated transitions in the system [14]. Because driving power is high, along with single excitation, two-photon process are also visible. They are represented by “/2”, eg $\omega_{ge}/2$ describes transmon absorbs two photons and gets excited from $|g\rangle$ to $|e\rangle$.

at resonance $\omega'_c(\phi)$, and qubit spectrum tone is swept to excite the system. When the qubit is excited, the dispersive shift changes its sign, resulting a different effective cavity resonance $\omega'_c = \omega_c + \chi_{ge}$. When the resonance of the cavity changes and the transmitted signal shows a smaller amplitude and different phase.

Because in this particular measurement the power of qubit spectrum tone is sufficiently high, both single-photon transition, eg. ω_{ge} , and multi-photon qubit transition $\omega_{gh}/2$ are visible, as well as two photon cavity excitation $\omega_c/2$. All bands can be explained by standard model of multi-level transmon-cavity interaction. See Figure 7.6.

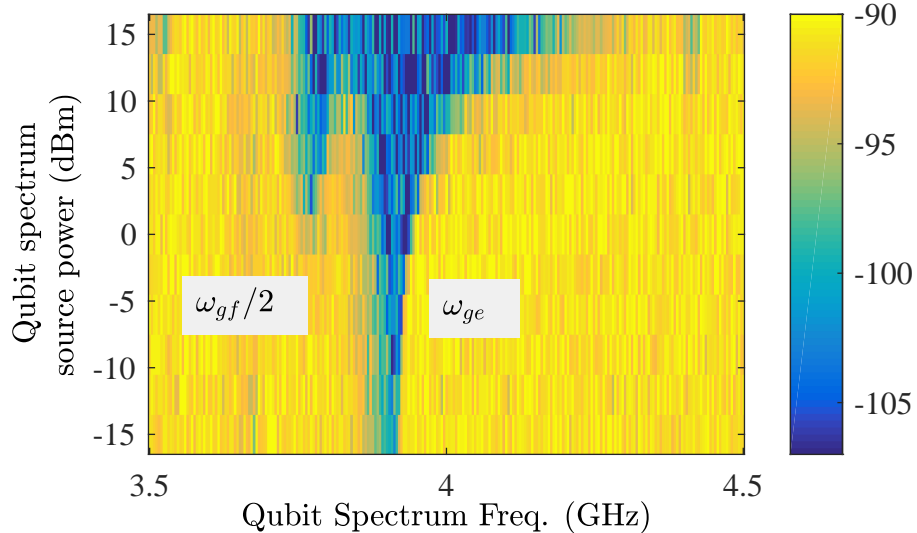


Figure 7.7: Spectroscopy of transmon at different spectrum power. At high power, both single-photon transition ω_{ge} and two-photon transition ω_{ef} are visible. When the power decrease, the multi-photon process will disappear and leave only single photon transition.

Power dependence When the driving power is high, the non-linearity plays an important role. Although for some transitions the first order coupling is zero, multiple-photon processes excite system through virtual states. [citeBraummuller2015multiphoton]

$$\omega_d = \omega_{j0}/j \tag{7.3}$$

As the power reduces, the multi-photon process are dramatically suppressed. In the low power limit, only single photon excitation is visible. We use this to distinguish and rule out higher order transitions. Fig 7.5 shows two set transmon spectrum data using high and low power of excitation. We decrease the excitation power until only one dip is left. The blue curve has 20dB lower amplitude than the high power (red) one. The dip at lower frequency $\approx 4.24\text{GHz}$ corresponds to two photon process $\omega_{gf}/2$, and the right corresponds to ω_{ge} . The difference of the two is

$$\omega_{ge} - \omega_{gf}/2 \approx E_c/2\hbar = 2\pi \cdot 0.12\text{GHz} \quad (7.4)$$

For our set up, the 75dB attenuation on RF input cable limits the total microwave power we can apply, thus we couldn't see higher order multi-photon transitions.

7.2.2 Cavity photon number splitting

As discussed in Chapter 2 the energy of transmon is shifted depends on the photon number in the cavity.

$$\omega'_j = \omega_j - \chi_{j-1,j} + (\chi_{j-1,j} - \chi_{j,j+1})c^\dagger c \quad (7.5)$$

where c^\dagger/c is the create/destroy operator for cavity photon. And when the linewidth of qubit resonance is thin enough,

$$(\chi_{j-1,j} - \chi_{j,j+1}) > \left[\frac{2\pi}{T_2^*}, \frac{2\pi}{T_1}, \kappa_c, \text{etc.} \right] \quad (7.6)$$

separate peaks for different photon number are possible to see. Each peak corresponds to a photon number state of cavity, known as photon number splitting [19]. Here we

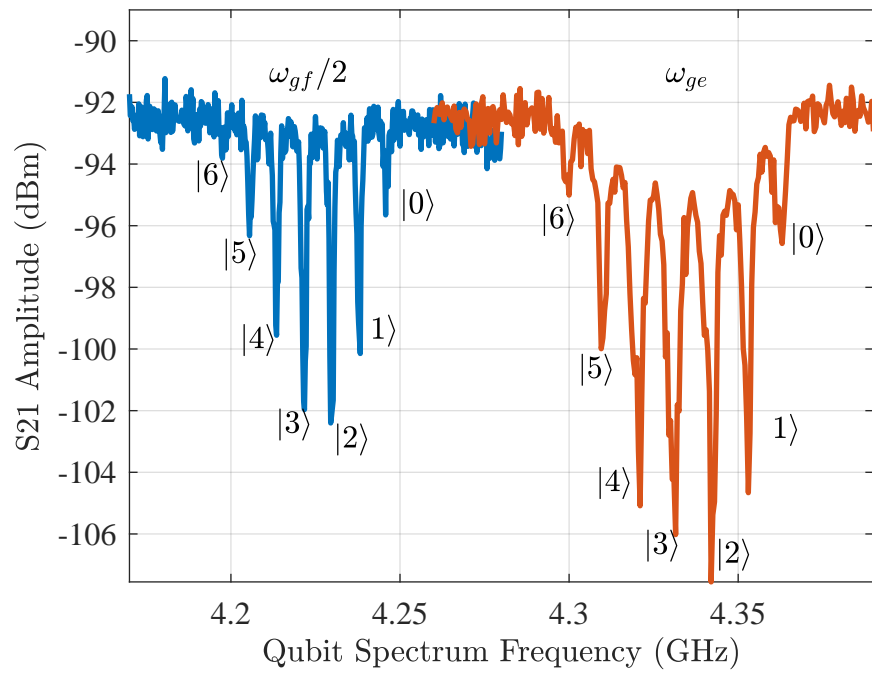


Figure 7.8: Two tone spectroscopy of transmon single photon g-e transition and g-f two photon transition, showing qubit energies split depending on number states of cavity photon, which are denoted using Arabic numbers.

show that using single-photon g-e transition and two-photon g-f transition of transmon, we observe number splitting, indicating coherent state of cavity, see Figure 7.8.

In this measurement, we use two tone continuous measurement set up. The cavity spectrum tone is fixed at maximum transmission when the transmon is in ground state $|g\rangle$. The cavity drive is applied continuously with fixed power such that there are only a few photon ($n_{\text{ave}} \approx 3$) in the cavity. The qubit spectrum excites the transmon to excited state $|e\rangle$ or $|f\rangle$, driving the transmon rotating between ground state and excited state.

In Figure 7.8 we show the measurement of number splitting for g-e (red) and g-f (blue) transition. Separate peaks are observed for each set of data. The corresponding photon number state are denoted using numbers. For the two sets of data, the cavity driving power is kept the same $\sim 130\text{dBm}$, and thus the envelop of two are the same. The driving power of qubit excitation is optimized for each curve.

Qubit driving power dependence Qubit driving power P_d determines the speed of Rabi-oscillation or flip-over of qubit. To detect the photon number state, the Rabi-oscillation frequency should be smaller than g , such that each photon measures a constant state of transmon. Also it should be bigger than the relaxation rate of excited state to saturate the excitation probability of qubit. To optimize the qubit driving power P_d , I took a map of qubit spectrum respect to qubit driving power. See Figure 7.9. For a small enough drive, $P_d \sim -130\text{dBm}$, the signal to noise is too small, thus the signal is not seen. And when the drive is too large $P_d > -105\text{dBm}$, the separate peak are merged into one big broad peak.

Driven state of cavity We first measure the number splitting at finite temperature. Especially in the “strong measurement limit” where the driven strength is much bigger

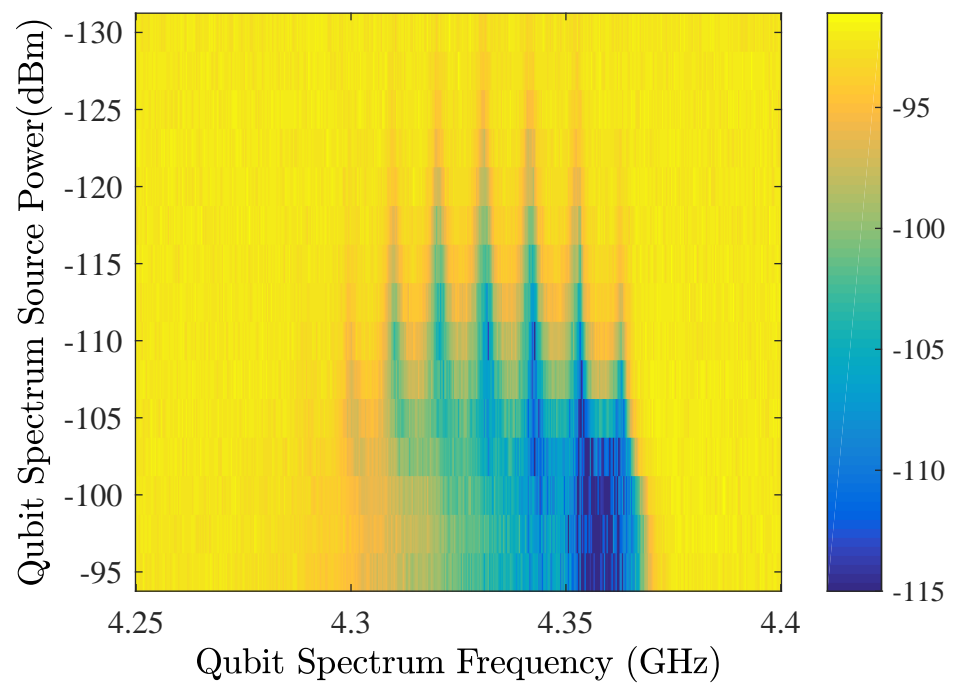


Figure 7.9: Qubit number splitting as a function of qubit driving power. The color scale indicates the amplitude of transmitted signal in the unit of dBm.

than the dissipation of system

$$\lambda_d \gg \kappa_c, \frac{2\pi}{T_1}, \frac{2\pi}{T_2} \quad (7.7)$$

the spectrum accurately reflects the number statistics of the mode.[citeClerk2007PhotonNumber]

In our experiment, the driven strength is close to dissipation of photon and qubit. It is expected the absorption of higher number state increases with driven power. Figure 7.10 shows the dependence of number splitting on cavity driving power. Curves are shifted manually for better display.

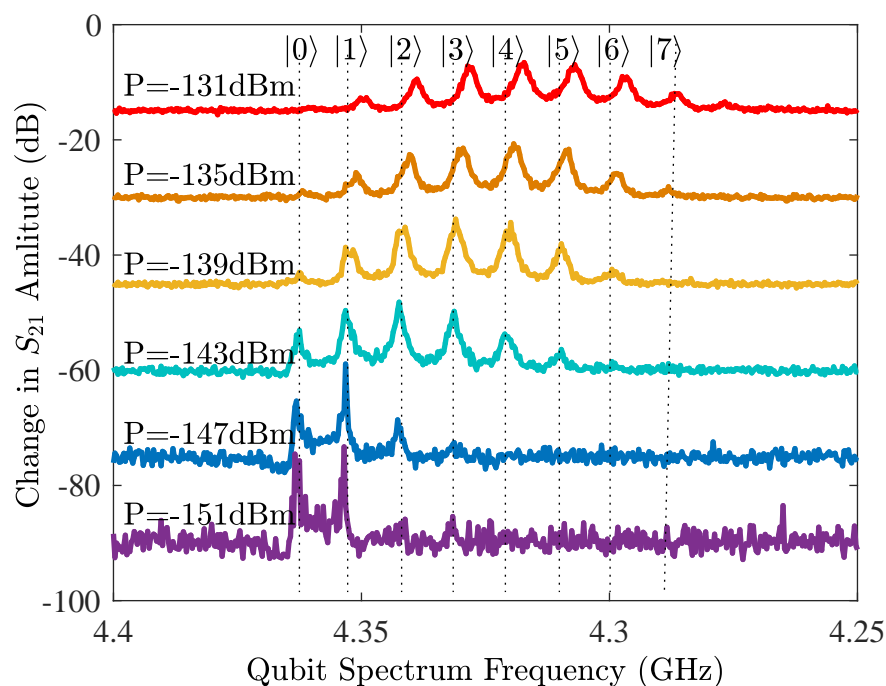


Figure 7.10: Qubit number splitting as a function of cavity driving power.

Thermal state of cavity To observe the thermal state of cavity, the cavity and transmon system needs to evolve freely without coherent driving on cavity. This is done by measuring the qubit spectroscopy in quasi-continuous mode. Different than continuous mode, the system is initially prepared at its equilibrium state by turning off all mi-

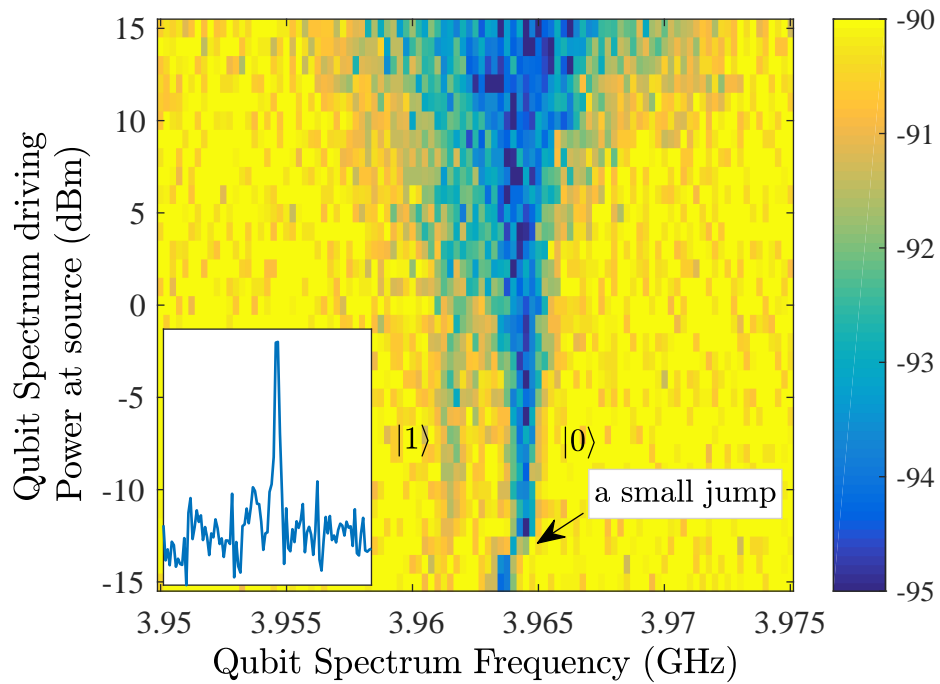


Figure 7.11: Power dependence of qubit spectrum at quasi-continuous mode. The horizontal axis is the frequency of qubit spectrum tone and vertical axis is the driving power at microwave source. The color scale is the output amplitude of output signal in the unit of dBm. At high power, only one broad dip is located at ω_{ge} . At low power, two sharp dips are observable and they correspond to the $|0\rangle$ and $|1\rangle$. The inset is average of two curves with lowest power plotted in linear scale.

microwave inputs. At the base temperature of fridge, thermal excitation is highly suppressed, $k_B T / \hbar \omega_{ge} \ll 1$, it is believed the system is relaxed to its ground state. The experiment cycle starts by applying a coherent driving pulse at close to qubit transition frequency $\omega_d \approx \omega_{ge}$ for a time longer than its relaxation, the qubit undergoes many periods of Rabi oscillation and loses its coherence. After this excitation pulse, a cavity spectrum pulse is sent to probe the state of the qubit by measuring the transmission.

Figure 7.11 shows the result of transmon spectrum ω_{ge} in quasi-continuous mode at different driving power. In low power limit $\lesssim -15$ dBm, only one peak is bigger than the noise floor corresponding to $|0\rangle$ of cavity. As power increases, a second peak on the left shows up, which corresponds to $|1\rangle$ of cavity. At even larger power, the first peak saturates and then the two merge into a broad peak. I also plotted the curve of low power limit in linear scale, see inset. From the amplitude we can estimate the upper limit of cavity photon number

$$\bar{n} < (0.04 \times 1 + 0.4 \times 0) / 0.04 + 0.4 = 0.091$$

which correspond to cavity temperature $T_c < 100$ mK.

This quasi-continuous spectroscopy is also advantageous for several reasons than continuous measurement. First in continuous mode, the qubit resonance changes with the power of cavity spectrum tone and qubit excitation tone, while in quasi-continuous mode, the first resonance $\omega_{ge, n_c=0}$ does not change. Second reason is that because the power of cavity spectrum measurement pulse can be tens to hundreds of photons, the signal-to-noise is better than in continuous measurement.

7.3 Time domain measurement

7.3.1 Rabi oscillation

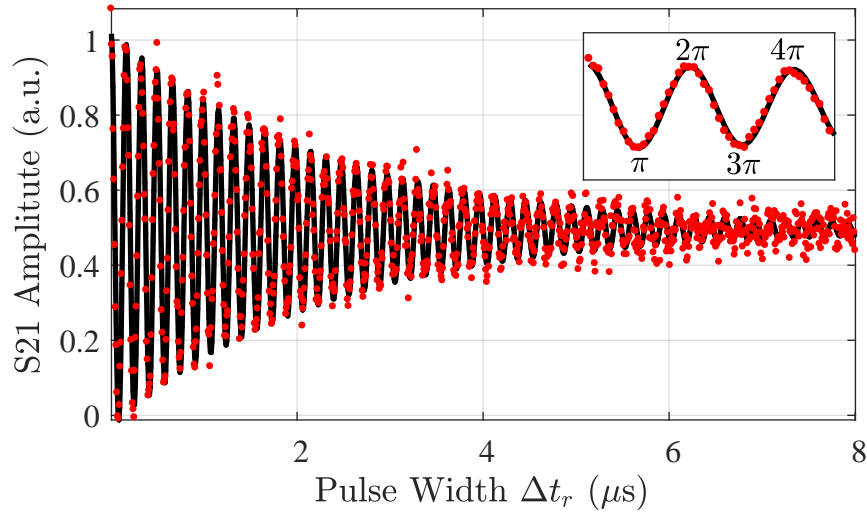


Figure 7.12: Rabi oscillation measurement. The red points are experimental data. The vertical axis is amplitude of transmitted cavity tone converted in linear scale. The data is fitted to $a_1 + a_2 \exp(-t/T_{rabi}) \cos(2\pi\nu_{rabi}t)$ (black solid line).

Rabi oscillation or Rabi cycle is a cyclic behavior of a two-level quantum system in the presence of coherent driving field. In our measurement, the qubit become “excited” after absorbing a excitation photon and re-emits it in stimulated emission process. The time of a cycle is $1/\nu_{rabi}$, where ν_{rabi} is called Rabi frequency. A multi-period Rabi oscillation is shown in Figure 7.12. The maximum and minimum in amplitude indicates qubit rotating along x axis in Bloch sphere, whose total phase change is indicated as π , 2π and etc. in the inset. However due to longitude and transverse noise of transmon, the coherence is lost over time resulting decrease in the envelop.

When Rabi pulse is applied, the cavity stays on its ground state $|n = 0\rangle$ ($n_c \ll 1$), frequencies of Rabi map is chosen near $|n = 0\rangle$ peak in the number splitting Figure 7.10

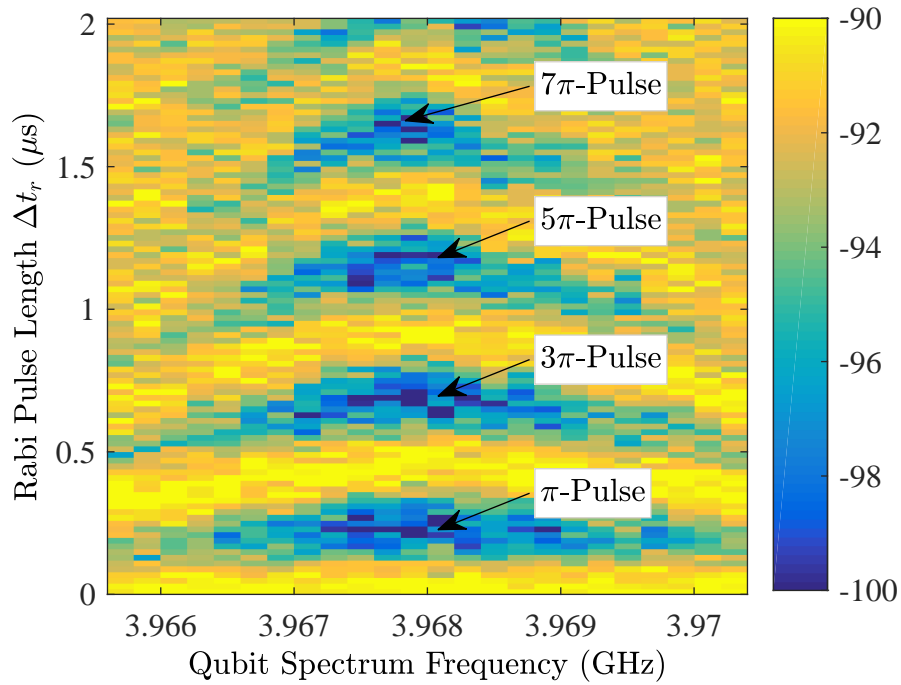


Figure 7.13: Rabi map of transmon qubit. The horizontal axis is the frequency qubit excitation pulse $\omega_d \approx \omega_{ge}$. The vertical axis is the length of Rabi pulse. The color scale is the amplitude of transmitted signal, whose frequency is fixed at the resonance when qubit is on ground state. The text “ π -pulse” indicates the pulse rotating qubit about x-axis for an angle of ϕ to its excited state $|e\rangle$.

or quasi-continuous spectrum Figure 7.11, $\omega_d \approx \omega_{eg, n_e=0}$. First we fixed the power of pulse and vary the length of Rabi pulse, and a cavity spectrum pulse is sent to measure the state of qubit. See Figure 7.13. Symmetric fringes in the plot indicate 4 Rabi cycles, and each cycle is a 2π rotation about x-axis in Bloch sphere.

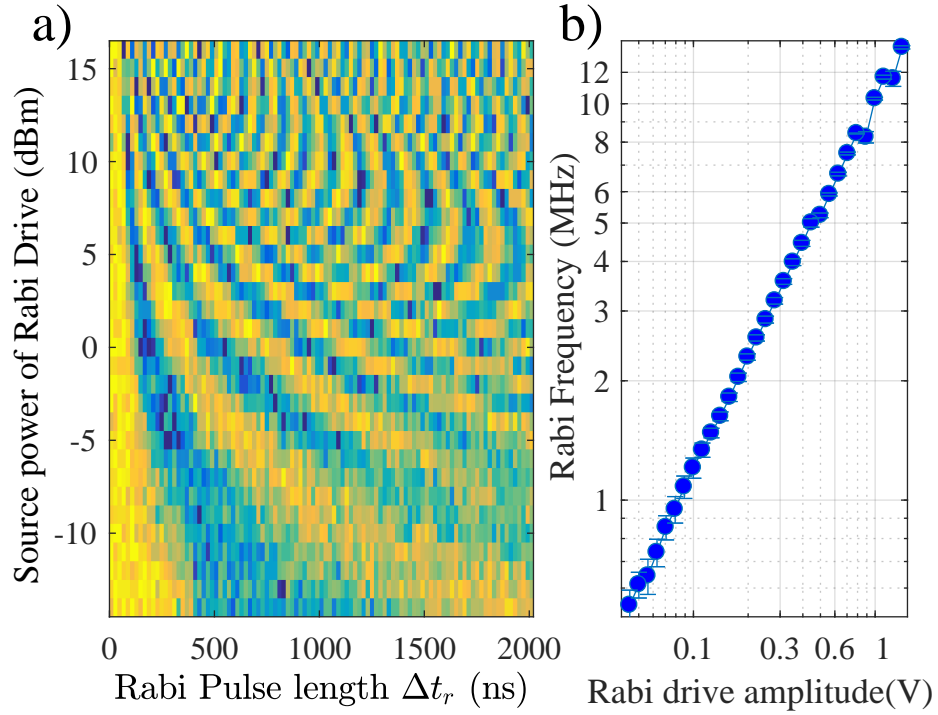


Figure 7.14: Power dependence of Rabi oscillation. (a) is measurement data of Rabi oscillations at different pulse power. The horizontal axis is the length of Rabi pulse and the vertical axis is the power of Rabi pulse at microwave source. The color scale is the amplitude of transmitted cavity tone. (b) is Rabi frequency ν_{rabi} extracted from (a) versus converted voltage at microwave source. Both axes are in logarithm scale. The Rabi frequency shows clear linear dependence on driving amplitude.

Driven strength dependence The frequency of Rabi oscillation is proportional to the driving amplitude

$$\nu_{rabi} \propto A_d \propto V_d \quad (7.8)$$

which is controlled by driving voltage. To demonstrate this, Rabi oscillation measurement is performed as a function of driving power, See Figure 7.14(a). The Rabi frequency of each curve is extracted and plotted respected to driving amplitude in linear scale, see Figure 7.14(b).

7.3.2 Longitude Relaxation measurement

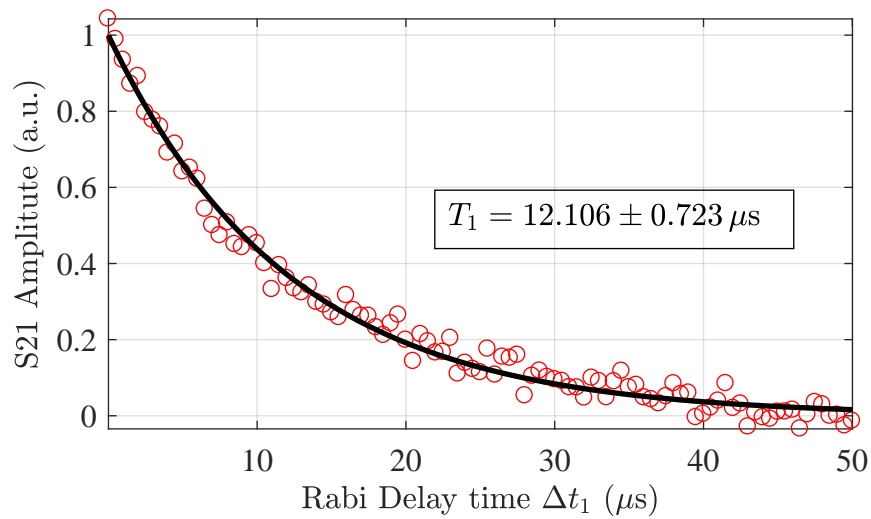


Figure 7.15: Relaxation measurement of transmon qubit. The data is fitted to exponential shape and extracted relaxation time T_1 is $12\mu s$.

Relaxation time T_1 characterizes how long time can qubit stay on its excited state before it is relaxed to its ground state. This measurement starts by applying a π -pulse on the qubit initially at its ground state $|g\rangle$. The the power of π -pulse is adjusted, so that its length is around 200ns, much smaller than its relaxation T_1 . When it is fully excited to its excited state $|e\rangle$, the system is allowed to evolve freely for δt_1 until a cavity measurement pulse is sent to detect the state of qubit. The probability to find the qubit on $|e\rangle$ decays over time

$$P_e = \exp(-t/T_1) \quad (7.9)$$

Figure 7.15 shows the measurement result of transmon at $\omega_{ge} \approx 4\text{GHz}$. $T_1 = 12\mu\text{s}$ is achieved.

7.3.3 Ramsey interference and dephasing measurement

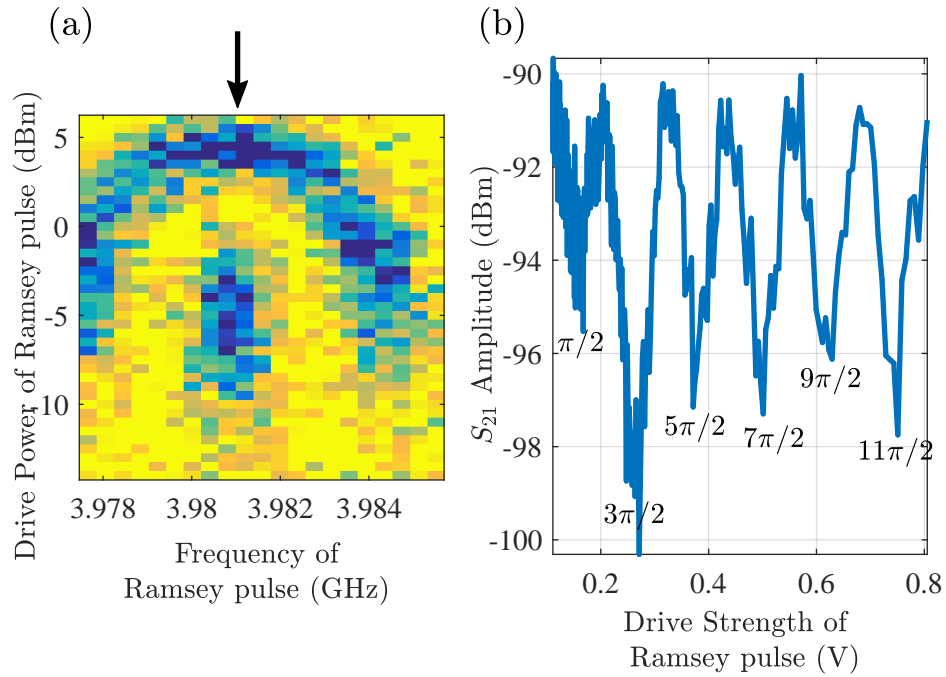


Figure 7.16: (a) Frequency and power dependence of Ramsey pulses. The color scale indicates output power of transmitted amplitude. The blue center at 3.98GHz and -5dBm is a $\pi/2$ pulse. (b) is the same measurement with fixed frequency though the arrow above (a). Periodic oscillations in amplitude come from cycles qubit rotating along x-axis in Bloch sphere.

The Ramsey interference is a technique to measure the dephasing rate of two-level system. It is performed by applying two phase coherent $\pi/2$ -pulses separated by a time interval Δt_2 . Ideally two $\pi/2$ -pulses together rotate qubit as a π -pulse to excited state.

Because of imperfection of pulse shape, the time of a $\pi/2$ -pulse is not just half of π -Pulse. In order to manipulate qubit accurately, the pulse length needs to be adjusted. The desired

Ramsey pulse time is around 100ns, much smaller than T_2 . However the resolution of pulse time generated by Agilent is 10ns. So instead of changing pulse length, we vary the power of pulse which has a resolution of 0.01dBm to achieve the most accuracy. This is done by performing Ramsey oscillation respected to pulse power with a fixed small delay Δt_2 . Figure 7.16 shows multiple cycles of qubit rotation. Unexpected among the dips, the $3\pi/2$ -pulse has the bigger change than $\pi/2$ pulse. The reason is not fully understood yet, but I tested both in T_2^* measurement and they gave the same result.

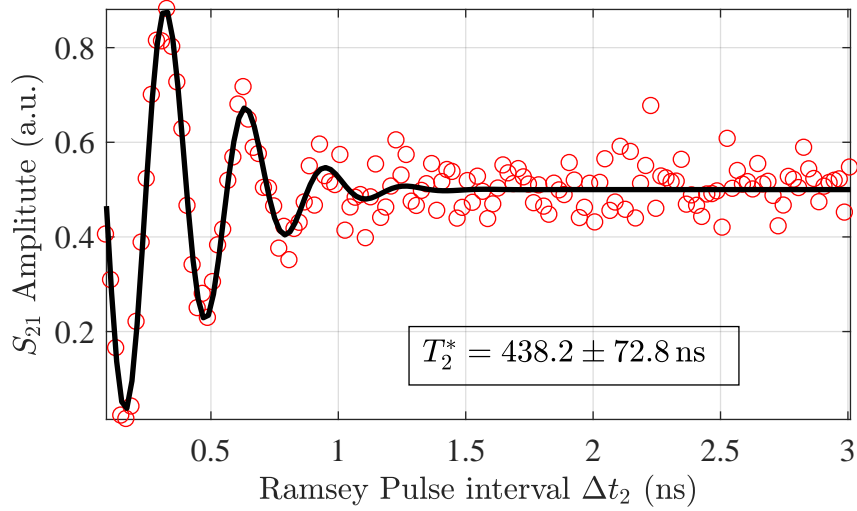


Figure 7.17: Ramsey oscillation of a transmon qubit at $\omega_{ge} = 3.98$ GHz. Dephasing time is fitted to be 430ns.

Chapter 8

Hybrid system of Cavity-Transmon-MR

In this chapter, I will present the central experimental results of my thesis involving the measurements of a qubit coupled mechanical resonator system embedded in a T-filter biased superconducting CPW cavity. We demonstrate that the mechanical resonator and transmon have commensurate energies and the transmon coherence times are an order of magnitude larger than in any previously reported qubit-coupled mechanical resonator systems. Moreover this work is the first experimental investigation of the interaction between an ultra-high frequency nano-mechanical resonator and a high-quality transmon qubit. From this work, we believe this system has the potential, given further development, to serve as a platform for more advanced experiments probing the quantum properties of motion in nano- and micro-scale systems. Some of work in this chapter are published in my paper Rouxinol et al[58].

In this chapter, I will present the experimental results of measuring the coupled transmon-

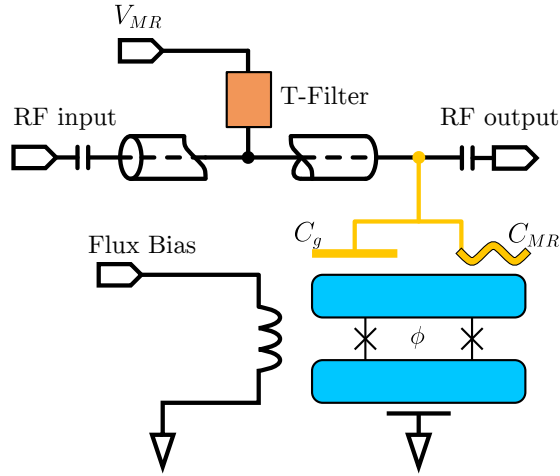


Figure 8.1: Schematic drawing of cavity-transmon-MR hybrid system.

MR system embedded in a filter-biased CPW cavity. We demonstrate that the mechanical resonator and transmon have commensurate energies and that the transmon coherence times are an order of magnitude larger than any previously reported qubit-coupled mechanical resonators.

8.1 Continuous single tone

We started by doing single tone continuous measurement for cavity. Microwave near cavity frequency is sent to the cavity and the transmitted signal is amplified and then recorded using Heterodyne detection circuits.

8.1.1 Single tone cavity spectroscopy at 0V

The gate voltage is first set at 0V. This sets the coupling strength λ between transmon and mechanical resonator zero, leaving only coupling between the transmon and CPW cavity[13, 14]. The cavity response behaves as the standard transmon dispersive coupled

Parameter	Value
$\omega_{cpw}/2\pi$	4.95GHz
E_C/h	0.227GHz
E_{J0}/h	15.4GHz
T_1	15 μ s
T_2^*	1.4 μ s
$\omega_{MR}/2\pi$	3.4GHz
$\omega_{MR,meas}/2\pi$	\simeq 3.47GHz
m	7fg
w	45nm
L	700nm
<i>thickness</i>	100nm
ρ	2.8g/cm ³
x_{zp}	25fm
α	0.447
β	0.17
$g/2\pi$	120MHz
$\lambda/(2\pi V_{NR})$	\approx 300kHz/V
Q_{MR}	150
$Q_{MR,calc}$	280
$\kappa_c/2\pi$	0.25MHz
$\kappa_{MR}/2\pi$	23MHz

Table 8.1: Experimental parameters characterizing the sample. The first set of values shows the CPW and transmon's characteristic energies, and T_1 and T_2^* for $\omega_{ge}/2\pi \simeq 4.2$ GHz. The nano-mechanical resonator mechanical properties are shown at the second set, and the last set displays the measured coupling and decoherence rates.

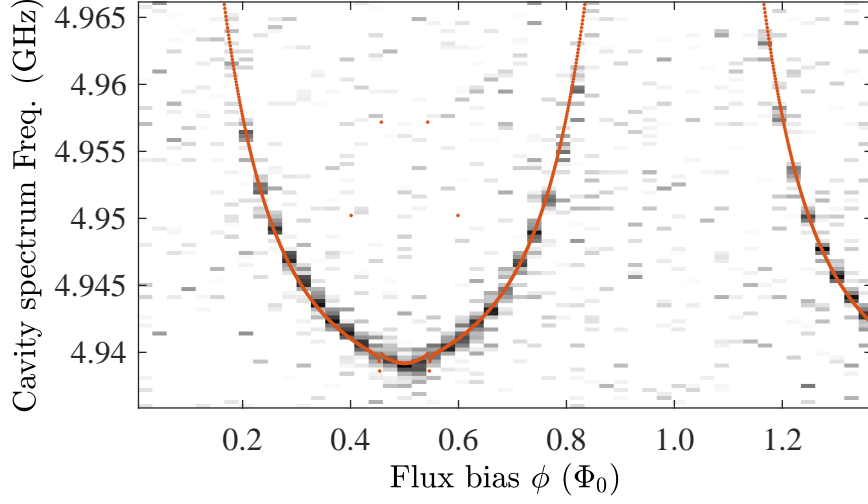


Figure 8.2: One tone spectrum of cavity-transmon-MR system. The bias voltage $V_g = 0$ turns off the coupling between transmon and mechanical resonator. The color scale shows the amplitude of the transmitted signal $|S_{21}|$. The red dotted line is a numerical simulation of the response.

cavity. The coupling between cavity and transmon is given by standard expression using in Chapter 2

$$g = 2 \frac{\beta e V_{zp}}{\hbar}$$

where $\beta = C_g/C_\Sigma = 0.17$ is the effective ratio CPW-transmon mutual capacitance. $V_{zp} = \sqrt{\hbar\omega_c/2C_T}$ is the rms zero-point fluctuations of CPW cavity. Fitting the cavity spectrum, the coupling strength is $g/2\pi \approx 120\text{MHz}$, close to the designed value, achieving strong dispersive coupling between cavity and transmon, where the effective dispersive coupling strength χ exceeded the linewidth of both the cavity and transmon (i.e. $\chi_{ge}/2\pi > \left[\frac{2\pi}{T_1}, \frac{2\pi}{T_2^*}, \kappa_c \right]$).

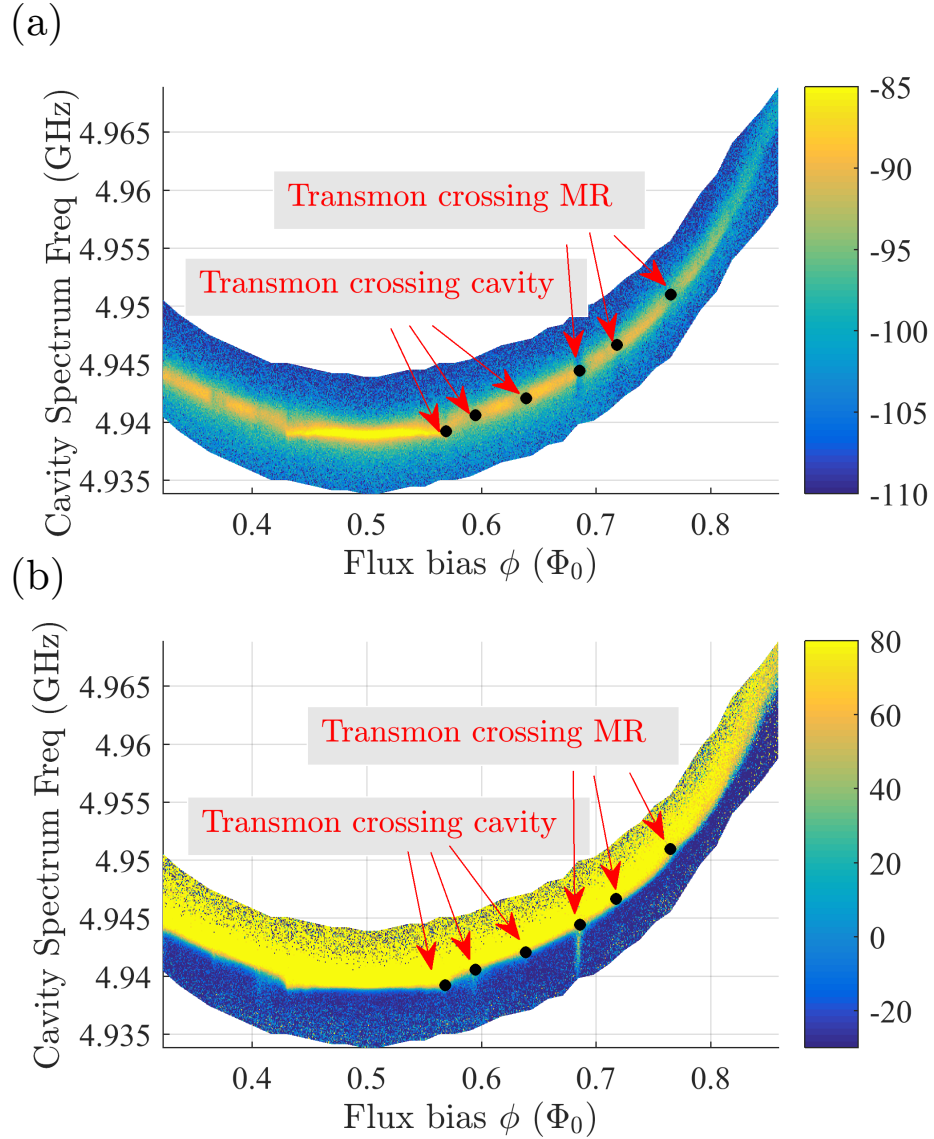


Figure 8.3: Cavity spectrum of hybrid system. $V_{MR} = -9.5\text{V}$. (a) Amplitude of transmitted signal. (b) Calibrated phase of transmitted signal. The split-up of the cavity spectrum in half of period, $\phi \in [0.5, 1]\Phi_0$, are marked using black dots. The three at lower cavity spectrum frequency are due to transmon energies in resonance with cavity, and the higher three are believed to be transmon-MR in resonance.

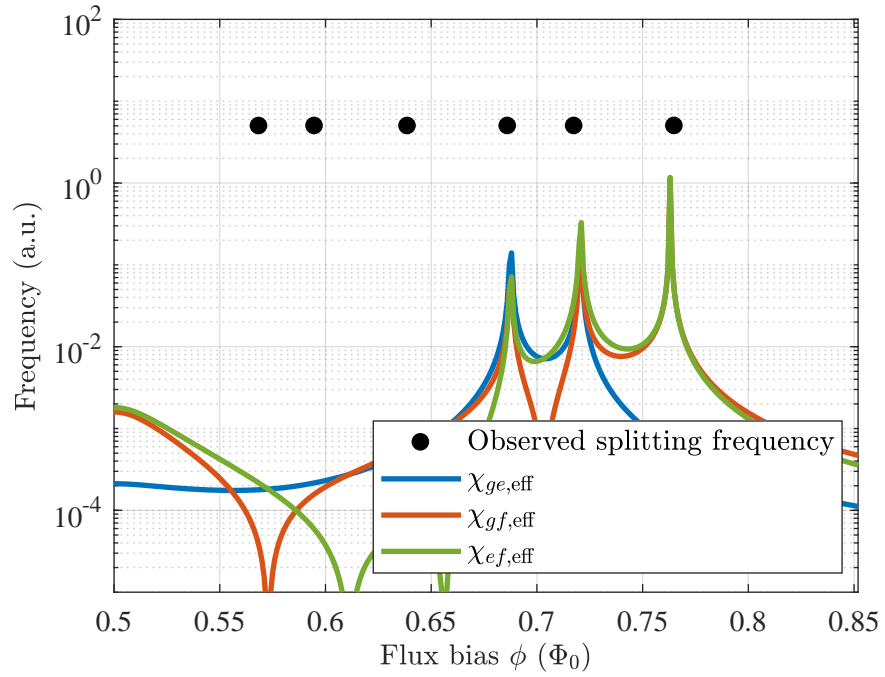


Figure 8.4: Comparison of split-up positions with transmon-MR resonances. This plot combines two parts: the black dots are the same as in Figure 8.3, and the colored lines are simulated dispersive shift of transmon. The peaks of $\chi_{ij,eff}$ locating roughly the same position of the three dots, is a strong evidence of MR resonance ω_{MR} crossing transmon energies ω_{ij} .

8.1.2 One tone cavity spectroscopy with gate voltage

In order to find the intersection of transmon and the third mode of mechanical resonator, we turned the bias voltage V_{MR} as high as possible. The highest voltage from our SRS dc voltage source is $\pm 20V$. However unexpectedly we observed heating on the sample and fridge. I will discuss the heating effect later in this chapter. So I chose voltage when the heating is slow and the mixing chamber thermometer shows no change in temperature, i.e. $R_{MC} > 200K\Omega$. During the whole process of measurement for this sample, we had several times of warming up and cooling down. We saw this critical heating voltage changed (from $\sim 10V$ to $\sim 8V$) after warming up.

Figure 8.3 is single-tone cavity spectroscopy at $V_{MR} = -9.5V$, (a) is the amplitude of transmitted signal. Tracing the maximum of the data, one can see six split-ups in half of the period. The three (labeled as “Transmon crossing cavity”) at lower cavity spectrum frequencies are the same as in Figure 7.5. The other three (labeled as “Transmon crossing MR”) at higher cavity spectrum frequencies are new after turning on bias voltage V_{MR} , which will be proven in details later. We believe they are lowest transmon states intersects with the third mode of mechanical resonator. To be clear, in this chapter, ω_{MR} refers to the third mode of MR.

The first proof of this to compare the position of the three higher splits. In Figure 8.8, the six black points are copied from Figure 8.7. Then I plot the dispersive shift of a harmonic oscillator (representing the MR) with frequency $\omega_{MR} = 3.47GHz$ coupled to this transmon. The goal of this figure is only to check the position matching of flux bias when the mechanical resonator in resonance transmon energy differences.

8.1.3 Voltage dependence

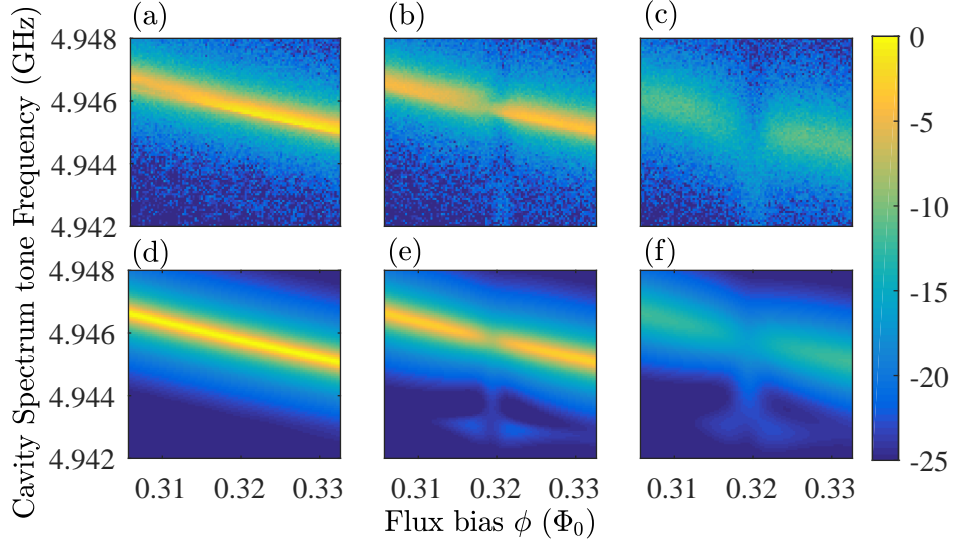


Figure 8.5: Measurements and simulation of single-tone spectroscopy of the cavity mode around ω_{cpw} as a function of ϕ over a range where $\omega_{eg} \approx \omega_{MR}$. The color scale indicates the amplitude of the transmitted signal. (a)-(c) The measurement data are plotted for three different bias voltage $V_{MR} = -4.5\text{V}, -5.5\text{V}, -6.5\text{V}$. (d)-(f) The simulation result for $\lambda = 1.35, 1.65, 1.95\text{MHz}$; $T_{MR} = 30, 100, 180\text{mK}$.

To see clear voltage dependence of transmon and mechanical resonator, we choose to zoom in split-up at $\phi \approx 0.32\Phi_0$. This one is thought to be two lowest transmon states ($|g\rangle$ to $|e\rangle$) and mechanical resonator crossing and it is also the biggest and the most clear one. Figure 8.5 is the measurement (a-c) and simulation (d-f) of single-tone spectrum near the gap $\phi \approx 0.32\Phi_0$. It is evident that for low coupling voltage ($V_{MR} \lesssim 5\text{V}$), the cavity only varied from transmon cavity interaction. However as V_{MR} increases ($5\text{V} \lesssim V_{MR} \lesssim 7.5\text{V}$), the transmon-MR interaction became prominent, producing a gap at $\phi \approx 0.32\Phi_0$, where $\omega_{ge} \approx 3.47\text{GHz}$ (see Figure 8.11). For larger values of coupling, $V_{MR} \gtrsim 8\text{V}$ (not shown), the cavity response are broadened significantly, the feature became obscure.

This behavior can be explained as the interplay between two different effects. First, as V_{MR} increases from zero, the corresponding growth of λ should lead to hybridization of

MR and transmon energy levels when $\omega_{ge} \approx \omega_{MR}$, producing well-known phenomenon of Rabi doublets in the coupled system. For the environment temperature at which the transmission measurements were made, both the transmon and the mechanical resonator should state in their ground state, $n_{th} \approx 0.004$, at $T=30\text{mK}$. The joint ground state $|n_{MR} = 0; g\rangle$ made no change in the transmission response. However, the increase in V_{MR} was accompanied by heating of the resonator. Refer to section 8.5.2 for details of spurious heating. This results in non-negligible thermal population of the MR ($n_{MR} > 0.1$). Qualitatively through the coupling λ , the thermally excited MR served as an effective thermal bath for the transmon, increasing the probability for transmon to be found in the excited states, eg. $|e\rangle$, and leading to a thermally averaged dispersive shift of cavity response.

8.2 Pulsed Cavity spectrum

8.2.1 Pulsed one tone

To observe the free evolution of the hybrid transmon-MR system near $\phi = 0.32\Phi_0$, pulsed measurement is performed at the same range of continuous measurements. The cavity is let relaxed to its ground state for a long enough time ($\sim 50\mu\text{s}$), at which time the transmon and mechanical resonator system evolves freely. And then a pulse of measurement microwave detects the state of the transmon. In this measurement setup, the MR-induced dispersive shift of cavity is not averaged out.

The Figure 8.8 shows plot of pulsed single tone measurement. Besides the measurement data, I also plotted the simulated shift of cavity spectrum when transmon is on the lowest three states $|g\rangle$, $|e\rangle$ and $|f\rangle$, to be comparison with data and a guidance for eye. It is

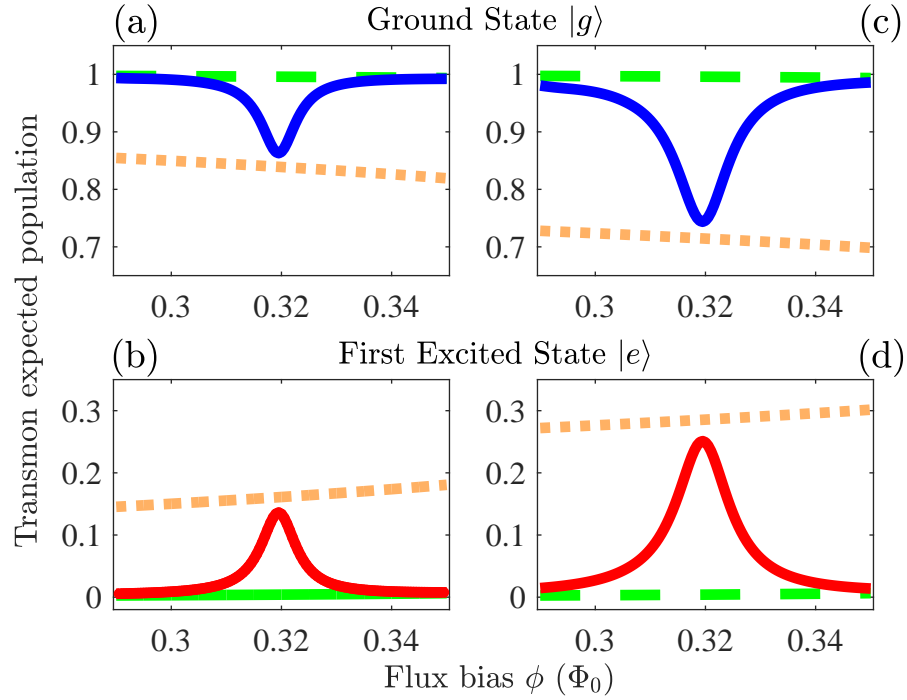


Figure 8.6: Numerical simulations (solid lines) of the expected populations of the transmon ground state (panels (a) and (c)) and first excited (panels (b) and (d)) states as a function of applied magnetic flux bias ϕ . The model assumes that the transmon is directly coupled to a $T=30\text{mK}$ thermal reservoir. As the transmon and nanoresonator are almost on resonance $\phi \approx 0.32\Phi_0$, it is observed that the transmon state population deviate from those imposed by 30mK reservoir (green dashed line), to ones much more related with a thermal reservoir at the MR temperature T_{MR} (orange dotted line). Panels (a) and (b) ((c) and (d)) show the case $V_{MR}=-5.5\text{V}$ (-6.5V).

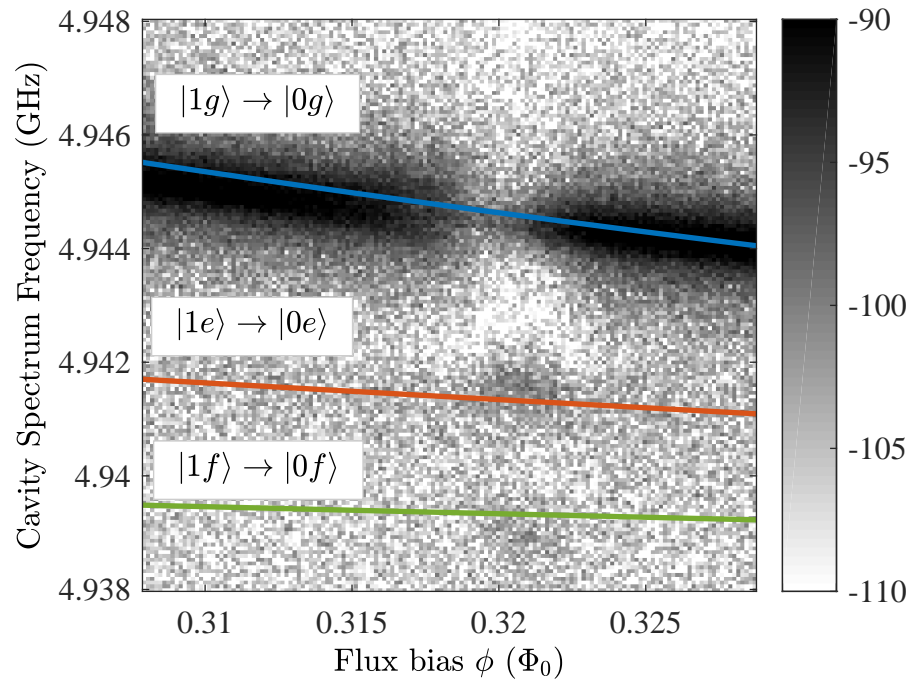


Figure 8.7: Pulsed measurement of single-tone cavity spectroscopy as a function of flux bias ϕ near $\phi \approx 0.32\Phi_0$. The bias voltage is $V_{MR}=-5.5V$. The grayness scale indicates the amplitude of the transmitted signal. The colored solid lines are simulated cavity response dispersively shifted by the state of the transmon. The blue (red, green) is when transmon is on $|g\rangle$ ($|e\rangle$, $|f\rangle$) respectively.

observed that at $\phi \approx 0.32\Phi_0$, the main response peak (where the blue line locates) breaks up (smaller amplitude, brighter color). On contrary, an increase in amplitude shows up at lower cavity spectrum frequency, whose positions accurately locate on red and green line, indicating explicitly the transmon is at least partly excited to excited states due to interaction with mechanical resonator.

8.2.2 Voltage dependence

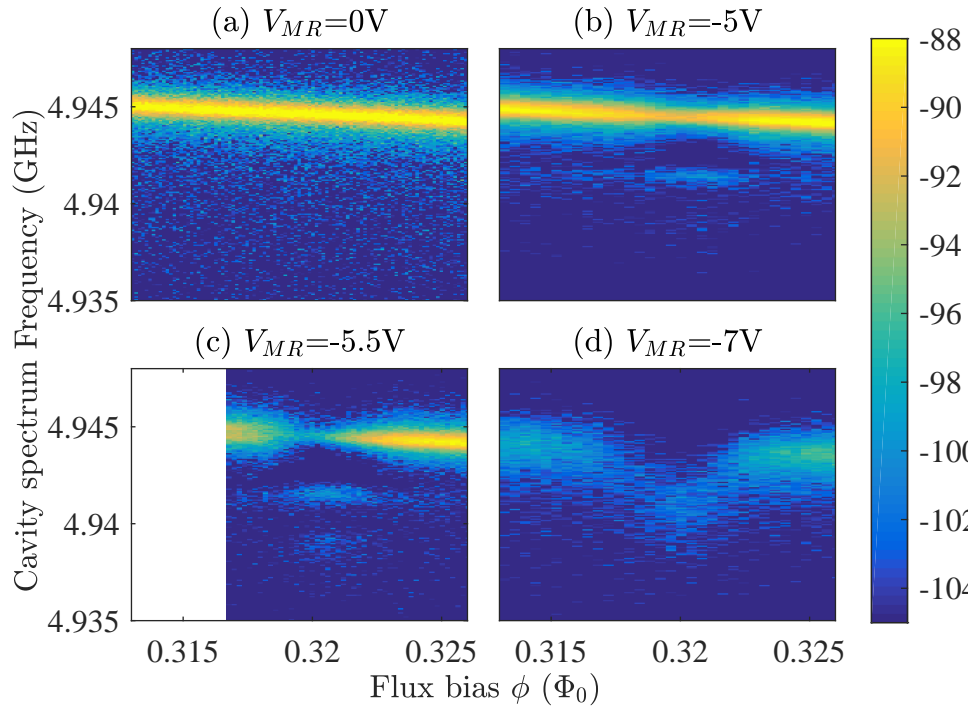


Figure 8.8: A set of pulsed measurement of single-tone cavity spectroscopy at different bias voltage V_{MR} .

Like continuous measurement, the voltage dependence is also studied using pulsed single-tone cavity spectrum. At $V_{MR}=0V$, the transmon-MR coupling is zero, and only transmon-induced cavity dispersive shift is observe. When voltage increases $V_{MR}=-5V$, both coupling and heating takes place, the second peak starts to show up indicating small popula-

tion of transmon staying on $|e\rangle$. Changing from -5V to -5.5V , the coupling only changes 10%. The bigger gap in the main peak suggests that the nonlinear increasing heating plays a more important role. At larger voltage $V_{MR} < -7\text{V}$, the heating effect dramatically reduces the linewidth of the cavity spectrum, dimming the fine features near the gap.

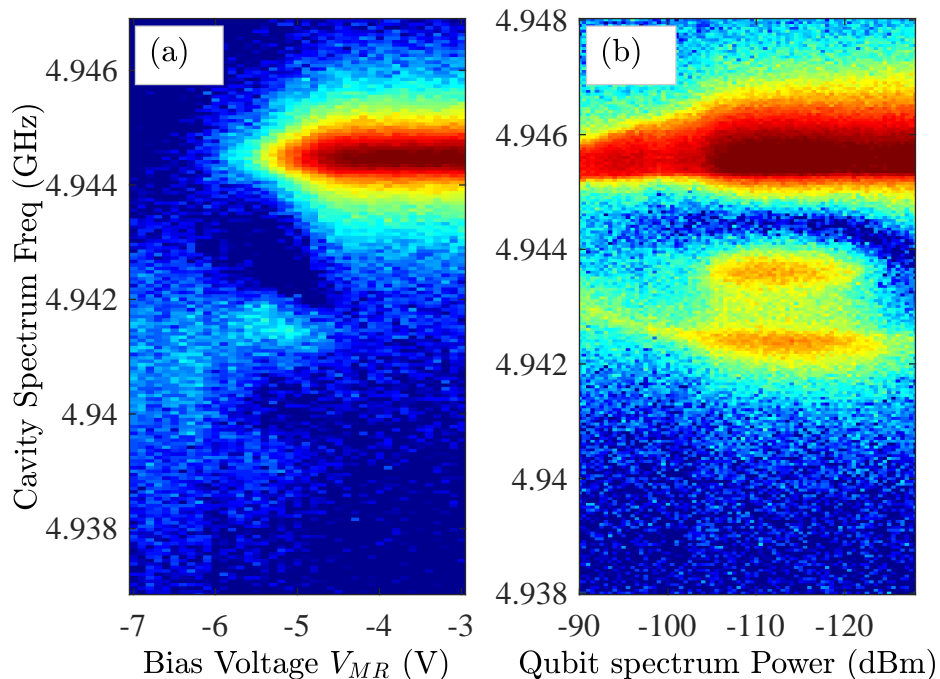


Figure 8.9: Comparison of cavity spectrum when qubit is excited by heated MR or coherent microwave.

To experimentally compare the difference of excitation between classical microwave driving and dissipative quantum bath generated by mechanical resonator, I did 2 sets measurements. The first one Figure 8.9(a) is quantum bath excitation versus bias voltage V_{MR} . The bias point is chosen right on the gap $\phi = 0.32\Phi_0$ and the cavity spectrum frequency is swept near the cavity resonance at different biasing voltage $V_{MR} \in [-3\text{V}, -7\text{V}]$. As shown in Figure 8.8, three separate peaks are observed below $V_{MR} \gtrsim -6\text{V}$, indicating three lowest transmon states. The main peak starts to drop at around -4.5V , and the

second and the third shows up. The main peak totally disappear at around -6.5V, and at even larger the separate became mixed. The classical comparison (b) is performed similarly. To avoid possible effect of mechanical resonator, I chose a slightly different flux bias ϕ_{cl} and accordingly y-axis is shifted to match the main peak in plot. The frequency of the qubit drive tone is the transmon g-e energy at this flux bias $\omega_d = \omega_{ge}(\phi_{cl})$. With this drive applied continuously at different power (x-axis in (b)), the cavity spectrum is swept and the pulsed transmitted signal is recorded. It is observed that at minimal power, the main peak (4.946GHz) is present with a weak peak at 4.942GHz, where matches $|e\rangle$ state of transmon. Then a third tone shows up at 4.944GHz and became one at large power (\sim -100dBm). The mechanism of this two measurements are yet not fully understood.

8.3 Continuous Qubit spectrum

Two tone spectroscopy is a tool to directly measure the absorption and emission spectrum of MR-coupled transmon. I first performed continuous two tone measurement where both cavity spectrum tone and transmon excitation tone are continuously applied.

To get a good map, the choice of bias voltage V_{MR} is critical and needs delicate thoughts. If the voltage is too small, then both the coupling strength and the excitation of transmon and MR are not excited enough, some transitions between higher levels of transmon is not seen. Or if the voltage V_{MR} is too big, even a lot before the cavity spectrum became over-dissipative, the gap is too deep so that the lines inside the gap lose their contrast. When I did the measurement, I carefully increase the voltage with small step until I can see as much transitions as possible. For Figure 8.10, $V_{MR} = -4.7V$.

I took the measurement using two different qubit excitation power, and all the other

parameters are the same. With two different power, it enables distinguishing between single-photon transition and multi-photon transition, providing more information to understand the system. In Figure 8.10(c) gives the simulated spectrum (color dashed lines) and can be used as a guide to understand the spectroscopy lines in (a)(low power) and (b)(high power). Because the bias voltage V_{MR} is low, the excitation of transmon is weak, the biggest spectroscopy line is g-e transition ω_{ge} (blue in (c)). The second line (yellow in (c)) is a two-photon excitation of transmon g-f transition, which significantly increases from low power to high power. The third line (red in (c)) is single photon excitation of e-f transition, which has bigger change inside than outside the gap, directly indicating a population of transmon staying on $|e\rangle$. The fourth line (purple in (c)) is a two-photon excitation of transmon e-h. It is not visible in low power and at high power, it shows inside the gap. Noted there is a thin spectrum line (noted as “a white line” in (c)) that has no corresponding simulated spectrum. I tried different possibilities but none of them fits the line perfectly. The closest is the green line in (c), it is a transition between dressed states $0.9|n_c = 0;f\rangle + 0.1|n_c = 1;e\rangle$ to $|n_c = 2;g\rangle$ and they have same slope. The most interesting feature the of white line is that unlike all the other spectroscopy lines, it is an emission line visible only inside the cavity, which suggests the excited transmon is “cooled” back down to its ground state by stimulated radiation. And this is the property of $0.9|n_c = 0;f\rangle + 0.1|n_c = 1;e\rangle$ to $|n_c = 2;g\rangle$ transition.

8.4 Pulsed Qubit spectrum

To study the dissipation of the transmon induced by mechanical resonator, one could do time-domain measurement, such as T_1 , T_2 measurement, or pulsed two-tone spectrum. The latter is advantageous for its simplicity to perform. Pulsed two tone spectrum is free

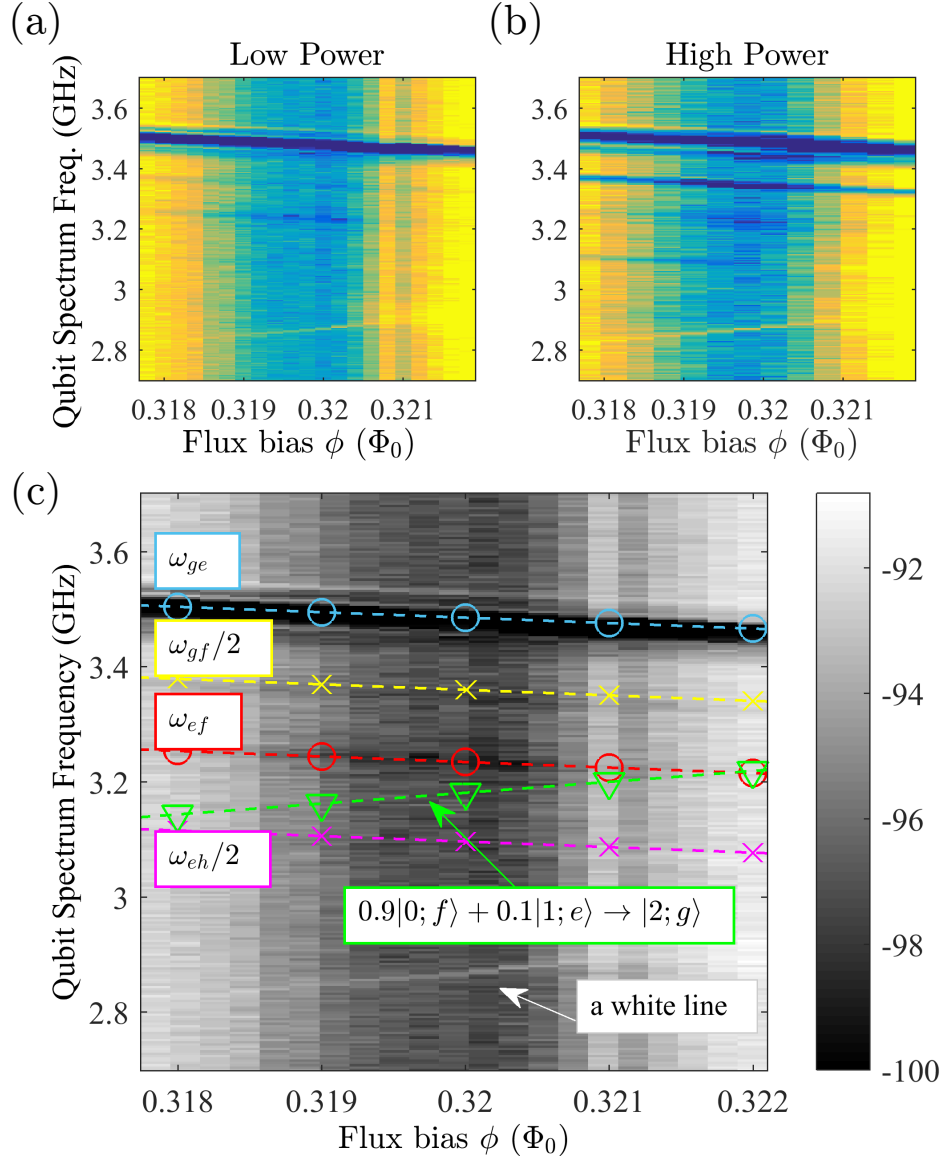


Figure 8.10: Two tone continuous spectroscopy versus flux bias at $\phi \approx 0.32\Phi_0$ at $V_{MR} = -4.7V$. (a) Low qubit excitation power. (b) High qubit excitation power. (c) Low power map with simulated spectroscopy (color dashed lines). The color scale in (a) (b) and grayness in (c) is the amplitude of transmitted signal of cavity spectrum.

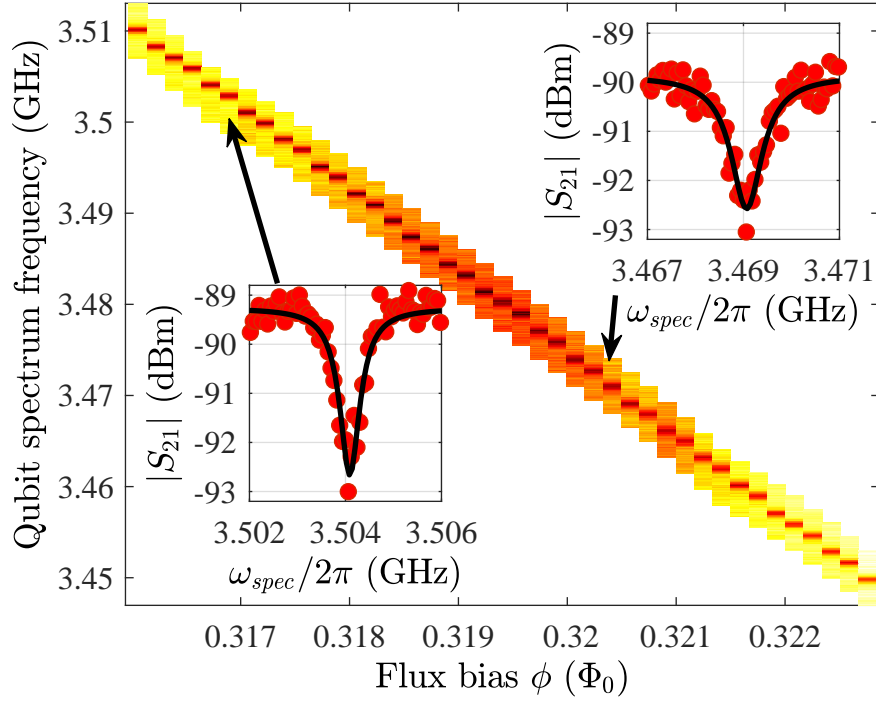


Figure 8.11: Pulsed two tone spectroscopy of transmon near MR frequency $\omega_{ge} \approx \omega_{MR} = 3.47\text{GHz}$ as a function of flux bias ϕ . The color scale indicates the amplitude of transmitted signal. For each flux, the cavity spectrum tone is fixed at its peak detecting the ground state of transmon. The red-ish color of the background at $\phi \approx 0.32\Phi_0$ implies the gap in single tone spectroscopy. The two inlets are two curves from the map. The left one chosen far from the gap (3.5GHz) has a bigger background (-89.5dBm) and a narrower dip. The right one chosen inside the gap (3.47GHz) has a smaller background (-90dBm) and a broader dip. The black solid line in each inlet is a numerical Lorentz fitting.

of broadening or mixing from cavity photon number splitting, makes it straightforward to extract the linewidth of the qubit, the inverse of which is the qubit relaxation rate γ discussed in chapter 2.

The complexity of this measurement is much higher than standard spectrum, it needs multiple steps to calibrate and parametric control of setting points. First a single-tone cavity spectrum versus flux bias ϕ is taken at a low or zero bias voltage. For each flux bias ϕ , the cavity probe frequency is pointed at its peak detecting the ground state of transmon $\omega_b(\phi)$. The second step is to perform a rough two tone spectrum map with parametric cavity bias frequency $\omega_b(\phi)$. From this map, the transmon spectrum frequency can be extracted. To get a well-averaged detailed map, it is very crucial to focus close spectrum region to speed up the measurement before flux jumps happens. The measurement shown in Figure 8.11 took one night to do average, if without focusing, it might take several days. The bias voltage $V_{MR} = -5V$ is also carefully selected similar as discussed for continuous measurement. The MR induced dissipation needs to be large enough to be measurable, but cannot be too large to meet the low phonon number limit $\langle n_{MR} \rangle \ll 1$.

Figure 8.11 the measurement of the pulsed two-tone spectroscopy. It is observed that from the gap (red-ish color), the peak is narrower. While inside the gap, the background is smaller and the dip is broader implying more dissipation from mechanical resonator interaction. For each curve, the width γ and center frequency are extracted by fitting it to a Lorentz shape as shown in the insets.

In Figure 8.12, the extracted transmon resonance linewidth is plotted against extracted center frequency, which is the energy of g-e transition ω_{ge} . As discussed in chapter 2, the

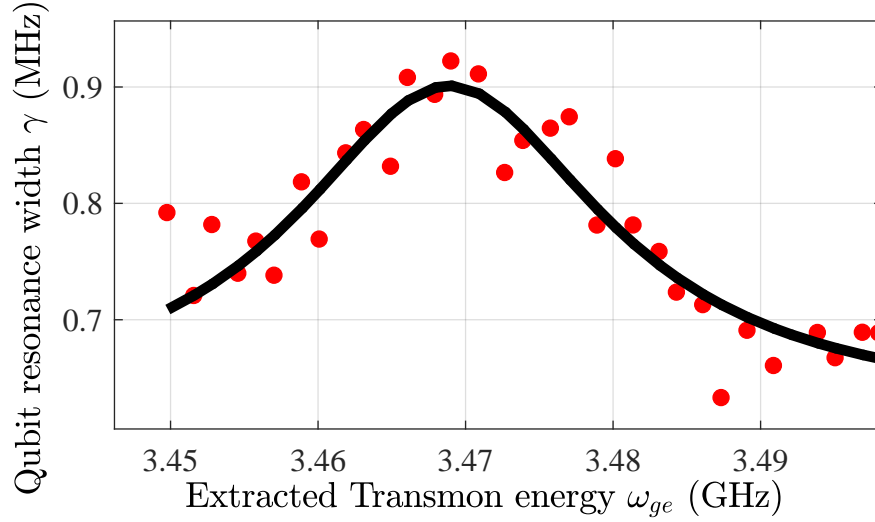


Figure 8.12: Extracted dip width (red points) from Figure 8.11 as a function of extracted center frequency, which is the transmon g-e transition energy ω_{ge} . The black line is a numerical Lorentz fitting with $Q_{MR} \approx 150$.

qubit linewidth near MR frequency follow a simple Lorentz form Eq. 2.37

$$\gamma(\omega_{ge}) = \frac{\lambda^2}{\hbar^2} \frac{\kappa_{MR}}{(\omega_{ge} - \omega_{MR})^2 + (\kappa_{MR}/2)^2} + \Gamma_B$$

One can fit the points to extract the MR frequency $\omega_{MR}=3.47\text{GHz}$, $Q_{MR} = \omega_{MR}/\kappa_{MR}=150$ and coupling strength $\lambda/2\pi V_{MR}=300\text{kHz V}^{-1}$. This is consistent with estimation from the shape of sample.

8.4.1 Decoherence times

We measured the decoherence times at 0V when it is far-detuned from either the cavity and mechanical resonator, $f_{ge} = 4.2\text{GHz}$. The process is the same in transmon-cavity experiment. We achieved relaxation time $T_1 = 15\mu\text{s}$ and dephasing time $T_2^* = 1.5\mu\text{s}$. It is believed that our relaxation time is limited by Purcell effect due to coupling to the

cavity, refer to section 3.1.4. For T_2^* , flux noise is one of the dominating loss channel, refer to section 3.3.2. These values are one order of magnitude better than the results in similar qubit coupled electromechanical system [11].

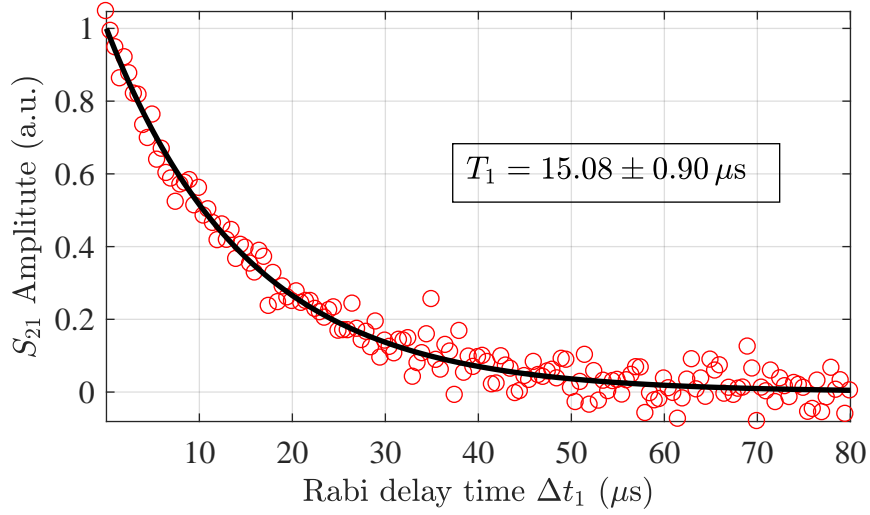


Figure 8.13: Relaxation measurement of transmon at $f_{ge} = 4.2\text{GHz}$. The fitted relaxation time $T_1 = 15\mu\text{s}$.

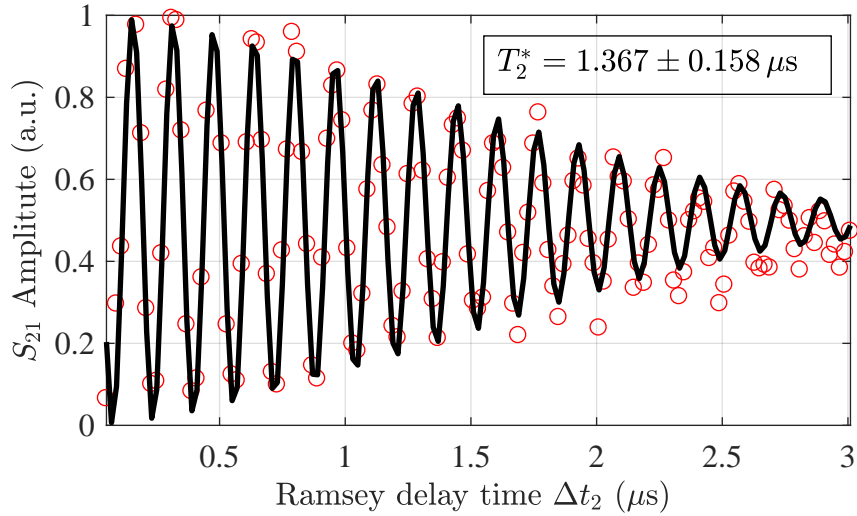


Figure 8.14: Ramsey measurement of transmon at $f_{ge} = 4.2\text{GHz}$. The fitted dephasing time $T_2^* = 1.4\mu\text{s}$.

8.5 Temperature of system

8.5.1 effective temperature without voltage

Although the sample is anchored at the mixing chamber $T_{MC}=30\text{mK}$, the effective temperature of each part of system cannot be naturally assumed to be 30mK. Each element of the system has its own temperature depends on the environment it is coupled to.

Cavity temperature The CPW cavity is cooled to 30mK and is capacitively coupled to 50Ω transmission lines. We assume the cavity temperature T_c is limited by black-body radiation from external circuitry. Because the cavity is engineered at over-coupled limit ($Q_l \approx Q_c \gg Q_{intrinsic} \sim 10^5$), the photon number balance of the cavity is

$$\kappa_c n_c = \kappa_{in} n_{in} + \kappa_{out} n_{out} \quad (8.1)$$

where n_c is the number of background photons inside the cavity, and $n_{in/out}$ is input/output photon number. In our symmetric cavity sample, $\kappa_c = \kappa_{in} + \kappa_{out} = 2\kappa_{in}$. The incident photon number can be calculated from using temperature of each fridge stage and resistive attenuation between them.

$$n_{in} = \frac{n_{300\text{K}}}{10^{6.6}} + \frac{n_{1\text{K}}}{10^{3.6}} + \frac{n_{400\text{mK}}}{10^3} + \frac{n_{100\text{mK}}}{10^2} + n_{30\text{mK}} = 0.005 \quad (8.2)$$

Similarly photons is assumed to be limited by thermal from HEMP at 4K and two isolators on mixing chamber.

$$n_{in} = \frac{n_{4\text{K}}}{10^{3.5}} + n_{30\text{mK}} \quad (8.3)$$

And we can get $T_c \approx 45\text{mK}$. For single-tone spectroscopy simulation in Figure 8.5, we set $T_c=45\text{mK}$.

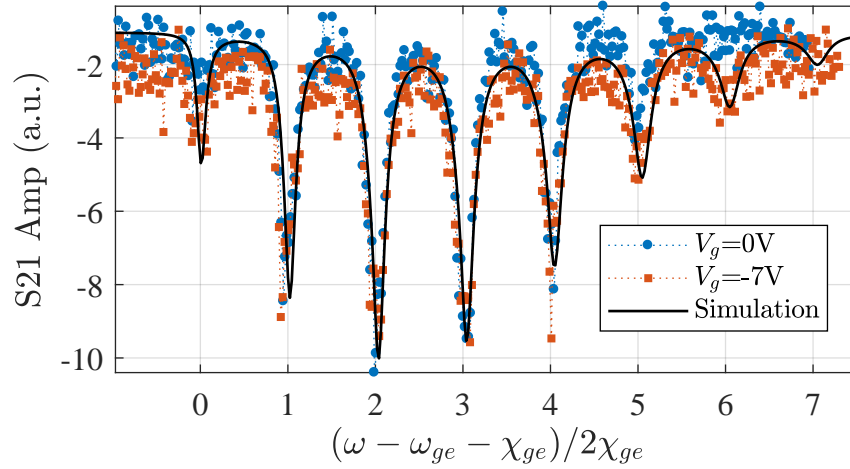


Figure 8.15: Two tone spectroscopy of transmon single photon g-e transition in cavity-transmon-MR experiment. The solid line is simulated curve done by Dr. Rouxinol using Python QuTip package. The temperature of qubit is 30mK, the temperature of cavity is 45mK.

We also observed cavity photon induced qubit energy splitting at -7V, see Figure 8.15. Comparing the number splitting with and without voltage bias, we see there is little change in photon distribution or peak width. This is another proof of cavity being cold with voltage applied.

Transmon temperature The temperature of the transmon is studied by checking the two tone spectroscopy far detuned from MR frequency. Two different power is used to explicitly show the position of ω_{ef} . In Figure 8.16, in both low power (red solid line) and high power (blue dashed line) no peak is visible, indicating the population of first excited

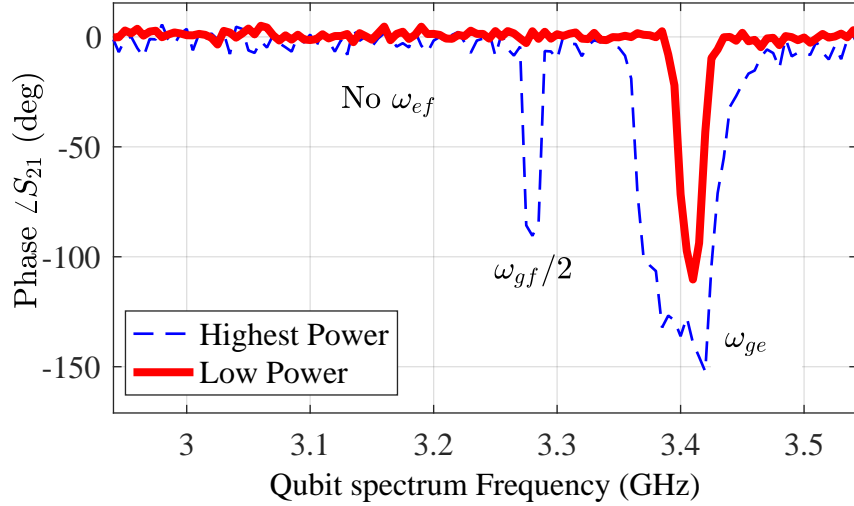


Figure 8.16: Transmon temperature estimate. Two-tone spectroscopy measurements of transmon at high and low power, illustrating the ω_{ge} and $\omega_{gf}/2$ transitions. The data is taken at $V_{MR}=-5V$. No peak is observed at the ω_{ef} transition frequency, indicating the transmon remains “cold” when far-detuned from the MR frequency.

state $|e\rangle$ is smaller than equivalent noise amplitude.

$$P_e = \frac{1}{e^{\hbar\omega_{ef}/kT_q}} \ll \frac{A_{ge}}{A_{ef}} = 0.051 \quad (8.4)$$

from which we find the upper bound of transmon temperature $T_q < 55\text{mK}$. For single-tone spectroscopy simulation in Figure 8.5, we set $T_q = T_{MC} = 30\text{mK}$.

8.5.2 Heating at high voltage

Heating effect observed when high bias voltage applied is unexpected when designing the sample. Among all seven samples we cooled down, the critical heating voltage varies from sample to sample, from cooling down to cooling down. One of the sample of bare cavity, no heating effect is observed through thermometer up to 20V. We believe it is due to leakage current though silicon substrate. In the T-filter and transmission line, the

distance between gate metal and ground is around $1\mu\text{m}$ and the voltage can be as high as 20V. The electrical field is $2 \times 10^7\text{V/m}$, already close to the breakdown voltage for silicon $3 \times 10^7\text{V/m}$ ¹. To quantitatively study the heat effect, we measured, in one of the sample, the current through voltage bias circuit as a function of voltage, see table. 8.2. Below 8V, the current is below the sensitivity of the measurement circuit(not shown here). And the current grows significantly at $V_{MR} > 9.5\text{V}$ and mixing chamber temperature T_{MC} became unstable.

Bias Voltage V_{MR} (V)	Current (nA)	Power (nW)
8	5	40
9	25	225
9.5	52	478

Table 8.2: Measured Leakage current of gate port when high voltage is applied. Below 8V, the current is below resolution of reading circuit. The data shows high nonlinearity.

Macroscopic picture The heating generated by leakage current can be qualitatively simulated using COMSOL simulation. The total heat power is equally distributed on the surface of gate-ground area. In our model we assume that the bottom of the silicon is attached to a 30mK reservoir. I tried to add a thin (eg. $50\mu\text{m}$) layer glue between silicon and reservoir, and the change is very little and negligible. Because superconductor has extremely low thermal conductivity[59, 60], the heat transportation is mainly through silicon wafer, building up a temperature gradient is built up from gate-ground area to bottom. Figure 8.17 shows simulated temperature of silicon in thermal equilibrium. The temperature at MR position and transmon position is plotted separately in Figure 8.18 as a function of total heat power.

¹www.el-cat.com/silicon-properties.htm

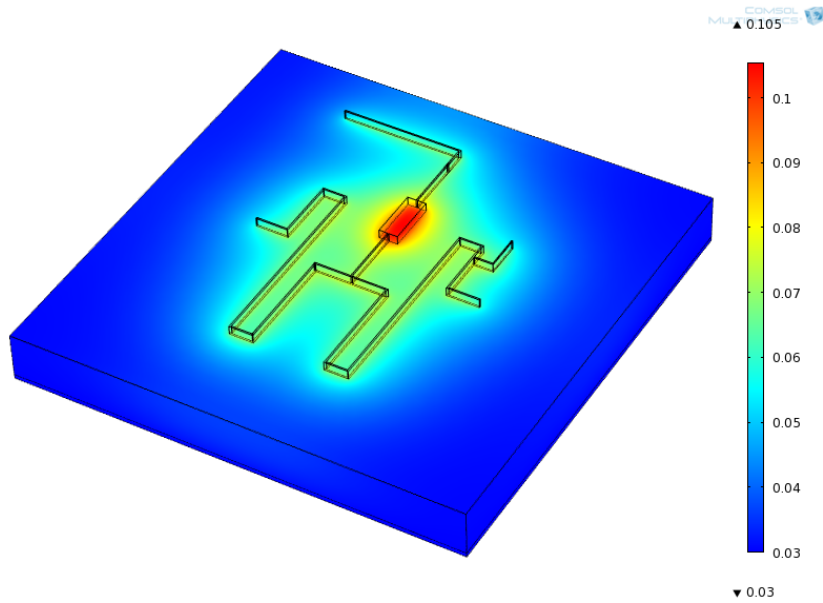


Figure 8.17: Finite element simulation of thermal gradient under total 40nW heat load on gate-ground area (black outline on top surface). The cubic is 0.5mm thick silicon whose bottom is attached to a 30mK reservoir. Color scale indicates local temperature.

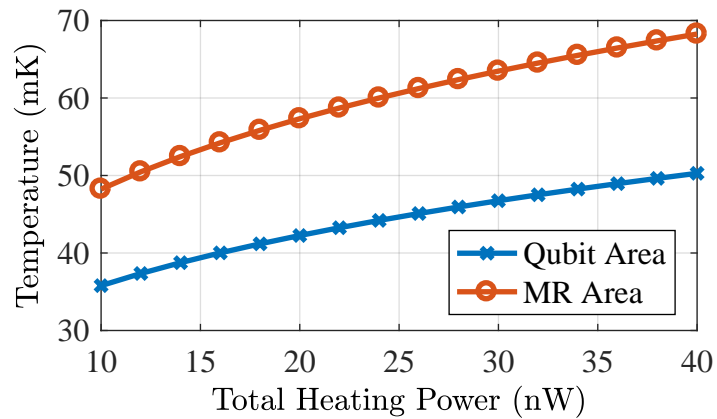


Figure 8.18: Simulated temperature at transmon position and MR position as a function of total heat power.

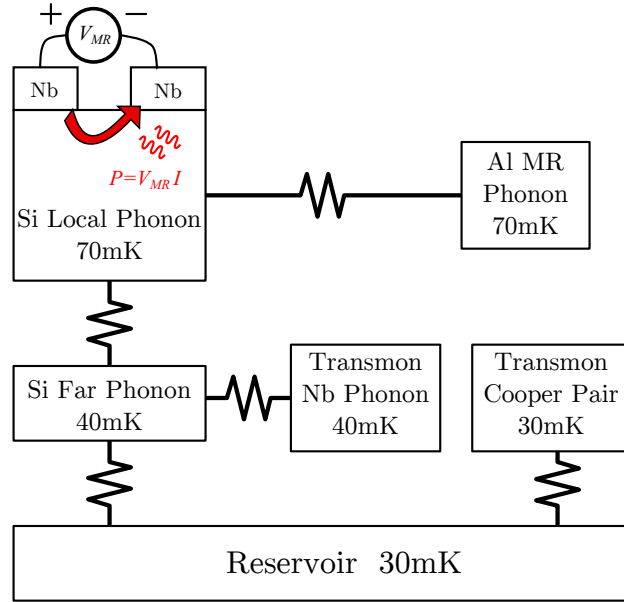


Figure 8.19: Schematic drawing of thermal coupling of transmon and mechanical resonator.

microscopic picture In the ongoing discussion, we calculated classical heat transportation in the substrate. Because the temperature is low, specific degree of freedom is frozen out, such as in superconductors the phonons and cooper pairs are highly decoupled with each other, resulting in very different thermal conductivity. I assume the heat is first generated by charge carriers inside silicon hitting silicon lattice (“local phonon”), see Figure 8.19. The aluminum mechanical resonator is attached to “local” substrate, so phonons in aluminum are in thermal equilibrium with “local phonon”. The local phonon excitation is transferred through phonon to the reservoir eventually. Transmon niobium pads locate geographically far from gate, thus niobium phonon thermalize with colder “far phonon”. The Cooper pairs inside transmon pads highly decoupling with phonons, remain cold at reservoir temperature. Noted that this is a simplified study to qualitatively explain the heat effect. A more systematic and quantitative research remains the subject of future work.

8.6 Conclusion

In conclusion, we have demonstrated a new hybrid quantum system that consists of an ultra-high frequency nano-mechanical resonator coupled with a high-quality transmon. The spectroscopy measurements of cavity and transmon proves interaction between the hybrid system: The strongly damped nano-mechanical resonator serves as a dissipative bath to the qubit. This system is well described by theoretical analysis and numerical simulations using multi-mode Jaynes-Cummings Hamiltonian. We believe this device can soon be compatible with state-of-art architecture currently being used in the development of superconducting quantum processors, as well as a large range of experiments to study the coherent quantum dynamics and quantum thermo-dynamics of complex system.

Chapter 9

Membrane Resonator

In this chapter, we describe an independent membrane measurement using impedance matching circuit. This technique probes the impedance change in LC resonator due to coupling to MR. We first derive the equivalent circuit model of voltage biased MR, and then the transmission is studied using transform network analysis. This technique is demonstrated on a doubly clamped MR at 77K.

9.1 Motional capacitance of MR

When oscillating voltage $V_{dc} + V_{ac}(t)$ is applied, there will be oscillating force on gate and MR pads. And this force will drive MR to vibrate, thus the capacitance will also change with time. The whole system should be reaching a steady state, and this effect is amplified a lot when driving frequency matches MR resonating frequency.

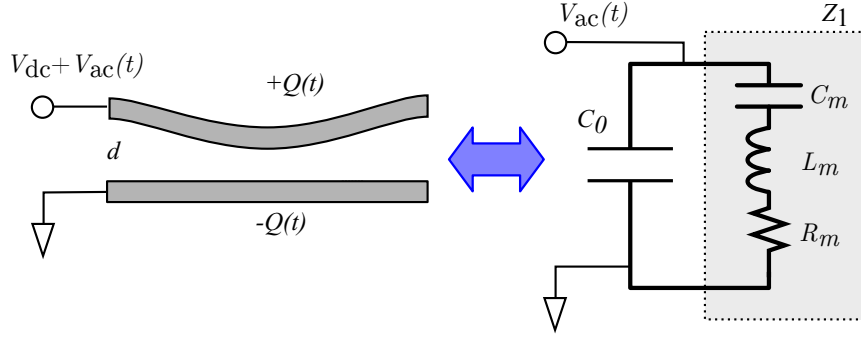


Figure 9.1: Electro-mechanical model of MR. The 2 plates are separated by a distance d , and are connected to a ac and dc source. Because of time-dependent voltage $V_{dc} + V_{ac}(t)$, charge $\pm Q(t)$ induced on two pads varies over time. This MR is described by a RLC model. C_0 is total static capacitance, and C_m, L_m, R_m are movement induced impedance, the sum of which is denoted as Z_1 .

$$\begin{aligned}
 Q(t) &= C(t) \cdot U(t) \\
 Q_0 + Q_{ac}(t) &= [C_0(t) + \frac{\partial C}{\partial x} x(t)][V_{dc} + V_{ac}(t)] \\
 Q_0 + Q_{ac} e^{i\omega t} &= [C_0 + \frac{\partial C}{\partial x} x_{max} e^{i\omega t}][V_{dc} + V_{ac} e^{i\omega t}]
 \end{aligned}$$

where ω is the angular frequency of drive frequency. x_{max} is the maximum displacement of MR vibration. If we only keep terms rotating at ω terms, and calculate current $I(t)$:

$$I_{ac}(t) = \frac{dQ}{dt} = i\omega \left(\frac{\partial C}{\partial x} x_{max} V_{dc} + V_{ac} C_0 \right) e^{i\omega t}$$

The current I_{ac} consist of two parts, the second part related with V_{ac} is usual term from capacitor impedance, while the first part is new. It is a result of MR vibration.

$$I_1(t) = i\omega \frac{\partial C}{\partial x} x_{max} V_{dc} e^{i\omega t} \quad (9.1)$$

To resolve x_{max} we treat MR as a classical Harmonic oscillator(HO) with self-vibration frequency ω_0 and quality factor Q . x_{max} is determined by external driving and Q :

$$x_{max} = \frac{F/K \cdot \omega_0^2}{\omega_0^2 - \omega^2 + i\omega_0\omega/Q}$$

$$F = \frac{\epsilon_0 S V_{dc} V_{ac}}{d^2} = \frac{C V_{dc} V_{ac}}{d}$$

where F is the force driving the HO, and ϵ_0 is electric constant, and S is the area of the parallel capacitor. Note there is valid for all ω and ω_0 .

We can calculate the effective impedance Z

$$Z_1 = \frac{V_{ac} e^{i\omega t}}{I_1(t)} = \left(\frac{\partial C}{\partial x} \frac{\epsilon_0 S V_{dc}^2}{d^2 K} \right)^{-1} \frac{1}{i\omega} \frac{\omega_0^2 - \omega^2 + i\omega_0\omega/Q}{\omega_0^2} \quad (9.2)$$

to get the effective capacitance C_m and inductance L_m of MR vibration, we compare Z_1 with equivalent circuit, as shown is Figure 9.1 in the limit of $\omega \rightarrow 0$, $\omega \rightarrow \infty$ and $\omega = \omega_0$:

$$Z_1|_{\omega \rightarrow \infty} = \left(\frac{\partial C}{\partial x} \frac{\epsilon_0 S V_{dc}^2}{d^2 K} \right)^{-1} \frac{1}{i\omega} \left(-\frac{\omega^2}{\omega_0} \right) \equiv i\omega L_m$$

$$Z_1|_{\omega \rightarrow 0} = \left(\frac{\partial C}{\partial x} \frac{\epsilon_0 S V_{dc}^2}{d^2 K} \right)^{-1} \frac{1}{i\omega} \equiv \frac{1}{i\omega C_m}$$

$$Z_1|_{\omega = \omega_0} = \left(\frac{\partial C}{\partial x} \frac{\epsilon_0 S V_{dc}^2}{d^2 K} \right)^{-1} \frac{1}{\omega_0 Q} \equiv R_m$$

we get equivalent for C_m and L_m :

$$\begin{aligned}
 C_m &= \frac{C^2 V_{dc}^2}{d^2 K} \\
 L_m &= \frac{d^2 K}{C^2 V_{dc}^2 \omega_0^2} \\
 R_m &= \frac{d^2 K}{C^2 V_{dc}^2 \omega_0 Q}
 \end{aligned}
 \tag{9.3}$$

9.2 MR coupled to LC resonator

In this section, we will calculate the effect of coupling this RLC model to a LC resonator close to MR frequency.

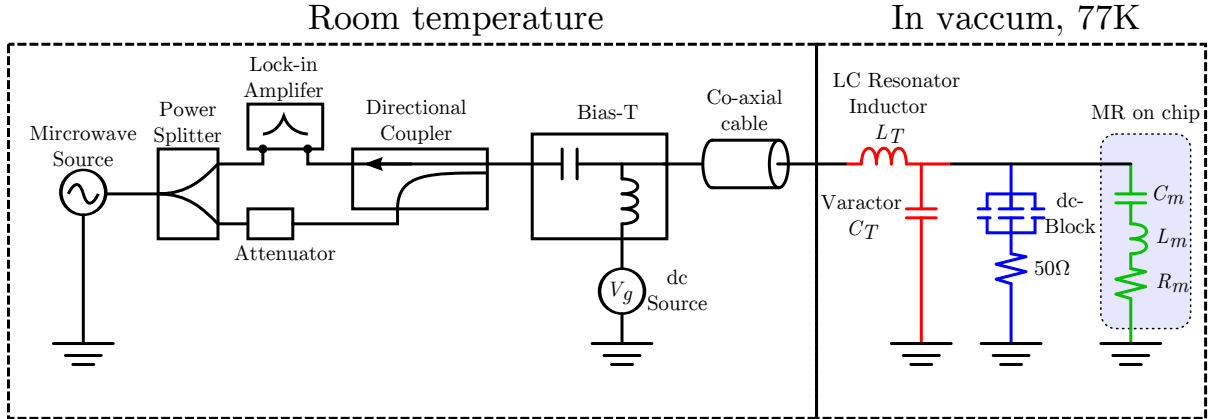


Figure 9.2: Sketch drawing of LC mis-match circuit. The ac signal generated from microwave source is sent to sample through a directional coupler and a bias-T. A dc source V_g controls the voltage bias V_{dc} . The LC resonator (red lines) and chip (green lines) are clamped inside a vacuum chamber cooled down to 77K. The blue lines is extra circuits to change the total impedance to 50 Ω .

Impedance was first demonstrated by Patrick[61]. The impedance of a MR $\approx 1/\omega C \sim 10^7 - 10^9 \Omega$ will have negligible impact on typical radio frequency circuits. But this situation will change if a voltage V_{dc} is applied. One can apply classical network analyze to circuits in Figure 9.2, with or without the 50 Ω in parallel, the movement induced induc-

tance decreases the total impedance, resulting a measurable change in S21 measurement.

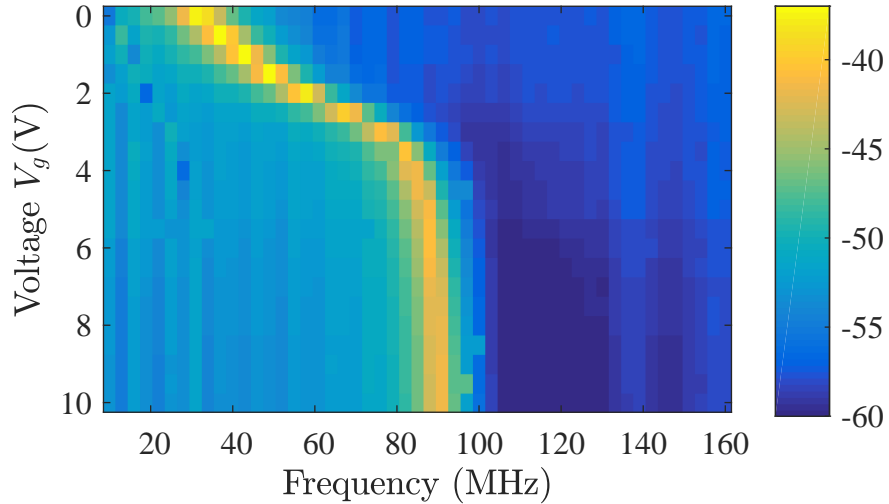


Figure 9.3: Reflection measurement of tunable LC resonator at different gate voltage V_g measured at room temperature. The LC resonator consists of an chip inductor and analog tunable capacitor, or a varactor. Resonance (Yellow color in the plot) of LC circuit changes with dc bias voltage. The frequency starts at 25MHz and saturates at ~ 90 MHz, there is no significant change in quality factor ~ 10 .

Tunable LC resonance One of the requirement of this analyze is LC resonance close to MR frequency. This is not always easily satisfied, especially when there is some uncertainty from fabrication parameters. To account for this uncertain, we replace the fixed capacitor with a varactor, which is an analog tunable capacitor and whose capacitance can be tuned with bias voltage. This tunability enable us to match the mechanical resonator frequency in a bigger range, especially in the early tests when the mechanical frequency is unknown. Figure 9.3 shows the reflection measurement of one of the LC resonator.

Difference of impedance match and impedance mismatch For nano-mechanical resonator in Ref.[61] or our membrane resonator, the induced change in LC resonance is

very small. And when the mechanical resonator frequency ω_m matches cavity frequency ω_0 , the MR signal sitting at the bottom of LC resonance is always lower than full transmission, and this sets a limit of mechanical signal we can measure. However if we change the LC resonance from a dip to a peak, limit no longer exists. Moreover Patrick's method requires accurate total impedance matching 50Ω at resonance, so that most of signal can be dumped into the cavity. Since total impedance is a function of R_m , which varies from sample to sample, or at different temperature, thus it adds more difficulties to achieve ideal impedance matching. In my impedance mismatching method, a 50Ω is connected in parallel with LC resonator, the total impedance is nearly 50Ω off resonance, and thus there is no strict requirement for total impedance, which gives more flexibility of this method.

9.3 Measurement Results

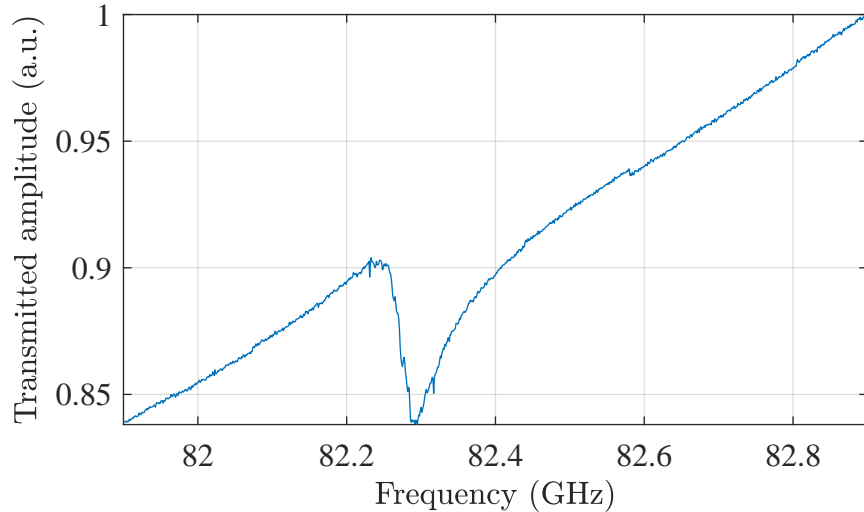


Figure 9.4: Response of a doubly clamped membrane coupled to LC impedance mismatch circuit. The membrane has a frequency of 82.3MHz and the loaded quality factor is 1400.

Using impedance match/mismatch circuit, at a sufficiently high voltage, one can observe

a small dip as shown in Figure 9.4. The doubly clamped membrane is coupled to LC50 home made PCB resonator circuit, the circuits is anchored in a vacuum ($\sim 1\text{mbar}$) probe and cooled in liquid nitrogen (LN_2). The frequency of the membrane is about 82.3MHz, which is twice higher than numerical simulation using COMSOL. The change could be a combined result of uncontrolled tension, inaccuracy from fabrication and needs more investigation in the future work. The loaded quality factor is around 1400. We expect this to get higher if we cool it down to milli-Kelvin temperature.

For several batches of samples I have tested at 77K, the successful rate of the doubly clamped membrane is relatively high $>90\%$. The free-free membrane is only about 50%.

9.3.1 Voltage dependence of doubly clamped Membrane

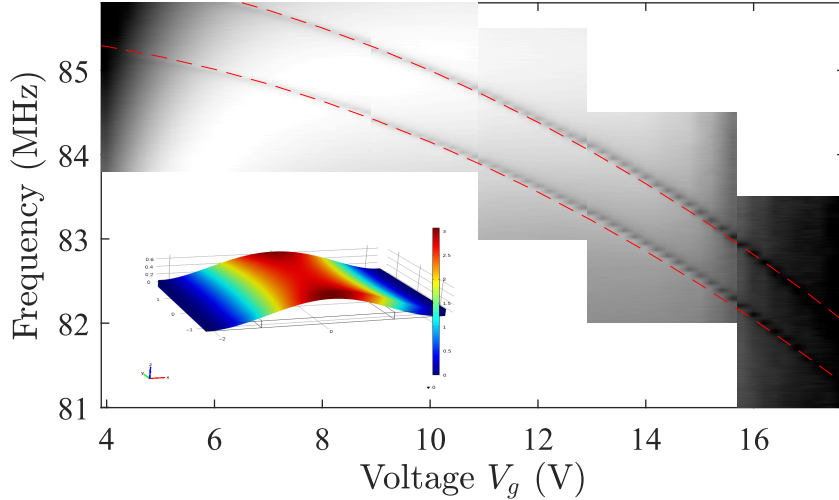


Figure 9.5: Voltage dependence of two doubly clamped membranes on the same chip. The grayness indicates the amplitude of transmitted signal. The two red dashed line are fitted results using 9.4. The inset shows the simulated mode shape of membrane.

When a voltage is applied on membrane, electrical potential decrease the distance of membrane in mechanical balance. It can be shown that the frequency of a doubly clamped

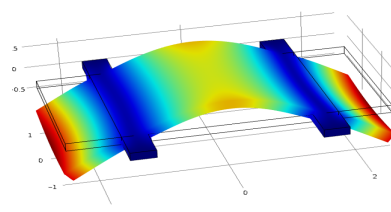
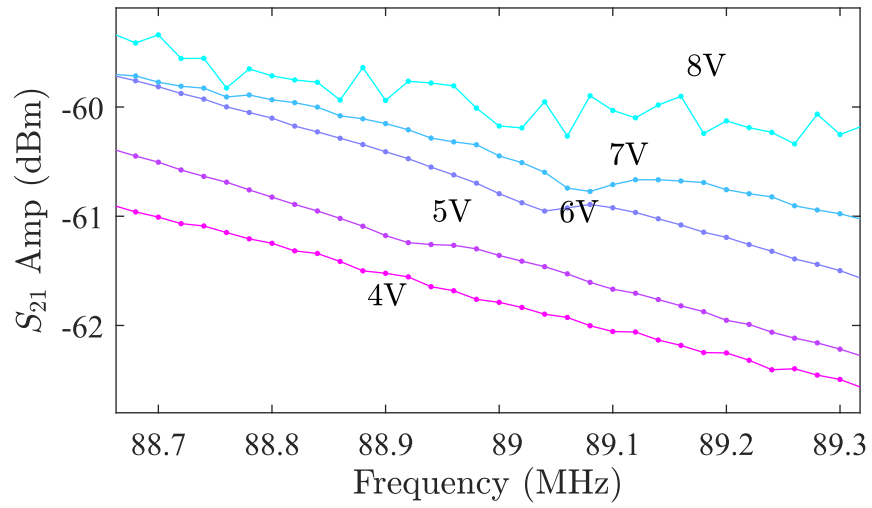
resonator is down-shifted by applied voltage V_g

$$\Delta f = -\frac{f_0 C_0}{2d^2 K_{\text{eff}}} \cdot V_g^2 \quad (9.4)$$

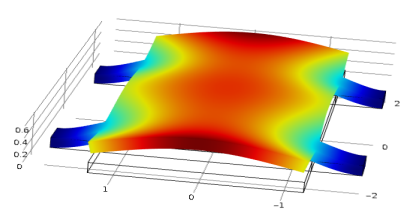
where f_0 is the bare frequency at 0V. $K_{\text{eff}} = (2\pi f_0)^2 K_{\text{eff}} = -1150\text{N/m}$ is the effective spring constant of membrane. And this is proven by varying the voltage applied on the membrane. Figure 9.5 shows the voltage dependence of two doubly clamped membrane on the same chip. It is observed that the frequency decreases at larger voltage. And the resonances can be fitted to parabola with second-order coefficient -1.35Hz/V^2 is very close to the estimation -2.78Hz/V^2 .

9.3.2 Voltage dependence of Free-free membrane

In the impedance matching method, the impedance change originates from periodic change in capacitance between the top membrane layer and bottom ground layer. Thus depends on the shape, different modes have different coupling strength, refer to Chapter 3. In the free-free membrane design, the bottom pads are divided into three parts. Thus the coupling of “differential mode” is zero and thus not detectable in this set up. But the mode of whole membrane moving up and down (I call it push-up mode) is measurable. Figure 9.6 shows the voltage dependence of the resonance. I observed small peak with lower quality factor at around 89MHz. It is interesting the voltage dependence of free-free membrane is the opposite to doubly clamped ones, the frequency shift up at the larger voltage. For membranes fabricated on the same wafer, the free-free membrane has a lower success rate, I could measure only half of them using impedance method. Also after applying high voltage ($>10\text{V}$), some free-free membranes got shorted. One



differential mode



push-up mode

Figure 9.6: Voltage dependence of a free-free membrane. The lines are shifted to spread in position, and from bottom to top, $V_g=4$ to 8V.

possible reason is that the free-free membrane is supported by four thin legs, thus by applying high voltage, the electrical attraction pulls the membrane too much and results in snapping-in. As shown in Figure 9.6, in this set of data, the 8V curve is clearly more noisy than 7V. At higher voltage, the LC resonance becomes unstable, thus the data is now shown here.

9.3.3 Power dependence of doubly Clamped membrane

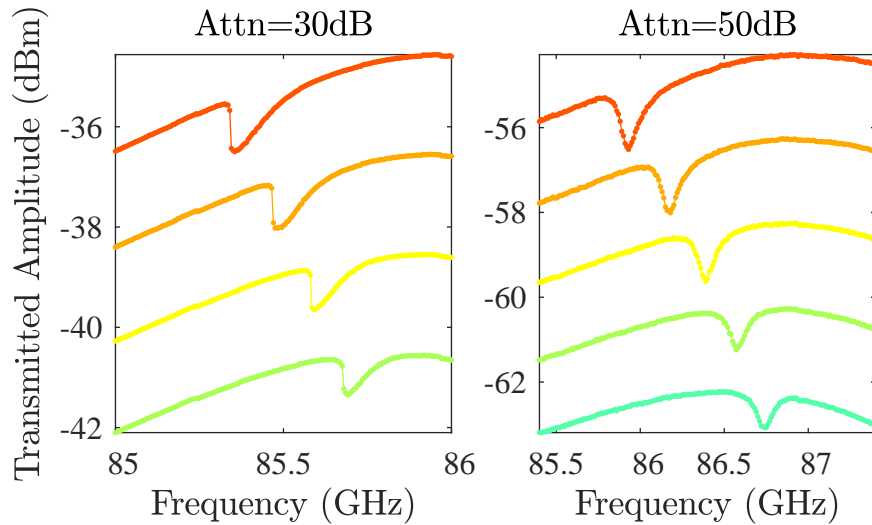


Figure 9.7: Membrane resonance at linear and nonlinear response. The set of curves on the left are excited using 20dB bigger power (or 20dB smaller attenuation), and the resonance shows more asymmetry.

In the ongoing discussion, the membrane is treated as harmonic oscillator, which is true under small drive amplitude. If the drive increases, the mechanical system starts to behave non-linearly. Figure 9.7 shows two sets of doubly clamped membrane measurement only with 20dB different driving strength (controlled by inserted attenuation).

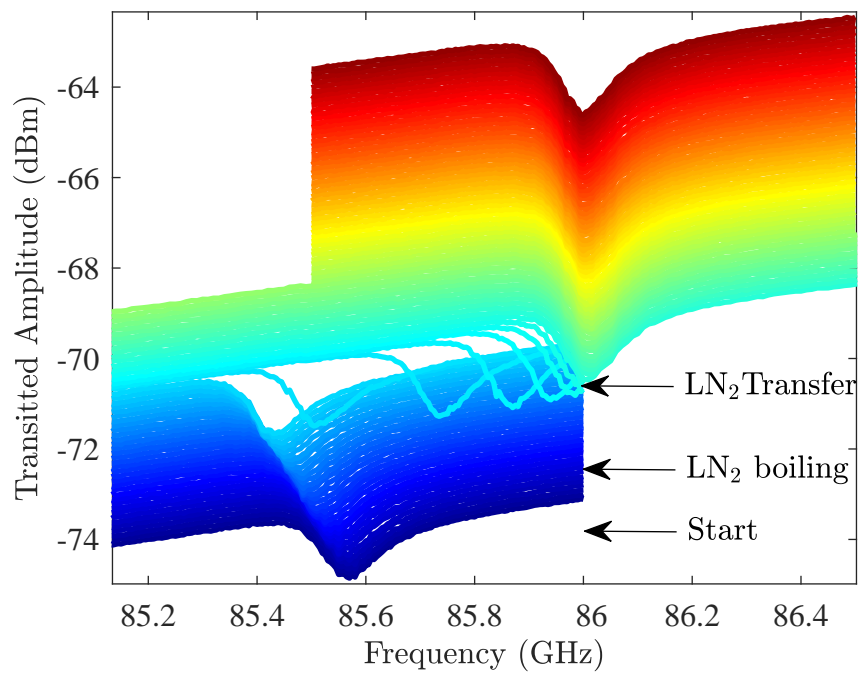


Figure 9.8: Temperature dependence of membrane resonance in the process of LN₂ boiling and transferring. The curves are shifted in y-axis so that the order of the line is from bottom to top as time elapses. The time difference between each curve is 5 minute.

9.3.4 Temperature dependence of doubly Clamped membrane

The successful realization of the measurement requires membrane staying at low temperature. I didn't intend to design and study the the effect of temperature on membrane system. The Figure 9.8 shows the frequency changes in the process of temperature changing. The measurement started when the left LN₂ was only enough to cool the bottom of the probe, and the data taking continued as LN₂ boiling off. One can observe the frequency became lower as temperature (not explicitly shown) got higher. And the frequency went back fast as soon as I transferred more LN₂ in the dewar, and saturated at 86MHz.

9.4 Conclusion

I have developed a recipe to fabricate micro-meter sized superconducting membrane resonators. The gap between the top membrane layer and bottom gate electrode layer is 40-50nm, comparable with the best results in this field. The membrane resonator is analyzed theoretically and simulated using finite element simulation software. The resonance of membrane resonator is further tested using impedance matching and impedance mismatching circuit. Quality factor of 1400 is achieved at 77K. This membrane resonator could be utilized with transmon, cavity or other type of quantum system to develop more complicated measurements.

Chapter 10

Future work

In the foregoing chapters, I presented my theoretical and experimental work on a hybrid MR-transmon-cavity system. We successfully proved interaction between the transmon and the mechanical resonator in weak resonance limit. Other goals such as observing phonon number state of mechanical resonator using dispersive shift of transmon qubit have not achieve yet. To develop more advanced experiments using this system, such as quantum thermal engine, building entanglement between mechanical resonators and generating phonon Fock state, we need to improve the sensitivity (coherence, coupling, and etc.) of transmon and improving the quality of mechanical resonator. Initial fabrication and tests of 2nd generation membrane resonator are presented in chapter 9. In this chapter, I will talk about how to increase the sensitivity using transmon as a probe.

10.1 Dispersive shift of higher energy states

In the foregoing discussion in chapter 2, we naturally choose the lowest two energy states of transmon $|g\rangle$ and $|e\rangle$ as the two level system. Now let's take a look at the dispersive shift of higher energy states. From the general equation 3.2. in chapter 2 for dispersive shift, we can further write the energy difference $\omega_j - \omega_i$ in form of

$$\omega_j - \omega_i = \hbar\chi_{ij,\text{eff}} b^\dagger b + \text{the other terms} \quad (10.1)$$

where explicitly for the lowest three states

$$\begin{cases} \chi_{ge,\text{eff}} &= \chi_{ge} - \chi_{ef}/2 \\ \chi_{gf,\text{eff}} &= (\chi_{ge} + \chi_{ef} - \chi_{fh})/2 \\ \chi_{ef,\text{eff}} &= \chi_{ef} - \chi_{ge}/2 - \chi_{ef}/2 \end{cases} \quad (10.2)$$

In transmon regime, χ_{ge} and $\chi_{ef}/2$ are usually very close. One can expect that $\chi_{ge,\text{eff}}$, which is the difference of the previous two terms, is largely nullified. This is one of the key reasons that transmon not being sensitive to charge noise in the background. On the contrast, $\chi_{gf,\text{eff}}$ is not canceled out. To easily quantize the difference, I define a dimensionless “qubit sensitivity” factor

$$\xi_{ij} = \chi_{ij,\text{eff}}/\omega_{ge} \quad (10.3)$$

By dividing ω_{ge} , one can get a dimensionless variable. And it helps to compare the ratio of change without worrying the frequency of transmon.

In Figure 10.1, I plot χ_{ij} for three lowest states. One can see that in a large range of

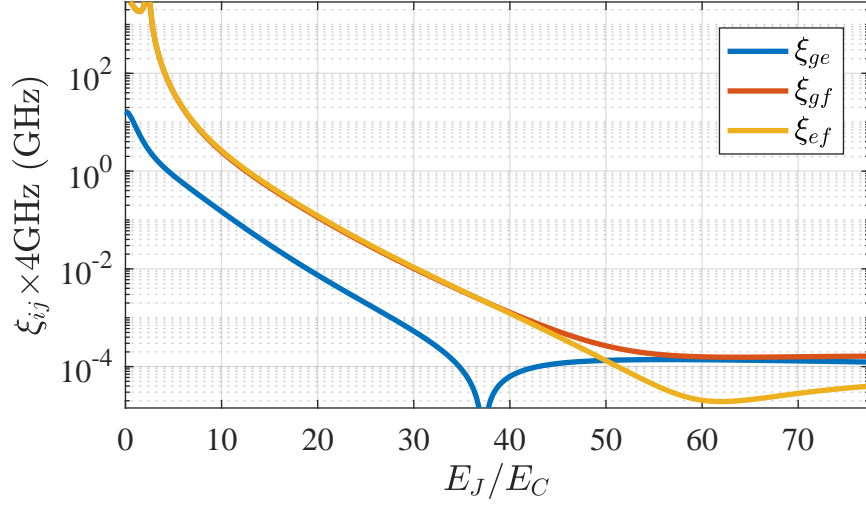


Figure 10.1: Numerically calculated ξ_{ij} as a function of E_J/E_C . To give better intuitive understanding of ξ , $\omega_{ge}=4\text{GHz}$ is multiplied. Mechanical resonator frequency is assumed $\omega_{MR}/2\pi=100\text{MHz}$.

$10 < E_J/E_c < 40$, ξ_{gf} is more than one order of magnitude bigger than ξ_{ge} , suggesting the same ξ_{ge} nullification fact mentioned above. A good experimental proof of this is the number splitting of g-e and g-f Figure 7.8 in chapter 7, it is apparent that the peaks in two-photon g-f transition have better resolution (sharper peaks).

10.2 Using two photon g-f transition as a probe

In the early proposals [62, 63] about coupling nanomechanical resonator with qubits, Cooper pair box in charge limit, which has $E_C \ll E_J$, is preferred for its big value of charge energy or high sensitivity to charge fluctuation. However high value of E_c increases the susceptibility of the CPB to charge noise, reducing its dephasing time, and in the end degrading the sensitivity of qubit. Besides, the charge jump problem requires frequent re-calibration of the bias point, adding up more difficulty to realize the measurement.

I propose to use two photon g-f transition as a probe to measure phonon number of mechanical resonator. First ξ_{gf} is more than ten times bigger, suggesting ten times bigger sensitivity than using g-e transition. At the same time, because the first order coupling $\langle g|n|f\rangle$ is zero, the charge noise induced relaxation is zero. Because the relaxation between $|e\rangle$ and $|f\rangle$ still exists, the width of resonance is going to be limit.

Optimistic E_J/E_C Another question is choice of aspect ratio of E_J and E_C . In order to decreasing the width of qubit transition, or achieving longer dephasing time T_2 , one can push more to transmon limit (larger E_J/E_C). However one will not benefit more by simply increasing ratio of E_J/E_C : the coherence times will be limited by other conditions, such as Purcell limit[39], dielectric loss, flux noise and etc [27, 39, 64, 65]. And at the same time ,the coupling strength λ between MR and tranmon, which is proportional to E_C , will decrease fast. It is difficult to directly point out the sweet point of E_J/E_C . The optimized method is to choose a relatively low aspect ratio E_J/E_C such that coherence times are limited by radiation loss though coupling capacitor to cavity. Using single junction transmon or asymmetric junctions always help to improve dephasing time.

10.3 Comparison of splitting in g-e and g-f transition

To numerically investigate the advantage of two photon g-f transition, I use Python Qutip package [66] to simulate the behavior of transmon. In this simulation, I use time-dependent evolution and finds the quasi-steady state of the system. Assuming $E_c = 0.23\text{GHz}$ and $E_J = 10\text{GHz}$, the transmon has $\omega_{ge} \sim 4\text{GHz}$ and $\omega_{ge}/2 \sim 3.9\text{GHz}$. The mechanical resonator's resonance is $\omega_{MR} = 100\text{MHz}$. The coupling strength between MR and transmon is 20MHz , an feasible value using membrane resonator.

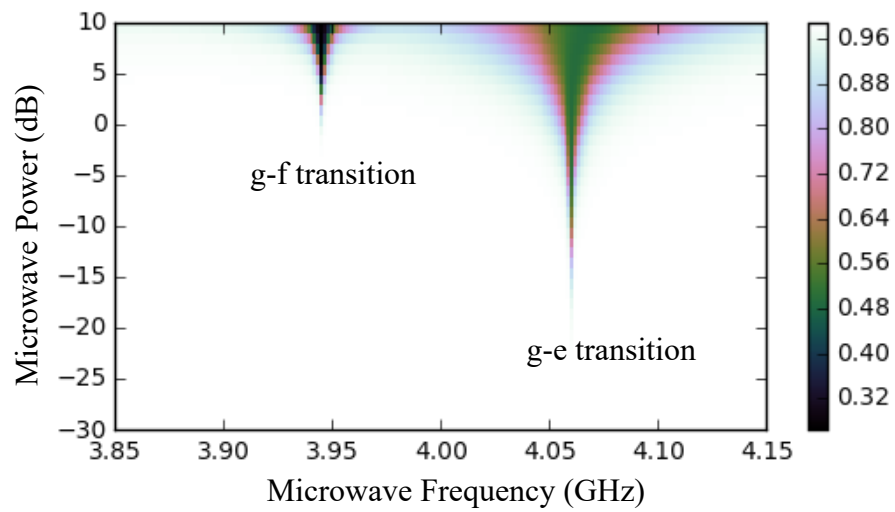


Figure 10.2: Simulation of transmon spectrum against microwave power.

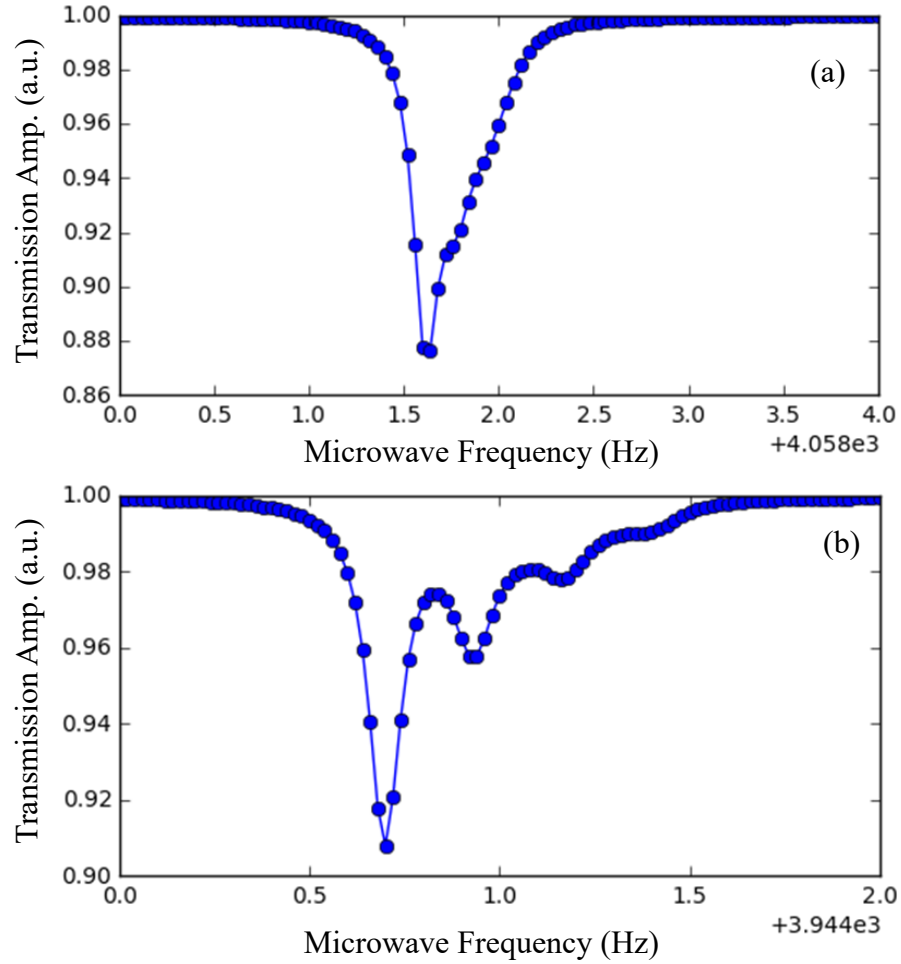


Figure 10.3: Simulation of transmon spectrum of (g-e single photon transition (a) and two-photon transition (b)). $\Gamma_q = 0.1\text{MHz}$, $Q_{MR} = 10000$, $\kappa_c = 0.28\text{MHz}$, thermal population of MR $n_t h = 1$.

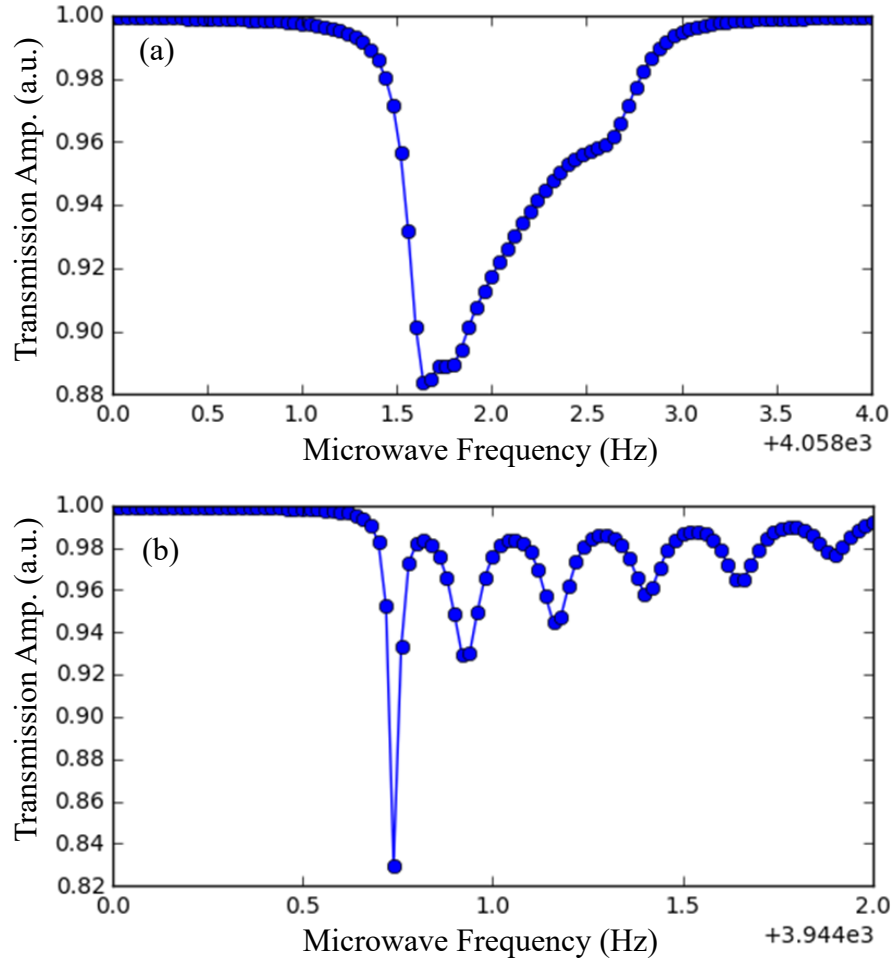


Figure 10.4: Simulation of transmon spectrum of (g-e single photon transition (a) and two-photon transition (b)). $\Gamma_q = 0.05\text{MHz}$, $Q_{MR} = 10000$, $\kappa_c = 0.28\text{MHz}$, thermal population of MR $n_t h = 3$.

Chapter 11

Conclusion

The results of this thesis is the development of hybrid system of qubit coupled mechanical resonator system. It is a platform to study coherent dynamics of hybrid electrical and mechanical degree of freedom in macroscopic eletro-mechanical systems. We first designed, fabricated, and measured a filter biased superconducting CPW cavity with the best loaded quality factor $Q_l \approx 200k$ at least one order of magnitude bigger than the results in biased CPW cavity system, which enable us to probe the microwave properties of the embedded hybrid system. Moreover this work is the first experimental investigation of the interaction between an ultra-high frequency nano-mechanical resonator and a high-quality transmon qubit. Then we fabricated and measured superconducting transmon qubit embedded in our filter biased CPW cavity. We performed continuous and time domain measurements of qubit, demonstrating basic state control and manipulation of the system. Third we designed, fabricated and measured the hybrid system of transmon qubit coupled mechanical resonator embedded in a voltage biased cavity. The best relaxation of transmon in this hybrid system is $T_1 > 15 \mu s$ and $T_2^* = 1.4 \mu s$, which is also one order of magnitude bigger than the results in electro-mechanical system

officially published. These values of cavity quality factor and qubit lifetimes move one step forward to engineer the electro-mechanical system in strong dispersive limit, where dispersive shift χ dominates all other dissipation. Truly reaching the strong coupling limit will require the quality factor of mechanical resonator to be improved by at least one order of magnitude. To achieve this goal, we designed, fabricated and measured membrane type resonator and proved quality factor $Q_{\text{MR}} \sim 1400$ at 77 K. This value, I believe, can be largely improved by cooling down to mili-Kelvin temperature and furthermore using free-free type membrane. Ultimately this will enable us to achieve strong dispersive limit of the hybrid system.

Based on the results presented in this thesis, the hybrid electro-mechanical system has at three potential for future research. The first is using transmon as a spectrometer to measure the noise and furthermore the asymmetry of the quantum noise of mechanical system. This asymmetry can be resolved by comparing the relaxation T_1 and polarization in the vicinity of ω_{MR} . Because it doesn't require the simultaneous use of sideband cooling/damping, it can provide a complimentary approach to recent experiments on quantum noise in cavity opto-mechanical system.[67][68] The second direction is to use the mechanical resonator as a reservoir with controllable coupling strength. The third direction is to use this hybrid system as a platform to explore the quantum coherent dynamics and related fundamental topics in quantum information and sensing. The tunability of transmon energy and coupling strength provide the possibility to study the system in both dispersive and resonant regime.[69],[70] [71]

Chapter 12

Appendix

12.1 High angle SEM tricks

Taking high angle($\approx 90^\circ$) SEM image is a tool to directly check the vacuum gap of membrane. It needs more steps and preparation than simply rotating the camera. For the image of membrane in chapter 5, whose angle from horizontal is $\theta < \text{atan}(50/2500) \approx 1^\circ$, the electrons have to move along the surface. Before arriving the the sample, the electron are very likely to be distorted or absorbed, resulting in charging the surface before aiming area. And when charging accumulates over time, the electron beam became highly unstable and impossible to get focused. In Figure 12.1, I am showing an SEM image distorted by charging effect.

To get a good high angle image, the sample needs to cut properly. It is better to have the membrane as close to the cross-section as possible, so the the electrons get least affected by the substrate. I used dicing saw to perform the cutting whose accuracy is about $10\mu\text{m}$. More than six membranes are fabricated on one line, so after a very close cutting, I was

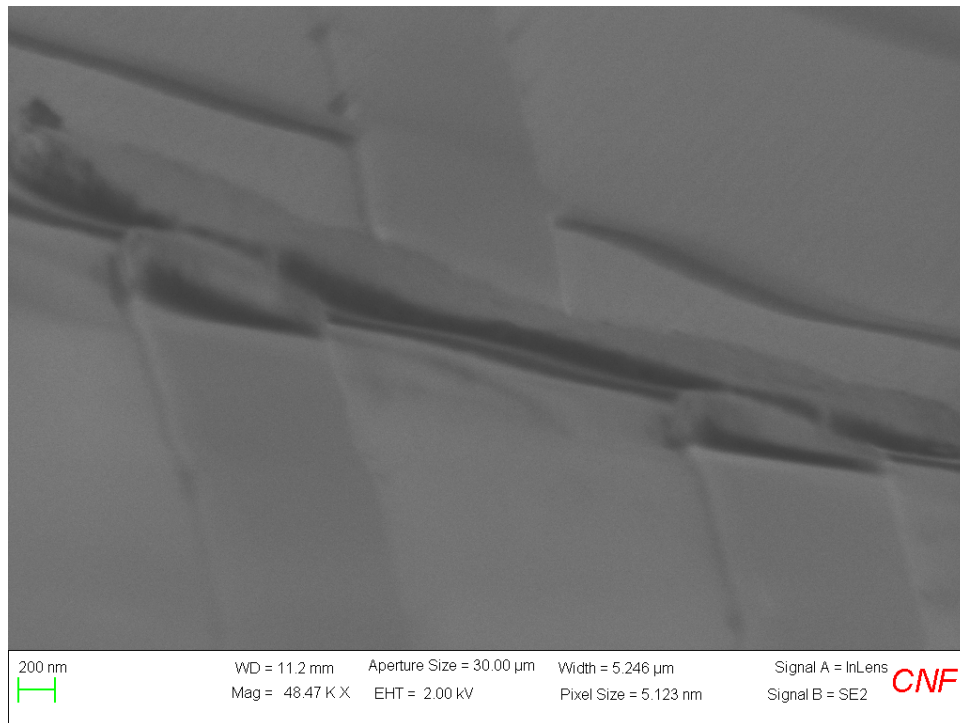


Figure 12.1: Distorted SEM image of free-free membrane by charging effect. The sample was not pre-cut.

able to have a few samples about several microns away from the edge. The dicing saw uses tap water to cool the blade, so the sample needs to be clean in isopropanol right after taking out

When imaging the membrane, the sample is prepared at a relative big angle $\sim 60^\circ$. I use a high accelerating voltage ($>10\text{kV}$) to reduce bending of the beam. Changing the angle must be accomplished slowly with shifting the sample at the same time to keep it in the center of view. I also need to change the focus intermittently. The ratio of scatter (SE2) and reflected (InLens) electrons needs to be balanced, because reflected electrons see better the side wall of membrane and electrons passing through the gap can only be captured using secondary scattered electrons. The brightness and contrast set-points are way off compared to vertical imaging. To see both (SE2 and InLens) electrons, the contrast needs to be very small and brightness is bigger.

12.2 Tools

12.2.1 Super cable Cutter

12.2.2 Twisted pair

Superconducting twisted pair is used to conduct flux bias current in our setup. Good uniformity of twisted pair increases magnetic shielding to flux noise. I develop the setup schematically shown in Figure 12.3. The key to uniformity is a constant and controllable tension. The wire is not cut into two pieces before twisting. The wire pass through the hole of a plastic washer, so that the tension everywhere on both sides of the wire is uniform. Then the washer is fixed at the end of a long spring, whose the other end

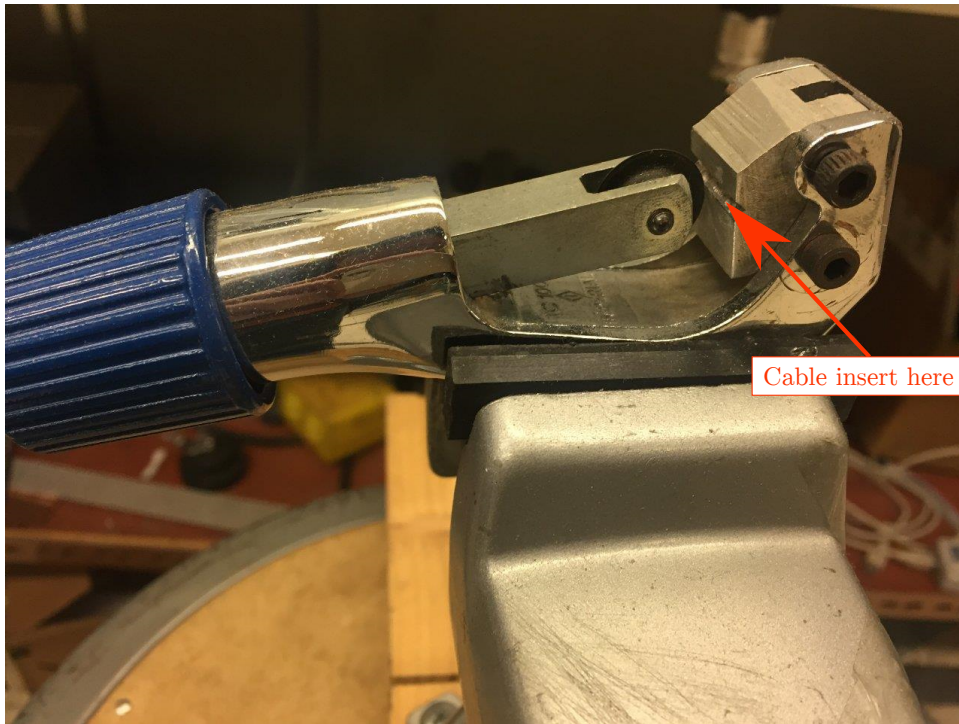


Figure 12.2: Schematic drawing of making superconducting twisted pair.

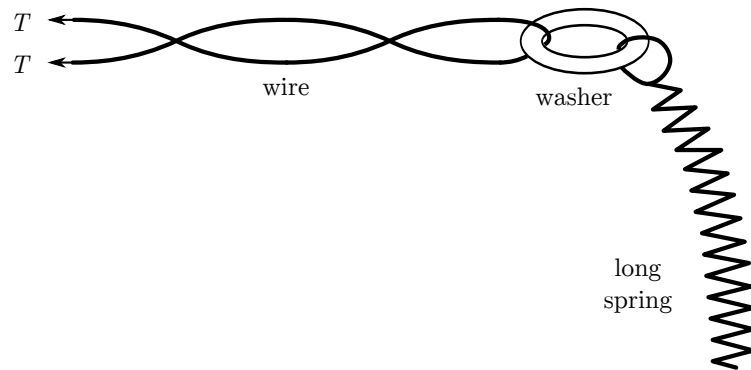


Figure 12.3: Schematic drawing of making superconducting twisted pair.

is fixed. The controllable tension is controlled by transversely bending the spring. It is advantageous for two reasons: the tension is easily controlled by pulling the ends and watched by spring bending; small movement or shaking of the wire does not lead to radical tension change.

12.3 Best MR coupling mode

In many MR electrically/optically coupled system, the freedom that is coupled is displacement \hat{x} . In the quantum regime limit, the distance is no longer a independent parameter: the zero-point displacement \hat{x}_{zp} is (not only) limited by the mode shape, as it is well know the higher order modes have much smaller zero-point displacement because of high elastic bending energy E_{el} , thus the total coupling strength is highly limited. So one would ask what is the best mode to maximize this coupling, i.e., what is the shape to maximize the ratio of \hat{x}/E_{el} .

for mode shape Before going to complicated math, several confinements can be made to simplify the search. First we are looking for symmetric curves, curves such as $\phi = k \cdot x$ giving displacement with no elastic energy are ruled out. Second, without losing generality, we can assume the mode shape $\phi(x)$ are place on the origin point. And further more, we can scale x axis, so we can study only half of the shape with $x \in [0, 1]$. So $\phi'(0) = 0$, and $\phi(0) = 0$.

The total elastic bending energy $E_{el} = \frac{1}{2}EI \int_0^1 |\phi''(x)|^2 dx$. For any $\phi(x)$, if $\phi(x_1) < 0$, we can always construct a new curve ϕ_1 that satisfies $\phi_1''(x) = |\phi''(x)|$, so that the new curve ϕ_1 has the same bending energy but gives a bigger displacement. This suggests that it is also reasonable to assume $\phi''(x) > 0$. Moreover, $\phi'(x) > 0$ is preferred.

Equation of extreme value condition In quantum limit, zero point displacement is the quantized $x_{zp} = \frac{x_{max}}{\sqrt{N}}$, and N is the number of energy quanta $N = \frac{E_{el}}{\hbar\omega}$. We can get $x_{zp} = \frac{x_{max}\sqrt{\hbar\omega}}{\sqrt{E_{el}}} \propto \frac{x_{max}}{\sqrt{E_{el}}}$.

In systems such as MR capacitively coupled to qubit, the change in capacitance $\Delta C =$ and $g = \frac{\epsilon_0 S}{d^2} x_{zp} \int_0^1 \phi dx \propto \frac{\int \phi dx}{(\int (\phi'')^2 dx)^{1/2}}$ or

$$g^2 \propto \frac{(\int \phi dx)^2}{\int (\phi'')^2 dx} \equiv \frac{F_y^2}{F_E} \equiv P$$

where F_y and F_E represent the integrals. P is the value we want to maximize by varying ϕ . One can calculate the functional derivatives of P ,

$$\frac{\delta P}{\delta \phi} = \frac{2F_y^2}{F_E} \frac{\delta F_y}{\delta \phi} - \frac{F_y^2}{F_E^2} \frac{\delta F_E}{\delta \phi} = 0$$

. And from definition we can get

$$F_y = \int \phi dx \quad \Rightarrow \quad \delta F_y = \int \delta \phi dx \quad \Rightarrow \quad \frac{\delta F_y}{\delta \phi} = 1$$

and

$$\begin{aligned}
F_E &= \int (\phi'')^2 dx \\
\delta F_E &= \int 2\phi'' \cdot \delta\phi'' dx \\
&= \int 2\phi'' \cdot \frac{\partial}{\partial x}(\delta\phi') dx \\
&= 2 \int \frac{\partial}{\partial x}(\phi'' \delta\phi') - \delta\phi' \frac{\partial}{\partial x}(\phi'') dx \\
&= 2\phi'' \delta\phi' \Big|_0^1 - 2 \int \delta\phi' \cdot \phi''' dx \\
&= 2\phi'' \delta\phi' \Big|_0^1 - 2 \int \frac{\partial}{\partial x}(\delta\phi) \cdot \phi''' dx \\
&= (2\phi'' \delta\phi' - 2\delta\phi \cdot \phi''') \Big|_0^1 + 2 \int \delta\phi \cdot \phi'''' dx
\end{aligned}$$

So

$$\frac{\delta F_E}{\delta\phi} = \phi''''$$

. Combined with $\frac{\delta P}{\delta\phi}$, we can get

$$\phi'''' = \frac{F_E}{F_y} \tag{12.1}$$

Note this means ϕ'''' is independent with x, indicating $\phi(x) = ax^4 + bx^3 + cx^2 + dx + e$. With the condition $\phi(0) = 0$ and $\phi'(0) = 0$, it is further simplified to $\phi(x) = ax^4 + bx^3 + cx^2$.

Then one can substitute this in P , and find out the partial derivatives

$$\left. \begin{aligned} \frac{\partial P}{\partial q_i} &= 0 \\ \frac{\partial^2 P}{\partial q_i^2} &< 0 \end{aligned} \right\} \text{for } q_i = a, b, c$$

The solutions can be found $a = \frac{1}{6}, b = -\frac{2}{3}, c = 1$.

$$\phi(x) = x^2 - \frac{2}{3}x^3 + \frac{1}{6}x^4. \quad (12.2)$$

Discussion This form is exact the same shape as a uniformly pressed beam clamped hung at center[25]. This is no coincidence: imagine a beam bent by gravitational force, and maximization of P is equivalent with minimization of Gibbs energy. P as an indication of coupling strength of specific mode shape, we can calculate and compare this value for different mode. For best case, $P = 0.05$. For a doubly clamped MR, $P = 0.0022$. For a free-free clamped MR, $P = 0$, but if we expand the definition of displacement to $|\phi(x)|$, $P = 0.02446$.

12.4 Transmon Capacitance matrix

To estimate the effective capacitance C_{eff} and charge energy E_C , we can follow the method as in Kock's paper[14]. See Figure 12.4, because the scale of transmon pads are much smaller than cavity frequency wavelength, the network can be treated as plain dc capacitances C_{ij} , where $i, j = 1, 2, 3, 4$. One can build a capacitance matrix

$$\mathbf{C} = \begin{pmatrix} C_{11} & C_{12} & C_{13} & C_{14} \\ C_{12} & C_{22} & C_{23} & C_{24} \\ C_{13} & C_{23} & C_{33} & C_{34} \\ C_{14} & C_{24} & C_{34} & C_{44} \end{pmatrix}$$

where $C_{ii} = -\sum_{i \neq j} C_{ij}$ is the total self-capacitance. Each metal is also associated with a voltage potential V_i , and a net charge Q_i . These obey linear equations, and can be

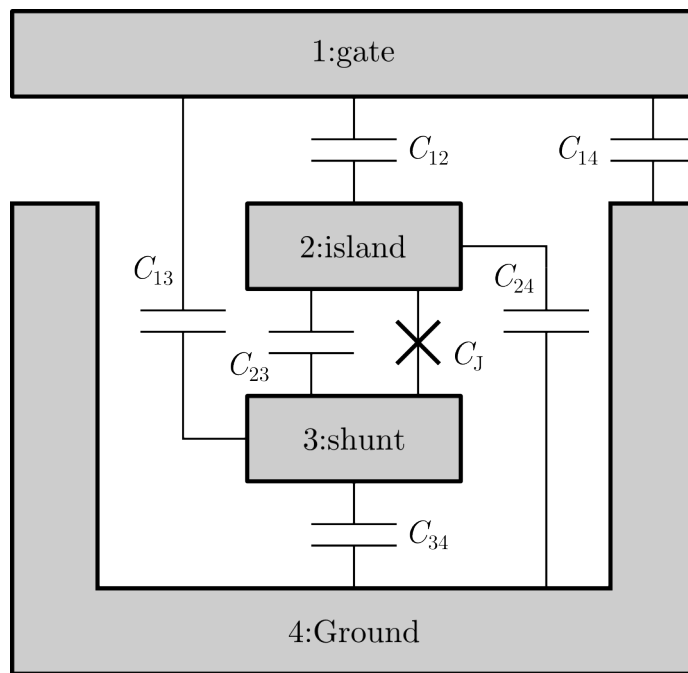


Figure 12.4: schematic drawing of transmon qubit and full network of capacitance matrix. 4 gray pieces are representing superconducting metals. Only metal near the qubit is shown. The size of transmon pad, $\sim 100\mu\text{m}$, are much smaller than GHz wavelength, so we can apply dc analyze to the network. C_{ij} is the mutual capacitance between metals. C_J is the capacitance of Josephson junction, which is usually much smaller than C_{23} and can be absorbed into C_{23} or simply neglected.

written as $Q_i = C_{ij} \cdot V_j$ or $\mathbf{Q} = \mathbf{C} \cdot \mathbf{V}$.

voltage division The voltage division β in equation 2.24 can be calculated by adding opposite charges on gate and Ground,i.e. $\mathbf{Q} = (1, 0, 0, -1)^\top$, and voltage potentials can be calculate from inverse of capacitance matrix $\mathbf{V} = \mathbf{C}^{-1} \cdot \mathbf{Q}$. According to definition,

$$\begin{aligned} \beta &= \frac{V_2 - V_3}{V_1 - V_4} \\ &= \frac{C_{12}C_{34} - C_{13}C_{24}}{C_{22}C_{33} - C_{23}^2} \end{aligned} \quad (12.3)$$

Note that I applied the approximation: $C_{44} \sim C_{34} \gg C_{11} \sim C_{14} \gg$ all the others.

Effective capacitance Similarly we can find the effective capacitance of transmon qubit by adding opposite charges on island and shunt metal,i.e. $\mathbf{Q} = (0, 1, -1, 0)^\top$.

$$\begin{aligned} C_{\text{eff}} &= 1/(V_2 - V_3) \\ &= \frac{C_{22}C_{33} - C_{23}^2}{C_{33} + 2C_{23} + C_{22}} \\ &= - \left(C_{23} + \frac{1}{\frac{1}{C_{24} + C_{12}} + \frac{1}{C_{34} + C_{13}}} \right) \end{aligned} \quad (12.4)$$

12.5 Interesting images

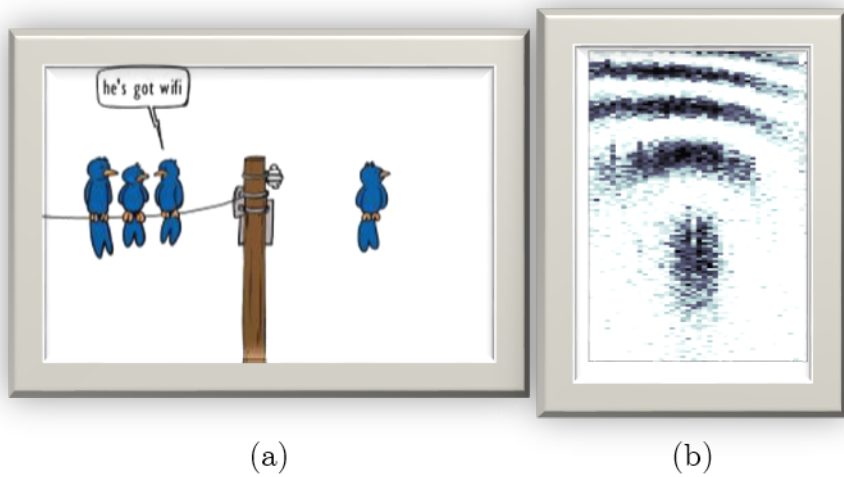


Figure 12.5: I've got wifi!! (a) A popular comics "he's got wifi". (b) A Ramsey oscillation versus excitation frequency. Color scale is adjusted manually.

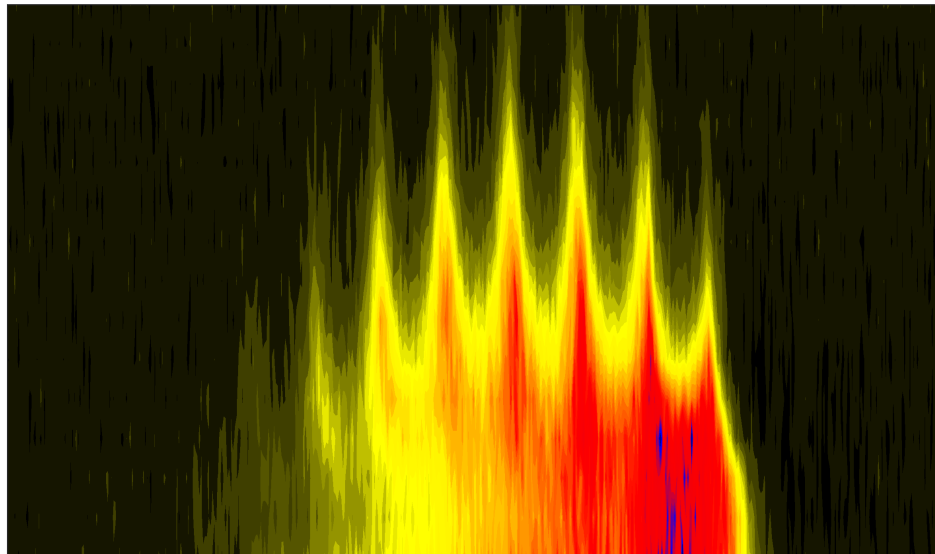


Figure 12.6: On fire!! Same data as Figure 7.9, color scale is manually adjusted to appear like fire.

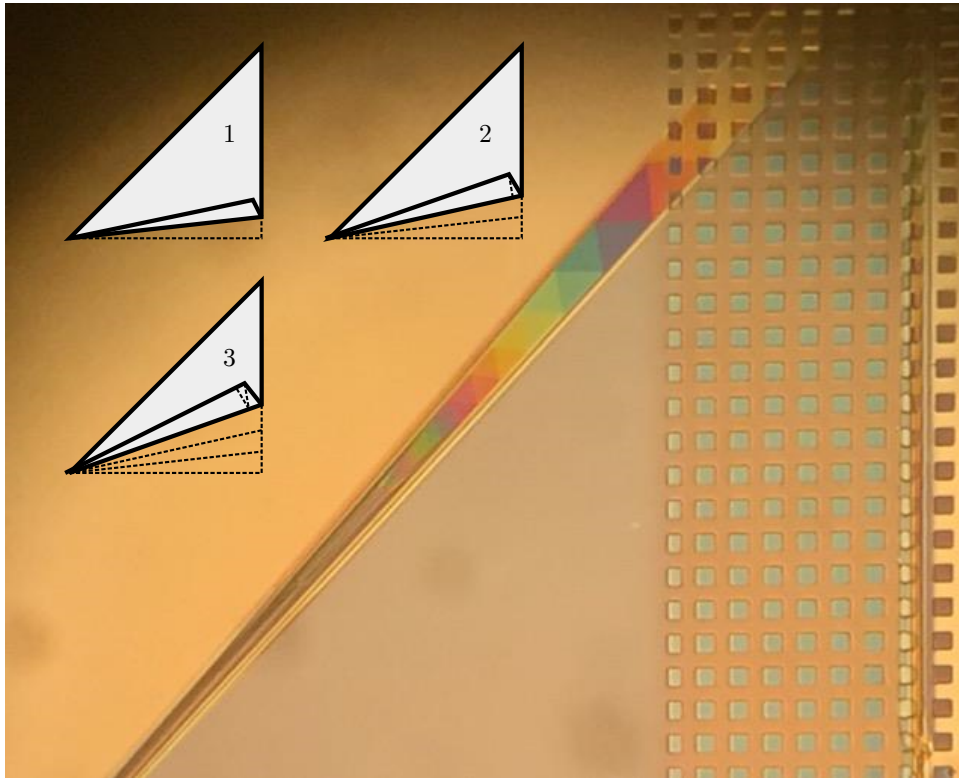


Figure 12.7: Rainbow of photo resist in microscope. This is optical reflection interference of a multi-layer photo resist. The resist is teared up from the right bottom corner and continue folding up, explained using schematic drawings denoted as “1”, “2”, “3”.

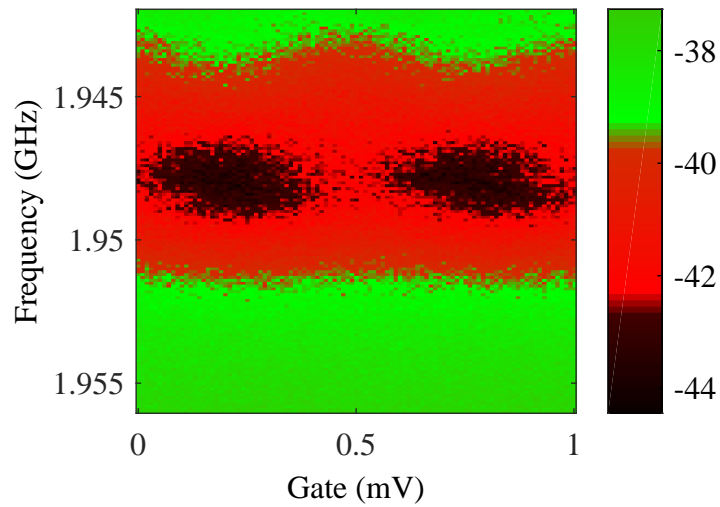


Figure 12.8: Eye mask of Ninja Turtle. One tone spectroscopy of 1st generation Lumped LC resonator coupled to a Cooper pair box. Color scale is manually changed.

Bibliography

- [1] a. N. Cleland and M. L. Roukes. Fabrication of high frequency nanometer scale mechanical resonators from bulk Si crystals. *Applied Physics Letters*, 69(18):2653–2655, 1996.
- [2] D. G. Blair, E. N. Ivanov, M. E. Tobar, P. J. Turner, F. Van Kann, and I. S. Heng. High sensitivity gravitational wave antenna with parametric transducer readout. *Physical Review Letters*, 74(11):1908–1911, mar 1995.
- [3] Sabine Hossenfelder. Minimal length scale scenarios for quantum gravity, mar 2013.
- [4] R. J. Schoelkopf, P. Wahlgren, A. A. Kozhevnikov, P. Delsing, and D. E. Prober. Radio-frequency single-electron transistor (RF-SET): a fast and ultrasensitive electrometer. *Doktorsavhandlingar vid Chalmers Tekniska Hogskola*, 280(1460):1238–1242, 1998.
- [5] M. Göppl, A. Fragner, M. Baur, R. Bianchetti, S. Filipp, J. M. Fink, P. J. Leek, G. Puebla, L. Steffen, and A. Wallraff. Coplanar waveguide resonators for circuit quantum electrodynamics. *Journal of Applied Physics*, 104(11), 2008.
- [6] Gregory M. Harry, Insik Jin, Ho Jung Paik, Thomas R. Stevenson, and Frederick C.

- Wellstood. Two-stage superconducting-quantum-interference-device amplifier in a high-Q gravitational wave transducer. *Appl. Phys. Lett.*, 76(2000):1446–1448, 2000.
- [7] M.D. LaHaye, O. Buu, B. Camarota, and K.C. Schwab. Approaching the quantum limit of a Nanomechanical resonator. *Science*, 304(5667):74–78, 2004.
- [8] K.L. L. Ekinici and M. L. Roukes. Nanoelectromechanical systems. *Review of Scientific Instruments*, 76(6):061101, jun 2005.
- [9] M D LaHaye, J Suh, P M Echternach, K C Schwab, and M L Roukes. Nanomechanical measurements of a superconducting qubit. *Nature*, 459(7249):960–4, 2009.
- [10] A D O’Connell, M Hofheinz, M Ansmann, Radoslaw C Bialczak, M Lenander, Erik Lucero, M Neeley, D Sank, H Wang, M Weides, J Wenner, John M Martinis, and a N Cleland. Quantum ground state and single-phonon control of a mechanical resonator. *Nature*, 464(7289):697–703, apr 2010.
- [11] J.-M Pirkkalainen, S U Cho, Jian Li, G S Paraoanu, P J Hakonen, and M A Silanpää. Hybrid circuit cavity quantum electrodynamics with a micromechanical resonator. *Nature*, 494(7436):211–5, 2013.
- [12] D M Pozar. *Microwave Engineering*. Wiley, 2004.
- [13] A Wallraff, D. I. Schuster, A Blais, L Frunzio, R. S. Huang, J Majer, S Kumar, S. M. Girvin, and R. J. Schoelkopf. Strong coupling of a single photon to a superconducting qubit using circuit quantum electrodynamics. *Nature*, 431(7005):162–167, sep 2004.
- [14] Jens Koch, Terri M. Yu, Jay Gambetta, A. A. Houck, D. I. Schuster, J. Majer, Alexandre Blais, M. H. Devoret, S. M. Girvin, and R. J. Schoelkopf. Charge-insensitive qubit design derived from the Cooper pair box. *Physical Review A - Atomic, Molecular, and Optical Physics*, 76(4):042319, oct 2007.

- [15] J. D. Teufel, T. Donner, Dale Li, J. W. Harlow, M. S. Allman, K. Cicak, A. J. Sirois, J. D. Whittaker, K. W. Lehnert, and R. W. Simmonds. Sideband cooling of micromechanical motion to the quantum ground state. *Nature*, 475(7356):359–63, jul 2011.
- [16] The Aspelmeyer Group, Markus Aspelmeyer, Pierre Meystre, and Keith Schwab. Quantum optomechanics. *Physics Today*, 65(7):29, jul 2012.
- [17] Elinor Kathryn Irish. *The Theory of Quantum Electromechanics : A Solid-State Analog of Quantum Optics* by. PhD thesis, University of Rochester, 2006.
- [18] Jochen Braumüller, Joel Cramer, Steffen Schlör, Hannes Rotzinger, Lucas Radtke, Alexander Lukashenko, Ping Yang, Sebastian T. Skacel, Sebastian Probst, Michael Marthaler, Lingzhen Guo, Alexey V. Ustinov, Martin Weides, Jochen Braumüller, Joel Cramer, Steffen Schlör, Hannes Rotzinger, Lucas Radtke, Alexander Lukashenko, Ping Yang, Sebastian T. Skacel, Sebastian Probst, Michael Marthaler, Lingzhen Guo, Alexey V. Ustinov, and Martin Weides. Multiphoton dressing of an anharmonic superconducting many-level quantum circuit. *Physical Review B - Condensed Matter and Materials Physics*, 91(5):054523, 2015.
- [19] D I Schuster, a a Houck, J a Schreier, A Wallraff, J M Gambetta, A Blais, L Frunzio, J Majer, B Johnson, M H Devoret, S M Girvin, and R J Schoelkopf. Resolving photon number states in a superconducting circuit. *Nature*, 445(7127):515–518, feb 2007.
- [20] A. A. Clerk and D. Wahyu Utami. Using a qubit to measure photon-number statistics of a driven thermal oscillator. *Physical Review A - Atomic, Molecular, and Optical Physics*, 75(4):042302, apr 2007.

- [21] A. A. Clerk, M. H. Devoret, S. M. Girvin, Florian Marquardt, and R. J. Schoelkopf. Introduction to quantum noise, measurement, and amplification. *Reviews of Modern Physics*, 82(2):1155–1208, apr 2010.
- [22] R. J. Schoelkopf, A. A. Clerk, S. M. Girvin, K. W. Lehnert, and M. H. Devoret. Qubits as Spectrometers of Quantum Noise. *Quantum Noise in Mesoscopic Physics*, pages 175–203, 2003.
- [23] Fei Chen, A. J. Sirois, R. W. Simmonds, and A. J. Rimberg. Introduction of a dc bias into a high- Q superconducting microwave cavity. *Applied Physics Letters*, 98(13):132509, mar 2011.
- [24] K D Petersson, L W McFaul, M D Schroer, M Jung, J M Taylor, A A Houck, and J R Petta. Circuit quantum electrodynamics with a spin qubit. *Nature*, 490(7420):380–3, 2012.
- [25] Silvan Schmid, Luis Guillermo Villanueva, and Michael Lee Roukes. *Fundamentals of nanomechanical resonators*. Springer International Publishing, 2016.
- [26] Evan Jeffrey, Daniel Sank, J. Y. Mutus, T. C. White, J. Kelly, R. Barends, Y. Chen, Z. Chen, B. Chiaro, A. Dunsworth, A. Megrant, P. J. O’Malley, C. Neill, P. Roushan, A. Vainsencher, J. Wenner, A. N. Cleland, and John M. Martinis. Fast accurate state measurement with superconducting qubits. *Physical Review Letters*, 112(19):190504, may 2014.
- [27] M. D. Hutchings, Jared B. Hertzberg, Yebin Liu, Nicholas T. Bronn, George A. Keefe, Jerry M. Chow, and B. L. T. Plourde. Tunable Superconducting Qubits with Flux-Independent Coherence. pages 1–5, 2017.
- [28] I Wilson-Rae. Intrinsic dissipation in nanomechanical resonators due to phonon

- tunneling. *Physical Review B - Condensed Matter and Materials Physics*, 77(24), 2008.
- [29] Frank Pobell. *Matters and methods at Low Temperatures*. Springer Berlin Heidelberg, 2007.
- [30] M. D. Reed, L. Dicarlo, B. R. Johnson, L. Sun, D. I. Schuster, L. Frunzio, and R. J. Schoelkopf. High-fidelity readout in circuit quantum electrodynamics using the jaynes-cummings nonlinearity. *Physical Review Letters*, 105(17):173601, oct 2010.
- [31] A. Schliesser, R. Rivière, G. Anetsberger, O. Arcizet, and T. J. Kippenberg. Resolved-sideband laser cooling of a micro-mechanical oscillator. *2008 Conference on Quantum Electronics and Laser Science Conference on Lasers and Electro-Optics, CLEO/QELS*, 1:415–419, 2008.
- [32] C. A. Regal, J. D. Teufel, and K. W. Lehnert. Measuring nanomechanical motion with a microwave cavity interferometer. *Nature Physics*, 4(7):555–560, jul 2008.
- [33] K. Bladh, D. Gunnarsson, E. Hürfeld, S. Devi, C. Kristoffersson, B. Smålander, S. Pehrson, T. Claeson, P. Delsing, and M. Taslakov. Comparison of cryogenic filters for use in single electronics experiments. *Review of Scientific Instruments*, 74(3 I):1323–1327, 2003.
- [34] David Schuster. Circuit Quantum Electrodynamics. *PhD Thesis*, 1, 2015.
- [35] A Lukashenko and A V Ustinov. Improved powder filters for qubit measurements. *Review of Scientific Instruments*, 79(1), 2008.
- [36] Henry W. Ott. *Electromagnetic Compatibility Engineering (Google eBook)*. Wiley, 2011.

- [37] Alexandre Blais, Ren Shou Huang, Andreas Wallraff, S. M. Girvin, and R. J. Schoelkopf. Cavity quantum electrodynamics for superconducting electrical circuits: An architecture for quantum computation. *Physical Review A - Atomic, Molecular, and Optical Physics*, 69(6):062320, jun 2004.
- [38] A. Wallraff, D Schuster, A. Blais, L. Frunzio, R.-S. Huang, J. Majer, S. Kumar, S. M. Girvin, and R. J. Schoelkopf. Circuit Quantum Electrodynamics: Coherent Coupling of a Single Photon to a Cooper Pair Box. *Nature*, 431(7005):162–167, sep 2004.
- [39] A A Houck, J A Schreier, B R Johnson, J M Chow, Jens Koch, J M Gambetta, D I Schuster, L Frunzio, M H Devoret, S M Girvin, and R J Schoelkopf. Controlling the spontaneous emission of a superconducting transmon qubit. *Physical Review Letters*, 101(8), 2008.
- [40] B.H. Bransden and C.J. Joachain. *Physics of Atoms and Molecules (2nd Edition)*. Pearson Education. Prentice Hall, 2003.
- [41] A. Wallraff, D. I. Schuster, A. Blais, L. Frunzio, J. Majer, M. H. Devoret, S. M. Girvin, and R. J. Schoelkopf. Approaching unit visibility for control of a superconducting qubit with dispersive readout. *Physical Review Letters*, 95(6), 2005.
- [42] Radoslaw C. Bialczak, R. McDermott, M. Ansmann, M. Hofheinz, N. Katz, Erik Lucero, Matthew Neeley, A. D. O’Connell, H. Wang, A. N. Cleland, and John M. Martinis. $1/f$ Flux Noise in Josephson Phase Qubits. *Physical Review Letters*, 99(18):187006, nov 2007.
- [43] Yu Hao, Francisco Rouxinol, and M. D. Lahaye. Development of a broadband reflective T-filter for voltage biasing high-Q superconducting microwave cavities. *Applied Physics Letters*, 105(22):222603–7, 2014.

- [44] J. Niemeyer and V. Kose. Observation of large dc supercurrents at nonzero voltages in Josephson tunnel junctions. *Applied Physics Letters*, 29(6):380–382, 1976.
- [45] G. J. Dolan. Offset masks for lift-off photoprocessing. *Applied Physics Letters*, 31(5):337–339, 1977.
- [46] Kirill Bordo and Horst Günter Rubahn. Effect of deposition rate on structure and surface morphology of thin evaporated al films on Dielectrics and Semiconductors. *Medziagotyra*, 18(4):313–317, 2012.
- [47] C. M. Quintana, A. Megrant, Z. Chen, A. Dunsworth, B. Chiaro, R. Barends, B. Campbell, Yu Chen, I. C. Hoi, E. Jeffrey, J. Kelly, J. Y. Mutus, P. J J O’Malley, C. Neill, P. Roushan, D. Sank, A. Vainsencher, J. Wenner, T. C. White, A. N. Cleland, and John M. Martinis. Characterization and reduction of microfabrication-induced decoherence in superconducting quantum circuits. *Applied Physics Letters*, 105(6):062601, aug 2014.
- [48] Adam M Urbanowicz, Kris Vanstreels, Denis Shamiryan, Stefan De Gendt, and Mikhail R Baklanov. Effect of Porogen Residue on Chemical, Optical, and Mechanical Properties of CVD SiCOH Low-k Materials. *Electrochemical and Solid State Letters*, 12(8):H292, 2009.
- [49] A D Armour, M P Blencowe, and K C Schwab. Entanglement and decoherence of a micromechanical resonator via coupling to a Cooper-pair box. *Physical Review Letters*, 88(14):148301/1–148301/4, 2002.
- [50] M P Blencowe and A D Armour. Probing the quantum coherence of a nanomechanical resonator using a superconducting qubit: II. Implementation. *New Journal of Physics*, 10(9):095005, sep 2008.

- [51] L. Tian, M. S. Allman, and R. W. Simmonds. Parametric coupling between macroscopic quantum resonators. *New Journal of Physics*, 10, 2008.
- [52] J. B. Hertzberg, T. Rocheleau, T. Ndukum, M. Savva, A. A. Clerk, and K. C. Schwab. Back-action Evading Measurements of Nanomechanical Motion. *Nature Physics*, 6(3):19, mar 2009.
- [53] Ze-Liang Xiang, Sahel Ashhab, J. Q. You, and Franco Nori. Hybrid quantum circuits: Superconducting circuits interacting with other quantum systems. *Rev. Mod. Phys.*, 85(2):623, apr 2013.
- [54] T. A. Palomaki, J. D. Teufel, R. W. Simmonds, and K. W. Lehnert. Entangling mechanical motion with microwave fields. *Science (New York, N. Y.)*, 342(6159):710–3, 2013.
- [55] Jiansong Gao. *The Physics of Superconducting Microwave Resonators*. PhD thesis, California Institute of Technology, 2008.
- [56] John M Martinis, K B Cooper, R. McDermott, Matthias Steffen, Markus Ansmann, K D Osborn, K Cicak, Seongshik Oh, D P Pappas, R W Simmonds, and Clare C Yu. Decoherence in Josephson qubits from dielectric Loss. *Physical Review Letters*, 95(21), 2005.
- [57] Aaron D. O’Connell, M. Ansmann, R. C. Bialczak, M. Hofheinz, N. Katz, Erik Lucero, C. McKenney, M. Neeley, H. Wang, E. M. Weig, A. N. Cleland, and J. M. Martinis. Microwave dielectric loss at single photon energies and millikelvin temperatures. *Applied Physics Letters*, 92(11):1–4, 2008.
- [58] F. Rouxinol, Y. Hao, Frederico Brito, A. O. Caldeira, E. K. Irish, and M. D. LaHaye.

Measurements of nanoresonator-qubit interactions in a hybrid quantum electromechanical system. *Nanotechnology*, 27(36):364003, 2016.

- [59] K. Mendelssohn. Thermal conductivity of superconductors. *Physica*, 24:S53–S62, sep 1958.
- [60] P Rowell. The Thermal Conductivity of Some Superconductors. *Proceedings of the Royal Society of London. Series A Mathematical and Physical Sciences*, 254:542–550, 1960.
- [61] Patrick A Truitt, Jared B Hertzberg, C C Huang, Kamil L Ekinci, and Keith C Schwab. Efficient and sensitive capacitive readout of nanomechanical resonator arrays. *Nano Letters*, 7(1):120–126, 2007.
- [62] A. D. Armour, M. P. Blencowe, and K. C. Schwab. Entanglement and Decoherence of a Micromechanical Resonator via Coupling to a Cooper-Pair Box. *Physical Review Letters*, 88(14):148301, mar 2002.
- [63] E. K. Irish and K. Schwab. Quantum measurement of a coupled nanomechanical resonator Cooper-pair box system. *Physical Review B*, 68(15):155311, 2003.
- [64] Josephine B Chang, Michael R Vissers, Antonio D Córcoles, Martin Sandberg, Jiansong Gao, W David, Jerry M Chow, Jay M Gambetta, Mary Beth Rothwell, George A Keefe, Matthias Steffen, P Pappas, D C Antonio, David W Abraham, and David P Pappas. Improved superconducting qubit coherence using titanium nitride. Improved superconducting qubit coherence using titanium nitride. 012602:18–21, 2013.
- [65] C Wang, C Axline, Y Y Gao, T Brecht, Y Chu, L Frunzio, M H Devoret, and

- R J Schoelkopf. Surface participation and dielectric loss in superconducting qubits. *Applied Physics Letters*, 107(16), 2015.
- [66] J. R. Johansson, P. D. Nation, and Franco Nori. QuTiP 2: A Python framework for the dynamics of open quantum systems. *Computer Physics Communications*, 184(4):1234–1240, nov 2013.
- [67] F Lecocq, J D Teufel, J Aumentado, and R W Simmonds. Resolving the vacuum fluctuations of an optomechanical system using an artificial atom. *Nature Physics*, 11(June):1–5, 2015.
- [68] Amir H Safavi-Naeini, Jasper Chan, Jeff T Hill, Thiago P Mayer Alegre, Alex Krause, and Oskar Painter. Observation of quantum motion of a nanomechanical resonator. *Physical Review Letters*, 108(3), 2012.
- [69] A J Leggett. Testing the limits of quantum mechanics: motivation, state of play, prospects. *Journal of Physics: Condensed Matter*, 14(15):R415–R451, 2002.
- [70] D Wahyu Utami and A A Clerk. Entanglement dynamics in a dispersively coupled qubit-oscillator system. *Physical Review A - Atomic, Molecular, and Optical Physics*, 78(4), 2008.
- [71] A Asadian, C Brukner, and P Rabl. Probing macroscopic realism via Ramsey correlation measurements. *Physical Review Letters*, 112(19), 2014.

Yu Hao

Email: yuhao@sry.edu

Address: Department of Physics, Syracuse University, Syracuse, NY, 13244

Education

B.S., Physics, Nanjing University, 2010

Professional Experience

2011 - 2017, Teaching or Research Assistant, Syracuse University

Publications

1. Rouxinol, F., **Hao, Y.** et al. Measurements of nanoresonator-qubit interactions in a hybrid quantum electromechanical system. *Nanotechnology* 27, 364003 (2016).
2. LaHaye, M. D., **Hao, Y.** et al. Superconducting Circuitry for Quantum Electromechanical Systems. in *Proc. SPIE 20* (International Society for Optics and Photonics, 2015). doi:10.1117/12.2182719
3. **Hao, Y.**, Rouxinol, F. , Lahaye, M. D. Development of a broadband reflective T-filter for voltage biasing high-Q superconducting microwave cavities. *Appl. Phys. Lett.* 105, 222603–7 (2014).

Presentations and Posters

1. APS March Meeting, Baltimore, March 14th-18th, 2016, “Investigations of a transmon-coupled nanoresonator in a CPW cavity”, Speaker
2. APS March Meeting, San Antonio, March 2nd-6th, 2015, “A broadband reflective filter for applying dc biases to high-Q superconducting microwave cavities”, Speaker

3. APS March Meeting, Denver, March 3th-7th, 2014, “A Qubit-Coupled Nanomechanical Resonator Integrated with a Superconducting CPW Cavity”, Speaker